KU LEUVEN

ARENBERG DOCTORAL SCHOOL
Faculty of Engineering Science

Investigation of the accuracy of an X-ray CT scanner for dimensional metrology with the aid of simulations and calibrated artifacts

Frank Welkenhuyzen

Dissertation presented in partial
fulfillment of the requirements for the
degree of Doctor in Engineering
Science

January 2016

Investigation of the accuracy of an X-ray CT scanner for dimensional metrology with the aid of simulations and calibrated artifacts

Frank WELKENHUYZEN

Examination committee:
Prof. dr. ir. P. Van Houtte, chair
Prof. dr. ir. J.-P. Kruth, supervisor
Prof. dr. ir. W. Dewulf, co-supervisor
Prof. dr. ir. M. Wevers
Prof. dr. ir. B. Lauwers
Dr. ir. J. Qian
Prof. dr. V. Cnudde
(Ghent University)

Dissertation presented in partial
fulfillment of the requirements for
the degree of Doctor
in Engineering Science

January 2016

Uitgegeven in eigen beheer, Frank Welkenhuyzen, Celestijnenlaan 300B box 2420, B-3001 Heverlee (Belgium)

Dankwoord

Er zijn vele mensen die hebben bijgedragen tot de verwezenlijking van dit werk. Via deze weg wil ik hen bedanken voor de vele hulp en steun.

Ten eerste wil ik mijn promotoren prof. Jean-Pierre Kruth en prof. Wim Dewulf bedanken. Jean-Pierre, in eerste instantie heb ik mijn masterthesis mogen afronden onder uw begeleiding. Vervolgens heeft u me de kans gegeven te starten in uw onderzoeksgroep, wat uiteindelijk leidde tot een doctoraatsonderzoek. U heeft me altijd goed ondersteund in mijn werk, en ik kon steeds rekenen op uw expertise en goede raad. Heel erg bedankt hiervoor. Wim, ook aan u heel erg bedankt voor al uw adviezen en bijdragen tot mijn onderzoek.

Daarnaast wil ik mijn dank betuigen aan prof. Martine Wevers, prof. Bert Lauwers, dr. ir. Jun Qian en prof. Veerle Cnudde voor het nalezen van de tekst en voor de constructieve opmerkingen. Prof. Paul Van Houtte dank ik voor het voorzitten van mijn preliminaire en openbare doctoraatsverdediging.

Mijn bureaugenoten, de gele trappers, wil ik bedanken omdat ze zo'n fantastische collega's waren. Iedereen die ooit deel uitmaakte van de dimensionele metrologiegroep: Philip, Nick, Bart, Ye, Gabriel, Kim, Haibin, Min, Evelina, Joachim, Catalin, Igor, Stijn, bedankt voor de fijne samenwerking. Bedankt Philip en Nick omdat jullie me in het begin van mijn onderzoek heel erg ondersteund hebben. Bart, merci voor het zo vaak nalezen van mijn teksten en voor al je steun. Joachim, bedankt voor je assistentie bij de vele metingen. Natuurlijk ook een welgemeende dankjewel aan de voltallige AM-groep, zonder jullie zou het maar stil zijn geweest op de gele trap.

Vervolgens wil ik me even richtten tot prof. Paul Vanherck. Paul, merci voor alle wijze raad die u mij heeft gegeven en voor de leerrijke babbels.

Bedankt ook aan alle collega's van het vaste personeel voor de ondersteuning. Merci Lieve, Karin, Anja, Marina, Valérie, Marijke, Eddy, Gunther, Carine, Pascal, Jan, Ronny, Ann, Jean-Pierre, Bertram, Stephanie, Peter, Regine, Luc, José, Frieda, Dirk, Rita en iedereen die ik zou vergeten zijn maar zeker niet minder dankbaar ben.

Met veel vreugde kijk ik terug op mijn tijd bij PMA. Ik wil de kleurenwiezers bedanken voor de fijne middagen en kaartavonden. De vele squashers bedank ik voor de sportieve momenten. Ook zal ik de koffietrein die regelmatig op pad ging nooit vergeten! Daarnaast zou ik nog twee mensen persoonlijk willen vernoemen: Fien en Elke, bedankt voor jullie aangename gezelschap tijdens de koffietjes, ommetjes rond de blok, spelletjesavonden en feestjes. Elke, in jouw dankwoord bedankte je me voor het luisteren naar jouw geklaag, nu is de tijd gekomen om jou terug te bedanken voor het luisteren naar míjn geklaag! Bedankt voor al je steun.

Natuurlijk heb ik ook steeds kunnen rekenen op de hulp van mijn familie. Pa, ma, bedankt voor alle kansen en de onvoorwaardelijke steun die ik van jullie kreeg. Jan, Wim, merci dat jullie als *grote broers* steeds klaarstonden met wijze raad.

Nele, schat, mijn laatste bedankje is natuurlijk voor jou. Merci om er altijd voor mij te zijn. Bedankt dat je het mij niet kwalijk nam als ik op sommige momenten te weinig tijd voor je had. Je hebt me altijd gesteund en staat altijd voor me klaar, dat apprecieer ik enorm! Bedankt voor alles, ik kijk heel erg uit naar onze verdere toekomst samen!

Frank,
Januari, 2016.

Samenvatting

Dimensionele X-stralen CT metrologie is een recente technologie die X-stralen computertomografie (CT) en dimensionele metrologie combineert. Dimensionele X-stralen CT metrologie is een aanvulling op de conventionele dimensionele meettoestellen (bv. tactiele coördinatenmeetmachines). Het onderscheidt zich van de conventionele meetmethoden door de mogelijkheid om de buitenkant zowel als de binnenkant van het object (bv. onzichtbare holtes) op een niet-destructieve manier op te meten. Dimensionele X-stralen CT metrologie is daarom een aantrekkelijk en uniek concept in de wereld van dimensionele metrologie.

Computertomografie is reeds lange tijd een veelgebruikte methode voor medische beeldverwerking en materiaalonderzoek. De uitbreiding naar dimensionele metrologie is een recente evolutie. Alle drie deze toepassingen baseren zich op hetzelfde principe maar verschillen in gebruikte hardware en procedures. Dimensionele metrologie focust op de dimensies van een product. Een correcte bepaling van de randen van het verkregen volumetrische model van het object zijn daarom cruciaal. Hoge nauwkeurigheid op het gebied van meetonzekerheid en herleidbaarheid tot de SI eenheid voor lengte, de meter, zijn bepalend. Dimensionele metrologie vereist daarenboven hoge vermogens voor het scannen van grote, dikke of dikwandige objecten of hoogabsorberende materialen. Deze verschillende doelen resulteren in verschillende toestellen en procedures.

Ondanks het vele werk verricht gedurende de laatste tien jaren in dimensionele X-stralen CT metrologie, is er nog veel verder onderzoek nodig. Dimensionele X-stralen CT metrologie blijft nog steeds een relatief nieuw concept waarvoor nog meer specifiek onderzoek en standaardisatie nodig is.

Dit proefschrift beschrijft vier bijdragen tot het onderzoek naar de nauwkeurigheid van een X-stralen CT scanner voor dimensionele metrologie:

- Veel van de invloedsfactoren gerelateerd aan computertomografie (op het gebied van medische en materiaalwetenschappen) en dimensionele metrologie gelden ook voor dimensionele X-stralen CT metrologie. Een volledige interpretatie en kwantificatie van deze en veel bijkomende factoren en hun invloed op de kwaliteit van dimensionele metingen is echter nog steeds afwezig. **Dit proefschrift bespreekt de gekende en ontdekte invloedsfactoren. Deze verschillende invloedsfactoren die de dimensionele X-stralen CT metingen en daardoor ook de meetnauwkeurigheid beïnvloeden worden geïdentificeerd, geanalyseerd en besproken. Tenslotte worden ook de effecten (de gevolgen) van de invloedsfactoren gedemonstreerd aan de hand van voorbeelden.**

- De mechanische structuur van de X-stralen CT scanner is een zeer belangrijke invloedsfactor die een grote impact heeft op de dimensionele metingen. Ondanks het grote effect van deze invloedsfactor wordt hier vaak minder aandacht aan besteed. **Dit proefschrift voert een gedetailleerde analyse uit van de mechanische structuur. Een kinematische model wordt beschreven en gekwantificeerd voor de onderzochte X-stralen CT scanner aangevuld met een onderzoek naar de uitlijningsfouten. De uitlijningsfouten bepalen de relatieve fouten tussen de X-stralen bron, rotatievector en detector. Een methode en object voor het berekenen van deze uitlijningsfouten wordt aangereikt.**

- Twee manieren kunnen overwogen worden om de nauwkeurigheid van een X-stralen CT scanner voor dimensionele metrologie te onderzoeken: experimenteel onderzoek en computersimulatie. Een studie enkel gebaseerd op experimenteel onderzoek stoot op vele beperkingen. Een onderzoeker kan bijvoorbeeld verschillende objecten scannen en parameters variëren om de invloed ervan te onderzoeken op de dimensionele metingen. De vele invloedsfactoren, tezamen met vele additionele ongekende invloeden (bv. uitlijningsfouten, verplaatsing van de bron in tijd, temperatuur) zorgen er echter voor dat het moeilijk wordt om aparte, door de gebruiker veranderde parameters (bv. geometrische vergroting), te correleren aan geobserveerde variaties in de dimensionele metingen. Bepaalde parameters kunnen zelfs niet gevarieerd worden, zodoende zal dit tot een ongekende meetonzekerheid leiden. Simulatie is daarom een onmisbare aanvulling op onderzoek op experimentele basis. **Dit proefschrift ontwikkelt een methode voor het generen van 2D**

projectiebeelden die gereconstrueerd kunnen worden in een 3D volumemodel gelijkaardig aan een werkelijke X-stralen CT scan. Het simulatiemodel is geïmplementeerd in Matlab® code. De simulatiesoftware maakt het mogelijk om observaties gemaakt tijdens de nauwkeurigheidsanalyse van dimensionele X-stralen CT metrologie te verifiëren of bevestigen.

- De ontwikkelde simulatiesoftware, samen met de geanalyseerde en gekwantificeerde invloedsfactoren kunnen nu gecombineerd worden met experimenteel onderzoek om een gedetailleerde nauwkeurigheidsanalyse van X-stralen CT scannen voor dimensionele metrologie uit te voeren. **Dit proefschrift voert een nauwkeurigheidsanalyse uit op basis van gekalibreerde objecten. Nauwkeurige objecten zijn gemaakt of verworven voor een diepgaande analyse van de nauwkeurigheid. De nauwkeurigheidsanalyse is uitgevoerd met experimenteel onderzoek gecombineerd met simulatie gebruikmakend van de ontwikkelde simulatiesoftware. De verworven informatie/data van de verschillende invloedsfactoren is hierbij gebruikt voor de simulatie(parameters). Het proefschrift publiceert eigen experimentele resultaten maar ook resultaten van andere X-stralen CT gebruikers, verkregen via een internationaal CT audit project.** Dit CT audit project, georganiseerd door de universiteit van Padova, voerde een vergelijking uit over verschillende X-stralen CT systemen bij uiteenlopende specialisten van CT systemen voor dimensionele metrologie, waaronder nationale metrologieinstituten, onderzoeksinstituten en fabrikanten uit Europa, Amerika en Azië.

Abstract

Dimensional X-ray CT metrology is a recent industrial technology which combines the fields of X-ray computed tomography (CT) and dimensional metrology. Dimensional X-ray CT metrology is a complement to the conventional dimensional measuring equipment (e.g. tactile Coordinate Measuring Machines). It distincts itselves from the conventional measuring methods due to its ability to measure the objects' outside as well as its inside (e.g. invisible cavities) in a non-destructive way. Dimensional X-ray CT metrology is therefore an attractive and unique concept in the world of dimensional metrology.

X-ray computed tomography is often used in the fields of medical imaging and material analysis. The expansion to the field of dimensional metrology is a recent evolution. All three application fields are based on the same principle but however differ in hardware and procedures. Dimensional X-ray CT metrology focuses on the dimensions of the object and thus correct determination of the edges of the obtained model is important. High accuracy in respect of the rules of measurement uncertainty and traceability to the SI unit of measurement, the meter, dominate. Dimensional X-ray CT metrology furthermore requires high penetration powers to scan large, thick objects or high absorbing materials. These different goals result in different devices and procedures.

Despite the progress made during the last ten years for dimensional X-ray CT metrology, still a lot of work has to be accomplished. Dimensional X-ray CT metrology remains a relative new concept which calls for more dedicated research and standardization.

This thesis describes four contributions to the accuracy investigation of an X-ray CT scanner for dimensional metrology:

- Many of the influence factors related to X-ray computed tomography (in the fields of medical and material science) and dimensional metrology are also valid for dimensional X-ray CT metrology. However a good understanding and quantification of these and additional factors and more specifically their influence on dimensional measurements is still absent. **This thesis identifies, analyzes and discusses the many factors affecting the dimensional X-ray CT measurements and therefore the measurement accuracy. Examples will be used to illustrate their effects on projection images.**

- One important influence factor which has a large impact on the dimensional X-ray CT measurements is the mechanical structure of the X-ray CT scanner. Less attention is often paid to this influence factor although it has an important effect on the dimensional X-ray CT measurements. **This thesis performs a detailed analysis of the mechanical structure. A kinematic model for the X-ray CT scanner under investigation will be described and quantified, supplemented by an examination of the alignment errors, i.e. relative errors between source, rotation vector and detector. A method and object to calculate the alignment errors will be presented.**
- Two options can be considered to investigate the accuracy of an X-ray CT scanner for dimensional metrology: experimental research and computer simulation. There are limitations with a study only based on experimental research. One can scan different objects and vary parameters to analyze the influence on dimensional measurements. However the many influence factors, together with many additional often unknown influences (e.g. alignment errors, drift of the source, temperature), make it difficult to correlate separate user adjustable influence factors (e.g. magnification) to observed variations in dimensional measurements. Some error sources can even not be altered, making its influence an unknown uncertainty. Simulation is therefore required to support experimental research. **This thesis develops a simulation method to generate 2D projection images which can be reconstructed into a 3D voxel model as if they are real projections from a CT scan. The simulation method is implemented in Matlab® environment. This simulation software enables to verify or confirm observations made during the accuracy analysis of dimensional X-ray CT metrology.**
- The developed simulation program together with the analyzed influence factors can now be combined with experimental research to perform a thorough accuracy analysis of an X-ray CT scanner for dimensional metrology. **This thesis presents an accuracy analysis based on calibrated objects. Accurate objects are manufactured or acquired enabling an in-depth accuracy analysis. The accuracy analysis is based on experimental research combined**

with simulation using the developed simulation software. The simulation hereby uses the gained information/data on the different influence factors. The thesis shows experimental results which are acquired from own scans but also results from other users, obtained through an international CT audit project, are presented. This CT audit project, organized by the University of Padova, performed an intercomparison which involved different X-ray CT systems selected among the most experienced users of X-ray CT systems for dimensional metrology, including national metrology institutes, research institutes, X-ray CT systems manufacturers, and industrial users from various laboratories in Europe, America and Asia.

Nomenclature

Abbreviations, acronyms

2D	Two Dimensional
3D	Three Dimensional
ANOVA	Analysis of Variance
BHC	Beam Hardening Correction preset
CLDA	Curved Linear Diode Array
CT	Computed Tomography
CMM	Coordinate Measuring Machine
CMS	Coordinate Measuring System
CsI	Cesium Iodide
DQE	Detective Quantum Efficiency
DTU	Technical University of Denmark (*Da.: Danmarks Tekniske Unversitet*)
FPD	Flat Panel Detector
GUM	Guide to the Expression of Uncertainty in Measurement
HDPE	High-Density PolyEthylene
INMETRO	National Institute of Metrology, Quality and Technology
ISO	International Organization for Standardization
MPE	Maximum Permissible Error
MRA	Motorized Receptacle Alignment
NIST	National Institute of Standards and Technology
NMI	National Metrology Institute
NPL	National Physical Laboratory
ROI	Region Of Interest
SDD	Source-Detector Distance
SI	International System of units (*Fr.: Système International d'unités*)
SOD	Source-Object Distance

SNR	Signal-to-Noise Ratio
PTB	Physikalisch-Technische Bundesanstalt
QFM	Quality Management and Manufacturing Metrology (*Ger.: Qualitätsmanagement und Fertigungsmesstechnik*)
VDI	Association of German Engineers (*Ger.: Verein Deutscher Ing.*)
VIM	International Vocabulary of Metrology (*Fr.: Voc. Int. de Métrologie*)

Symbols

General symbols

u	Standard uncertainty
u_c	Combined standard uncertainty
U	Expanded uncertainty
k	Coverage factor

Contents

Chapter 1

Introduction

This chapter introduces the domain of this thesis. Dimensional X-ray CT metrology (section 1.3) combines the worlds of X-ray computed tomography (section 1.1) and dimensional metrology (section 1.2). Basic concepts and procedures (sections 1.4 to 1.6) related to dimensional X-ray CT metrology as well as the available hardware and software (section 1.7) will be covered. The chapter ends with the goals and scope of the aimed research in this thesis.

1.1 X-ray computed tomography

X-ray computed tomography (CT) is a well known technique in the medical world and in the field of material inspection [73]. Its application field has recently been broadened to include dimensional metrology. CT enables measuring an objects' outside as well as the inside (e.g. invisible cavities) in a non-destructive way.

1.1.1 Evolutions in X-ray CT

The evolutions in X-ray CT from the first X-rays to applications in the medical world, material science and dimensional metrology are sketched in figure 1.1. The German physicist Wilhelm Röntgen is regarded as the discoverer of X-rays [115]. He made the first radiograph of a human body part in 1895: a radiograph of the hand of his wife. The first CT scanner for medical imaging is built by the Nobel Prize winner Sir Hounsfield in 1969 [3]. Sir Godfrey N. Hounsfield

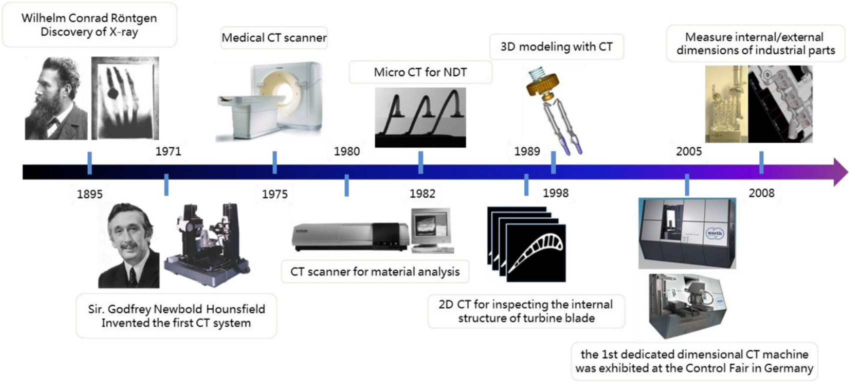

Figure 1.1: Evolutions in X-ray CT after [133] who based this figure on [121].

and Allan M. Cormack were jointly awarded the Nobel prize in Physiology or Medicine for the 'development of computer assisted tomography' [97]. Allan Cormack was the first, from a theoretical point of view, to analyze the conditions for demonstrating a correct radiographic cross-section in a biological system. His results were published in two papers in the Journal of Applied Physics in 1963 and 1964. CT for material analysis and non-destructive testing became attractive since 1980 [111]. Besides initial attempts for size measurements in medical or materials applications, the first attempts to perform traceable dimensional measurements on industrial components were reported in 1991 ([26], [15], [166], [84]). This was done using existing scanners and the accuracy was no better than about $0.1mm$ [73]. In 2005 the first CT machine dedicated to dimensional metrology has been exhibited at the Control Fair in Germany [164].

A tremendous amount of research has yet been carried out related to X-ray imaging and X-ray CT for material and medical science (see section 1.3 for research on dimensional X-ray CT metrology). Research has hereby been conducted on a large range of objects, going from living 'objects' like animals and persons to objects as fruit, polymers, scaffolds, etc. Investigated objects include stationary objects as well as objects which change during the CT scan. Referencing all this work is unfortunately not possible. Instead hereby a small selection of interesting references related to these topics: [165], [1], [118], [63], [41], [65], [64], [109], [141], [29], [28], [66], [2], [77], [116], [42], [37], [104], [59].

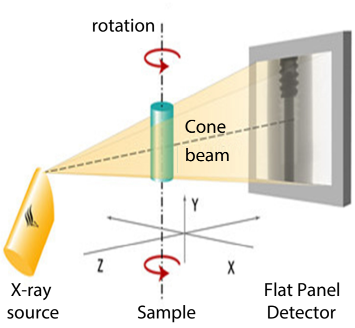

Figure 1.2: Principle of industrial X-ray Computed Tomography (after [45]), illustrated in case of a flat panel detector.

1.1.2 Working principle of X-ray CT

Figure 1.2 illustrates the principle of computed tomography. The X-ray source produces X-rays. These X-rays penetrate the workpiece (sample) and attenuate, due to absorption or scattering. The amount of attenuation is determined by the energy of the X-rays, the penetration length, material composition and corresponding densities. After penetrating the workpiece, the attenuated X-rays are captured by means of a flat panel detector, resulting in a 2D projection (gray) image. 2D projection images are taken for many angular views of the workpiece. Reconstruction based on these projected images leads to a 3D voxel model (a voxel is the 3D analogue of a pixel). The gray value of each voxel is a measure for the attenuation of the material in that voxel, which is generally characterized by a linear attenuation coefficient of the material. The reconstruction is usually performed with a filtered back-projection algorithm. The filtered back-projection algorithm applies the Lambert-Beer law and *linear integral transformation*, a mathematical model developed by J. Radon in 1917 [73]. Equation 1.1 describes the law of Lambert-Beer which expresses the measured X-ray intensity along a straight line after passing a sample. Equation 1.1 is only valid for monochromatic X-ray, the polychromatic equivalent will be demonstrated in section 4.2.2 (see equation 4.3).

$$I(x) = I_0 \, e^{-\mu \, x} \tag{1.1}$$

where:

I_0 = The initial intensity.
$I(x)$ = The intensity after attenuation.
μ = Linear attenuation coefficient of the material.
x = Traveled distance through the material.

During the reconstruction step different image processing techniques can be applied such as beam hardening correction, noise reduction, scatter reduction. The remaining steps concern the post-processing of the voxel data, including edge detection (segmentation), and (dimensional) quality control.

1.2 Dimensional metrology

Quality control is a crucial step in the manufacturing industry. This step ensures the quality of a product and therefore the well functioning of this product. One stage of the quality control concerns the dimensional accuracy of the product. Each product is designed with certain dimensions and accompanying tolerances. Dimensional metrology concerns checking the dimensional properties of a product, ensuring they comply with the specified tolerances. Different technologies are available to perform dimensional metrology.

[151] explains the topic of dimensional metrology in detail. This e-learning package by Welkenhuyzen, Vogeler et al. explains the basic principles of 3D coordinate measurement techniques. It furthermore discusses the different available technologies and their advantages and disadvantages categorized in conventional coordinate measuring machines, optical coordinate measuring machines and mobile coordinate measuring machines.

Many national and international institutes have contributed to the research on dimensional metrology. There are too many to mention but among them are:

- NIST (National Institute of Standards and Technology), United States.
- NPL (National Physical Laboratory), United Kingdom.
- PTB (Physikalisch-Technische Bundesanstalt), Germany.
- NMI (National Metrology Institute), Netherlands.

- Inmetro (National Institute of Metrology, Quality and Technology), Brazil.

There are furthermore many standards and guidelines available, published by institutes such as the ISO (International Organization for Standardization), NIST (National Institute of Standards and Technology) and the VDI (Verein Deutscher Ing.).

An enormous amount of research has been conducted through the years resulting in many publications. Following works are some of the important works in the field which discuss the main topics and include many more important references: [123], [103], [119], [40], [154], [30].

Traceability to the SI unit of measurements (i.e. the meter), measurement accuracy and uncertainty, etc. are critical aspects in dimensional metrology. These aspects will be covered in sections 1.5 and 1.6.

1.3 Dimensional X-ray CT metrology

Dimensional X-ray CT metrology combines the world of X-ray computed tomography and dimensional metrology. It is a complement to the conventional measuring equipment. The big difference lays in the fact that it is able to measure the objects' outside as well as the inside (e.g. invisible cavities) in a non-destructive way [62], [101], [45], [54], [6]. The ability to measure the inside of a part makes industrial computed tomography attractive and unique in the world of dimensional metrology. Assemblies, complex structures as well as the inner geometry of parts made by additive manufacturing can be measured in a non-destructive way.

(a) (b) (c)

Figure 1.3: X-ray CT scanners for different purposes: medical CT scanner (a), CT scanner for material investigations (b) and CT scanner for dimensional metrology (c). [73]

Computed tomography is often used in the fields of medical imaging and material analysis. The expansion to the field of dimensional metrology is a recent evolution. All 3 applications are based on the same principle but however differ in hardware and procedures (figure 1.3). The main differences can generally be noted as follows. Medical CT uses limited X-ray dose and hence power to protect the patient. Large X-rays source spot diameters are possible as there is no need for high precision. The object (patient) furthermore does not rotate in this particular case. Material science is more interested in the inner structure of the object. Beam hardening, the artifact that results in non-uniform gray value for voxels of same material is a major concern. Less interest is put in the material boundaries, which are crucial for dimensional metrology. Beam hardening can accentuate the boundaries and can therefore be beneficial to dimensional X-ray CT metrology. Software corrections to compensate for beam hardening can be favorable for material science as they can make the voxels more uniform, but can be inappropriate for dimensional metrology due to the change in boundaries position. Material science moreover mostly investigates small samples. Dimensional X-ray CT metrology focuses on the dimensions of the object, correct determination of the edges is therefore important. Incorrect representation of the inner structure (pores etc.) is not that critical. High accuracy in respect of the rules of measurement uncertainty (section 1.5) and traceability to the SI unit of measurement (section 1.6) , the meter, dominate [73]. Dimensional X-ray CT metrology furthermore requires high penetration powers to scan large, thick objects of high absorbing materials. These different goals result in different devices and procedures.

The last ten years quite some research ([7], [34], [54], [67], [121], [156], [133], [72], [31], [91], [61], [22], [98], [27], [95], [83], [50], [169], [53], [79], [38], [113], [149], [117], [76], [24], [90], [87], [14], [6], [45], etc.) has been performed on dimensional X-ray CT metrology. Two papers which cover and include references to the main research topics, applications, issues regarding dimensional X-ray CT metrology have been written by Kruth et al. [73] and by De Chiffre et al [32]. Much more interesting papers and other documents will be referenced in this thesis at the topics of interest.

Despite the progress accomplished during the last ten years for dimensional X-ray CT metrology, still a lot of work has to be accomplished. Dimensional X-ray CT metrology remains a relative new concept which calls for more dedicated research and standardization. As mentioned by Kruth et al. [73]: there is a lack of well defined reference objects and procedures to assess and compare the accuracy of dimensional X-ray CT measurements. Furthermore does this paper [73] emphasize the absence of international standards and guidelines concerning the evaluation of uncertainty for X-ray CT based dimensional measurements. The German guideline VDI/VDE 2630 [147] is currently the only standard for dimensional X-ray CT metrology devices.

Many of the influence factors related to computed tomography (in the fields of medical and material science) and dimensional metrology are also valid for dimensional X-ray CT metrology. However a good understanding and quantification of these and additional factors and more specifically their influence on dimensional measurements is still absent. All previous mentioned considerations result in following important facts:

- Little is known about the actual measurement accuracy of X-ray CT based dimensional measurements.
- Measurands are often assessed with large measurement errors due to incorrect execution and evaluation of the dimensional X-ray CT metrology measurements.
- Industrial X-ray CT users are unable to provide an appropriate statement of the CT measurement uncertainty.
- Dimensional X-ray CT metrology research often results into incorrect conclusions made by the researcher.
- Dimensional X-ray CT metrology is not yet a widely accepted part of dimensional metrology by the industry.

Fundamental research on the accuracy and the factors influencing this accuracy is therefore necessary.

1.4 CT metrology procedure

Figure 1.4 clarifies the different steps in X-ray CT metrology.

Preparation. The first step incorporates the preparation of the CT scan. Different steps can be distinguished, like the choice of the acquisition parameters. Also the well functioning of the X-ray CT device is part of this step, for instance the conditioning of the X-ray source.

Acquisition. The actual CT scanning (acquisition) can start after the setting up step. This step includes the capturing of the 2D X-ray images. Stable conditions are crucial in this step.

Reconstruction. Reconstruction based on these projected 2D X-ray images leads to a 3D voxel model. Different settings (e.g. settings related to beam hardening correction, noise reduction, scatter reduction) can be

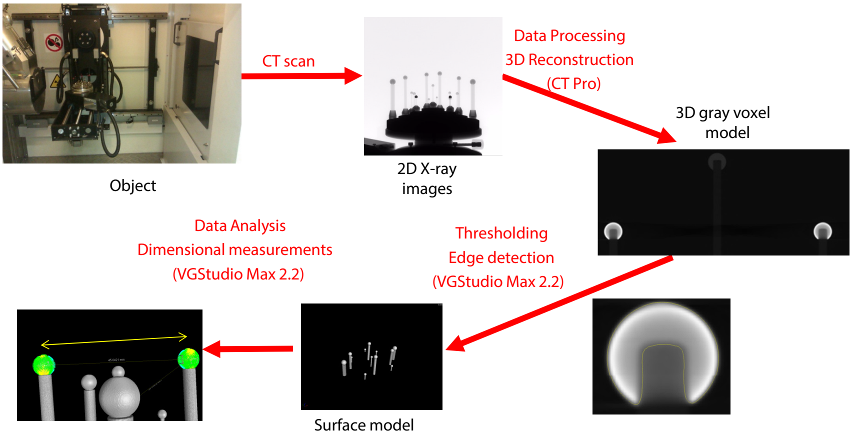

Figure 1.4: Brief overview of the X-ray CT metrology procedure.

selected in this reconstruction step which will influence the measurement accuracy.

Edge detection. After the voxel model has been reconstructed one has to define the material boundaries (edges). These will be used to obtain the dimensional measurements and thus influence the measurement accuracy.

Dimensional measurements. The last step consist of performing the dimensional measurements and quality control.

All of these steps include many parameter choices and influence factors with uncontrollable relationship with the measurement results. There are furthermore improvement and correction strategies possible in each step [162]. The process is often an iterative process: results of one step often leads to reconsideration of a previous step.

1.5 Measurement accuracy

A measurement result is never exact, there will always be a measurement error. A similar event is true when manufacturing a product: one can not make the product with the exact dimensions. A specification (or tolerance) zone will be specified in the design phase for the measurands. This tolerance zone specifies the acceptable deviations of the true value to the nominal value [151]. Regarding the measurement result it is absolutely necessary to specify the measurement uncertainty of a measurement in order to have a quantitative indication of the quality of the measurement. ISO-GUM (section 0.1) states this very clearly [57]:

> “When reporting the result of a measurement of a physical quantity, it is obligatory that some quantitative indication of the quality of the result be given so that those who use it can assess its reliability. Without such an indication, measurement results cannot be compared, either among themselves or with reference values given in a specification or standard.”

This section looks at the most important available definitions regarding evaluation of the measurement result. A measurement result will never be exact as already explained, but there will always be measurement error. The measurement error can be defined by definition 1.1.

Definition 1.1. *Measurement ERROR =*
MEASURED quantity value - TRUE quantity value.

The true value is unfortunately unknown. The international vocabulary of metrology (VIM) [58] uses a twofold definition (def. 1.2) to overcome this issue [143]:

Definition 1.2. *Measurement ERROR =*
MEASURED quantity value - REFERENCE quantity value.

In which the reference quantity value can be:

- the true quantity value. In this case the measurement error can not be known, as the true value is never and will never be identifiable.
- a reference standard with a measured quantity value having a negligible measurement uncertainty, or a conventional quantity value. In this case the measurement error is known.

The measurement error can be divided in a systematic error component and a random error component. Definitions 1.3 and 1.4 define these components [58].

Definition 1.3. *The SYSTEMATIC MEASUREMENT ERROR is the component of measurement error that in replicate measurements remains constant or varies in a predictable manner.*

Definition 1.4. *The RANDOM MEASUREMENT ERROR is the component of measurement error that in replicate measurements varies in an unpredictable manner.*

In the section above the measurement error has been discussed, but what is now the accuracy of a measurement? The measurement accuracy is given by definition 1.5 [58].

Definition 1.5. *The MEASUREMENT accuracy is the closeness of agreement between a measured quantity value and a true quantity value of a measurand.*

This is however not a good concept to complete the measurement results as this can not be quantified. Following remark associated to the definition explains this.

Remark 1.1. *The concept 'measurement accuracy' is not a quantity and is not given a numerical quantity value. A measurement is said to be more accurate when it offers a smaller measurement error.*

The concept 'measurement uncertainty' is therefore better suited to give an idea of the accuracy of a measurement [58].

Definition 1.6. *The MEASUREMENT UNCERTAINTY is a non-negative parameter characterizing the dispersion of the quantity values being attributed to a measurand, based on the information used.*

This concept of uncertainty is more clearly defined by ISO-GUM section 2.2.3 [57]:

> “Parameter, associated with the result of a measurement, that characterizes the dispersion of the values that could reasonably be attributed to the measurand”

The 'measurement error' and 'measurement uncertainty' have now be defined. To end the often used concepts 'measurement repeatability' and 'measurement reproducibility' are stated by definitions 1.7 and 1.8, where definitions 1.9, 1.10 and 1.11 explain the applied concepts in these definitions [58].

Definition 1.7. *MEASUREMENT REPEATABILITY is the measurement precision under a set of repeatability conditions of measurement.*

Definition 1.8. *MEASUREMENT REPRODUCIBILITY is the measurement precision under reproducibility conditions of measurement.*

Definition 1.9. *The REPEATABILITY CONDITION OF MEASUREMENT is the condition of measurement, out of a set of conditions that includes the same measurement procedure, same operators, same measuring system, same operating conditions and same location, and replicate measurements on the same or similar objects over a short period of time.*

Definition 1.10. *The MEASUREMENT PRECISION is the closeness of agreement between indications or measured quantity values obtained by replicate measurements on the same or similar objects under specified conditions.*

Definition 1.11. *The REPRODUCIBILIY CONDITION OF MEASUREMENT is the condition of measurement, out of a set of conditions that includes different locations, operators, measuring systems, and replicate measurements on the same or similar objects.*

1.6 Metrological traceability

As already explained in section 1.3, a high accuracy in respect of the rules of measurement uncertainty and traceability to the SI unit of measurement, the meter, is crucial in X-ray CT metrology. Two important concepts hereby are the 'metrological traceability' and the 'calibration hierarchy'. Definitions 1.12 and 1.13 define these concepts [58]. Figure 1.5 illustrates these concepts.

Definition 1.12. *The METROLOGICAL TRACEABILITY is the property of a measurement result whereby the result can be related to a reference through a documented unbroken chain of calibrations, each contributing to the measurement uncertainty.*

Definition 1.13. *The CALIBRATION HIERARCHY is a sequence of calibrations from a reference to the final measuring system, where the outcome of each calibration depends on the outcome of the previous calibration.*

At last the concept of 'metrological traceability to a measurement unit' is given by definition 1.14 [58].

Definition 1.14. *The 'metrological traceability to a measurement unit' is the metrological traceability where the reference is the definition of a measurement unit through its practical realization.*

Remark 1.2. *The expression 'traceability to the SI' hereby means the 'metrological traceability to a measurement unit of the International System of Units'.*

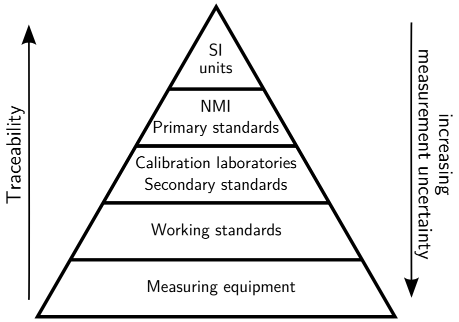

Figure 1.5: Metrological traceability through a calibration hierarchy. [143]

1.7 Hardware and software

Different X-ray CT devices have been used during this research. Tactile reference measurements have been performed using the Mitutoyo FN-905 CMM.

Nikon Metrology XT H 225 CT scanner. The Nikon Metrology XT H 225, at the venue of Nikon Metrology Belgium, has a minimal spot size of $3\mu m$. This CT scanner is equipped with a VARIAN Paxscan 2520V flat panel detector (16 bit, 1516x1900 active pixels, CsI converter, pixel size: $127\mu m$). The source uses a tungsten target to produce X-rays.

Nikon Metrology XT H 450 CT scanner. The Nikon Metrology XT H 450 (figure 1.6) has a minimal spot size of $80\mu m$, which expands linearly with powers higher than 80W. This CT scanner is equipped with two detectors: a 2D Perkin Elmer XRD 1620 AN3 CS flat panel detector (16 bit, 2000x2000 active pixels, CsI converter, pixel size: $200\mu m$) and a Nikon Metrology curved linear diode array detector (CLDA) (16 bit, 2000 pixels, Cadmium Tungstate converter, pixel size: $400\mu m$, focus imager distance: $1200mm$). The source uses a tungsten target to produce X-rays.

Nikon Metrology XT H 225 ST CT scanner. The Nikon Metrology XT H 225ST (figure 1.7) has a minimal spot size of $3\mu m$. This CT scanner is equipped with a 2D Perkin Elmer XRD 1620 AN3 CS flat panel detector (16 bit, 2000x2000 active pixels, CsI converter, pixel size: $200\mu m$). It is furthermore foreseen with linear scales on all axes. A look up table has been integrated in the software to correct for magnification positioning errors. The source contains a multi-metal target: in this case different target materials (copper, tungsten, silver and molybdenum) are fitted onto an indexable head.

Mitutoyo FN-905 CMM. Moving bridge coordinate measuring machine (CMM) with specification: $U1 = 4.2 + 5 * L/1000 \mu m$. This CMM (figure 1.8) has been used for the reference measurements.

The Nikon Metrology XT H 225 CT scanner has mainly been used at the beginning of the thesis. The other equipment was available in house. The Nikon Metrology XT H 225ST CT scanner is with its small spot size, scales on the linear axes and look up table for magnification positioning errors, more suited for dimensional metrology. The Nikon Metrology XT H 450 CT scanner allows measuring components made of more absorbing materials and/or larger components.

The in house devices are installed in rooms equipped with their own air conditioning unit, designed to keep the temperature in the rooms at a constant 20 °C.

The CT devices make use of different software programs.

Inspect-X. Acquisition software of Nikon Metrology. This software controls the CT devices. It handles the different acquisition steps to set up a CT scan.

CT agent. CT Agent (Nikon Metrology software) manages the writing of projection images, reconstruction parameter files and the reconstruction services.

CT Pro. Reconstruction software of Nikon Metrology. This software handles the reconstructing of the obtained projection images to obtain a reconstructed voxel model.

VGStudio Max. Ensuing volume reconstruction, the volume is loaded in VGStudio Max from Volume Graphics. Thresholding (edge detection) and dimensional measurements are performed in this software.

The simulation program which will be presented in this thesis has been worked out in Matlab® but can be translated to other programming languages.

Figure 1.6: Nikon Metrology XT H 450 CT scanner.

Figure 1.7: Nikon Metrology XT H 225ST CT scanner.

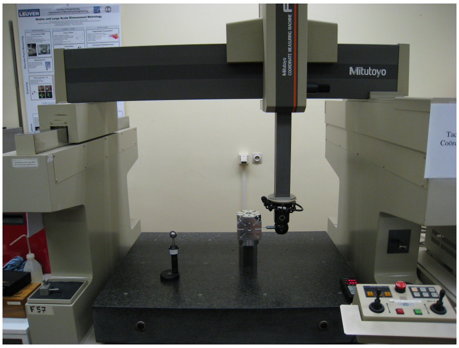

Figure 1.8: Mitutoyo FN-905 CMM.

1.8 Goals and scope of the research

Dimensional X-ray CT metrology is a quite new concept. Therefore there are different important questions which still need to be answered:

- What is the dimensional accuracy of X-ray CT scanners?
- How can we improve the dimensional accuracy?
- Which factors influence the dimensional accuracy?
- In which amount does each separate factor influence the accuracy?

Experimental research and research based on simulation is needed to be able to answer these questions. Experimental research on its own is often insufficient: repeating a same experiment a month later often leads to different conclusions which is of course unacceptable.

These considerations have led to the following main goal for this thesis:

Analyze the accuracy of dimensional X-ray CT metrology.

Realization of this main goal is achieved by meeting following sub goals:

- List and quantify the factors influencing the dimensional X-ray CT metrology accuracy.
- Produce a simulation program which supports the experimental research.
- Fabricate accurate objects to investigate the dimensional accuracy.
- Analyze the dimensional accuracy with these objects and simulation.

1.9 Conclusion

This chapter has introduced the scope of this thesis and the used hardware and software. Two existing fields, X-ray computed tomography and dimensional metrology, are combined into a new field: dimensional X-ray CT metrology. Dimensional X-ray CT metrology is a new concept, which requires new research. Different basic concepts related to dimensional X-ray CT metrology and a procedure to perform dimensional X-ray CT metrology have been introduced. The chapter has ended with the main goal of this thesis i.e. to analyze the accuracy of dimensional X-ray CT metrology. This main objective will be achieved by meeting different sub goals:

- List and quantify the factors influencing the dimensional X-ray CT metrology accuracy.
- Produce a simulation program which supports the experimental research.
- Fabricate accurate objects to investigate the dimensional accuracy.
- Analyze the dimensional accuracy with these objects and simulation.

Chapter 2 will identify, analyze and discuss the influence factors affecting the dimensional X-ray CT measurements and therefore the measurement accuracy. The discussions will not be restricted to the generally discussed influence factors but will attempt to cover all possible influencing factors.
A good knowledge of all the influence factors will be crucial to perform and improve the dimensional X-ray CT measurements. The quantified values will be used as input for the simulation program.

Chapter 3 will focus on one single but important error source: the mechanical structure of the X-ray CT device. A kinematic model will be described and quantified for the investigated Nikon Metrology XT H 450 CT scanner. Furthermore will a method and object to calculate the alignment errors between source, rotation table and detector be worked out. This kinematic model as well as the calculated alignment errors will be implemented in the simulation program.

Chapter 4 will cover the simulation program developed to support research on dimensional X-ray CT metrology. The simulation software will enable to verify or confirm observations made during the accuracy analysis of dimensional X-ray CT metrology on experimental base. This simulation program generates X-ray projection images which can be reconstructed into a 3D voxel model as if they are real projections from an X-ray CT scan. It will include many options, including options which are not or rarely available in other softwares, but crucial for dimensional X-ray CT metrology research. The quantified errors in chapters 2 and 3 will be used as input for the simulation program. It will thus be possible to investigate issues as source drift, alignment errors, etc. with true values. This software is flexible, giving the possibility to other researchers to implement their own subprograms for their specific research.

Chapter 5 will perform an in-depth analysis of the accuracy of dimensional X-ray CT metrology with the aid of calibrated objects. This analysis will be carried out by using experimental analyzes as well as by using simulations, applying the simulation program of chapter 4. Combining the experimental results with the simulations complemented by the acquired knowledge on influence factors in chapters 2 and 3 will result in a good understanding of the process, detection of main error sources and improvements of the accuracy.

This dissertation will end with a summary of the main results, main contributions and suggestions for future research in chapter 6.

Chapter 2

Influence factors

Many parameters affect the obtained measurement results when performing X-ray CT metrology. Figure 2.1 gives a small overview of the main influence factors. This chapter reviews these influence factors per component and quantifies them for later use in the simulation and experimental research performed later on (sections 2.2 to 2.6). The influence factors of the mechanical structure will only shortly be noted in this chapter. A detailed analysis on this topic follows in chapter 3. Chapter 2 ends with a discussion on the measurement accuracy (section 2.7).

2.1 State of the art

Kruth et al. [73] and the VDI/VDE standard ([146], [147], [148]) give a nice general overview of the different influencing parameters concerning dimensional computed tomography.

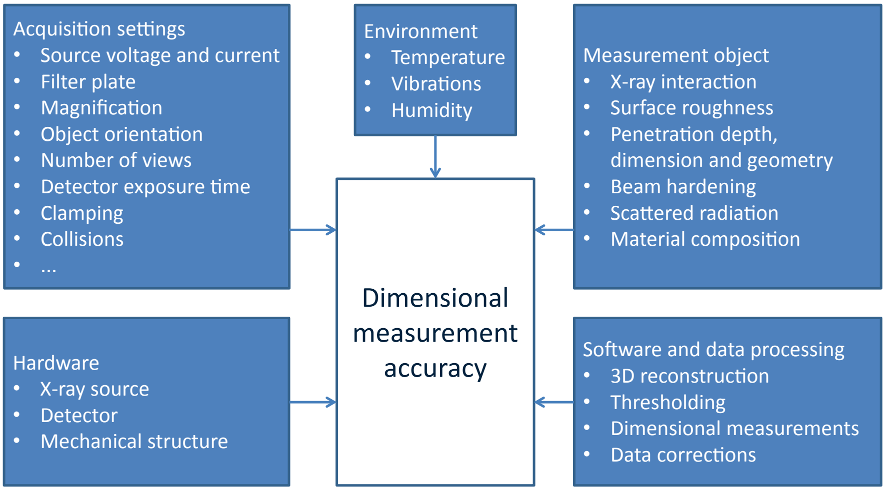

Figure 2.1: Overview of the parameters influencing the dimensional measurement result in CT metrology.

2.2 Hardware

2.2.1 X-ray source

Figure 2.2 illustrates the working principle of the X-ray tube (vacuum tube), available in the CT scanners used in this thesis. Electrons are emitted from the heated filament (cathode) and accelerated by the applied kV to the anode. The electrons pass through the center of the anode ring, travel across the beam tube, and subsequently hit the target. The fast electrons are now very suddenly decelerated, causing their energy to convert into heat (over 99%) and X-rays (less than 1%) [73].

Figure 2.3 focuses on the processes at the target (in case of a reflection target, which is utilized in the scanners under investigation). The electrons reach the target and the X-ray photons are subsequently emitted into another direction. The produced X-rays radiation consists of Bremsstrahlung (German term for braking radiation) radiation and characteristic radiation. Bremsstrahlung is caused by the sudden deceleration of the electron when interacting with the target material. Bremsstrahlung generates a continuous spectrum from very low energies to the full energy of the impacting electrons (i.e. applied keV). Characteristic radiation is the result of following process: a high energy electron impacts and excites an inner shell electron in an atom of the target.

De-excitation of that or a substituting electron releases the electron's energy and a photon of characteristic radiation [73]. This characteristic radiation has a specific energy depending on the particular composition of the target, hence the name characteristic radiation. Two additional aspects should be mentioned: the size of the impacting electron beam differs from the outgoing X-ray beam (as can be understood from figure 2.3). The characteristics of the Bremsstrahlung spectrum change with the length of the absorption path due to varying target absorption of the generated X-rays (Heel effect) [47].

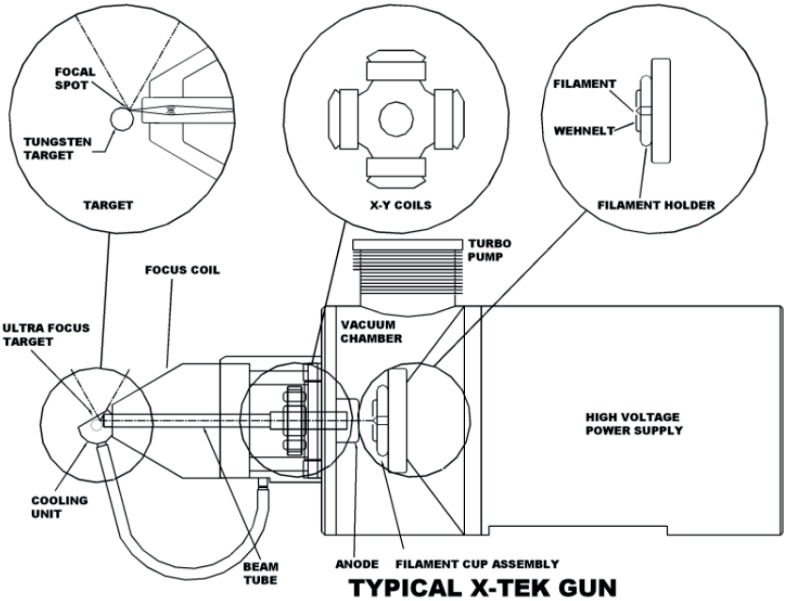

Figure 2.2: Typical X-ray tube. [93]

Spectrum

The generation of X-rays has already been discussed in previous section: the produced X-rays radiation consists of Bremsstrahlung radiation and characteristic radiation. The generated X-ray spectrum is characterized by its intensity (flux) and its quality or energy distribution [11]. The quality describes the penetrating power of an X-ray beam. The higher the applied voltage, the higher the penetrating power of the X-ray beam into matter. The intensity (flux) is a measure of the amount of radiation energy flowing per unit of time.

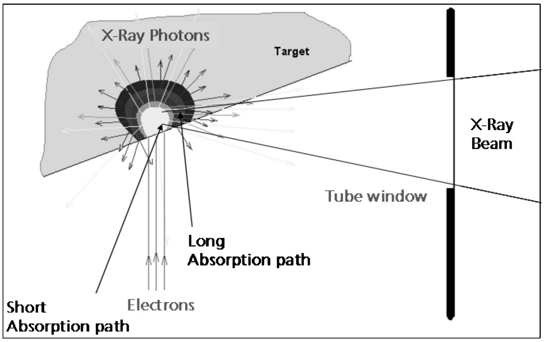

Figure 2.3: X-ray generation with a reflection target [47]: the electron beam enters from the bottom, hits the target, and the X-ray beam leaves to the right. (courtesy of Viscom AG)

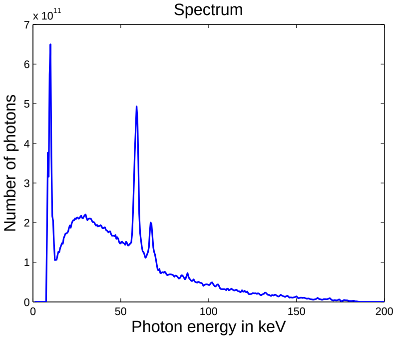

Figure 2.4: $190kV$ X-ray source spectrum generated with a tungsten target.

The higher the applied current, the higher the intensity of the X-ray beam will be.

The **Nikon Metrology XT H 450 CT scanner** uses a tungsten target. The **Nikon Metrology XT H 225 ST CT scanner** is equipped with a multi-metal target: in this case different target materials (copper, tungsten, silver and molybdenum) are fitted onto an indexable head. This allows to use a specific target material (and hence its spectrum) for each measurement. The molybdenum target is for instance suited for measurements of plastic materials, whereas the tungsten target is mostly applied for dense and hence difficult to penetrate materials.

There is quite some literature to predict and generate X-ray spectra in function of the applied source voltage. [81] uses the GEANT4 code for generation of X-ray spectra based on the Monte Carlo method. The obtained simulated X-ray spectra are compared with measured spectra of an industrial 450 kV X-ray tube. [139] and [140] apply a semi empirical model for generating resp. tungsten and molybdenum target X-ray spectra. The freely available program SpekCalc [107], [108], [106] allows to calculate photon spectra from tungsten anode X-ray tubes. Furthermore [125], [21] and [19] can be applied to compute energy spectra of a tungsten target. At last [46] provides absolute energy spectra for an industrial X-ray source which have been measured using a Compton scattering spectrometer.

It is nevertheless important to be aware that these spectra never perfectly match the spectra generated with the CT systems under investigation. Even when using the same target material and applied voltage, the source spectra will differ.

Spot size

Figure 2.5 illustrates the effect induced by the spot size. The smaller the spot size, the sharper the edges will be. In case of large spot sizes unsharpness will occur, known as the penumbra effect. A disadvantage of a smaller spot size is the concentrated heat produced at the spot on the target inside the X-ray tube, requiring cooled targets and limiting the maximum applicable voltage.

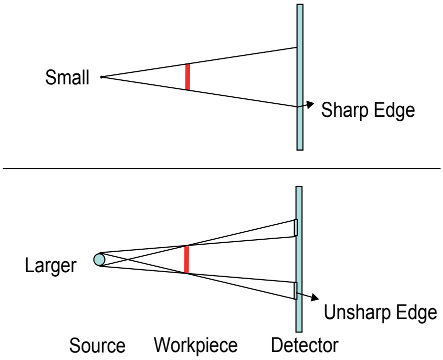

Figure 2.5: Influence of the spot size: small spot size (top) compared to large spot size (bottom). [162]

Figure 2.3 showed the X-ray generation with a reflection target. It is clear that the effective spot size is difficult to determine and is furthermore dependent of several parameters: electron beam alignment, applied power, focus settings, etc.

Section 2.3 discusses these parameters. The ASTM E1165 - 12 [9] and the DIN EN 12543 [36] are available standards to define the spot size of an X-ray source.

According to machine specifications equation 2.1 defines the spot size in μm for the **Nikon Metrology XT H 450 CT scanner**. This equation will be applied in the simulation program to calculate the spot size automatically.

$$SpotSize = max(80, \frac{Voltage * Current}{1000}) \tag{2.1}$$

where:

$Voltage$ = Source voltage in $[kV]$.
$Current$ = Source current in $[\mu A]$.

Spot position

The spot position is influenced by several parameters: filament position, electron beam alignment, applied source voltage and current, pitting, drift etc. The target can become pitted due to the concentrated heat produced at the spot on the target. Therefore the target is regularly rotated to work with a fresh spot. The spot position will furthermore drift during a CT scan as will be discussed in the next section.

Spot drift in time

Figures 2.6 illustrate the effect of spot drift during a scan. An object (figure 2.6a) is placed close to the source, and images are captured for 1 hour. The first and last image is compared by subtracting these images from each other resulting in figures 2.6b and 2.6c (when subtracting the images, negative values will become zero). The effect of the spot drift is clear on the image, this test allows to estimate the spot drift. It is importance to notice that this drift is dependent of several factors: applied voltage, current, wear of the target, etc.

An estimation of the spot drift inside the **Nikon Metrology XT H 450 CT scanner** (coordinate system as in figure 3.3) has been obtained for simulation purposes. An estimation in vertical direction (y) has been made by comparison of the above images, which resulted in a value of $-40\mu m$ for a scan of one hour. The same experiment with the object turned over 90 degrees gives an idea of the spot drift in x-direction: obtained drift in x is 0. The spot drift in z-direction (magnification) is set to $20\mu m$. These values will be used for the simulation

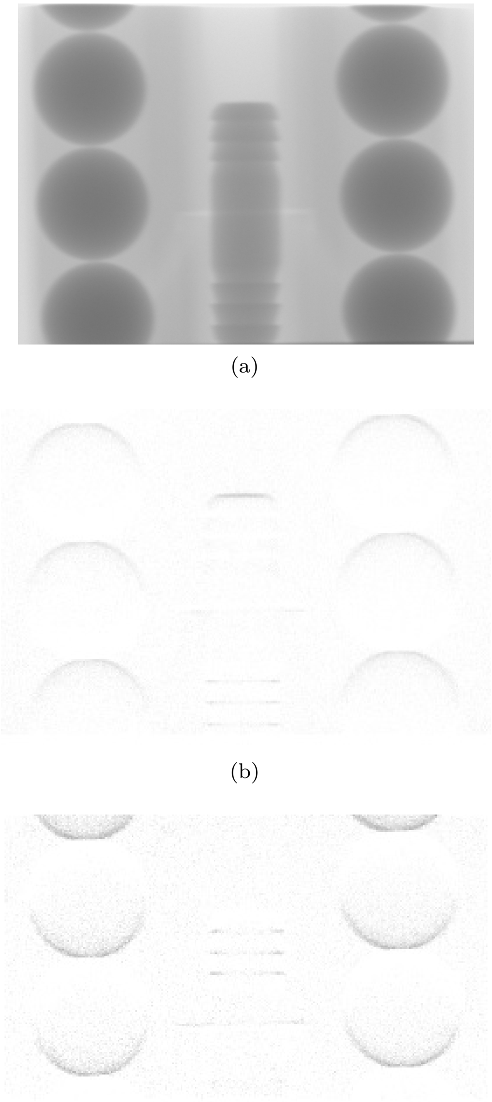

(a)

(b)

(c)

Figure 2.6: Effect of spot drift during a scan by comparing the images of a fixed object (a). Subtracting the first image from the last image (b) and vice versa (c). The received images have been inverted (black to white and vice versa) to make the difference more clear.

program. The obtained drift values can be compared with the values applied by [52] in his simulations. [52] uses values of $8.45 * 10^{-3} \mu/s$ and $4.03 * 10^{-3} \mu/s$ for the source drift in x and y direction. This results in drifts of resp. $30.4 \mu m$ and $14.5 \mu m$ for a scan of an hour. This source drift is often assumed to be linear, [150] however measured an arc tangent trend in the source drift.

Filament

The tungsten filament inside the X-ray tube has to be replaced regularly [93]. Replacement is needed in case of a broken filament or when it is not functioning well anymore. This replacement is carried out by the user. An important part of this replacement concerns the correct positioning of the filament. The position of the filament will affect the CT measurements. It is furthermore important to carefully clean the X-ray tube as remaining dirt influences the stability of the generated X-rays.

Stability of the generated X-rays

The produced X-rays should be stable and not fluctuate in time. Dirt in the X-ray tube will cause fluctuations and instability. Conditioning of the source ensures a stable X-ray production, and hence a steady image. This conditioning should be done regularly, daily conditioning is recommended [93]. Conditioning is further discussed in section 2.3.21.

2.2.2 Detector

There are three types of detectors. Either the output of the detector is proportional to the total number of photon impacts (counting-type detectors), or it is proportional to the total photon energy (scintillation-type detectors or 'indirect' detectors), or it responds to energy deposition per unit mass (ionization detectors) [60]. In our case the detector is a scintillation-type detector or 'indirect' detector.

Different aspects related to the detector affect the dimensional measurements: the scintillator material and thickness, pixel size, detector shape (e.g. flat panel detector versus curved linear diode array detector), correctness of this detector shape (is the flat panel detector indeed flat?), noise and Detective Quantum Efficiency (DQE). Information on these aspects can be found in [92], [114], [153], [168], [126], [47], [100], [102], [145].

The **Nikon Metrology XT H 450 CT scanner** used in this study is equipped with a flat panel detector (FPD) and a curved linear diode array detector (CLDA). The FPD can shift along a vertical axis, to be able to work with the CLDA detector. This shifting, and repositioning of the FPD gives an extra inaccuracy on the position of this detector, which will influence the CT measurements (see section 3.1).

Curved linear diode array detector (CLDA) versus flat panel detector (FPD)

The working principle of computed tomography with a flat panel detector is already explained in section 1.1. Figure 2.7 illustrates the working principle with a line detector. This picture contains a straight line detector; the detector of the 450 CT scanner is a curved one. A line detector acquires images slice by slice. The object is positioned at one height and turns around, which results in a sinogram as pictured in figure 2.8 (one sinogram is made per slice). The table and object shift in vertical direction after scanning one slice, hence multiple slices can be scanned. Reconstruction of each sinogram and putting these reconstructed slices together will lead to a voxel model of the object. The user can scan the entire object in this manner, but often only a few sections are scanned instead of the entire object.

The curved linear diode array detector has some advantages and disadvantages compared to the flat panel detector.

Less pixel interaction. The CLDA features inter pixel shielding, resulting in less pixel interaction from adjacent pixels.

Less scatter. The CLDA is mostly used with collimators to obtain a fan beam, which results in less scattered X-rays hitting the detector.

A thicker and different scintillator. The CLDA has a cadmium tungstate scintillator instead of a CsI scintillator used for the FPD. This scintillator thickness is moreover much thicker. A CLDA therefore has a better signal-to-noise ratio.

Curvature. The CLDA is curved with the arc center coinciding with the X-ray spot. This reduces the image deformation when moving away from the central pixel.

More time consuming. The object will be scanned slice per slice. This requires one rotation per slice, subsequently moving the object in vertical direction and scanning the next slice.

Extra movement. The extra vertical movement leads to an extra inaccuracy.

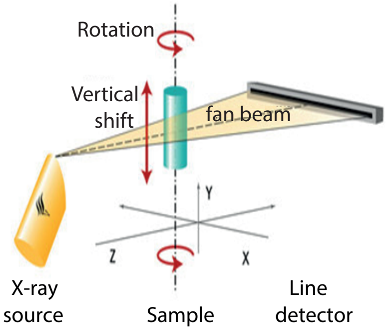

(a)

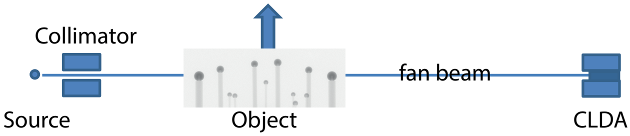

(b)

Figure 2.7: Working principle of a line detector in 3D view (a) and in front view (b). The X-ray beam is mostly collimated to obtain a fan beam as pictured in figure (b).

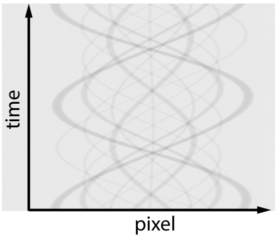

Figure 2.8: Example of a sinogram (output of a line detector). A sinogram pictures the gray values for one slice after one object rotation. The abscissa contains the pixel number and the ordinate pictures time (proportional to the view angle).

Noise

The CT process is suspect to different types of noise [130]: quantum noise, electronic noise and round-off/quantization noise due to the limited dynamic range of the detector. Quantum noise is the main noise contributor. Quantum noise occurs due to the statistical nature of X-rays, which can be represented by a Poisson distribution. The amount of noise in the reconstructed volume depends on the reconstruction algorithm (applied software filters and interpolation methods influence the reconstructed image noise) and the total exposure (increasing the exposure increases the SNR). The total exposure depends on the applied source current, detector exposure time, etc.

DQE

The Detective Quantum Efficiency is often used to quantify the quality of an imaging system [145]. Equation 2.2 shows the formula for the DQE, which is typically calculated by equation 2.3. [145]

$$DQE(\overline{q}, u) = \frac{SNR_{out}^2}{SNR_{in}^2} \tag{2.2}$$

where:

SNR_{out} = Output Signal-to-Noise ratio from the image.
SNR_{in} = Input Signal-to-Noise ratio from the image.

$$DQE(\overline{q}, u) = \frac{\overline{d}^2 \times MTF^2(u)}{\overline{q}^2 \times NPS^2(\overline{q}, u)} \tag{2.3}$$

where:

d = Average produced output signal.
MTF = Modulation Transfer Function which is a measure for the resolution.
q = Number of incident X-ray quanta.
NPS = Noise spectrum produced by the imager.

Bad Pixel Correction

Flat panel detectors, as used in this thesis, contain bad pixels (i.e. pixels which are not functioning well). A bad pixel map corrects for these bad pixels. The bad pixels will be replaced with an average of the surrounding pixels [93].

2.2.3 Mechanical structure

Different aspects related to the mechanical structure can be distinguished:

- Distance from source to object, and distance from source to detector.
- Relative errors between source, turntable and detector.
- Errors in moving the turntable by the kinematic system and the subsequent errors.
- Inherent problems of the rotation of the table like the wobble and eccentricity.

A thorough investigation of the first 3 topics is carried out in chapter 3.

Source-object and source-detector distance

The distance from source to object and the distance from source to detector define the geometrical magnification of the object on the detector screen. This immediately results in the calculation of the voxel size and therefore the obtained dimensions (see section 2.3.5). The source-detector distance and the source-object distance (offset) is calibrated by the manufacturer. Errors on these values will influence the magnification and obtained dimensions.

Relative errors between source, turntable and detector

The rotation axis is supposed to be aligned parallel, resp. perpendicular to the detector and its pixel rows or columns [73]. The manufacturer performs an alignment calibration to satisfy these conditions as good as possible. Errors on this requirement will affect the measurement results. Chapter 3 discusses this item.

Errors in moving the turntable by the kinematic system

The kinematic system of the CT scanner enables the positioning of the turntable. This will be further investigated in chapter 3.

Wobble and eccentricity of the rotation table

Tolerances for the wobble and eccentricity of the rotation stage inside the **Nikon Metrology XT H 450 CT scanner** are provided by the manufacturer of this stage. They are defined as $20\mu rad$ or $\pm 10\mu rad$ and $4\mu m$ or $\pm 2\mu m$. Both errors are implemented in Matlab® with their corresponding maximum error. Figure 2.9 illustrates these errors.

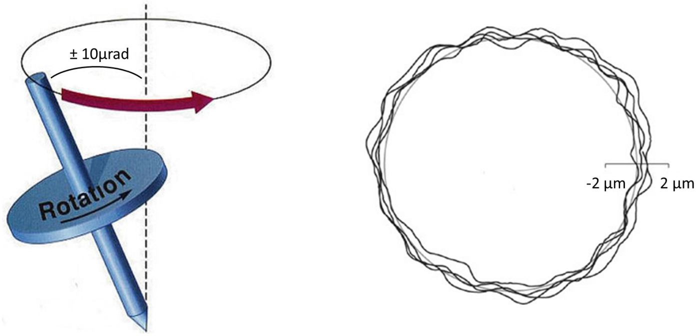

(a) (b)

Figure 2.9: Tolerances of the rotation stage: wobble (a) and eccentricity (b). [55]

2.3 Acquisition settings

The user has to make many decisions when he sets up a CT scan. [110], [112] and [146] provide information which helps a CT user to set up a good CT scan. This section discusses the different parameters related to the acquisition.

2.3.1 X-ray source current

Figure 2.10 illustrates the influence of doubling the source current on the spectrum. A higher current results in a higher intensity (flux) of the X-ray beam. This is beneficial for the Signal-To-Noise (SNR) ratio. A disadvantage of a higher current is the increasing spot size.

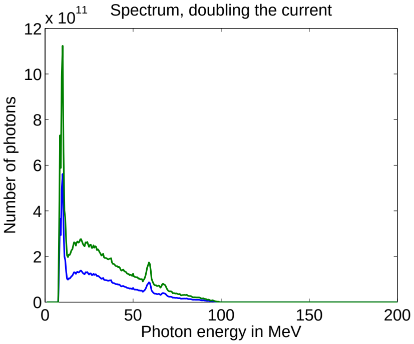

Figure 2.10: The effect of doubling the source current on the X-ray spectrum. The plotted data is obtained from [46].

2.3.2 Acceleration voltage

Figure 2.11 shows the influence of doubling the acceleration voltage. Changing the acceleration voltage changes the penetrating power of the X-ray beam. The voltage should be chosen high enough such that the X-rays are able to penetrate the entire object for each view (i.e. each angular position). Increasing the voltage also has its disadvantages: a too high voltage can for instance saturate the image. A higher voltage furthermore results in a larger spot size.

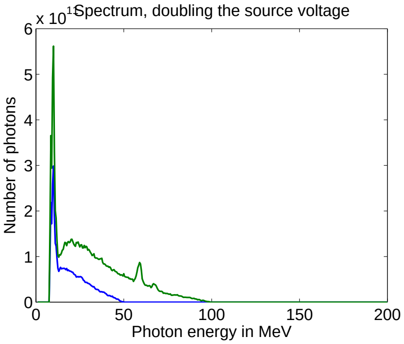

Figure 2.11: The effect of doubling the source voltage on the X-ray spectrum. The plotted data is obtained from [46].

2.3.3 Filter plate

Figure 2.12 gives the effect of different filter plates and filter plate thicknesses on the spectrum. Typical used filter plates are aluminum, tin, copper and silver. These will all influence the spectrum in a different way. A filter plate is often used to reduce beam hardening artifacts (section 2.5.4). It filters out the low energy X-rays, hence approximating a more monochromatic energy distribution. A more attenuating filter plate will however decrease the signal-to-noise ratio and will furthermore require a higher power setting which enlarges the X-ray spot size. The use of different filter plate materials and thicknesses is investigated in chapter 5.

2.3.4 Proper choice of the X-ray source current, acceleration voltage and filter plate

There is no simple textbook describing the optimal settings. The user needs to determine the values based on his own knowledge and experience, or by prior testing or computer simulation. The values are chosen based on the acquired X-ray image. Different aspects are taken into account like:

- No parts of the detector image may be in saturation.
- The X-rays should be able to penetrate the part sufficiently in all angular positions.
- Contrast optimization.

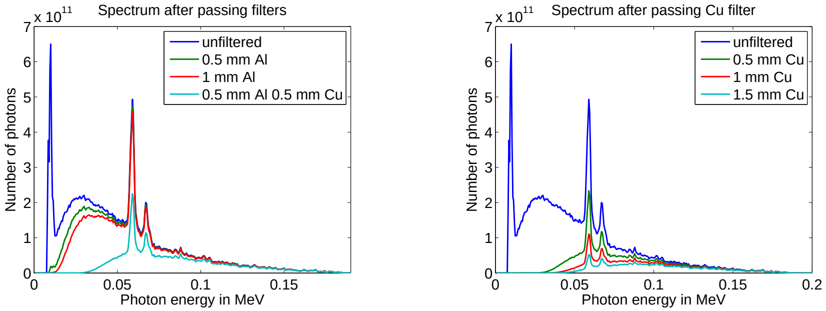

(a) (b)

Figure 2.12: The effect of filtering on the X-ray spectrum: using different filter plates (a) and using Cu filters with different thicknesses (b). The plotted data is based on a combination of the material attenuation databases provided by NIST [96] and source X-ray spectra data measured by Hammersberg et al. [46].

2.3.5 Magnification

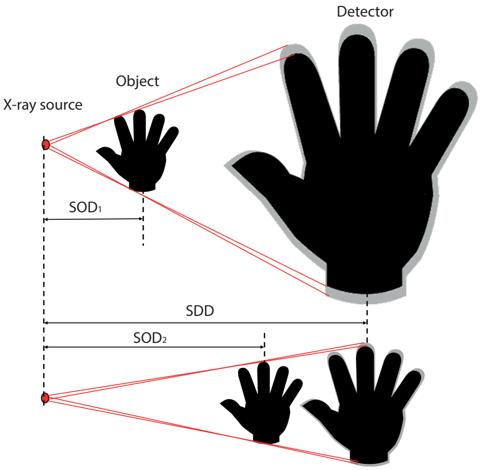

Figure 2.13: Influence of magnification. [73]

The user can magnify or demagnify the object by positioning it closer or further away from the X-ray source. Figure 2.13 illustrates the consequences of the magnification. A higher magnification causes more blurred images but this increases the image resolution.

Equation 2.4 specifies the obtained magnification. This magnification determines the voxel size. Equation 2.5 illustrates the relationship between the magnification and the corresponding voxel sizes.

$$M = \frac{SrcDetDist}{SrcObjDist} \tag{2.4}$$

$$VoxelSize = \frac{Pixelsize}{M} \tag{2.5}$$

where:

M = Magnification [/]
$SrcDetDist$ = Distance from source to detector $[mm]$.
$SrcObjDist$ = Distance from source to object (rotation axis) $[mm]$.
$VoxelSize$ = Voxel size of the reconstructed model $[mm]$.
$Pixelsize$ = Pixel size of the detector $[mm]$.

The influence of the applied magnification is investigated for different objects in chapter 5.

2.3.6 Object orientation

An experiment illustrates the influence of the object orientation [162]. The investigated object is a stepped workpiece with several length dimensions in two directions. Figure 2.14 demonstrates 2 possible orientations to scan the workpiece. The step lengths in both directions were measured after scanning the object in the two orientations. The length measurements in the rotational plane (xz plane) appeared to be much more accurate than those in the y-direction. Figure 2.15 shows the higher noise presence for the planes parallel to the xz plane. It is therefore important to avoid planes parallel to the rotational plane (xz plane).

It is furthermore important to bear in mind the maximum penetration lengths for each rotation angle. A larger penetration length results in more attenuation of the X-rays. Too much attenuation leads to defects in the reconstruction process.

Sections 5.2.2 and 5.4.3 investigate the influence of the object orientation and position with respect to the rotation table.

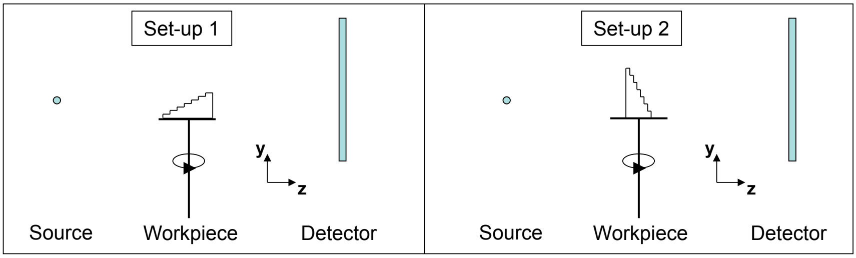

Figure 2.14: Two possible orientations for the stepped workpiece. (front view of a CT scanner as in figures 3.1 and 3.3)

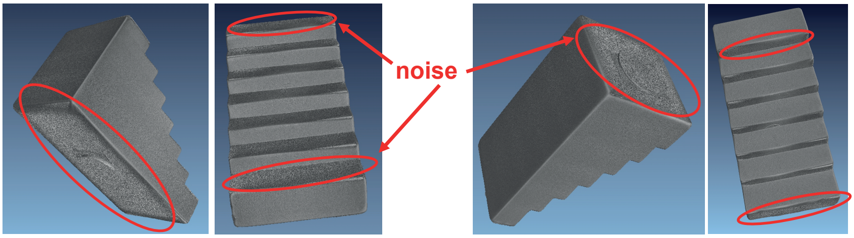

Figure 2.15: Effects of orientation (left: set-up 1, right: set-up 2) on the workpiece measurements: noise on planes parallel to xz plane.

2.3.7 Number of views

Figure 2.16 illustrates the influence of the number of views (angles) on the reconstruction accuracy when scanning 3 aligned spheres. Increasing the number of poses leads to a more precise reconstruction.

The optimal number of views in function of the reconstruction accuracy can be calculated as follows:

$$NumberOfViews = \frac{\pi}{2} * RequiredVoxels \tag{2.6}$$

where:

$RequiredVoxels$ = Largest number of voxels required along the two horizontal axes of the volume.

This optimal number optimizes the reconstruction accuracy. The additional negative effect of a longer scanning time has not been taken into account.

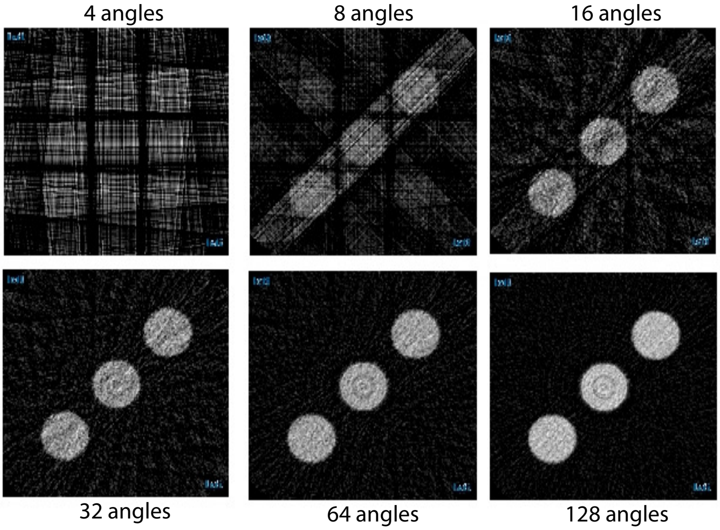

Figure 2.16: Influence of the number of views on the reconstruction accuracy. [73]

Moreover a longer scanning time will have its influence on other influence factors like flux fluctuation, drift of components due to temperature changes (e.g. spot drift).

Nikon Metrology's acquisition software Inspect-X [93] hands the user the option to optimize the number of views, which will use above rule, or to specify the number of views manually.

Sections 5.4.3, 5.5.3, 5.6.3 investigate the influence of the number of views.

2.3.8 Frames per view

The number of frames per view determines the number of frames averaged for each projection. This value is kept to 1 in this thesis.

2.3.9 Flux normalisation

Inspect-X [93] offers the possibility to use flux normalization. Flux normalization compensates for flux variations during the acquisition of a CT data set. The user selects an area within the projection image which contains no projection data. Detection of the image brightness variation of this area is used to correct the entire projection image. Flux normalization has always been used in this thesis.

2.3.10 Shading correction using reference images

Projection images are always corrected by reference images. These reference images correct for the variation in gain across the imaging device and the variation in intensity of the X-ray photons reaching the detector. The standard procedure makes use of 2 reference images. The first reference image corresponds to the detector output without incoming X-rays: i.e. 'dark' gray value for each individual pixel of the detector. The second reference image corresponds to the detector output with the X-rays switched on without any object in view, i.e. 'bright' gray value for each pixel of the detector. The reference images should be taken under the same settings, e.g. source voltage and current, as will be used for CT scanning the object. The user defines the number of frames averaged to define these images.

Later Inspect-X software versions have the ability to apply more than 2 reference images for correction (multi-point shading correction). During this thesis the standard procedure using 2 reference images has been used.

2.3.11 Warm up period

There is not much information available on the required warm up time for a system to get into steady state condition. But there will be certainly a difference between a CT scan taken with a cold (not used) CT system, and a scan taken with a machine which has already been scanning for several hours. For instance the focal spot position can change due to heating up of the source tube.

2.3.12 Detector exposure time

The detector exposure time is the integration time per image. Doubling the exposure time more or less doubles the scanning time. An advantage of a higher exposure time is the better Signal-to-Noise Ratio (SNR) obtained in the projection images. The standard exposure time used in this thesis is $1000ms$. Section 5.6.3 looks at the influence of the detector exposure time in combination with the detector gain.

2.3.13 Clamping

An important aspect when performing a CT scan is the clamping of the object. The clamping has two main requirements. The first one is keeping the object stable such that the object only makes the required rotation during the scan and no additional movements. The second requirement is that the clamping should not influence the reconstruction. The material should not be too dense, and the clamping system should not be too large. Parts of the clamping system being in detector view for some images and not for other images can lead to artifacts in your reconstructed volume.

2.3.14 Gain

There are two types of gains which can be applied in Inspect-X [93]: digital gain and detector gain. The digital gain setting results in a simple multiplication of the gray value and will not be used. Use of detector gain amplifies the photo diode signal in the detector. This is an interesting option. The operator can for instance use a higher exposure time if the detector gain is lowered. This leads to a better SNR value, but a longer scanning time. Section 5.6.3 investigates the influence of the detector gain combined with the detector exposure time.

2.3.15 Minimize ring artifacts

Ring artifacts are caused by improper correction of non-ideal or defective pixels. These defects appear as rings of sharp contrast concentric to the center of rotation [73]. Inspect-X [93] offers an option to minimize the ring artifacts by shifting of the object between the acquired images. This method shifts the projection images, such that the repeatable character of these improper corrected or defective pixel fades away. The user can specify a value between 0 and 15 as maximum pixel shift for minimization of ring artifacts [93].

2.3.16 Continuous versus stepwise rotation

When discussing about the captured projection images, one often assumes each image to be captured for constant angle steps while the object is not rotating anymore during image exposure. In reality the images are mostly captured during continuous rotation of the rotation table. This results in an important difference illustrated in Figure 2.17. The left figure illustrates the case in which the projection images are captured during continuous rotation of the object, while the right figure illustrates the case in which the rotation table stops each time to take the image. It has to be noticed that these images have been taken during a CT scan with only 30 images, which emphasized this effect.

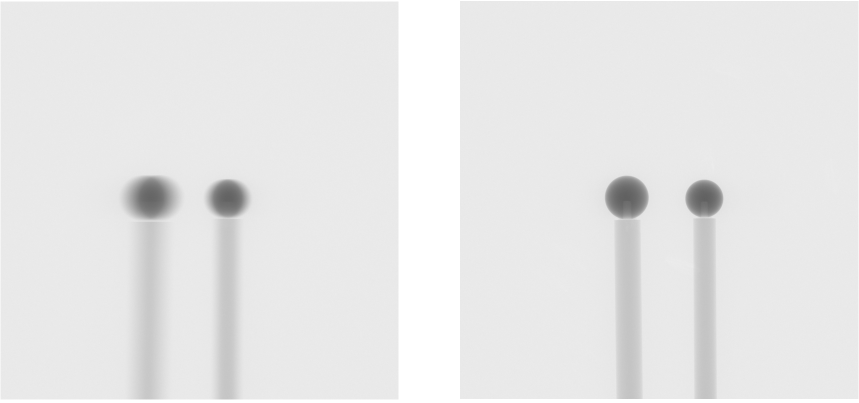

(a) (b)

Figure 2.17: Continuous scanning (a) versus stepwise scanning (b).

A way to perform stepwise scans in the inspect-X software is by using the 'Minimize ring artifacts' option with the displacement set to 0. This will lead to capturing of the projection images while the table is not rotating. A possible problem with step by step rotation is the fact that it will be more probable to have angular differences in the subsequent rotation angles, which are expected to be constant. This leads to errors during reconstruction.

The stepwise rotation possibility is investigated in section 5.4.3.

2.3.17 WhiteLevel

The *WhiteLevel* is a predefined user value which defines the gray value when no material is penetrated (no object in view). The detector pixels with no material penetration will produce values fluctuating around this value. They will not exactly report this *WhiteLevel* value due to noise, scatter, etc. This *WhiteLevel* value should not be taken to near to the maximum output value of the detector (i.e. 65536 for a 16 bit detector). Otherwise values which are actually higher than this maximum output value, due to noise and scatter, will be set to the maximum values. This would influence the projection images and therefore the reconstructed model and dimensional measurements. A too small value will limit the range of possible gray values and hence also have a negative influence on the measurements. The maximum outputted number of a 16-bit detector, used in the investigated CT devices, is $65536 = 2^{16}$. The value $WhiteLevel$ is set to 60000 for the measurements in this thesis.

2.3.18 Filament demand

The filament demand [93] controls the temperature of the filament which generates the electron beam within the X-ray source (see section 2.2.1). A correct setting ensures the generation of a bright and sharp image. This setting is generally only changed after a filament replacement.

2.3.19 Electron beam alignment

The alignment of the electron beam which hits the target is done using the Motorized Receptacle Alignment controller (MRA). This should ideally be done before each scan as it depends of the used settings (applied kV, etc.). Unfortunately this alignment is suspect to quite some user influence and it is furthermore quite hard to do it correctly. This aspect will certainly has its influence on the resulting scans. This electron beam alignment has been carried out before each scan in this thesis.

2.3.20 Focusing mode

Two options are possible for the focusing mode: 'Normal' and 'Auto-Defocus' [93]. The normal mode uses focus current values from a recorded look-up table. In case of the auto-defocus mode a defocus factor on the current values is applied after the X-ray power reaches a certain defocus threshold. This enlarges the focal spot, which increases the target life but decreases the resolution.

The 'Auto-defocus' mode is normally used at our department. Setting up of the look-up table by the manufacturer will obviously have its influence on the measurement accuracy.

2.3.21 Conditioning

The user has to condition the X-ray source regularly [93]. Section 2.2.1 has already shortly introduced this topic. Conditioning is the process to achieve a stable operating voltage and steady image. When this conditioning has not been done, or when it has been done for an insufficient amount of time or voltage setting, the X-ray generation will not be stable.

2.3.22 X-ray control

One of the settings available in Inspect-X [93] regarding the X-ray control is the possibility to restart the CT scan from the previous angular position after tripping of the X-rays. The X-rays can start to trip during a CT scan, due to filth in the X-ray tube. The user can opt to continue the scan from the previous/last angle, or he can restart the entire scan after tripping of the X-rays. In this thesis it is always opted to restart the entire scan, as restarting from the previous angle will introduce extra errors.

2.3.23 Rotation speed calibration

The rotation speed of the rotation table has to be calibrated. When this is not done correctly the capturing of the images will not be performed over 360 degrees like required. This will lead to an overshoot (rotation table turned to far) or the contrary. An estimation of this overshoot, for the **simulation program** developed further on in this thesis, can be based on the angle file which is produced for each CT scan. This angle file keeps track of the angular positions of the rotation table for each view. Section 5.5.3 discusses the influence of incorrect rotation angles, due to overshoot, on the dimensional measurements.

2.4 Environment

Factors like temperature, humidity and vibrations will have an influence on the measurement.

2.4.1 Vibrations

It is important to exclude vibrations as much as possible. There are different sources of vibrations: vibrations can for instance originate from other machines (e.g. vibrations from one machine to the other machine transmitted through the floor), the own machine elements, etc. The cooling systems of the CT scanner are therefore positioned in a separate room, which excludes this negative influence.

2.4.2 Temperature

The temperature is a main environmental factor influencing the CT scans. Dimensional metrology should be carried out at 20 degrees. A different temperature will result in expanding or shrinking of the object and possible thermal distortion of the structure of the CT scanner. Not only the temperature but also temperature gradients in time and space will affect thermal distortions and hence the measurements. The Nikon Metrology XT H 450 CT scanner and the Nikon Metrology XT H 225 ST CT scanner used in this thesis are standing in a temperature controlled room with $T = 20 \pm 0.5$ degrees, while the scanner cabinet and X-ray source have separate cooling units. The cooling units are positioned in a separate room, such that their heat does not influence the room temperature.

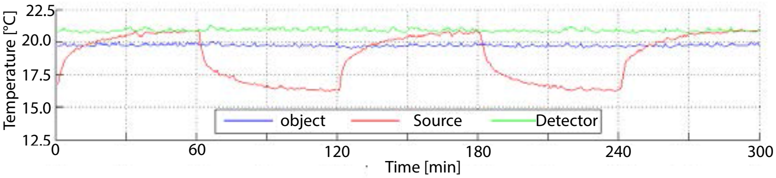

Figure 2.18: Temperature measurements at the X-ray source, object and detector inside a CT scanner. The X-rays are alternatively switched on and off for 60 minutes. [150]

Vogeler et al. [150] investigated the temperature manifestations in a Nikon Metrology 225 CT system. Three temperature sensors were mounted inside the CT machine. The first sensor was mounted on the X-ray source, the second on the object and the third one on the detector. Figure 2.18 gives the results. The X-rays were turned on for one hour, during which 2D X-ray images were taken of the object, with a frequency of 1 image per minute. Next the X-rays were switched off for one hour. This process was repeated 3 times (the third period with the X-rays switched off was not monitored). The temperature at the object and detector stays quite constant during the entire time. The temperature at the source raised when switching on the X-rays and stabilized. The temperature decreased when the X-rays were switched off. It has to be noticed that a problem with the cooling unit of the source was identified after these experiments. An additional remark is that the X-ray system tested here was not standing in a temperature controlled environment.

2.5 Measurement object

2.5.1 Interaction with matter

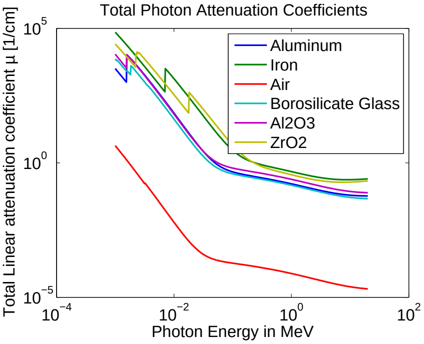

Figure 2.19: Total attenuation coefficient for different materials. The plotted data is obtained via the databases provided by NIST [96].

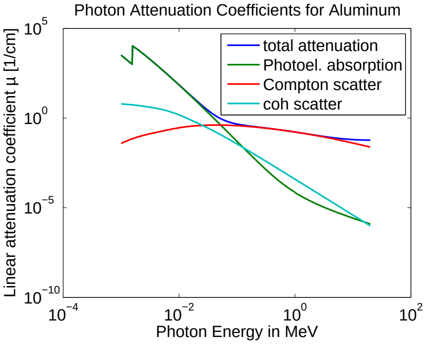

Figure 2.20: Detailed attenuation coefficients for aluminum. The plotted data is obtained via the databases provided by NIST [96].

The X-rays penetrating the workpiece are attenuated due to several physical interactions [80]. Figure 2.19 gives the total attenuation coefficient versus energy level for different materials, whereas figure 2.20 pictures the various attenuation coefficients for aluminum.

Photoelectric absorption. Photoelectric absorption occurs when the total energy of an incoming X-ray photon is transferred to an inner electron, which causes the electron to be ejected [73].

Compton scattering or incoherent scattering. Compton scattering occurs when the incoming X-ray photon interacts with a free or outer electron, ejecting the electron. The X-ray photon is deflected in a different direction with loss of energy [73].

Rayleigh scattering or coherent scattering. Rayleigh scattering or coherent scattering happens when the X-ray photon interacts with the whole atom. The photon is scattered with no loss of energy.

Pair production. Pair production only occurs at higher energies and will not take place in our CT systems and will therefore not be discussed.

The statistical nature of these interactions will affect the accuracy of the dimensional measurements.

2.5.2 Surface roughness

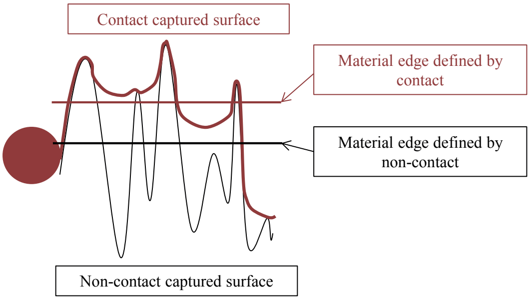

Figure 2.21: Difference in evaluation due to surface roughness in case of contact (tactile CMM) and non-contact (e.g. CT) measurements [20].

The surface roughness influences dimensional measurements. It is hereby important to notice the difference in evaluation between CT and tactile probing [73], as illustrated in figure 2.21 [20]. Computed tomography has an integrative characteristic. In case of a tactile measurement, there is no integrating effect but the measurement is linked to the surface maxima. The probe measures on the tops of the surface roughness profile and an envelope is created by the finite probe radius. In case of CT a kind of center line average roughness profile is used. This leads to roughness offsets [17]. [20] investigated the influence of the roughness of a workpiece on the edge offset present between contact and non-contact measurements. This work showed a clear offset. Figure 2.21 illustrates the evaluation difference.

Arenhart et al. [8] and [88] manufactured a multi-wave standard which enables to evaluate the frequency response of CT measuring systems on one hand, and to investigate the unwanted CT-induced random surface deviations on the other hand.

2.5.3 Penetration depth, dimension and geometry

The dimensions, geometry and penetration depths of the object will influence the measurement results [110], [73]. The object should ideally always be in view (in horizontal direction) when rotating as the reconstruction might otherwise encounter problems. The attenuation is dependent on the penetration length and will therefore influence the results. Too much attenuation will lead too image artifacts: there will be a lack of information provided by these image pixels as too few or no X-ray photons reach the detector.

2.5.4 Beam hardening

The polychromatic character of conventional X-ray sources causes the well known effect of beam hardening: while the X-ray beam penetrates material, the low-energy X-rays (soft X-rays) are more easily attenuated than the high-energy X-rays. As a consequence the image on the detector differs from the expected image, resulting in observable errors in the reconstructed volume. The amount of beam hardening depends on the initial X-ray spectrum as well as on the composition, density and the length of material traversed. [136], [135], [137], [134], [72], [31], [91], [142], [61], [22] discuss this topic and make suggestions to correct for beam hardening artifacts. Often a filter plate is used to decrease these beam hardening (section 2.3.3). A filter plate filters out the soft X-rays and hence the CT scan is only performed with the hard spectrum of the beam. A more attenuating filter plate will however decrease the signal-to-noise ratio and will furthermore require a higher power setting which enlarges the X-ray spot size and deteriorates the results. Software-based correction for beam hardening artifacts is another possibility [61], [22], [133] (see also section 2.6.1).

2.5.5 Scattered radiation

X-rays are attenuated due to absorption or by scattering as discussed in section 2.5.1. These scattered X-ray photons can still hit the detector. The amount of scattered X-rays reaching the detector differs for each view and will influence the measurements. [83], [10], [79], [82], [138], [75] present methods for calculation and simulation of scatter X-ray data. Software-based methods exist to reduce this unwanted effect (see also section 2.6.1). Reducing the amount of scattered X-rays can be done by placing a filter plate between the object and the detector.

In case of the CLDA, one can use a pair of collimators as demonstrated in figure 2.7: two thick blocks of lead are put close to the source to eliminate a part of the X-ray cone beam and hence to obtain a flat fan beam.

2.5.6 Material composition

Different aspects related to the material composition affect the measurement accuracy: the linear attenuation coefficient, dimensions, features, multi-material character. Multi-material measurements are a known problem in computed tomography. A common issue is the appearance of metal streak artifacts. [33] listed and studied several potential causes of metal streak artifacts using phantom measurements and simulations. [72], [61] and [4] developed correction methods to reduce artifacts in multi-material measurements. Sections 5.4 and 5.5 investigate objects with multiple materials.

2.6 Software and data processing

After the CT acquisition the software and data processing start. This includes different steps:

3D reconstruction. Reconstruction of the projection images into a 3D voxel model.

Threshold determination. Determination of the respective interfaces between solid material and surrounding air or between different solid materials.

Dimensional measurements. Performing the required dimensional measurements.

Data correction. Different corrections can be performed. This step can take place at different moments during the data processing and is many times an iterative process. It often includes repeating all or some of the previous steps.

2.6.1 3D reconstruction

[41], [129] and [2] describe algorithms to reconstruct the volume. The reconstruction is mostly based on the filtered back projection method. This method is based on the *Linear Integral Transformation*, a mathematical method developed by J. Radon in 1917 [73]. The algorithm applies equation 4.3. Figure 2.22 shows the simple back projection method. Each projection image is back projected to the volume at the collected rotation angle. In fact each view is smeared back to the image in the direction it was originally acquired. The final image is the sum of all the back projected views [127]. The results is a blurry image. A remedy is to filter the images first (images are Fourier transformed, filtered and then inverse transformed). Figure 2.23 shows the results of filtered back projection.

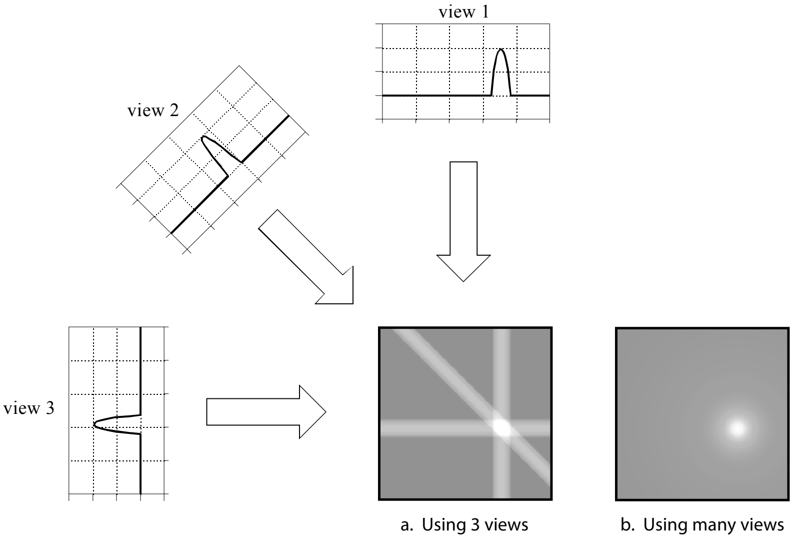

Figure 2.22: The back projection principle. [127]

CT Pro of Nikon Metrology [94] is used during this thesis for reconstructions. This software leads the user through different initiating steps, before starting the actual reconstruction.

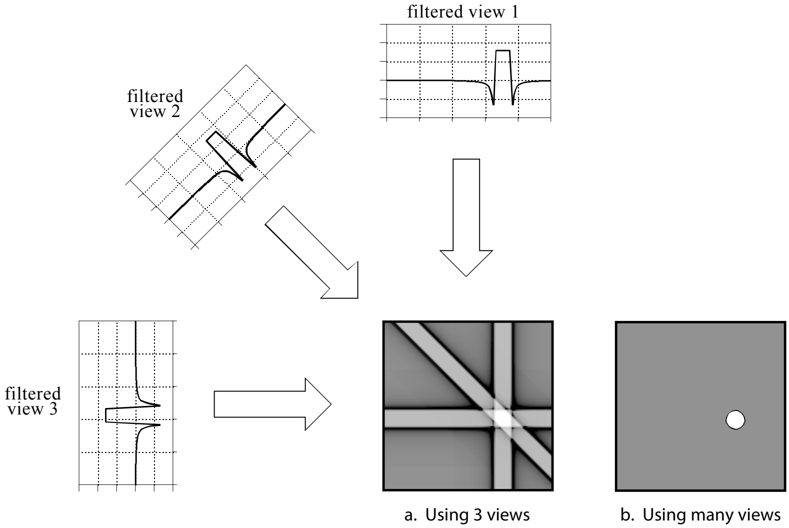

Figure 2.23: The filtered back projection principle. [127]

Center of rotation

The rotation axis is supposed to be aligned parallel, resp. perpendicular, to the detector and its pixel rows or columns [73]. Unfortunately this will never be exactly the case and will cause errors in the reconstruction as the reconstruction algorithm expects the projection images to be perfectly vertical and centered on the rotation axis. See section 3.4 for further discussion on this problem.

A software-based solution is provided in CT Pro [94] by shifting and shearing the projection images prior to reconstruction. To determine the needed correction, 1 or 2 test slices are investigated. The test slice is reconstructed iteratively, and shifts its center of rotation until the optimal center of rotation point has been found. The user selects the number (1 or 2) and position of the test slices and the reconstruction quality (fast, standard or high quality). Hence a shift and shear is calculated for the projection images. This method will correct for a misalignment parallel to the detector plane, but will have less effect when the misalignment is situated in the other direction: i.e. the rotation axis is tilted towards or away from the detector plane.

During this thesis correction has been executed by calculating the error in 2 test slices using the high quality option.

Beam hardening correction

CT Pro provides [94] algorithmic beam hardening correction using a linearization technique based on polynomial curves of maximum fourth order:

$$Y = a(b + cX + dX^2 + eX^3 + fX^4) \tag{2.7}$$

where:

X = The initial gray value of a pixel in an X-ray image.
Y = The corrected (linearized) gray value.
a to f = Coefficients which can be fine tuned in order to obtain images. without beam hardening artifacts.

Six beam hardening correction presets (BHC1-BHC6) are predefined (table 2.1) in the software. CT Pro offers the possibility to reconstruct a single slice. Figure 2.24 illustrates this using the different beam hardening correction presets and noise reduction presets. This should allow the user to define the correct correction settings.

Parameter	Preset					
	BHC1	BHC2	BHC3	BHC4	BHC5	BHC6
a	1	1	1	1	1	1
b	0	0	0	0	0	0
c	1	0.75	0.5	0.2	0.1	0
d	0	0.25	0.5	0.8	0.9	0.2
e	0	0	0	0	0	0.8
f	0	0	0	0	0	0

Table 2.1: Software-based beam hardening correction presets, predefined by the software manufacturer.

Noise reduction

The reconstruction is based on filtered back projection. The noise in the reconstructed image is dependent of the used filter and settings (e.g. voltage, current, exposure time). CT Pro [94] provides 6 presets for noise reductions. These presets depend on filter type (ramp filter or Hanning) and cut off frequency. A lower cut-off frequency leads to more suppressing of the noise. But suppressing high frequencies also removes detail and can lead to a loss of resolution [110]. It is recommended for dimensional metrology applications to use preset 1, which is the Ramp filter with no cut-off (100 percent cut off frequency).

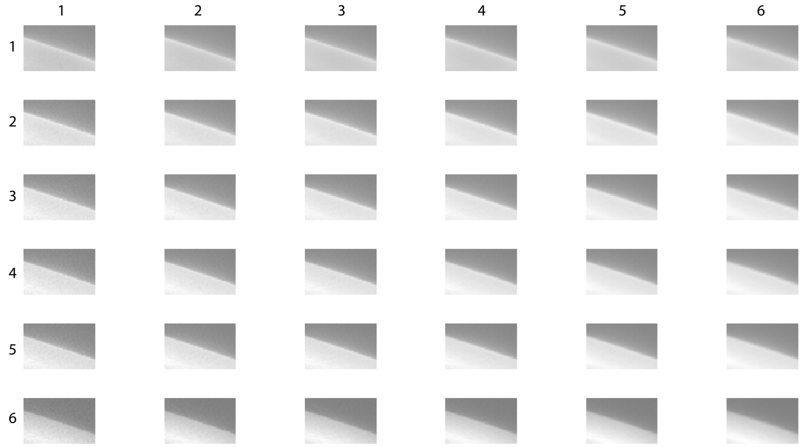

Figure 2.24: CT Pro has the possibility to reconstruct a single slice. This figure illustrates this using the different beam hardening correction presets and noise reduction presets. This should allow the user to define the correct correction settings.

Scatter reduction

CT Pro [94] has the ability of scatter reduction. This in fact only subtracts a constant value from all pixels in the projection images.

Reconstruction resolution quality

The resolution quality defines the resolution of the voxels generated in the volume. The standard value is 100 percent. This setting defines the voxel size by formula 2.5 (section 2.3.5) which is a direct determination by the pixel size of the detector and the magnification. A higher resolution quality value leads to a longer reconstruction time. Section 5.4.3 examines the difference between resolution quality 100 and 150 percent.

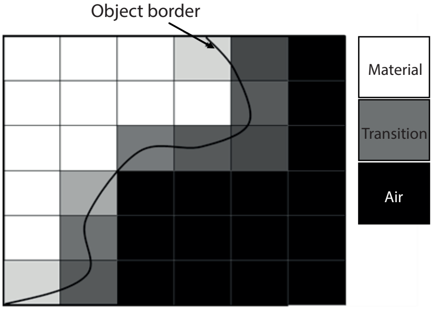

Figure 2.25: The object border and the corresponding gray values in the reconstructed voxel model, pictured in the ideal situation. Adapted from [63].

2.6.2 Threshold determination and surface generation

Edge (surface) detection or segmentation determining the respective interfaces between solid material and surrounding air or between different solid materials is a next crucial step in CT metrology. Various techniques exist to identify object or material edges [73]: assigning a threshold gray value to “edge voxels”, interpolation between voxel gray values, search for maximum gray value derivatives, mid gray value between light air voxel and dark material voxel levels, local adaptive gray threshold, etc. Figure 2.25 illustrates the border of a material and the corresponding voxel values. Threshold determination will be carried out on subvoxel level. [85] and [48] compare different softwares and feature measurement techniques. The differences of the CT measured values is calculated and compared to CMM measurements and/or other optical measurements. The analysis are furthermore made with different softwares and different techniques to determine the interface between air and material or two different materials.

The Volume Graphics software has been applied during this thesis for all analyzes on the voxel model. Volume Graphics [152] offers the possibility to define the edge based on a global threshold value or via a local adaptive gray threshold. This latter one re-evaluates an existing boundary (start contour). Polynomial functions are fitted within a predefined region along the normal direction of the starting contour [133]. Subsequently the largest gradient of this function (first derivative) is calculated which will be seen as the new boundary [133]. Different options should be chosen to support the advanced calculations like single or multi-material, search distance, starting contour smoothing, and many more.

Figure 2.26 illustrates the use of advanced thresholding (local adaptive surface determination) in Volume Graphics. Different lines can be distinguished:

- White line: current contour.
- Thin yellow line: starting contour to search optimal contour via advanced mode.
- Small yellow lines perpendicular to the thin yellow line: Search domain.
- Thick yellow line: calculated contour using advanced mode.

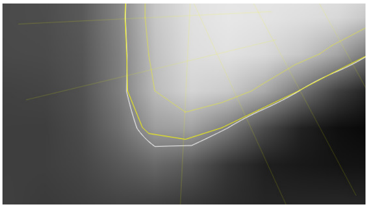

Figure 2.26: Advanced thresholding by Volume Graphics.

Section 2.6.5 compares the difference between global and advanced thresholding. The influence of the start contour will be investigated in chapter 5.

2.6.3 Dimensional measurements

The next step includes performing the dimensional measurements. The accuracy of the dimensional measurement assessment is influenced by many parameters [73]: the identification and definition of the measurand and furthermore by the common error sources affecting conventional coordinate measuring processes. These common error sources include the influence of used measured points (amount, location, distribution, uncertainty on individual coordinates), datum definition (local coordinate system, reference features), etc [167]. [85] compares different sofwares with respect to the dimensional measurement assessment. Volume Graphics [152] has again been used for this step. Volume Graphics offers many options regarding the feature definition/fitting: e.g. fitting method, number of fit points, search distance to find the fit points. Furthermore many options are available regarding the datum definition. Volume Graphics also offers the possibility to select a Region of Interest (ROI) in the voxel volume. This way calculations can be applied only taking into account the ROI. Section 5.4 illustrates the effect of working with a ROI.

2.6.4 Data corrections

There exist different possibilities to correct and improve the obtained reconstructed CT voxel model. The voxel sizes are often rescaled and an offset value for the detected edge is commonly calculated. The voxel size is determined by equation 2.5. This is mostly incorrect due to e.g. the inaccuracy of the magnification axis. The obtained voxel sizes should therefore be rescaled. This can be accomplished using equation 2.8. The voxel sizes are hence corrected by multiplication wih a correction factor. This correction factor can be determined by comparison of a CT measured value to a reference value obtained by a more accurate sensor (for instance the CMM measurement of the same measurand). A distance between 2 spheres is often used as the measurand for rescaling as this measurand is less influenced by beam hardening and threshold errors.

$$Voxelsize_{corr} = Voxelsize_0 \times \frac{Distance_{Ref}}{Distance_0} \qquad (2.8)$$

where:

$Voxelsize_0$ = Initial voxel size $[mm]$.
$Distance_0$ = Initial CT measured distance $[mm]$.
$Distance_{Ref}$ = Reference distance $[mm]$.
$Voxelsize_{corr}$ = Corrected voxel size $[mm]$.

The determined edge often contains an offset error. This offset error will be in a different direction for inner and outer dimensions. Figure 2.27 pictures the influence of an offset error for inside and outside diameters. This can be corrected by adding or subtracting a correction value from the measured quantity as in equation 2.9. The correction factor is dependent on the measurand: the edge offset correction value on a diameter measurement is for instance the double of the edge offset correction value on the radius measurement.

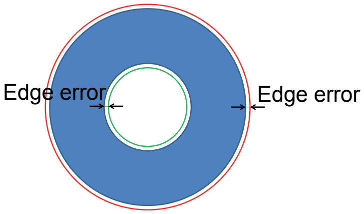

Figure 2.27: Influence of incorrect edge detection on inner and outer diameter.

$$measurement_{corr} = measurement_{resc} \pm edge\_offset_{correction} \tag{2.9}$$

where:

$measurement_{resc}$ = Rescaled measurement value.
$edge\_offset_{correction}$ = Correction value for the edge offset.

More complex data fusion techniques are often applied for data correction. Different possibilities are hereby described.

Combining scans on different magnitudes, positions or orientations.

Combining scans on different energy levels. [71] combines multi-energy tiff image stacks for improved reconstruction of workpieces of high aspect ratios and multi-material objects.

Using measurements with more accurate sensors. [162] discusses this improvement option. The principle is often used, applying an additional tactile or optical sensor. Some manufacturers even combine the CT principle and additional measurement systems in one device. Another possibility is accomplishing the additional measurement with a stand-alone machine. [91] uses an additional optical measurement system to enhance the overall accuracy of CT data by merging the dataset obtained by CT measurement and a dataset obtained by optical measurement. [44] explains a method which uses an additional optical sensor for beam hardening correction. This results in a quality and speed improvement for the industrial CT measurement.

2.6.5 Simulation example

The simulation program (chapter 4) is used to illustrate the influence of the beam hardening correction presets, the threshold method, and the influence of multi-material. A simple situation is simulated with a $6mm$ diameter pin partly surrounded by a hollow cylinder (inner diameter $8mm$ and outer diameter $10mm$) [128]. Figure 2.28 gives a cross section of the object. 2 parts can be distinguished: the first part in which there is only the pin, and the second part with the cylinder surrounded by the hollow cylinder. The pin material is steel, the hollow cylinder is simulated one time as steel and one time as aluminum.

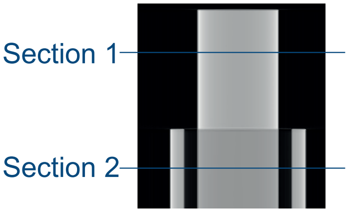

Figure 2.28: Simulation of a pin inside a hollow cylinder, measurements have been performed in sections 1 and 2.

Tables 2.2 and 2.3 give the diameter results in the different situations for respectively the steel pin inside the hollow steel cylinder and inside the hollow aluminum cylinder. Global versus advanced, section 1 versus section 2 and different Beam Hardening Correction presets BHC1 versus BHC2 versus BHC3 clearly gives differences. The best results are obtained using BHC preset 1 and local thresholding. Global thresholding fails in the evaluation of objects which are a bit more complex. It gives for instance a clear difference in evaluation between inner and outer surface as can be interpreted from the hollow cylinder diameter (errors on inner ($8mm$) versus outer ($10mm$) diameter).

Figure 2.29 sketches the gray value profiles (gray value on the blue lines of figure 2.28) for the different situations. The effect of the beam hardening correction is clearly visible. Looking at section 2 a different influence of the surrounding material is observable. The hollow steel cylinder 'absorbs' most of the beam hardening artifact (clearly visible with preset BHC1), which is not the case for the steel pin in the aluminum hollow cylinder. This is also the reason why the diameter of the pin is the same using BHC1 for both sections in the situation where it is surrounded by the hollow aluminum cylinder (table 2.3) in contrary to the situation of the steel pin in the hollow steel cylinder. In CT for material science, one will often prefer to use beam hardening correction preset 2 in the given situation: this makes the inside material value more or less constant. This however deteriorates the edges of the workpiece which are important for dimensional CT metrology.

		Nominal $[mm]$	Error $[mm]$		
			BHC1	BHC2	BHC3
Global	Section 1	6	0.016	-0.006	-0.036
Global	Section 2	6	0.005	-0.002	-0.007
Advanced	Section 1	6	0.001	-0.005	-0.017
Advanced	Section 2	6	-0.001	-0.002	-0.004
Global	Section 2	8	-0.008	0.002	0.007
Global	Section 2	10	0.014	-0.007	-0.033
Advanced	Section 2	8	0.000	0.002	0.002
Advanced	Section 2	10	0.001	-0.005	-0.018

Table 2.2: Measurements of the different diameters of the steel pin partly surrounded by a hollow steel cylinder in section 1 and 2, using global or advanced thresholding and using different beam hardening correction (BHC) presets.

		Nominal $[mm]$	Error $[mm]$		
			BHC1	BHC2	BHC3
Global	Section 1	6	0.016	-0.007	-0.038
Global	Section 2	6	0.016	-0.005	-0.028
Advanced	Section 1	6	0.001	-0.005	-0.017
Advanced	Section 2	6	0.001	-0.004	-0.013

Table 2.3: Measurements of the different diameters of the steel pin partly surrounded by a hollow aluminum cylinder in section 1 and 2, using global or advanced thresholding and using different beam hardening correction (BHC) presets.

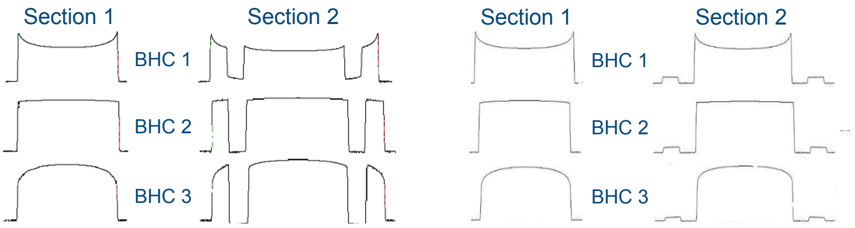

(a) (b)

Figure 2.29: Gray profiles for the different BHC/section combinations for the steel pin inside a hollow steel cylinder (a) and inside a hollow steel aluminum cylinder (b). [128]

2.7 Dimensional measurement accuracy

All above discussed influence factors contribute to the overall measurement accuracy. There are many possibilities to improve this measurement accuracy [162]:

- Improvement of dedicated CT components.
- Improvement of the hardware stability.
- Optimization of user defined settings.
- Improvement of data processing.
- Reduction of systematic measurement errors via calibrated reference standards.
- Additional measurement of the workpiece.

Influence of several parameters on the accuracy and repeatability of dimensional measurements has been investigated experimentally [155], [5], [43] and by simulation [163], [51], [52] and [50].

A good value to express the accuracy of a measurement is the measurement uncertainty. Different authors propose methods to define the measurement uncertainty of a measurand obtained by CT: [68], [35], [89], [157], [120], [86], [155], [163], [16] and [52].

2.8 Conclusion

This chapter has discussed the many influence factors affecting the dimensional X-ray CT measurements and therefore the measurement accuracy. The influence factors have been divided into different main categories: hardware, acquisition settings, environment, measurement object and software and data processing. The factors have been analyzed and the effects of different factors on projection images have been illustrated using examples. The mechanical structure will be thoroughly investigated in chapter 3. The effect of the different influence factors on the dimensional measurements will be further explored using a simulation software developed in chapter 4 and experimental research in chapter 5.

Chapter 3

Mechanical structure

Chapter 2 has given an overview of the many factors disturbing dimensional X-ray CT measurements and therefore influencing the accuracy and measurement uncertainty of these CT measurements. There is quite some literature which describes, investigates and/or provides corrections for beam hardening effects, scatter artifacts, ring artifacts, etc. Furthermore different suggested calibration objects for voxel size calibration (rescaling), beam hardening correction, etc. can be found in literature e.g. [136], [135], [137], [134], [72], [31], [91], [142], [61], [22], [73], [147] and [148]. Less attention is often paid to the kinematic system although this has an important impact on the dimensional X-ray CT measurements.

This chapter first reports the problems related to the mechanical structure (section 3.1). Section 3.2 describes the kinematic model for the Nikon Metrology XT H 450 CT scanner under investigation. This kinematic model defines the errors related to the turntable positioning system. Quantification of the error components in this kinematic model is performed in section 3.3. The errors related to the positioning system are only a part of the problem. The relative position between the source, turntable and detector is the next part. Section 3.4 investigates these alignment errors. A first version discussing this topic has been worked out in [160].

3.1 Problem description

The kinematic system of the investigated CT scanner is illustrated in figure 3.1. It consists of a turntable for stepwise or continuous rotation, two axes for horizontal translation (x and z) and a vertical translation axis (y). The flat panel detector (FPD) can furthermore shift along a vertical axis, to be able to work with the curved linear diode array detector (CLDA) which is positioned behind the FPD (figure 3.1, right).

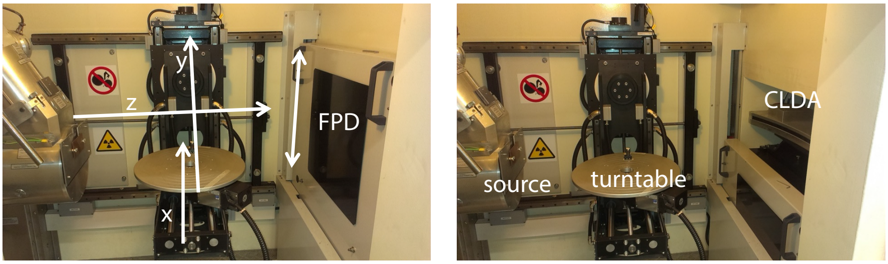

Figure 3.1: Kinematic system of the Nikon Metrology XT H 450 CT scanner. A schematic representation will be depicted in figure 3.3.

Errors of the kinematic system on one side and the relative errors between the source, turntable and detector on the other side will unambiguously introduce errors on the dimensional measurements:

- Positioning errors and repeatability problems of the z-axis directly influence the measured dimensions through a change in magnification factor and subsequently the voxel size (see section 2.3.5).
- The rotation axis is supposed to be aligned parallel, resp. perpendicular, to the detector and its pixel rows or columns [73].
- Error from wrong identification of rotation center. The reconstruction software will try to identify the location of the axis around which the part was rotated during CT image capturing. Failure in precise identification of the rotation center/axis will introduce reconstruction errors [73].
- Errors of the kinematic system will hinder the initial machine calibration performed by the manufacturer. This initial machine calibration serves to align the rotation axis parallel, resp. perpendicular, to the detector and its pixel rows or columns, and to determine the source/object and source/detector distances (section 2.2.3).

A better knowledge of the kinematic system errors and the relative errors between the source, turntable and detector furthermore allows to perform better measurement uncertainty calculations. The uncertainty parameters related to the mechanical structure (e.g. tilt of the detector) are often (incorrectly) defined by taking a symmetrical uncertainty interval around the ideal case (i.e. no error). But in reality there is usually a systematic error on these errors. It is therefore needed to know the errors of the mechanical structure in advance to make an accurate estimation of the measurement uncertainty.

3.2 Kinematic model

3.2.1 State of the art

Methods to define a kinematic model for a Coordinate Measuring System (CMS) is available in several works (e.g. [122], [12], [74] and [13]). A method to define the kinematic model of the COORD3 Coordinate Measuring System (CMS) available at our facilities has been worked out by Nick Van Gestel [143]. This kinematic model is here adapted to the Nikon Metrology XT H 450 CT scanner.

3.2.2 Error components

Error components according to the ISO 230-1 [56] are used to describe the kinematic model. The ISO 230 specifies methods for testing the accuracy of machine tools, operating either under no-load or under quasi-static conditions, by means of geometric and machining tests. The methods can also be applied to other types of industrial machines.

Figure 3.2 illustrates the use of these error components in case of the z-axis. A combination of 18 error motions (6 errors of motion for each axis) and 3 additional squareness errors between the axes enables to define the geometrical errors of the CT scanner. The 3 additional squareness errors are needed as the axes will not be perpendicular to each other. It is important to know that the 18 error motions are not constant values, they are in contrary dependent of their respective axis position. E.g. exz is a variable defined in function of z.

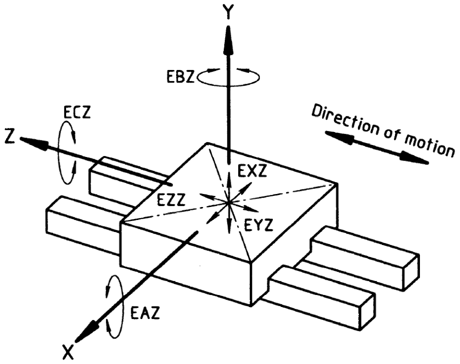

EXZ: Straightness error motion of z in x direction.
EYZ: Straightness error motion of z in y direction.
EZZ: Positioning error of z.
EAZ: Tilt error motion of z around x (pitch).
EBZ: Tilt error motion of z around y (yaw).
ECZ: Roll error motion of z.

Figure 3.2: Error components for a straight line motion along the z-axis. Adapted from [56].

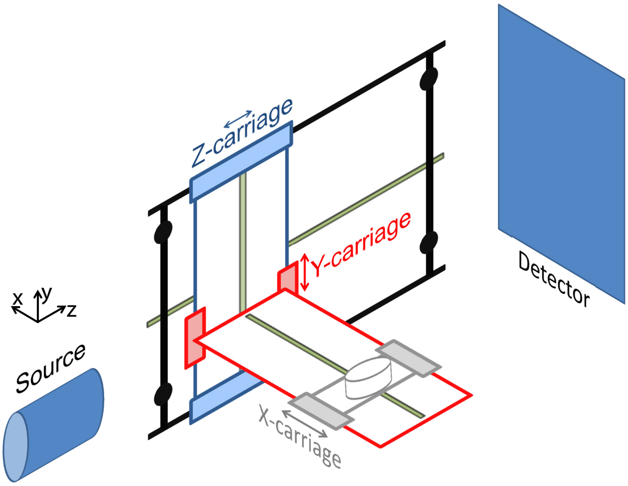

Figure 3.3: Schematic representation of the kinematic system of the Nikon Metrology XT H 450 CT scanner.

3.2.3 Kinematic model CT scanner

Figure 3.3 gives a schematic representation of the kinematic system of the Nikon Metrology XT H 450 CT scanner: It can be modeled as a kinematic chain of four rigid bodies connected by three prismatic joints. The frames have been assigned as follows:

- Frame $\{0\}$ connected to the fixed structure.
- Frame $\{1\}$ connected to the z-carriage.
- Frame $\{2\}$ connected to the y-carriage.
- Frame $\{3\}$ connected to the x-carriage.
- Frame $\{rt\}$ which is positioned at the center of the turntable. Frame $\{rt\}$ is a translation of frame $\{3\}$ to the center of the turntable.

Equation 3.1 describes the homogeneous coordinates of a point with respect to frame $\{rt\}$ in frame $\{0\}$.

$$\begin{bmatrix} {}_0x \\ {}_0y \\ {}_0z \\ 1 \end{bmatrix} = {}^1_0T\,{}^2_1T\,{}^3_2T\,{}^{rt}_3T \begin{bmatrix} {}_{rt}x \\ {}_{rt}y \\ {}_{rt}z \\ 1 \end{bmatrix} \tag{3.1}$$

The coordinate $({}_0x, {}_0y, {}_0z, 1)$, with respect to frame $\{0\}$, is calculated by multiplying the coordinate $({}_{rt}x, {}_{rt}y, {}_{rt}z, 1)$, with respect to frame $\{rt\}$, by a sequence of homogeneous transformation matrices.

Transformation matrix ${}^{rt}_3T$. ${}^{rt}_3T$ (equation 3.2) performs a simple translation of the coordinates from frame $\{rt\}$, at the center of the turntable to frame $\{3\}$. $({}_3x0rt, {}_3y0rt, {}_3z0rt)$ corresponds to the position of the center of the rotation table expressed in frame $\{3\}$.

$${}^{rt}_3T = \left[\begin{array}{ccc|c} 1 & 0 & 0 & {}_3x0rt \\ 0 & 1 & 0 & {}_3y0rt \\ 0 & 0 & 1 & {}_3z0rt \\ \hline 0 & 0 & 0 & 1 \end{array}\right] \tag{3.2}$$

Transformation matrix ^3_2T. ^3_2T (equation 3.3) resembles the motion of the x-carriage (frame $\{3\}$) with respect to the y-carriage (frame $\{2\}$). The error motions $e**$ are used as defined in figure 3.2. Although it is not literally written down, it is important to keep in mind that these error components are variables, in this case dependent of the x-position. x_{enc} is the position read out by the encoder of the x-axis. $({}_2x0x, {}_2y0x, {}_2z0x, 1)$ corresponds to the home position of the x-scale expressed in frame $\{2\}$. The origin of frame $\{3\}$ is connected to this reference point.

$$^3_2T = \left[\begin{array}{ccc|c} 1 & -ecx & ebx & {}_2x0x + x_{enc} + exx \\ ecx & 1 & -eax & {}_2y0x + eyx \\ -ebx & eax & 1 & {}_2z0x + ezx \\ \hline 0 & 0 & 0 & 1 \end{array}\right] \tag{3.3}$$

Transformation matrix ^2_1T. The motion of the y-carriage (frame $\{2\}$) with respect to the z-carriage (frame $\{1\}$) is given by ^2_1T (equation 3.4). $({}_1x0y, {}_1y0y, {}_1z0y, 1)$ corresponds to the home position of the y-scale expressed in frame $\{1\}$. Similar notation is used as explained for equation 3.3.

$$^2_1T = \left[\begin{array}{ccc|c} 1 & -ecy & eby & {}_1x0y + exy \\ ecy & 1 & -eay & {}_1y0y + y_{enc} + eyy \\ -eby & eay & 1 & {}_1z0y + ezy \\ \hline 0 & 0 & 0 & 1 \end{array}\right] \tag{3.4}$$

Transformation matrix ^1_0T. The motion of the z-carriage (frame $\{1\}$) with respect to frame $\{0\}$ can be notated in a similar way by ^1_0T (equation 3.5). $({}_0x0z, {}_0y0z, {}_0z0z, 1)$ corresponds to the home position of the z-scale expressed in frame $\{0\}$. This equation uses similar notations as explained for equation 3.3.

$$^1_0T = \left[\begin{array}{ccc|c} 1 & -ecz & ebz & {}_0x0z + exz \\ ecz & 1 & -eaz & {}_0y0z + eyz \\ -ebz & eaz & 1 & {}_0z0z + z_{enc} + ezz \\ \hline 0 & 0 & 0 & 1 \end{array}\right] \tag{3.5}$$

Figure 3.4: Measurement of the error components with the laser interferometer (a), electronic level (b) and verification with the dial gauge and a granite square with a precise angle of 90 degrees (c).

3.3 Determination of the error components

3.3.1 Measurements

The errors (as described in section 3.2) for each axis (one positional error, two straightness errors and three angular errors) in function of the axis position, and the squareness errors between the axes, have been determined using a laser interferometer (Renishaw ML10) and an electronic level (figure 3.4). Furthermore a granite square with a precise angle of 90 degrees and dial gauge have been used to verify the measured errors (figure 3.4c). Figures 3.5 and 3.6 show these error components.

Some error components are not determined. First of all the three positioning errors exx, eyy and ezz. These are difficult to measure with the available equipment without influence of the other error components. It is important to execute these measurements as close to the relevant scales as possible, to avoid influence of the other errors as illustrated in figure 3.7. Figure 3.7 shows the resulting error dz due to a positioning error ezz (green) and a yaw error ebz (red) at a distance x from the z-scale. The high influence of tilt error motions (e.g. ebz), certainly in the case of this CT device, moreover makes the positioning errors (e.g. ezz) negligible. It is furthermore not possible to measure the angular error eby with the available equipment.

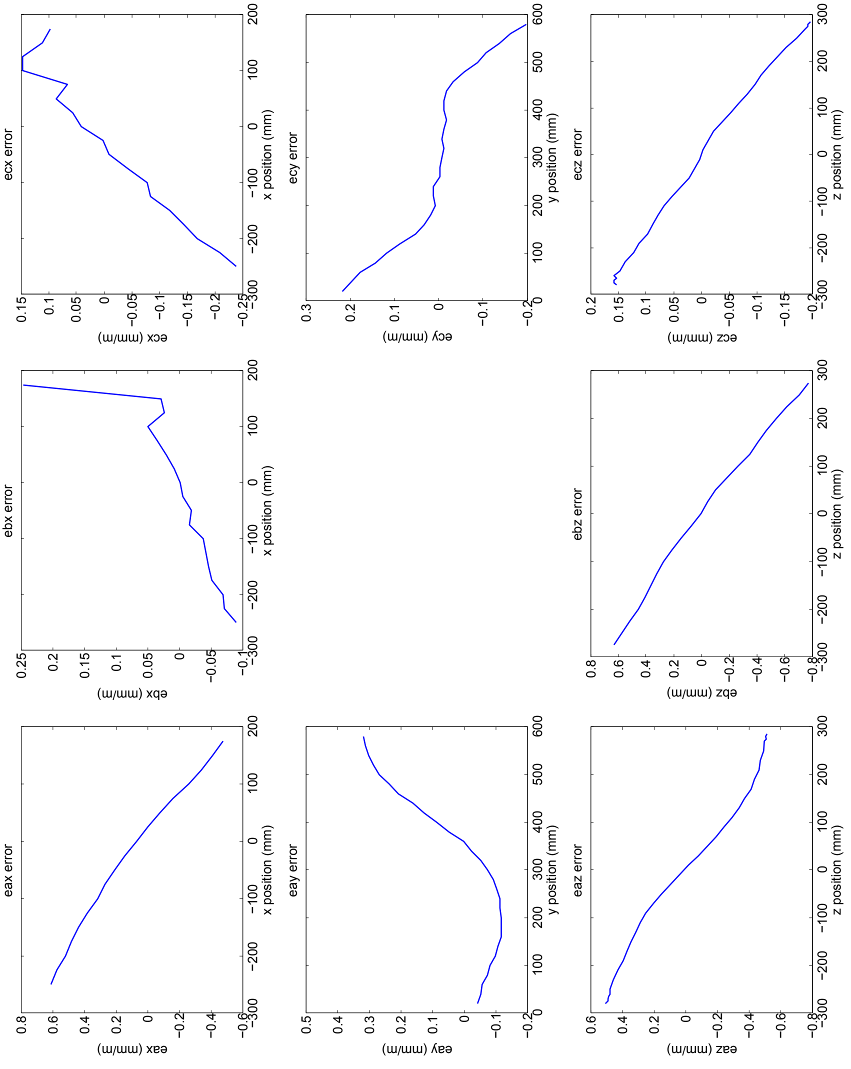

Figure 3.5: Angular error components.

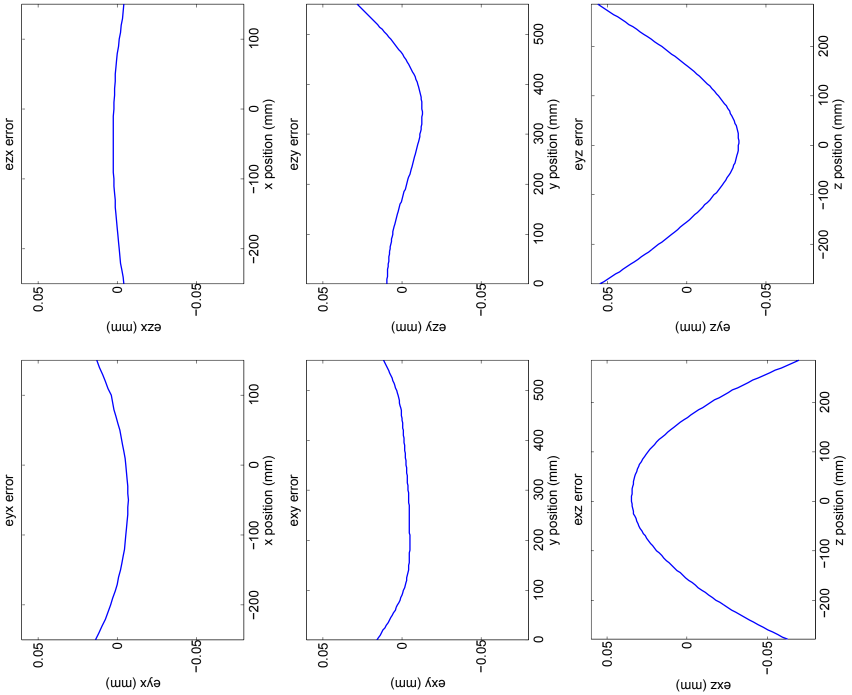

Figure 3.6: Straightness error components.

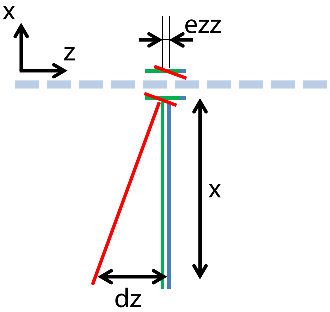

Figure 3.7: Error in z due to a positioning error ezz (green) and a yaw error ebz (red) at a distance x from the z-scale.

Besides the aforementioned 18 error motions there are still 3 squareness errors. These squareness errors have following values:

- xz squareness error: 2.319mm/m.
- yz squareness error: -1.520mm/m.
- xy squareness errors: 0.977mm/m.

These squareness errors can be included into some of these 18 error functions as stated and described in [12] and [74]. This approach has been used in this thesis, hence the squareness errors have afterwards been integrated into the errors described in figures 3.5 and 3.6.

3.3.2 Discussion on the error components

This section shortly discusses some results which can be concluded from the error component measurements. More in particular will this section discuss the influence of the straightness error ezy, the pitch error measurement eaz and the combined error on the requested magnification position. Furthermore is the applicability of the extra options of the Nikon Metrology XT H 225 ST CT scanner, available at our facilities, discussed with respect to our 450 kV CT scanner.

The straightness error ezy of the y-axis (figure 3.6, squareness error is not yet included) points out that scanning a calibration object for rescaling should be done with the same table height (y) position as which is used to scan the investigated object. This error will moreover have a large influence when scanning with the curved linear diode array detector (CLDA). The object will then be scanned slice by slice after shift of the rotation table along the y-axis (section 2.2.2). The unwanted shift in z, coming along with the shift in y will result in a magnification difference.

The pitch error measurement eaz along the z-axis clearly shows the differing tilt between the rotation vector and the detector.

Figure 3.8 illustrates the resulting error on the requested magnification position for two table heights. It is clear that these errors will have a negative influence on the determination of the magnification, and therefore also on the voxel sizes and dimensional measurements. These errors should ideally be taken into account when determining the voxel scaling factor during reconstruction based on the encoder position of the z-axis (section 2.3.5). Moreover these factors should be taken into account when determining the source-object (offset) distance and the source-detector distance during calibration of the machine (section 2.2.3).

The Nikon Metrology XT H 225 ST CT scanner available at our facilities contains two additions with respect to the 450 CT scanner:

- Each axis is foreseen of a linear scale.
- A look up table has been integrated in the software to correct for magnification positioning errors.

The linear scales will improve the positioning errors of the three axes: exx, eyy and ezz. These errors are however negligible as discussed in section 3.3.1. Installing these scales on the available 450 kV CT scanner, like has been done for the Nikon Metrology XT H 225 ST CT scanner, makes therefore no sense.

The available Nikon Metrology XT H 225 ST CT scanner is also foreseen of a look up table. The magnification errors have been measured when moving along the magnification axis by means of a laser interferometer and compensated. The result of such a measurement is comparable to the result of figure 3.8. The laser interferometer measurements have been done at a certain height (y). The compensation is therefore suited for CT measurements on this height position as can be concluded from figure 3.8. This leads to the fact that compensation should be position dependent and not only dependent of the magnification position.

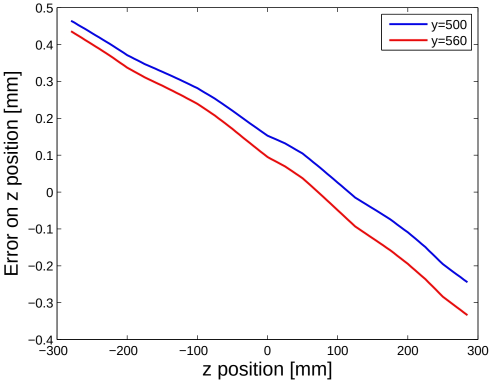

Figure 3.8: Error on the magnification (z) position.

3.4 Relative errors between source, turntable and detector

Sections 3.2 and 3.3 have described the kinematic model of the Nikon Metrology 450 kV CT scanner. This kinematic model calculated the positions/errors with respect to frame $\{0\}$ connected to the fixed structure. The next step is to calculate the errors with respect to the source and detector position and orientation.

3.4.1 State of the art

Calibration methods for misaligned CT scanner geometry have been presented in different works, e.g. [98], [27] and [132]. All of these methods can calibrate the misalignments more or less but often have limitations, e.g. [98] assumes the detector being parallel to the rotation axis of the scanner. This assumption of course does not hold for the investigated CT scanners.

3.4.2 Calculation alignment errors

It has been opted in this thesis to apply a simplified method to calculate the misalignments. This method has been worked out based on the current calibration method (performed by the manufacturer) used to align the detector and source relative to the rotation table. It has been extended and the errors have been quantified instead of just trying to eliminate them by moving the elements. On one hand it quantifies the misalignments, on the other hand it gives an idea of the accuracy of the geometric alignment carried out by the manufacturer as the basics thoughts of this method are used by the manufacturer to perform the alignment between source, detector and rotation table.

All errors are relative to the other elements (source, rotation table/axis, detector) of investigation. The misalignment errors can be described in several ways. The method proposed here calculates the errors relative to the source position.

Figure 3.9 illustrates the ideal case: The (projected) source is positioned in the center of the detector, and the rotation axis is supposed to be aligned parallel, resp. perpendicular to the detector and its pixel rows or columns. Figure 3.9a sketches the situation when looking along the x-direction of figures 3.1 and 3.3. The detector view (figure 3.9b) is obtained by looking along the z-direction of figures 3.1 and 3.3.

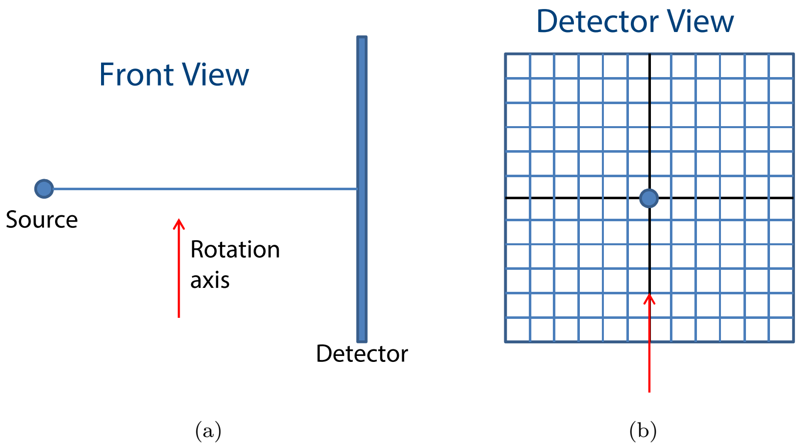

(a) (b)

Figure 3.9: Ideal alignment of the source, rotation axis and detector in front view (a) and detector view (b). The front view is obtained by looking along the x-direction in figures 3.1 and 3.3. The detector view is obtained by looking along the z-direction in figures 3.1 and 3.3.

Following errors describe the misalignments:

- Shift of the detector along its y-axis.
- Tilt of the detector around its x-axis.
- Tilt of the rotation axis around its x-axis.
- Shift of the detector along its x-axis.
- Tilt of the detector around its y-axis.
- Tilt of the detector around its z-axis.
- Tilt of the rotation axis around its z-axis.

The different methods to define these errors will now be described. The methods use the movements of a point. An 'x' is used in the figures instead of a point to facilitate the understanding. The center point of the 'x' can be seen as the point.

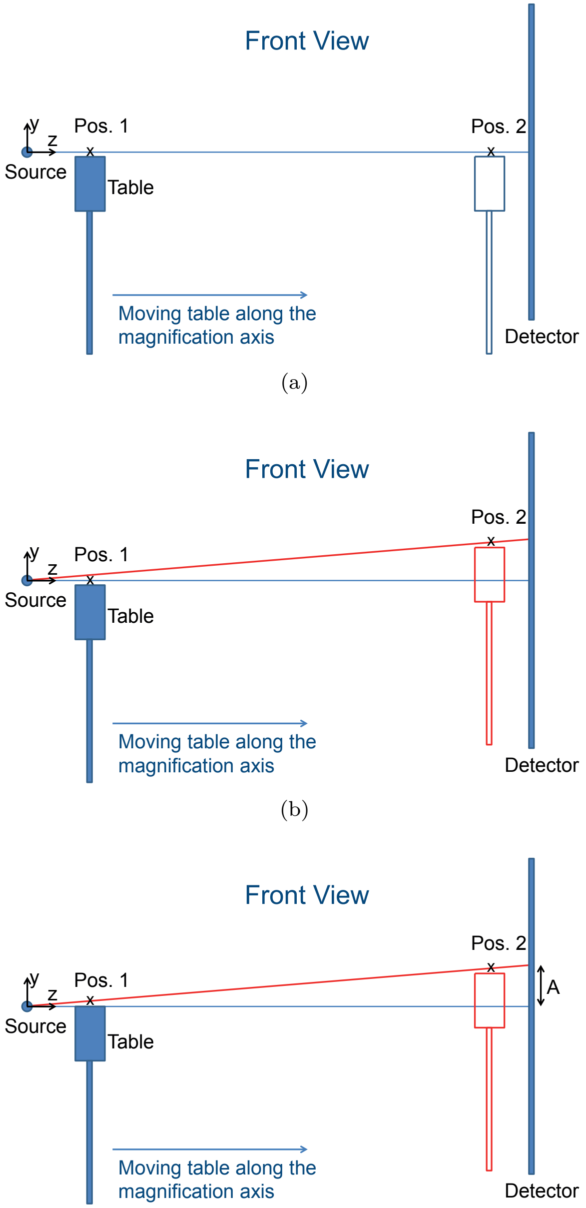

(a)

(b)

(c)

Figure 3.10: Method to check a shift of the detector along the y-axis: the ideal case (a), the real case (b) and the calculation method (c).

Shift detector along its y-axis

If a point of an object is set at the (horizontal) center line of the detector (as shown in figure 3.10) and subsequently the object is moved along the magnification axis (moving from position 1 to position 2), this point should stay at the center line of the detector. In the other case this can be interpreted as the detector having a shift in vertical direction. Figure 3.10a shows the ideal case while figure 3.10b pictures the real case: the point does not stay at the center pixel, but there is a certain shift. It is now important to find the horizontal detector pixel line in which the point stays when moving along the magnification axis (see figure 3.10c) this way the shift A of the detector is determined.

Tilt detector around its x-axis

Figure 3.11 describes the procedure to test whether the detector is tilted around its x-axis. A point is positioned on the horizontal center line of the detector (position 1). When moving the point upwards by a certain length L (position 2), or downwards by the same length L (position 3), the achieved movement on the detector (A) should be the same. If the detector is tilted over an angle β, around its x-axis, the upward movement will result in a distance B on the detector and the downward movement in a distance C on the detector. Figure 3.11a shows it in case you are standing in front of the CT scanner. Figure 3.11b gives the result on the detector, where the black 'x' resembles the ideal case, and the red 'x' the real case. The values B and C can now be used to calculate the tilt β.

Tilt rotation axis around its x-axis

Figure 3.12 illustrates the method to check and calculate the error for a tilt of the rotation axis around its x-axis. A point of an object (e.g. center point of a sphere, apex of cone, see section 3.4.3) is positioned at the side of the rotation table, with the table height adapted such that the point of the object is at the horizontal center line of the detector. Now the table will be turned around 180 degrees, resulting in position number two for the object/point. In the ideal case (figure 3.12a) the point should stay at the center line. In the real case the point will shift (to a lower point in the situation of figure 3.12b) over a distance A on the detector, which will result in the situation at the detector illustrated at figure 3.12c. The knowledge of A allows to calculate the vertical distance from point position 2 to the horizontal line from source to detector and hence the angle between the rotation axis and the horizontal line from source to detector.

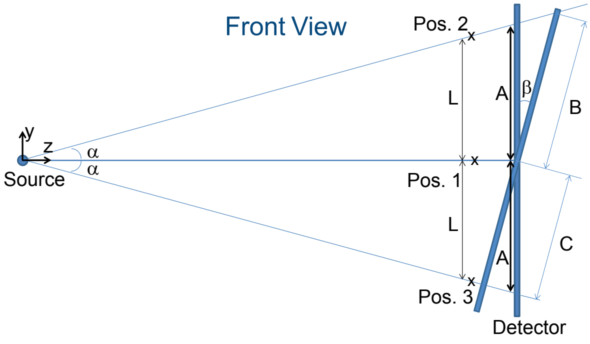

(a)

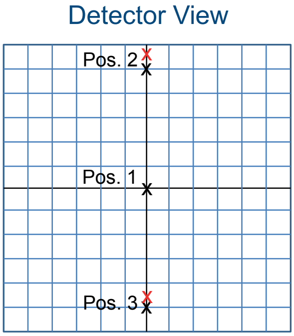

(b)

Figure 3.11: Method to check a tilt of the detector around its x-axis: front view (a) and detector view (b).

Shift detector along its x-axis

Figure 3.13 (top view, looking along negative y-axis of figures 3.1 and 3.3) illustrates the situation to check a shift of the detector along its x-axis. It is similar to a shift of the detector along its y-axis, but now the point is set at the vertical center line of the detector.

Tilt detector around its y-axis

The situation is similar to the one to check the tilt of the detector around its x-axis. Figure 3.14 illustrates the situation.

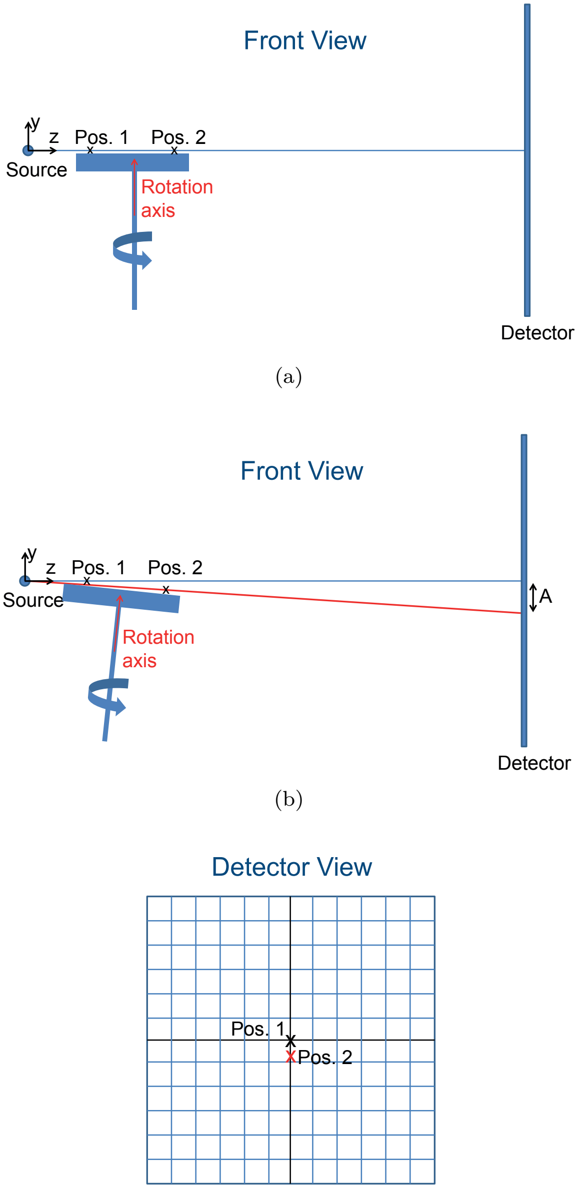

(a)

(b)

(c)

Figure 3.12: Method to check a tilt of the rotation axis around its x-axis: ideal case (a), real case in front view (b) and real case in detector view (b).

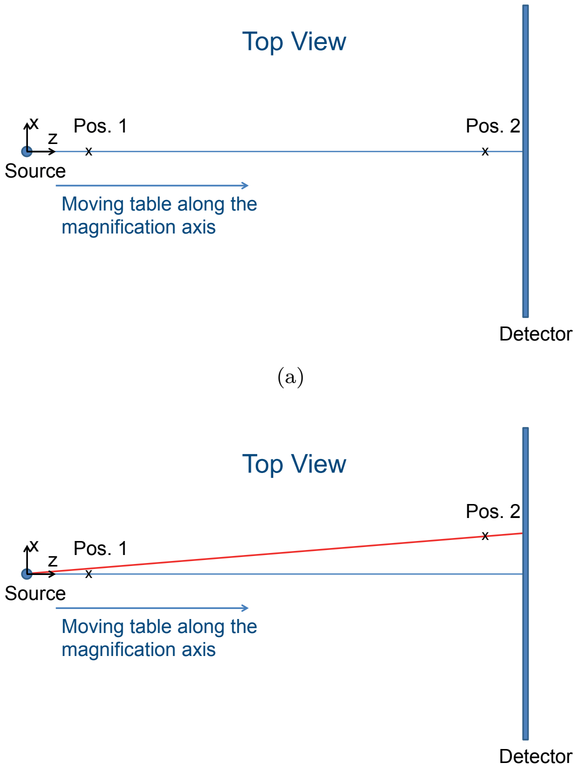

(a)

(b)

Figure 3.13: Method to check a shift of the detector along the x-axis: the ideal case (a) and the real case (b).

A point is now positioned at the vertical center line of the detector (position 1). Next the point is moved along the x-axis by a certain length L in positive and negative direction (positions 2 and 3), which should result in the same distance (A) on the detector. If the detector is tilted over an angle β, around its y-axis, one movement will result in a distance B on the detector and the other in a distance C on the detector. Figure 3.14a shows the situation in top view. Figure 3.14b gives the resulting situation on the detector, where the black 'x' resembles the ideal case, and the red 'x' the real case.

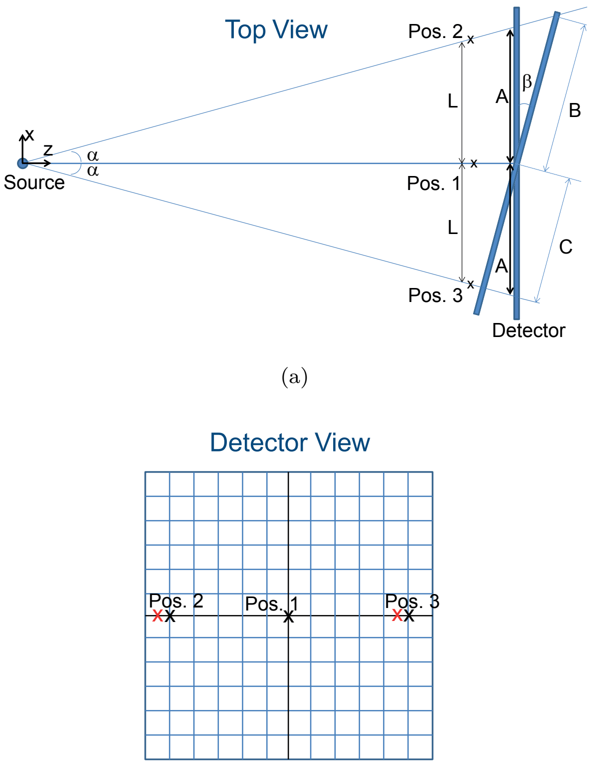

(b)

Figure 3.14: Method to check a tilt of the detector around its y-axis: front view (a) and detector view (b).

Tilt detector around its z-axis

An experiment similar to the test for checking the tilt of the detector around its y-axis is used. Figure 3.15 shows the situation. Again the point will be positioned at the horizontal center line of the detector (point 1), and subsequently the table will be translated over the x-axis. In the ideal case the point stays at the horizontal center line (black cross) of the detector. The red cross shows the real case: the point is in this case lower than the horizontal center line. The distance A allows to calculated the detector tilt (with respect to the real movement).

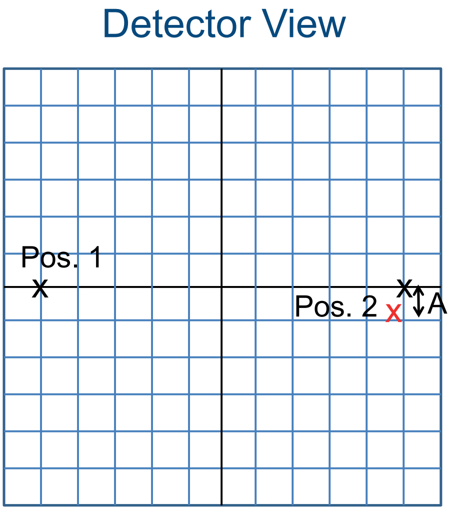

Figure 3.15: Method to check a tilt of the detector around its z-axis

Tilt rotation axis around its z-axis

Figure 3.16 shows the method to check the tilt error of the rotation axis around its z-axis. The object is again placed at the side of the rotation table with the point at the height of the center line of the detector. The object is rotated about 180 degrees. In the ideal case the point should stay at the centerline (black cross) instead of ascending or descending (in this example descending, red cross). A similar calculation as for the tilt of the detector around the z-axis can be executed. It is important to take into account the tilt of the detector around the z-axis when calculating the error.

Discussion

The measurement of the alignment errors should not been done in a random order (above applied order is a suitable order). Some errors are dependent of other errors, and this should be taken into account.

It is furthermore important to mention that the errors of the axes (quantified in section 3.3) have been compensated for during the measurement of the alignment errors.

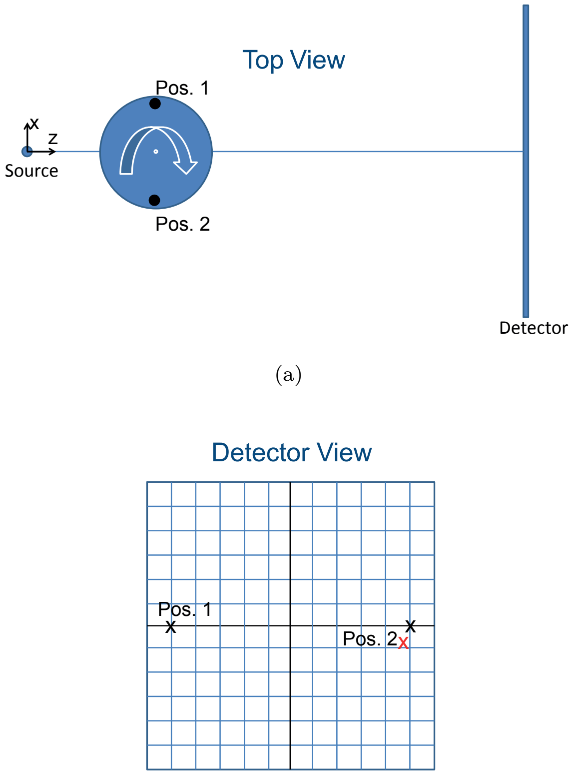

(a)

(b)

Figure 3.16: Method to check a tilt of the rotation axis around its z-axis: top view (a) and detector view (b).

Currently the checks explained in beneath list are executed for the alignment calibration performed by the manufacturer.

- Shift of the detector along its y-axis: figure 3.10.
- Tilt of the rotation axis around its x-axis: figure 3.12.
- Shift of the detector along its x-axis: figure 3.13.
- Tilt of the rotation axis around its z-axis: figure 3.16.

This alignment is executed without taking into account the errors of the axes, quantified in section 3.3. The alignment of the different elements (source, table, source) is adapted during these checks to minimize the errors. To quantify the alignment errors more experiments are required as illustrated.

The object used in this thesis to quantify the alignment errors is furthermore different from the object currently used by the manufacturer for the geometrical calibration of the machine elements. The current object and object used in this thesis will be discussed in section 3.4.3.

3.4.3 Objects

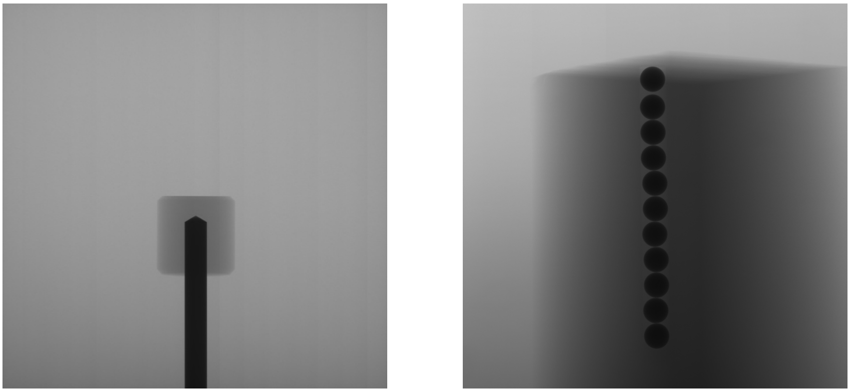
(a) (b)

Figure 3.17: Objects used for geometrical calibration of the CT machine: the currently used object (a) and the new object used in this thesis (b).

Figure 3.17 represents the currently used object for alignment correction (a) and the object used in this thesis (b) to quantify the alignment errors. The object should have a clear transition or point to be used for the alignment procedures. The currently used object exists of a cylindrical rod, while the object used in this thesis consists of 2 spheres touching each other (the touching point functions as the point mentioned in the calculation procedure). Figure 3.18 depicts the observed gray value transition on a line for both objects. It is clear that there is a transition zone for the currently used object, while the object used in this thesis shows a peak. It is obviously easier to determine a point or transition zone on the object used in this thesis. It is furthermore a lot less dependent of the used settings: the edge will not shift when adapting the current and voltage settings of the source. Playing with the scale of the gray values furthermore allows to determine the point of transition very accurate. The object has been rotated about 90 degrees, in case of methods which set the transition point on a vertical pixel line (e.g. tilt of the detector around the y-axis).

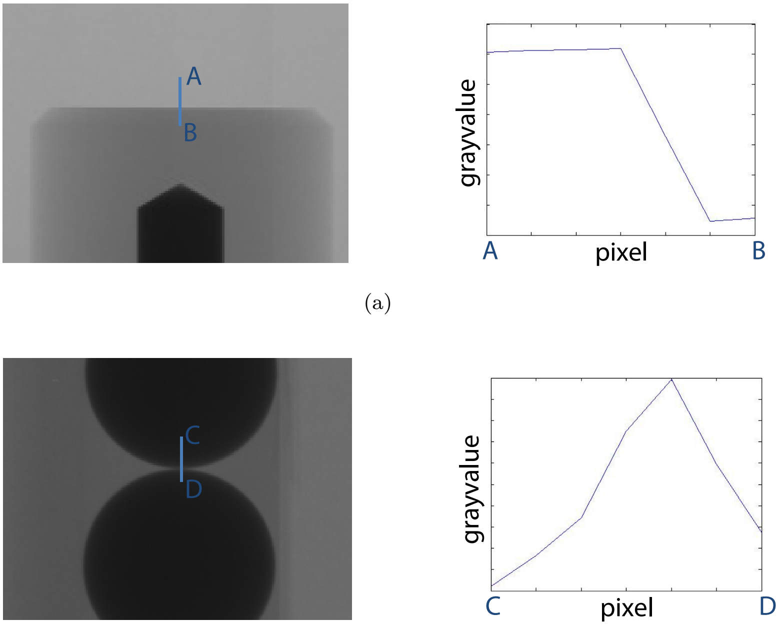

(a)

(b)

Figure 3.18: Gray value transition for the currently used object (line AB) on figure (a) and the object used in this thesis (line CD) on figure (b).

3.4.4 Alignment errors: results

The alignment errors have been measured using above procedure. The results can be found in table 3.1. The errors of two alignments have been measured for the alignment errors of the 450 kV CT scanner under investigation. The first set shows among others a large tilt error of the rotation axis around x. This error was also concluded from the measurements at that time (see section 5.5.3). Therefore the alignment has been redone by the manufacturer. Hereafter the alignment errors have been measured again resulting in the errors in the last column (in cooperation with [49]). The tilt error of the rotation axis around x is a lot smaller now, but unfortunately there now appears to be a large tilt of the detector around its x axis. Estimated uncertainties have been added to the values based on user experience.

Error	Alignment 1	Alignment 2
Shift detector along y	$0\mu m \pm 300\mu m$	$340\mu m \pm 300\mu m$
Tilt detector around x	$0mm/m \pm 2mm/m$	$-7mm/m \pm 2mm/m$
Tilt rotation axis around x	$5.8mm/m \pm 2mm/m$	$-0.5mm/m \pm 2mm/m$
Shift detector along x	$-500\mu m \pm 300\mu m$	$580\mu m \pm 300\mu m$
Tilt detector around y	$-6mm/m \pm 2mm/m$	$4.5mm/m \pm 2mm/m$
Tilt detector around z	$0.7mm/m \pm 1mm/m$	$0.6mm/m \pm 1mm/m$
Tilt rotation axis around z	$-0.6mm/m \pm 1mm/m$	$-0.6mm/m \pm 1mm/m$

Table 3.1: Overview of the measured alignment errors.

3.5 Conclusion

The chapter has started (section 3.1) with a description of problems associated with the mechanical structure of an X-ray CT scanner. Two main parts were distinguished:

- Positioning of the turntable by the kinematic system and the subsequent errors.
- Relative errors between source, turntable and detector.

Sections 3.2 and 3.3 have described and quantified the kinematic model for the Nikon Metrology XT H 450 CT scanner under investigation. Section 3.3.2 proved the relevance of this issue. For instance, a direct error on the magnification position, and therefore on the voxel size and dimensional measurements, is observed.

Section 3.4 has focused on the relative errors between source, turntable and detector. A method to quantify the misalignment errors, which also gives an idea of the accuracy of the geometric alignment carried out by the manufacturer, has been worked out. An object to perform the tests for this method has been suggested. Quantification of the alignment errors has been performed for two different alignments which have been used on the Nikon Metrology XT H 450 CT scanner. This has resulted in different alignment errors which will be further investigated in chapter 5.

Elaboration and validation has been performed on the Nikon Metrology XT H 450 CT scanner under investigation. But the content is also applicable for use on other X-ray CT scanners.

Chapter 4

Simulation program

Chapters 2 and 3 have discussed the many influence factors affecting the dimensional X-ray CT measurements and therefore the measurement accuracy. Influence factors have been analyzed and quantified. The next step consists of investigating the resulting errors from these factors on the dimensional X-ray CT measurement. Two options can be considered to investigate the influence of these factors on the dimensional measurement. The first option consists of experimental measurements on an X-ray CT scanner. One can scan different objects and variate parameters to analyze the influence on dimensional measurements. There are however some limitations on experimental research. The many influence factors, together with many additional often unknown influences (e.g. alignment errors, drift of the source, temperature), make it difficult to correlate separate user adjustable influence factors (e.g. magnification) to observed variations in dimensional measurements. The second option consists of computer simulation. Simulation allows the analysis of separate influence factors and research on parameters which cannot be controlled in experimental research (e.g. alignment errors). It furthermore helps to reach a better understanding of the different steps in the CT process. Simulation is therefore an indispensable supplement to the research of dimensional X-ray CT metrology on experimental basis.

This chapter gives a general overview of the simulation program which has been written in Matlab® environment. It shows the used basic principles and addresses the main parameters. This chapter will therefore also serve as a manual for the simulation program users. Detailed information and further references are available in the source code.

The simulation program generates 2D projection images which can be reconstructed into a 3D model as if they are real projections from an X-ray CT scan. Section 4.2 starts by analyzing these 2D projection images. Section 4.3 discusses the actual implementation. It declares the main functions as well as the required information related to the main components. It explains the different needed input parameters for these main components and in parallel the spectra transitions which will be summarized in section 4.3.8.

Denis Indesteege [55] and Celine Souvagie [128] have contributed to this simulation program. A first version of this program has been worked out in [159].

4.1 State of the art

There are different simulation programs on the market: [95], [83], [10], [52], [50], [18], [144], [169], [124], [53], [79], [131], [38], [113] and [149]. There are however many disadvantages associated with the use of these (commercial) available simulation programs. The main disadvantages are the flexibility, absence of crucial parameters and black box principle. Many of the available simulation programs have large parts implemented as black boxes: the critical programming steps are not available for the user, making it impossible to have a thorough understanding of the entire process and results. There is furthermore often a lack of flexibility. Different parameters are implemented but the user is restricted to the use of these parameters, which hinders a thorough investigation of all influence factors.

4.2 Generation of 2D projection images

The simulation program generates 2D projection images (see figure 4.1) which can be reconstructed into a 3D voxel model as if they are real projections from a CT scan. This section discusses the content of these 2D projection images.

4.2.1 Projection image values

The 2D projection images (figure 4.1), consist of $t_1 \times t_2$ values where t_1 and t_2 correspond to the number of detector pixels in both dimensions. 2D images are taken for many rotation steps of the workpiece as explained in section 1.1. A projection image, which can be represented as a matrix, has to be calculated for each rotation step of the object. The following formula describes the values

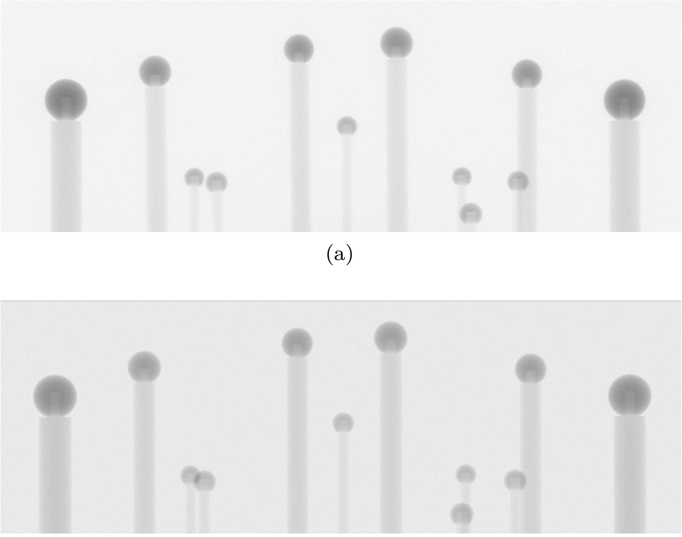

(a)

(b)

Figure 4.1: 2D projection image of the real CT scan (a) and a simulated CT scan (b). The captured view angle is slightly different as can be seen.

of the matrix elements of a projection image.

$$proj\_image(i,j) = \frac{Det_{output\_w\_obj}(i,j) - BlackLevel(i,j)}{Det_{output\_wo\_obj}(i,j) - BlackLevel(i,j)} WhiteLevel \tag{4.1}$$

where:

(i,j) = Detector pixel designation. i and j are integers from resp. 1 to t_1 and 1 to t_2.

$BlackLevel(i,j)$ = Detector pixel output without generated X-rays.

$WhiteLevel$ = Predefined uservalue, often set to 60000 or 64000 for a 16 bit detector.

$Det_{output\_w\_obj}(i,j)$ = Detector pixel output with the object in view.

$Det_{output\_wo\_obj}(i,j)$ = Detector pixel output without the object in view.

The detector output is dependent of the detector type. The detectors of the investigated CT devices belong to the category of the scintillation-type detectors or 'indirect' detectors (see section 2.2.2 for more information about different detector types). These detectors have an output proportional to the total photon energy [60]. Equation 4.2 describes the output of such a detector.

$$Det_{output}(i,j) = \int_{0}^{E_{max}} n(E,i,j)\, E \, \mathrm{d}E \tag{4.2}$$

where:

E = Energy level of a photon.
$n(E,i,j)$ = Number of photons per photon energy level detected by detector pixel (i,j) after all attenuation steps.

4.2.2 Spectra transitions

The detector output is dependent of the factor $n(E,i,j)$. Hence to be able to simulate 2D X-ray projection images, one needs to know the number of photons per photon energy level $n(E,i,j)$ detected by each detector pixel. This means that the spectra transitions from source to detector need to be tracked. This is done by tracing the rays leaving the X-ray source. The easiest method simulates one ray for each detector pixel, starting from a single point (i.e. an ideal point source) to the pixel center. Multiple rays starting from different points on the source and ending in multiple points per detector pixel will later be used to have a more realistic simulation.

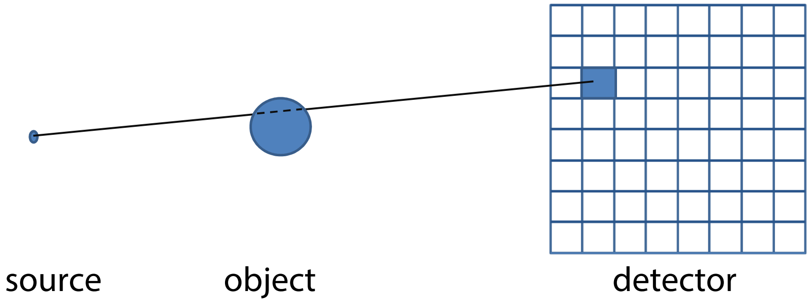

Figure 4.2: Example of tracing a single ray.

Figure 4.2 illustrates the tracing of a single ray. The ray starts with a certain polychromatic spectrum at the source. This spectrum changes due to attenuation by the filter plate, the object, the surrounding air and lastly by the processes in the detector. Equation 4.3 formulates each transitions from the initial spectrum emitted by the source to the spectrum detected by the detector. This equation goes back to the Lambert-Beer law.

$$I(E) = I_0(E)\, e^{-(\sum_{m=1}^{M} (\mu_m(E)\, x_m))} \tag{4.3}$$

where:

$I_0(E)$ = The initial polychromatic X-ray spectrum.
$I(E)$ = The polychromatic X-ray spectrum after attenuation.
$\mu_m(E)$ = Linear attenuation coefficient of material m as a function of photon energy.
x_m = Penetrated length through material m.

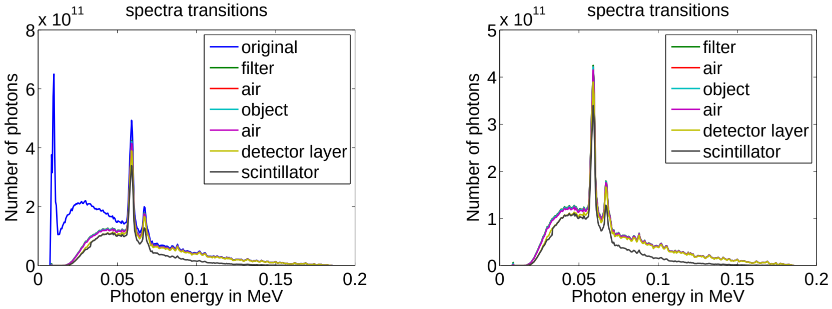

(a) (b)

Figure 4.3: Spectra transitions from source to detector: starting before (a) and after (b) filtering.

Figure 4.3 shows the spectrum changes along one ray. The ray starts at the source with a spectrum of $100kV$, then passes through a copper filter of $0.1mm$. Subsequently the ray penetrates $300mm$ air (with little change in spectrum), then an Al_2O_3 object of length 3 mm is penetrated and afterwards $684.4mm$ of air is penetrated before reaching the detector (simulated as an Al detector layer and a CsI scintillator). Figure 4.3b does not include the starting spectra. This figure starts with the filtered spectrum.

The different (penetration) lengths $x_m(i, j)$ through the different materials (objects, filter, surrounding air, etc.) should be calculated and the attenuation coefficients of the different materials (e.g. air, Cu, Al, Al_2O_3) have to be known to solve equation 4.3. The needed penetration matrices are separate matrices containing the lengths (per pixel) through the objects, through air, the thin plate filter, etc. Linear attenuation coefficients in function of energy should be available for each penetrated material composition (objects, air, filter, etc.). Section 4.3.12 will discuss about attenuation.

4.3 Matlab® implementation

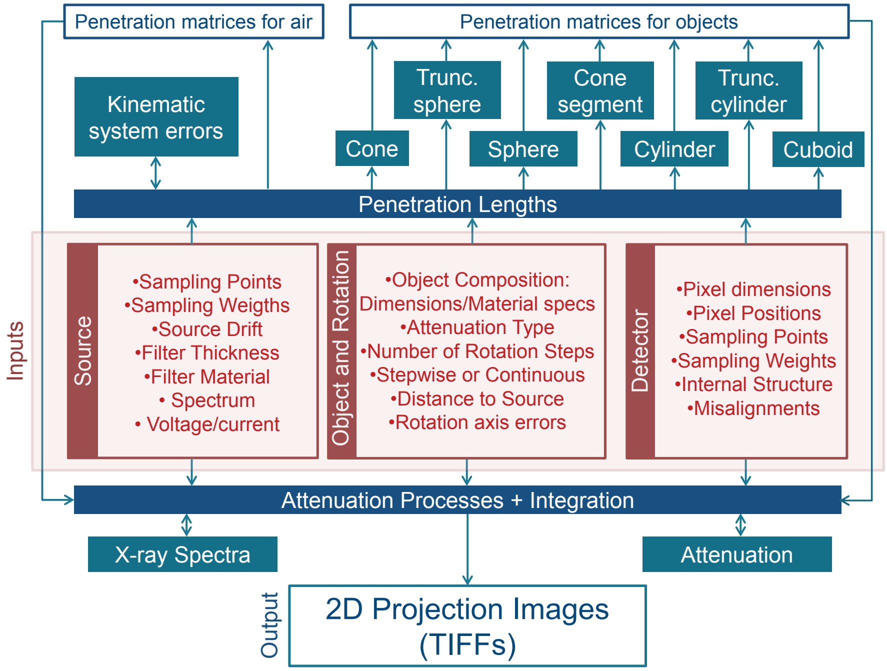

Figure 4.4: Overview of implemented Matlab® structure. Only the main components are shown.

Figure 4.4 illustrates the implementation in Matlab® . This figure only shows the main components. There are many more subprograms but those will not be discussed.

There are two main programs:

- 'Calculation penetration lengths' which calculates the penetration lengths trough different objects (section 4.3.1). These penetration lengths are input for the second main program.

- ’Attenuation processes and integration’ which performs the material dependent processes (section 4.3.2). The output of this main program are the 2D projection images, outputted as tiff images.

These main programs make use of multiple subprograms. The main subprograms are:

- ’Kinematic system errors’ calculates the errors due to incorrectness of the table positioning system (section 4.3.9).
- Generic objects as ’cuboid’, ’sphere’, ’truncated sphere’, ’cylinder’, ’truncated cylinder’, ’cone’, ’cone segment’ (section 4.3.10). These functions perform the penetration calculations per object.
- ’X-ray spectra’ (section 4.3.11) which provides the source X-ray spectra.
- ’Attenuation’ which is in charge of reading out the attenuation coefficients for different materials (section 4.3.12).

At last input is needed for the different main components of the CT scanner and will be discussed:

- Source (section 4.3.3).
- Filter plate (section 4.3.4).
- Object and air (section 4.3.5).
- Rotation table (section 4.3.6).
- Detector (section 4.3.7).

The spectrum transition are discussed in parallel and summarized in section 4.3.8.

4.3.1 Calculation of penetration lengths

The first main program manages the calculations of the different penetration matrices (through the different materials). Input of the user is required related to the X-ray source, the object, rotation table and the detector. Subprograms able to calculate penetration lengths through specific generic objects are accessed by this main program. The obtained output consists of matrices containing penetration lengths. These matrices are input for the other main program which handles the energy dependent calculations.

This first main program sends angle independent and angle dependent information to the subprograms. The matrix 'AngleInformation' bundles the angle dependent information. The columns contain different angle dependent parameters (projection number; rotation angle; source drift values; wobble values; eccentricity values).

This main program furthermore interacts with the 'Kinematic system errors' function. The 'Kinematic system errors' function manages the calculation of the real position and orientation of the rotation table, taking into account the errors of the kinematic system (sections 3.2 and 3.3).

Figure 4.5 pictures the different applied coordinate systems and their relationship. The parameter designation corresponds to the Matlab® simulation code. The origin of the coordinate systems has been assigned with respect to a global coordinate system. The rotation vector is resembled as the red arrow with vector value [0, 0, -1].

Required input parameters

Uncertainty If *Uncertainty* = 1, a value is chosen of a statistically defined distribution.

NumberOfCores Specification number of cores to be used for parallel computing.

Other parameters The other parameters will be explained in the next sections.

4.3.2 Attenuation processes and integration

The second main program handles the energy dependent calculations: attenuation processes and integration. This program needs input of the user related to the X-ray source, the object and the detector. Furthermore the calculated penetration matrices are used as input. It also interacts with the subprograms in charge of the X-ray spectra and the attenuation properties. This second main program calculates the detected value for each detector pixel using the equations mentioned in section 4.2, and writes the projection images as output (in tiff format). At this moment tiff files from real CT scans are rewritten instead of writing new tiff files. This way it is sure the background information attached to the tiff is also valid for the reconstruction program.

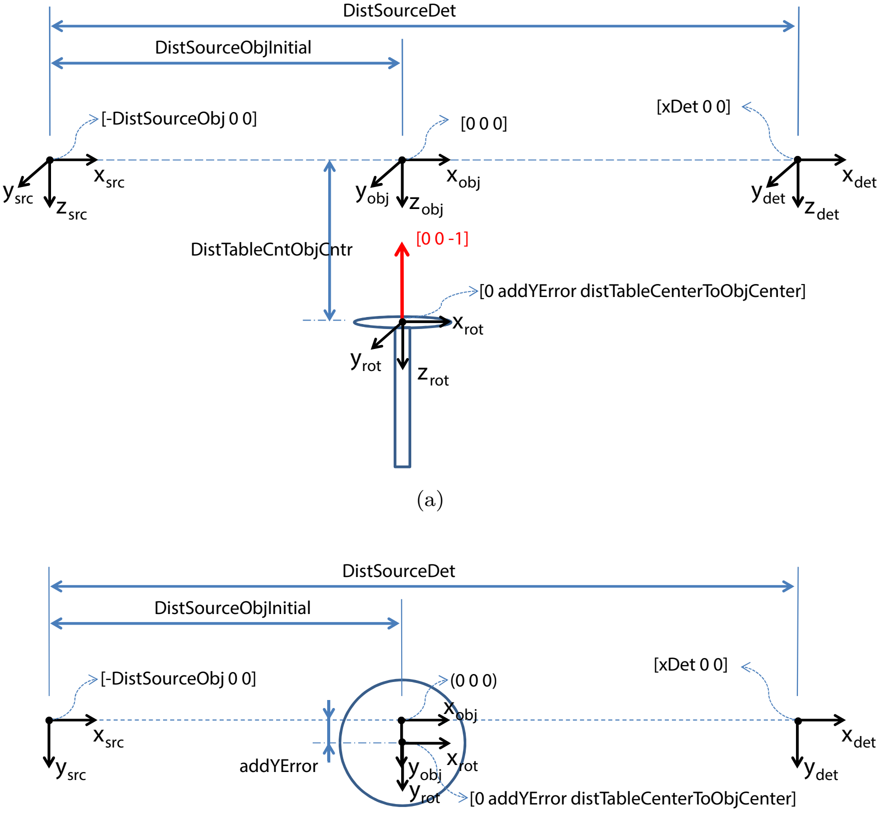

(a)

(b)

Figure 4.5: Different coordinate systems and their relationship: 3D view (a) and top view (b).

Sections 4.3.3 to 4.3.7 will now discuss the crucial parameters and implementations per main component. The spectrum transition are discussed in parallel and summarized in section 4.3.8.

Required input parameters

FileName Link to the tiff files to be rewritten. 'Filename' will be automatically extended with the numbering '0001',... '1234' as in the usual process.

4.3.3 Source

X-ray spectra

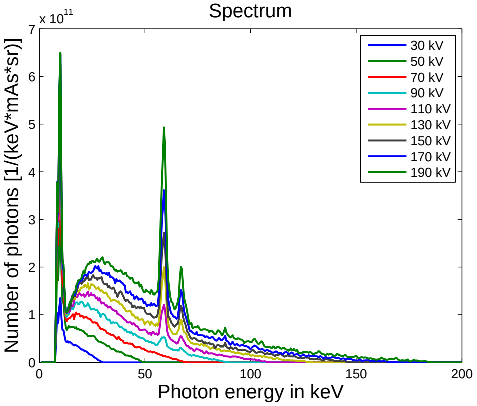

Figure 4.6: X-ray spectra in function of source energy. The plotted data is obtained from [46].

Generation of X-ray spectra and literature predicting these spectra has already been discussed in section 2.2.1. Common CT scanners work with a polychromatic source spectrum. The simulation program additionally hands the possibility to choose a monochromatic source spectrum for research purposes.

The simulation program holds three options related to the applied polychromatic energy spectrum: 'Simulated', 'Measured', 'ManualSpecInput'. 'Simulated' uses the simulated X-ray spectra of [107]. 'Measured' uses the X-ray spectra which have been measured using a Compton scattering spectrometer in [46] (figure 4.6). [46] provides absolute measured spectra for an industrial micro focal X-ray source as a function of source voltage (30-190kV for every multiple of 10kV). 'ManualSpecInput' allows the user to use his own X-ray spectra data.

Sampling points and weights

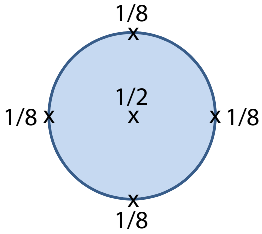

Figure 4.7: A finite source simulated as five single point sources, applying certain weighting factors.

The spot from which the X-rays leave is specified by sampling points and weights. The sampling points are defined by their x, y, z-coordinate with respect to the source coordinate system of figure 4.5. Calculations are executed for multiple discrete 'point' sources. Adding the detector values obtained for each point of the source (multiplied by the appropriate weighting factor) simulates a finite source. Figure 4.7 gives a possible implementation of a finite source. The source is in this case built up with five point sources. The resulting spectrum is

$$
\begin{aligned}
I(E,i,j) = {} & \frac{I_1(E,i,j) + I_2(E,i,j) + I_3(E,i,j) + I_4(E,i,j)}{8} \\
& + \frac{I_{center}(E,i,j)}{2}
\end{aligned} \tag{4.4}
$$

where:

$I_{center}(E,i,j)$ = Final spectrum at detector pixel point (i,j) from the rays started at the source center.

$I_t(E,i,j)$ = Final spectrum at detector pixel point (i,j) from the rays started at edge point t.

The equation valid for the Nikon Metrology XT H 450 CT scanner, explained in section 2.2.1 (equation 2.1) to define the spot size, is also implemented. This will define the spot size using equation 2.1 and simulate the spot as pictured in figure 4.7.

Figure 4.8 compares the simulated projection images in case of a point source and a finite spot size. Figure 4.8b is obtained after subtracting one image from the other.

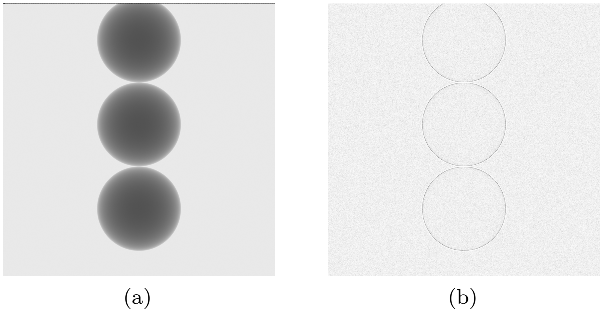
(a) (b)

Figure 4.8: Simulation example showing the effect of the spot size. The object consisted of 3 spheres on top of each other (a). The resulting projection image (a) of the object has been simulated with a spot size of $80 \mu m$ and a point source. The difference in projection image is not visible by eye and is therefore shown in (b) by subtracting one image from the other.

Source drift

Source drift has been discussed in section 2.2.1. This source drift is often assumed to be linear. [150] measured an arc tangent trend in the source drift. The source drift in x, y and z with respect to the first image can be specified for each separate view in the simulation program. The simulation program also offers two predefined options: 'linear' and 'arc tangential' for resp. a linear and arc tangential relationship. In this case the user has to additionally define the total increment in x, y and z-direction. Figure 4.9 illustrates the effect of source drift. Three spheres have been simulated which are positioned close to the source. The first image (angular position 0 degrees) and last image (angular position 360 degrees) are compared by subtracting the last images from the first image. The resulting image is inverted (black to white and vice versa) to make the difference more clear. This is the image shown in Figure 4.9.

Required input parameters

Voltage The source voltage has to be specified in kV.

Current The source current has to be specified in μA.

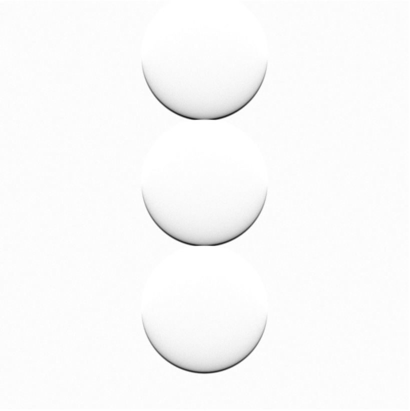

Figure 4.9: Simulation example showing the effect of spot drift during a scan by comparing the projection images of a fixed object. The last images has been subtracted from the first image. The received image has been inverted (black to white and vice versa) to make the difference more clear.

SourcePoints The position of the source point(s) have to be defined in the source coordinate system. Either the positions can be manually inputted in matrix form or they are automatically calculated. Equation 2.1 which uses the source current and voltage to define the spot size is applied in the latter case.

SourceWeightsSet Applied weighting factors for the source points. These factors should be defined in the same order as the corresponding SourcePoints. Sum needs to be 1.

SourceDrift Three possible values: 'linear', 'arc tangential' or 'manually'. 'linear' and 'arc tangential' automatically generate the source drift per view angle based on the 'IncrementX', 'IncrementY' and 'IncrementZ' parameter. 'manually' uses the source drift vectors specified in 'ManualSourceDriftX', 'ManualSourceDriftY' and 'ManualSourceDriftZ'.

IncrementX, IncrementY, IncrementZ The amount of drift in time from the source between the first and last projection image for the x, y and z-direction.

ManualSourceDriftX, ManualSourceDriftY, ManualSourceDriftZ Vectors (for x, y and z-direction) with as elements the source drift for each separate view with respect to the initial source position.

SpecType Two options: 'monochromatic spectrum' or 'polychromatic spectrum'.

ReadSpec Three possible options: 'Simulated', 'Measured' or 'ManualSpecInput'. 'Simulated' uses simulated spectra, 'Measured' uses measured X-ray spectra and 'ManualSpecInput' uses the X-ray spectra specified in 'ManualSpec'.

ManualSpec Manual definition of X-ray spectra using 2 column matrices. The first column holds the keV values, and the second column the corresponding number of photons.

Uncertainty parameters Uncertainty parameters are implemented for the calculated 'SpotSize', a general shift for all 'SourcePoints' positions (uncertainty for x, y and z value) and for each separate 'SourcePoints' position (uncertainty for x, y, z value) and for the 'IncrementX', 'IncrementY' and 'IncrementZ' parameters.

4.3.4 Filter plate

Section 2.3.3 already explained the functioning of a filter plate. The attenuation is dependent on the material and the thickness of the filter (see figure 2.12). This can be expressed in following formula for one ray.

$$I(E)_{filtered} = I_0(E)\, e^{-(\mu_{filter}(E)\, x_{filter})} \tag{4.5}$$

where:

$I_0(E)$ = The initial polychromatic X-ray spectrum.
x_{filter} = Filter thickness.
μ_{filter} = Linear attenuation coefficient of the filter material.

The simulation user needs to define the filter thickness $[mm]$ and the filter material as a chemical element.

Required input parameters

FilterThickness Thickness of the filter in mm.

FilterType Filter plate material.

4.3.5 Object and air

For each detector point and view angle, the penetration length $x_{object,m}$ through the object is calculated through analytical calculations. Penetration matrices through different features (spheres, cylinder, cone, rectangular cuboids and combinations of these features) can be calculated. The Matlab® implementation to calculate these penetration lengths will further be discussed in section 4.3.10. The length penetrated through air for one ray is defined by equation 4.6:

$$x_{air} = x_{air\_src\_det} - x_{filter} - \sum_{m=1}^{M} x_{object,m} \tag{4.6}$$

where:

$x_{object,m}$ = Distance penetrated through object m, along a ray starting from the source to the detector intersection point.
$x_{air\_src\_det}$ = Penetration length through air calculated as the distance between point source and intersection point with the detector pixel.
x_{filter} = Filter thickness (as penetration depth measured along the same ray as above).

Object m should hereby exist of one single material (e.g. Al_2O_3 , Cu, Al, etc.). Multi-material objects have to be modeled as superposition of distinct objects.

Equation 4.7 formulates the spectrum $I(E)_{det\_in}$ of a single ray reaching the detector.

$$\begin{aligned} I(E)_{det\_in} = I(E)_{filtered}\, & e^{-(\mu_{air}(E)\; x_{air})} \\ & \prod_{m=1}^{M} e^{-(\mu_{object,m}(E)\; x_{object,m})} \end{aligned} \tag{4.7}$$

where:

$I(E)_{filtered}$ = Filtered X-ray spectrum, using equation 4.5.
$x_{object,m}$ = Distance penetrated through object m, along a ray starting from the source to the detector intersection point.
$\mu_{object,m}(E)$ = Linear attenuation coefficient of material m as a function of photon energy.

x_{air} = Penetration length through air.
μ_{air} = Linear attenuation coefficient of air.

Required input parameters

ObjectToCalculate There are some predefined objects (see objects in section 5). See section 4.3.10 to define objects manually. The objects need to be specified with respect to the object coordinate system.

ObjectTransX, ObjectTransY, ObjectTransZ Translation of the entire object in x, y and z-direction of the object coordinate system.

RotObjX, rotObjY, rotObjZ Rotation of the entire object around the x, y and z-axis of the object coordinate system.

Uncertainty parameters Uncertainty parameters can be taken into account for 'ObjectTransX', 'ObjectTransY', 'ObjectTransZ', 'RotObjX', 'RotObjY', 'RotObjZ'.

4.3.6 Rotation table

Rotation axis definition and misalignments

Different settings related to the rotation axis has to be defined.

- Rotation vector 'RotAxis'.
- Rotation origin 'RotOrigin'.
- Source-object distance 'DistSourceObjectInitial' (figure 4.5).
- Distance between the object coordinate system and rotation table coordinate system 'DistTableCntObjectCenter' (figure 4.5).

Furthermore different errors are specified.

- Incorrect zero position of the rotation position with respect to the y-axis 'AddYerror' (figure 4.5).
- Tilt of the rotation table vector around x and y specified by 'RotAxisAroundx', 'RotAxisAroundy'.

Stepwise versus continuous scanning

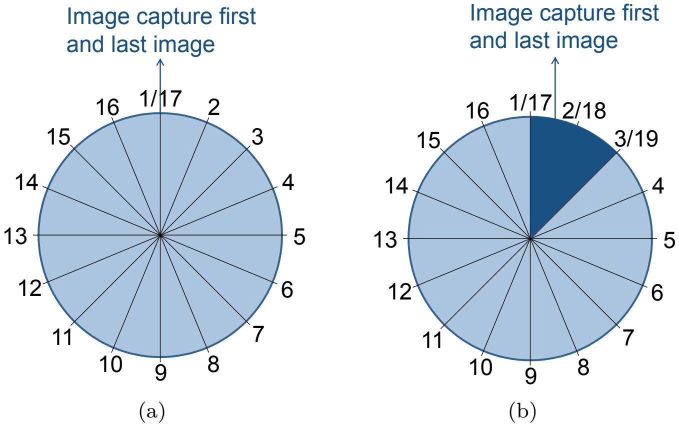

(a) (b)

Figure 4.10: Working principle of stepwise (a) and continuous scanning (b). Stepwise scanning over 17 views, which needs 17 angles to be calculated. Continuous scanning over 9 views, integrating over 3 angles, which requires calculations over 19 angles.

Section 2.3.16 discusses the difference between stepwise and continuous CT scanning. The simulation program offers both possibilities. In case of the continuous scanning option the projection image will be the result of a weighted integration over different angles. The user has to specify the number of images to integrate. Figure 4.10 compares the implementation of a stepwise (a) and a continuous scan (b). A stepwise scan calculates a projection image for each defined view (17 views in this case). The number of angles in the matrix 'AngleInformation' corresponds to the number of views. The first image and last image is theoretically at the same position. Figure 4.10b sketches the continuous scanning situation. The illustrated situation has 9 views and integrates over 3 angles. The first projection images uses the information of angles 1, 2 and 3. The second projection image takes information from angles 3, 4 and 5. The last projection image is theoretically again captured between angles 1, 2 and 3. The number of angles in the 'AngleInformation' matrix will be 19 in this case (1, 2 and 3 are repeated with their specific errors).

Figure 4.11 shows the influence of this option for a simulated CT scan with 30 views.

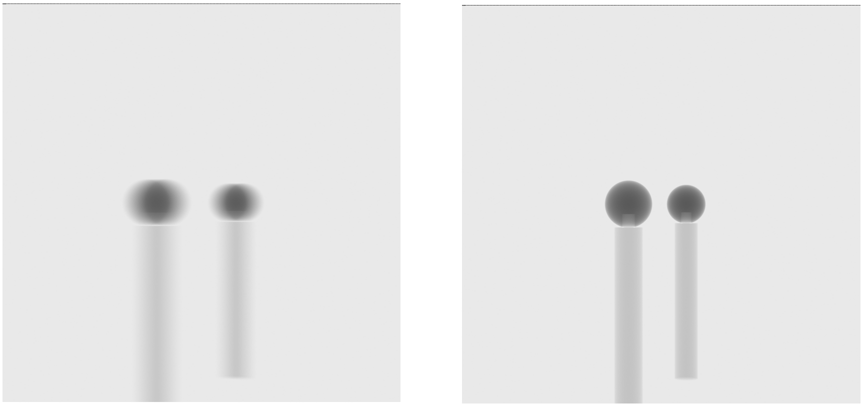

(a) (b)

Figure 4.11: Continuous scanning (a) versus stepwise scanning (b).

Wobble and eccentricity

Wobble and eccentricity of the rotation table has been reported in section 2.2.3. Both errors can be calculated 'automatically' or 'manually' in the simulation program. Rotation angles around the x and y-axis of the table coordinate system define the wobble errors. Shift errors along the x and y-axis define the eccentricity errors. 'manually' gives the user the option to define these errors for each angle. 'automatically' calculates the errors based on the maximum eccentricity and the maximum defined wobble rotation angle around x and y.

Rotation angle errors

Section 2.3.23 explained the importance of the rotation speed calibration. An incorrect calibration leads to an angular error. The user of the simulation program has two options concerning angular errors of the rotation table angle: 'automatically' and 'manually'. The 'automatically' option calculates a constant angular error value based on the overshoot with respect to the nominal 360 degrees rotation. The 'manually' option offers the possibility to define the angular error for each rotation angle.

Required input parameters

DistSourceObjectInitial Nominal distance between source and object.

RotAxis Vector resembling the rotation axis vector: normally [0 0 -1] as depicted in figure 4.5.

RotOrigin Origin of the rotation axis vector.

rotAxisAroundx, rotAxisAroundy Errors of the rotation axis vector: tilt of the vector around the x and y-axis of the rotation table coordinate system.

DistancePosTableCenterToObjectCenter Vertical distance between object center and table center as depicted in figure 4.5. This is automatically calculated for our Nikon Metrology 450 kV CT scanner using the parameters 'TablePosition' and 'TableZeroPosition'.

TablePosition Position of the table as outputted by the machine device.

TableZeroPosition Height position of the table as outputted by the machine device when the table (rotation axis coordinate systems) is situated in the horizontal center plane formed by the source and detector coordinate system.

AddYError Additional fixed table position error in y-direction due to incorrect zero setting of this axis.

RotAngleErrors Two possible values: 'automatically' or 'manually'. 'automatically' uses the 'Overshoot' parameter. 'manually' uses the vector 'AngularErrors'.

Overshoot Deviation to the nominal angular position of the last projection image.

AngularErrors Vector with as elements the angular errors of the rotation table for each separate angle.

Wobble Two possible values: 'automatically' or 'manually'. 'automatically' uses the 'Max_wobble_Rx' and 'Max_wobble_Ry' parameters. 'manually' uses the vectors 'WobbleX' and 'WobbleY'.

Max_wobble_Rx, max_wobble_Ry Maximum wobble error of the rotation table around the x and y-axis.

WobbleX, WobbleY Vectors with as elements the wobble angle of the rotation table around resp. x and y for each separate angle.

Eccentricity Two possible values: 'automatically' or 'manually'. 'automatically' uses the 'Max_eccentricity' parameter. 'Manually' uses the vectors 'EccentricityX' and 'EccentricityY'.

Max_eccentricity Maximum eccentricity error of the rotation table.

EccentricityX, EccentricityY Vectors with as elements the eccentricity of the rotation table in resp. x and y for each separate view.

Uncertainty parameters Uncertainty parameters can be taken into account for 'DistSourceObjectInitial', 'RotOrigin', 'RotAxisAroundx', 'RotAxisAroundy', 'Overshoot', 'Max_wobble_Rx', 'Max_wobble_Ry', 'Max_eccentricity'.

4.3.7 Detector

The detectors of the CT devices in this thesis are categorized as scintillation-type detectors or 'indirect' detectors (see section 2.2.2).

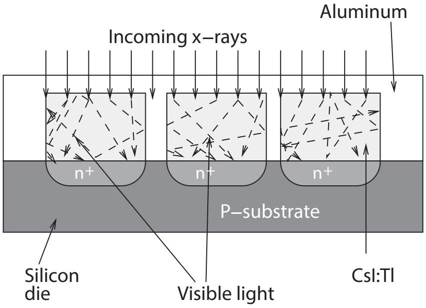

Figure 4.12: Working principle of a scintillator-based X-ray detector [114].

Figure 4.12 illustrates the different steps (or detector attenuation processes) in a scintillator-based X-ray detector [114]:

- Transmission of the X-rays through the reflective layer.

$$I(E) = I_0(E)_{det\_in}\, e^{-(\mu_{refl\_layer}(E)\, x_{refl\_layer})} \tag{4.8}$$

where:

μ_{refl_layer} = Linear attenuation coefficient of the reflective layer.
x_{refl_layer} = Thickness of the reflective layer.
$I_0(E)_{det\_in}$ = X-ray spectrum entering the detector (equation 4.7).

- Absorption of X-rays by scintillating crystal and conversion into visible light.

$$I(E) = I_0(E)_{det\_in}\, e^{-(\mu_{refl\_layer}(E)\, x_{refl\_layer})} \\ (1 - e^{-(\mu_{scintillator}(E)\, x_{scintillator})}) \tag{4.9}$$

where:

$\mu_{scintillator}$ = Linear attenuation coefficient of the scintillator.
$x_{scintillator}$ = Thickness of the scintillator.

- Reflection of the visible light by the reflective layer.
- Transmission of the visible light to the photo detector .

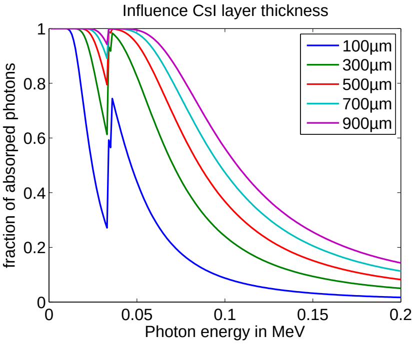

Figure 4.13: Influence of the scintillator thickness.

Figure 4.13 shows the influence of the scintillator thickness (in this case CsI) on the fraction of absorbed X-ray photons.

Detector creation

The detector is currently simulated as a flat panel detector without form error. The spectrum of multiple detector points (at least one per pixel) is traced. These points are defined in the detector coordinate system. Different parameters are needed from the user: pixel dimensions, number of pixels in both direction, alignment errors and number of sampling points. The simulation automatically generates a pixel grid on the detector dependent of these parameters. The user is of course free to define a more realistic detector which for instance contains a flatness error.

Sampling points and weights

$$\begin{bmatrix} 1 & 2 & 2 & 2 & \dots & 2 & 2 & 1 \\ 2 & 4 & 4 & 4 & \dots & 4 & 4 & 2 \\ 2 & 4 & 4 & 4 & \dots & 4 & 4 & 2 \\ \vdots & \vdots & \vdots & \vdots & \ddots & \vdots & \vdots & \vdots \\ 2 & 4 & 4 & 4 & \dots & 4 & 4 & 2 \\ 1 & 2 & 2 & 2 & \dots & 2 & 2 & 1 \end{bmatrix}$$

Figure 4.14: Use of a weighting grid on a detector pixel.

As already explained in section 4.2 it is not realistic to calculate the pixel values by looking at the spectrum of a single ray per detector pixel. Integration over the detector pixel area is needed. This is done by calculating the results for multiple rays penetrating multiple points per detector pixel. The user can define the value 'pixelgrid' which results in a $pixelgrid \times pixelgrid$ pixel grid. The user must additionally define the weighting factors. Figure 4.14 gives a possible method to define the weighting factors per point on each detector pixel. This method is in fact a 2D version of the Trapezoidal rule. In case of a 3 by 3 grid the resulting spectrum for one pixel, using the method of figure 4.14 would be as in equation 4.10.

$$\begin{aligned} I(E,i,j) = {} & (I_{1,1}(E,i,j) + 2\,I_{1,2}(E,i,j) + I_{1,3}(E,i,j) + 2\,I_{2,1}(E,i,j) \\ & + 4\,I_{2,2}(E,i,j) + 2\,I_{2,3}(E,i,j) + I_{3,1}(E,i,j) + 2\,I_{3,}(E,i,j) \\ & + I_{3,3}(E,i,j))/(1+2+1+2+4+2+1+2+1) \end{aligned} \tag{4.10}$$

where:

$I_{a,b}(E,i,j)$ = spectrum entering at point (a,b) of pixel (i,j).

Detector misalignments

Rotation around the x, y and z-axis of the coordinate system and shift of the detector along the y and z-axis can be applied by the user.

Required input parameters

Pixelgrid To define a grid per pixel for integration over the pixel purposes. E.g. if *pixelgrid* is set to 3, a 3 by 3 grid is used.

GridPointWeightsSet Applied weighting factors for the grid points.

Pixelsize Size of the detector pixels.

Npixels Number of horizontal detector pixels.

Npixelsheight Number of vertical detector pixels.

DistSourceDet Distance source to detector.

RotX, RotY, RotZ Errors of the detector position to its normal position: rotation around x, y and z-axis of the detector coordinate system.

ShiftY, ShiftZ Errors of the detector position to its normal position: translation along the y and z-axis of the detector coordinate system.

WhiteLevel Predefined user value which defines the gray value for no penetration, i.e. when no object is in view (see section 2.3.17 and equation 4.1).

NoiseSigma Sigma of random noise on detector pixel value.

Uncertainty parameters Uncertainty parameters are possible for the calculated magnification, 'RotX', 'RotY', 'RotZ', 'ShiftY' and 'ShiftZ' value.

4.3.8 Spectrum transition

Equation 4.11 summarizes the spectrum transition from source to detector.

$$
\begin{aligned}
I(E) = I_0(E)\, & e^{-(\mu_{filter}(E)\, x_{filter})}\; e^{-(\mu_{air}(E)\, x_{air})} \\
& \prod_{m=1}^{M} e^{-(\mu_{object,m}(E)\, x_{object,m})}\; e^{-(\mu_{refl\_layer}(E)\, x_{refl\_layer})} \\
& (1 - e^{-(\mu_{scintillator}(E)\, x_{scintillator})})
\end{aligned}
\tag{4.11}
$$

where:

$I_0(E)$ = The initial polychromatic X-ray spectrum.
$x_{object,m}$ = Distance penetrated through object m, along a ray starting from the source to the detector intersection point.
$\mu_{object,m}(E)$ = Linear attenuation coefficient of material m as a function of photon energy.
x_{air} = Penetratrion lengths through air.
μ_{air} = Linear attenuation coefficient of air.

x_{filter} = Filter thickness.
μ_{filter} = Linear attenuation coefficient of the filter material.
μ_{refl_layer} = Linear attenuation coefficient of the reflective layer.
x_{refl_layer} = Thickness of the reflective layer.
$\mu_{scintillator}$ = Linear attenuation coefficient of the scintillator.
$x_{scintillator}$ = Thickness of the scintillator.

4.3.9 Kinematic systems errors

Calculation of errors due to incorrectness of the table positioning system can be applied. Figure 4.15 illustrates the Matlab® implementation. These errors are implemented using the kinematic model of section 3.2. At the moment the errors are based on the Nikon Metrology XT H 450 kV CT scanner as measured in section 3.3, but the simulation program user can easily adapt this for another CT scanner. The first main program (section 4.3.1) sends input related to the table position, rotation axis vector and rotation origin to the subprogram 'Kinematic system errors'. This program outputs the new rotation axis vector and the error on its origin. It hereby uses the program 'CalculateRealPos' which calculates the real position of a point taken into account the errors specified in the subprograms eax, ebx, ezz, etc. These subprograms contain the information related to the error components (section 3.3). Input from the user is hereby needed for the table position.

Required input parameters

TablePosition Position (x, y, z) of the rotation table as outputted by the CT device software.

4.3.10 Generic objects

Calculation of the penetration lengths between rays (lines) and several generic objects has been implemented. It has been chosen to calculate these intersections analytically i.e. using analytical expressions for the line (between source point and point on detector) and the generic objects. Using a triangulated surface model or a voxel model of the objects would have been another option. This option would afterwards raise the question whether the accuracy of the calculated penetration lengths was sufficient. Subsequently one can ask himself whether the errors on the dimensional measurements of the reconstructed voxel models were a consequence of the CT process or due to the incorrect penetration length

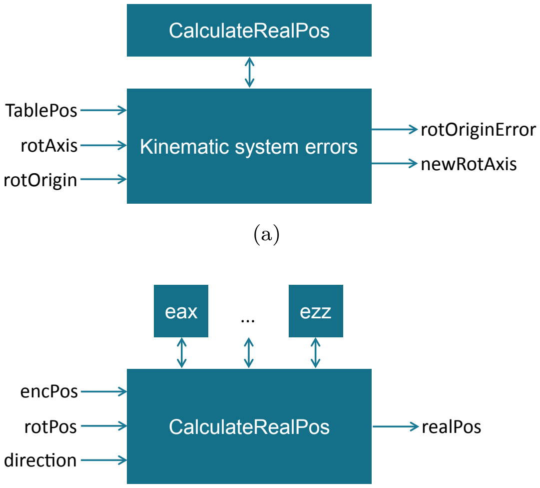

(a)

(b)

Figure 4.15: Matlab® implementation to calculate errors due to the table positioning system (cfr. section 3.2): calculation of the errors (a) and the subprogram 'CalculateRealPos' (b).

determination. The main program can however simply be adapted by the user. The user can for instance add functions to calculate penetration lengths through objects defined by a triangulated surface model or he can add different generic objects.

General approach

Equation 4.12 gives the analytical expression of a line.

$$\mathbf{p} = d\mathbf{l} + \mathbf{l_0} \tag{4.12}$$

where:

$\mathbf{l}$ = Normalized direction vector of the line.
$\mathbf{l_0}$ = Point on the line
d = A scalar.

The next step is to define all possible intersections of the lines (rays) from the source to the detector pixel with the generic object elements. These intersections are characterized by their parameter d_i. The following step includes the categorization of these parameters d_i as ingoing or outgoing.

The general approach will now be explained in the case of the penetration length calculation between a line and a cuboid. A similar approach is used for the other generic objects.

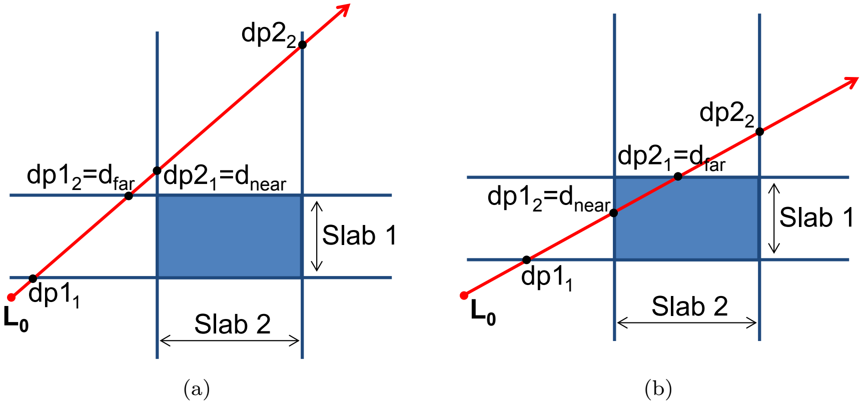

Figure 4.16: Intersection possibilities of a ray and a cuboid: (a) $min(d_{far}) < max(d_{near})$ which means no intersection and (b) $min(d_{far}) > max(d_{near})$ which means there is intersection.

A method to define the intersection points of a ray (or line) and a box (or cuboid) based on slabs has been worked out by Kay and Kayjia [99] (figure 4.16 illustrates this method in the 2 dimensional case, which will be further explained in next paragraph). The slab is the space between two parallel infinite planes. A box is defined by a combination of 3 sets of parallel (infinite) planes. The method looks at the intersection of the ray with the 2 planes of a slab. d_{far} (or d_{out}) and d_{near} (or d_{in}) is determined for each pair of planes. The ray misses the box if the overall largest d_{near} (or d_{in}) value is greater than the smallest d_{far} (or d_{out}) value. The ray hits the box in the other case. A special situation occurs when the ray is parallel to the border planes of a slab. The calculated d values for this slab will be $infinite$ or NaN (0/0). In this case it is needed to check whether the ray is situated in between the the border planes of the slab or not. In case not, there is no intersection, otherwise there is still intersection but only the d values of the other slabs should be taken into account.

Figure 4.16 illustrates the method in the 2 dimensional case. $dp1_1$ and $dp1_2$ are resp. the near and far value of slab 1, whereas $dp2_1$ and $dp2_2$ are resp. the near and far value of slab 2. The largest d_{near} value is set to the largest value of $dp1_1$ and $dp2_1$. The smallest d_{far} value is the minimum of $dp1_2$ and $dp2_2$. Figure 4.16a pictures the case where $d_{far} < d_{near}$, which results in no intersection. Figure 4.16b illustrates the case when $d_{near} < d_{far}$ which gives intersection.

Figure 4.17 resumes the general approach to be used for calculating the penetration lengths of a line and an object. The next sections discuss the different implemented generic objects.

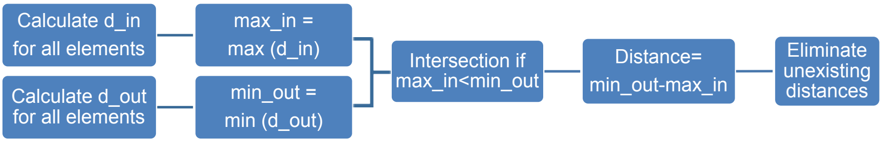

Figure 4.17: General approach after calculation of the intersection parameters d.

cuboid

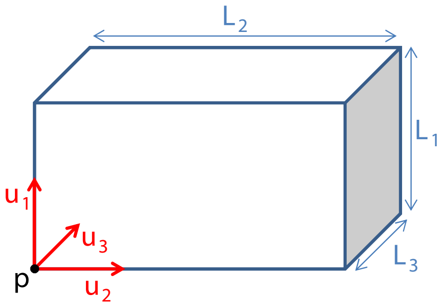

Figure 4.18: Parameters to define a cuboid object.

Figure 4.18 illustrates the parameters to determine a cuboid.

- $\mathbf{p}$. Corner point of the cuboid.
- $\mathbf{u_1}$, $\mathbf{u_2}$, $\mathbf{u_3}$. Perpendicular unit vectors.
- $\mathbf{L_1}$, $\mathbf{L_2}$, $\mathbf{L_3}$. cuboid lengths belonging to the unit vectors.

The cuboid is defined by 6 entities (6 infinite planes) leading to 6 possible intersection point parameters dp.

Equation 4.13 expresses the vector notation for points $\mathbf{p}$ on an infinite plane.

$$(\mathbf{p} - \mathbf{p_0}) \cdot \mathbf{n} = 0 \tag{4.13}$$

where:

$\mathbf{p_0}$ = Point on the plane.
$\mathbf{n}$ = Normal vector to the plane.

Combining equations 4.12 and 4.13, and solving for the parameter d (dp) results in 3 cases.

- $dp = r$ (r a real number). This gives the intersection point as the distance along the line from $\mathbf{l_0}$.
- $d = \frac{r}{0} = \infty$. In this case the line is parallel to the plane.
- $d = \frac{0}{0} = NaN$. This means that the line lays in the plane.

Figure 4.19 illustrates the general method to define the intersection parameters d. d values equal to ∞ are set to NaN to avoid further influence in the calculations. If the source point is not situated between the couple of slabs, no intersection is possible for the lines parallel to a couple of slabs, and therefore these situations are eliminated by setting them to 0 in the parameter $CheckMatrix$. This $CheckMatrix$ will afterwards be multiplied (element by element) with the calculated distances. Further calculations are performed as illustrated in figure 4.17.

Sphere

Figure 4.20 shows the parameters to define a sphere object.

The vector equation for a sphere is:

$$\|\mathbf{p} - \mathbf{c}\|^2 = r^2 \tag{4.14}$$

where:

$\mathbf{c}$ = Center point of the sphere.
r = Sphere radius.
$\mathbf{p}$= Points of the sphere.

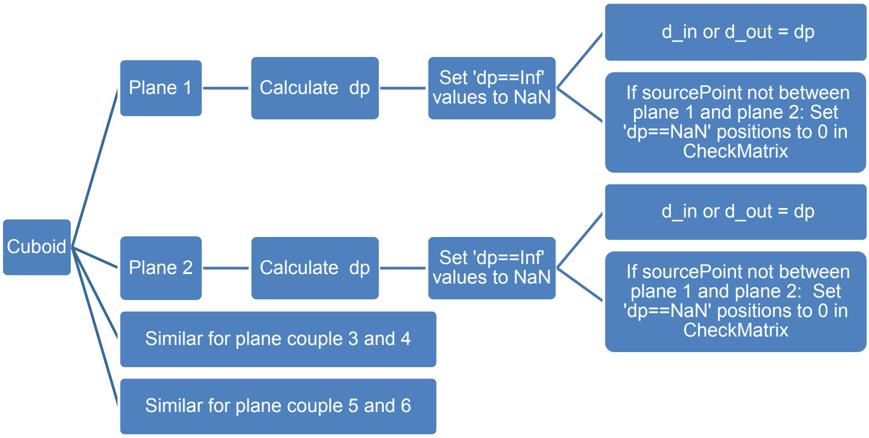

Figure 4.19: Used method to define the intersection parameters d for a cuboid.

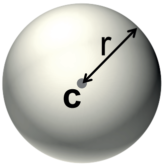

Figure 4.20: Parameters to define a sphere object.

Combining equations 4.12 and 4.13, and solving for the parameter d will after simplification result in:

$$d = -(\mathbf{l} \cdot (\mathbf{l_0} - \mathbf{c})) \pm \sqrt{\Delta} \tag{4.15}$$

where:

$\mathbf{l}$ = Line direction vector.
$\mathbf{c}$ = Center point.
$\mathbf{l_0}$ = Origin of the line.
Δ = As defined in equation 4.16.

$$\Delta = (\mathbf{l} \cdot (\mathbf{l_0} - \mathbf{c}))^2 - \|\mathbf{l_0} - \mathbf{c}\|^2 + r^2 \tag{4.16}$$

Equation 4.16 has three possible solutions:

- $\Delta < 0$. Which results in no intersection.
- $\Delta = 0$. This means that the line touches the sphere.
- $\Delta > 0$. In this case 2 solutions exist.

Figure 4.21 illustrates the applied working principle for line/sphere intersections. Negative Δ values are set to 0 to simplify the calculations.

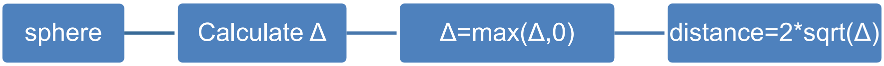

Figure 4.21: Method to calculate the penetration lengths in a sphere.

Truncated sphere

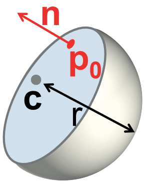

Figure 4.22: Parameters to define a truncated sphere object.

A truncated sphere is defined by 2 entities as shown in figure 4.22: a sphere, defined by center point $\mathbf{c}$ and radius r, and an (infinite) plane, defined by a point on the plane $\mathbf{p_0}$ and the normal vector of the plane $\mathbf{n}$ pointing to the outside. Intersection parameters d are calculated for the sphere (equation 4.15) and for the infinite plane (equation 4.13). Figure 4.23 illustrates the used working method. After defining the intersection parameters d, the principle shown in figure 4.17 is applied.

Cylinder

Figure 4.24 illustrates the parameters to describe a cylinder: 2 points ($\mathbf{c_0}$ and $\mathbf{c_e}$) and the radius r. The cylinder is built up with 3 entities: an infinite cylinder mantle and 2 infinite planes. Calculations of the intersection parameters d for the line/plane intersections are similar as for the cuboid object (equation 4.13).

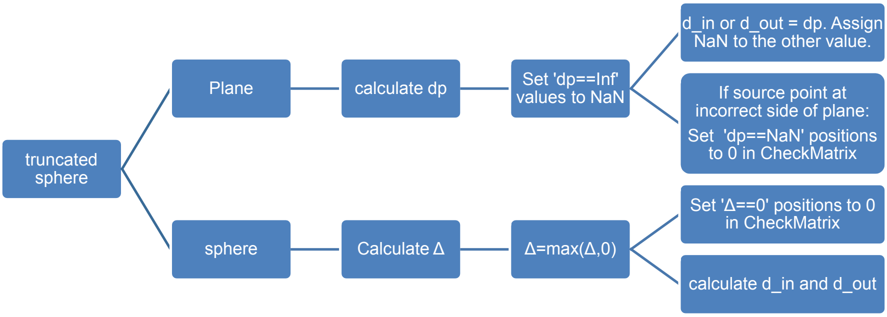

Figure 4.23: Method to calculate the penetration lengths in a truncated sphere.

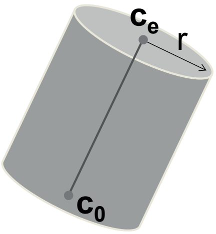

Figure 4.24: Parameters to define a cylinder object.

The points $\mathbf{p}$ of the cylinder mantle are defined by equation 4.17.

$$(\mathbf{p} - \mathbf{c_1} - (\mathbf{v} \cdot (\mathbf{p} - \mathbf{c_1}))\mathbf{v})^2 - r^2 = 0 \tag{4.17}$$

where:

$\mathbf{v}$ = Direction vector of the cylinder.
$\mathbf{c_1}$ = Point on the center line.
r = Radius of the cylinder.

Combination of equations 4.12 and 4.17 leads to a 2nd order equation, which has to be solved to find the intersection parameters d.

Figure 4.25 shows the used approach to calculate the intersection parameters d. Afterwards the method explained in figure 4.17 is utilized.

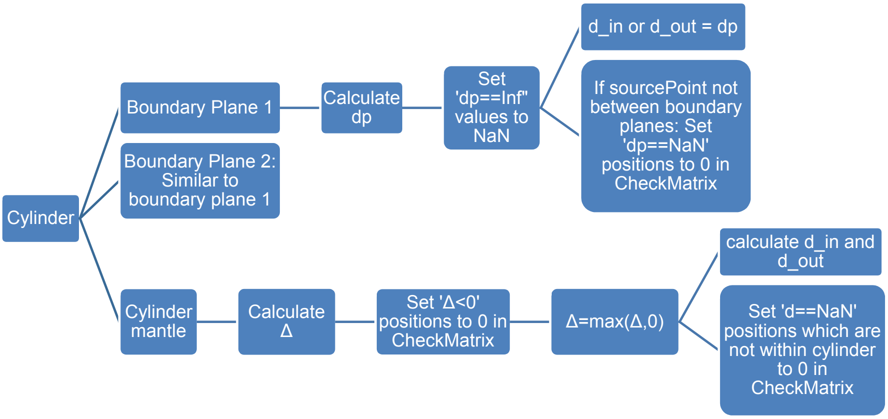

Figure 4.25: Method to calculate the penetration lengths in a cylinder.

Truncated cylinder

A truncated cylinder is described by 4 entities: a infinite cylinder mantle, 2 infinite planes and an extra intersecting plane as shown in figure 4.26. The cylinder (infinite cylinder mantle, with the two boundary planes) is defined by 2 points ($\mathbf{c_0}$ and $\mathbf{c_e}$) and the radius r. The intersecting plane is defined by a point on the plane $\mathbf{p_0}$ and the normal vector of the plane $\mathbf{n}$ pointing to the outside. Intersection parameters d are calculated for the cylinder mantle with 2 boundary planes (similar to the cylinder object) and for the infinite plane (equation 4.13). The approach to calculate the intersection parameters d is illustrated in figure 4.27. Next the method in figure 4.17 is used to calculate the actual distances.

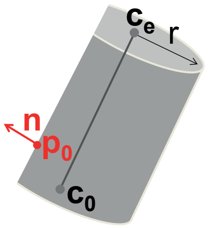

Figure 4.26: Parameters to define a truncated cylinder object.

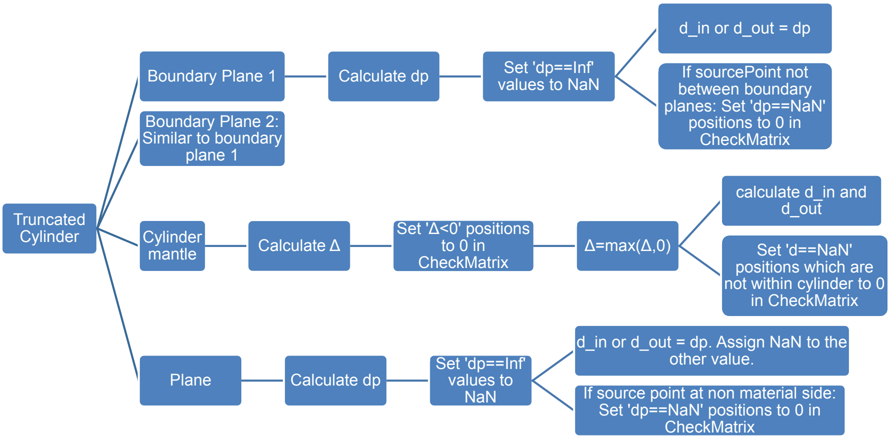

Figure 4.27: Method to calculate the penetration lengths in a truncated cylinder.

Cone

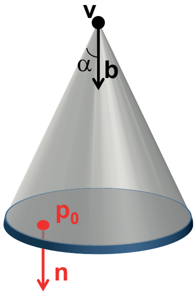

Figure 4.28: Parameters to define a cone object.

Figure 4.28 shows the construction of a cone. Two entities are combined, a cone mantle and an intersecting plane. A vertex V, angle α and direction vector $\mathbf{b}$ are the input parameters of the cone mantle. The intersection plane is again defined by a point $\mathbf{p_0}$ and direction $\mathbf{n}$. Intersection parameters d are calculated for the cone mantle and the infinite plane (equation 4.13). [39] explains the intersection of a line and a cone. A point x on the (double) cone is defined by equations 4.18, 4.19 and 4.20. It should be notified that equation 4.18 gives the intersection points for the investigated cone but also for its reflected cone. Therefore equation 4.20 is applied to all calculated intersection points to eliminate the intersection points at the reflected cone side.

$$(\mathbf{x}-\mathbf{v})^T M(\mathbf{x}-\mathbf{v}) = 0 \tag{4.18}$$

$$M = ((\mathbf{b}-\mathbf{b}^T - \cos^2(\alpha)I) \tag{4.19}$$

$$\mathbf{b}(\mathbf{x}-\mathbf{v}) \geq 0 \tag{4.20}$$

where:

$I =$ The unit matrix.
$\mathbf{b} =$ Direction vector of the cone.
$\mathbf{v} =$ Vertex of the cone.
$\alpha =$ Vertex angle.

Substitution of equation 4.12 in equation 4.18 leads to following quadratic equation.

$$c_2 d^2 + 2c_1 d + c_0 = 0 \tag{4.21}$$

where:

$\Delta = \mathbf{l_0}$-$\mathbf{v}$.
$c_2 = \mathbf{l}^T M \mathbf{l}$.
$c_1 = \mathbf{l}^T M \Delta$.
$c_0 = \Delta^T M \Delta$.

Solving this equation can lead to two cases: $\mathbf{c_2 = 0}$ or $\mathbf{c_2 \neq 0}$

Case 1: $\mathbf{c_2 = 0}$. In this case equation 4.21 is solved by defining δ as in equation 4.22.

$$\delta = c_1^2 - c_0 c_2 \tag{4.22}$$

Depending on the achieved value for δ following solutions are distinguished.

- $\delta < 0$. Which results in no intersection.
- $\delta = 0$. This means that the line touches the double cone mantle.

- $\delta > 0$. In this case 2 solutions exist.

Case 2: $\mathbf{c_2 \neq 0}$. The case $\mathbf{c_2 \neq 0}$ categorizes the solutions in following possibilities.

- $\mathbf{c_1 \neq 0}$. There is one intersection point with the double cone mantle.
- $\mathbf{c_1 = 0}$ and $\mathbf{c_0 = 0}$. This means that the line is contained by the double cone mantle.
- $\mathbf{c_1 = 0}$ and $\mathbf{c_0 \neq 0}$. Which results in no intersection.

Figure 4.30 shows the method to calculate the intersection parameters d. Figure 4.17 calculates the actual distances.

Cone segment

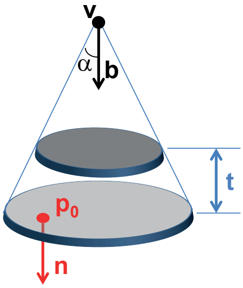

Figure 4.29: Parameters to define a cone segment.

Figure 4.29 illustrates the truncated cone parameters. There is one extra parameter compared to the cone object: thickness parameter t. This cone segment consists of 3 entities: the cone mantle and 2 infinite planes. Calculations are similar to the cone object, but taking into account the extra boundary plane. Figure 4.31 illustrates the method to define the intersection parameters d. Figure 4.17 is used to calculate the actual distances.

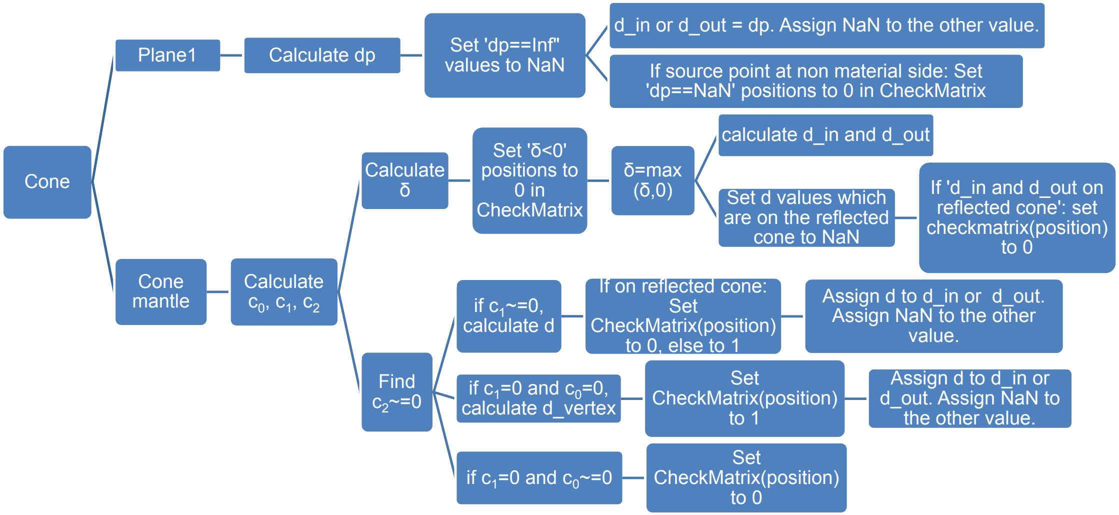

Figure 4.30: Method to calculate the penetration lengths in a truncated cylinder.

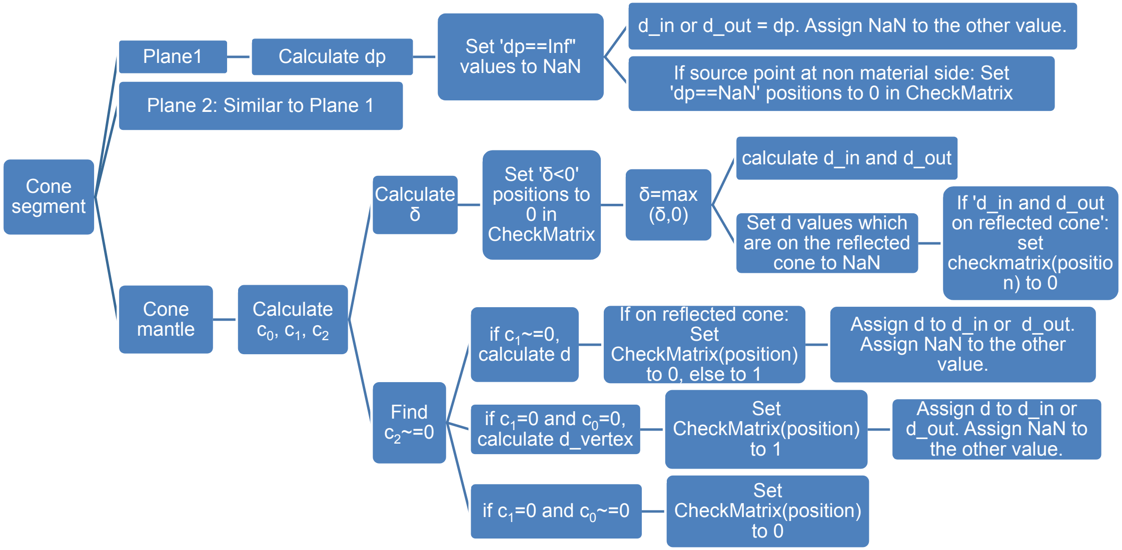

Figure 4.31: Method to calculate the penetration lengths in a truncated cylinder.

4.3.11 X-ray spectra

The part on X-ray spectra has been integrated in section 4.3.3.

4.3.12 Attenuation

Section 2.5.1 discussed the possible interactions with matter. The simulation program contains following possibilities:

- 'mac w coh' - returns total attenuation with coherent scattering in cm^2/g.
- 'mac wo coh' - returns total attenuation without coherent scattering in cm^2/g.
- 'coh scatter' - returns attenuation due to coherent scattering in cm^2/g, which is the difference between 'mac w coh' and 'mac wo coh'.
- 'incoh scatter' - returns attenuation due to incoherent scattering in cm^2/g.
- 'photoel abs' - returns attenuation due to photoelectric absorption in cm^2/g.

These options are based on tables available from the National Institute of Standards and Technology (NIST) databases. These tables are freely available on their website [96]. Use of these options requires to copy the table of a specific material composition from this website to the function 'ReadAttenuationNIST'. Additionally the density should be copied into the function 'ReadAttenuationNISTDensity'. The database allows calculating the attenuation of elements, compounds and mixtures. The user of the simulation program has to specify a name to the saved attenuation table and density. Subsequently addressing the specific name in the main program will automatically lead to accessing the appropriate density and attenuation table.

Besides these functions which require the user to copy paste attenuation tables one time per material composition, there is an extra automatic function 'mac'. This option is based on Matlab® code written by Jarek Tuszynski [105]. The function 'mac' will return the total attenuation with coherent scattering in cm^2/g, like the 'mac w coh' function. Attenuation can be requested for following options without extra input from the simulation program user:

- Element atomic number Z - in 1 to 100 range.

- Element symbols - 'Pb', 'Fe'.
- Element names - 'Lead', 'Iron', 'Cesium'.
- Some common names and full compound names - 'Water', 'Polyethylene'.
- Compound formulas - 'H_2SO_4', '$C_3H_7NO_2$'.
- Mixtures of any of above with fractions by weight - like 'H(0.057444)C(0.774589)O(0.167968)' for Bakelite or 'B(10)H(11)C(58)O(21)' for Borated Polyethylene (BPE-10).

Required input parameters

AttType Following options are possible: 'mac', 'coh scatter', 'incoh scatter', 'photoel abs', 'mac w coh', 'mac wo coh'. 'mac' is an automatic function. The other options require input of the user in the functions 'ReadAttenuationNIST' and 'ReadAttenuationNISTDensity'.

IncludeCompEdgeMaterial 0 or 1. In case of 1, the compton edges of the material are taken into account (to define extra sampling points on the spectrum).

4.3.13 Simulation examples

Figures 4.1 and 4.32 illustrates projection images obtained by the simulation program. Figure 4.1 presents a multi-material object. This object consists of ruby spheres and carbon fibre rods. Figure 5.2a is an example of an object which contains cylinders and cones. 4.32b at last is a research object ([70] and [69]) with parallel grooves, therefore simulated with cuboids.

4.4 Conclusion

This chapter has given a general overview of the simulation program which has been written in Matlab® environment. The used basic principles and main parameters have been discussed. Detailed information and further references are available in the source code. Simulation and experimental investigation will be carried out in parallel in chapter 5. The simulation software enables to verify or confirm observations made during the accuracy analysis of dimensional CT metrology. Many aspects have been implemented which were needed to support the experimental investigation in chapter 5. The user of the simulation program

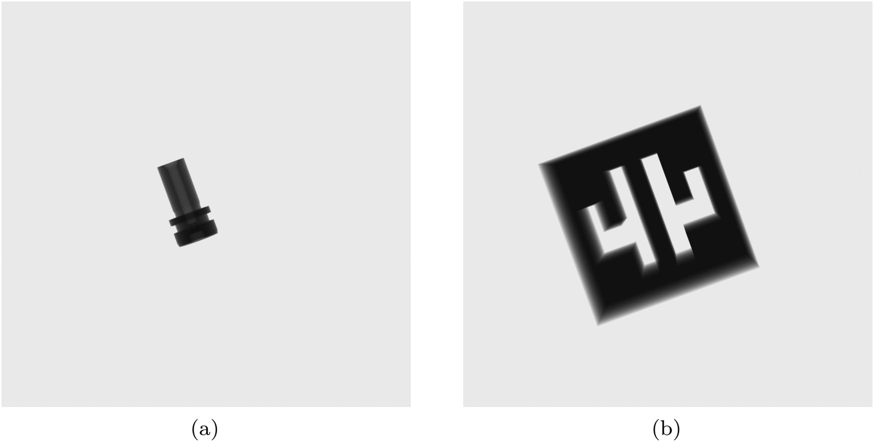
(a) (b)

Figure 4.32: Projection image of two simulated objects: an industrial object (a) of section 5.2 and a test object with parallel grooves for calibration and accuracy assessment of industrial CT metrology (b) along [70] and [69].

can easily adapt parts of the code for his own research. The fact that the code is available through Matlab® code, gives the user the possibility to know each single step. This simulation program has therefore different advantages over other (commercial) available simulation programs:

- The source code is available, making it possible to see all steps. In (commercial) available simulation programs many parts will have the principle of black boxes: one does not know the critical programming steps.
- The simulation program is flexible. The user can easily adapt or add code for his own research.
- Many options are already available. Some options are rarely available in other simulation programs or have even never been seen in other simulation programs. There is for instance no simulation program known which offers the possibility to calculate the projection images during continuous scanning.

Chapter 5

Calibrated objects

This chapter investigates the dimensional accuracy of an X-ray CT scanner. It aims to answer different questions:

- In which magnitude lays the accuracy of dimensional X-ray CT metrology?
- What is the effect of the different influence factors on the dimensional accuracy?
- How can the accuracy be improved?

This chapter uses calibrated objects to explore the dimensional accuracy. It hereby uses the simulation program and the other results of the previous chapters to perform an in-depth analysis. Section 5.2.2 starts with an example. It shows the difficulties in dimensional X-ray CT metrology. An object is scanned multiple times on the Nikon Metrology X TH 225 ST CT scanner and leads to different dimensional measurement results. Section 5.3 presents the results of a CT audit in which our group was one of the participants. This CT audit project was organized by the University of Padova [25], [23]. An intercomparison using 4 objects was carried out on 15 X-ray CT systems, from various laboratories in Europe, America and Asia. This nicely shows and compares the possibilities, accuracies and issues of dimensional X-ray CT metrology. Section 5.4 introduced an artifact with CMM ruby styli of different diameters. An extension of this object with new material (Si_3N_4 and ZrO_2) is presented in section 5.5. These sections (section 5.4 and 5.5) thoroughly inspect the dimensional X-ray CT accuracy of the Nikon Metrology X TH 450 CT scanner available at our facilities, it furthermore discusses the problems and improvements. At last a stepped cylinder object is introduced and investigated in section 5.6 using the Nikon Metrology XT H 450 CT scanner.

5.1 State of the art

At the start of this PhD thesis, little knowledge was available on the accuracy of dimensional X-ray CT metrology. There was a lack of available knowledge on the different influence factors related to dimensional X-ray CT metrology.

To determine the accuracy of an X-ray CT scanner, the necessity of reference objects arises. [73], [147], [148], [117], [76], [24], [90], [87], [14], [69], [70] and [45] propose different reference objects to access the accuracy of CT devices. Figure 5.1 gives an overview of currently used reference artifacts.

5.2 Problem description

This section illustrates the issues when performing dimensional X-ray CT metrology. An industrial object (figure 5.2) has been fabricated and different dimensions and tolerances need to be checked. This object was delivered by the company Maex Precision-Production nv [78] and used as a case study object in frame of the Tetra project 'Multi-sensor cöordinaten meettechniek voor snel en accuraat opmeten van complexe producten (MuSeS - 120167)' funded by 'Innovatie door Wetenschap en Technologie (IWT)'. Computed tomography has been applied for the dimensional quality control. The object has been scanned several times. Comparison of these results gives an idea of the correctness of the CT results, as the object did not change and the measurands should therefore be the same. A combination of the results furthermore leads to a value of the repeatability and reproducibility for the measurements of the measurands.

It has to be pointed out that there still can be remaining errors to the true value. A good repeatability or reproducibility does not necessarily mean an accurate measurement in terms of correctness of the measurement. This section aims to indicate whether a measurement will change due to different influences and what the measurement differences will be in case of repeating the same measurement multiple times. The measurement errors are however given with respect to the reference value measured by a more accurate measurement device. This way one also has an idea of the measurement error to the true value.

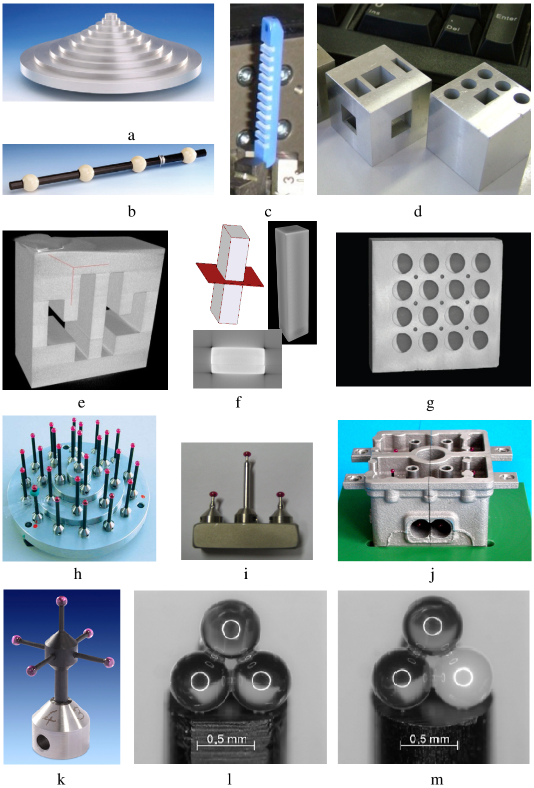

Figure 5.1: Possible reference objects to access the accuracy of CT metrology devices. [73]

5.2.1 Object description

The object has been produced by turning and electrical discharge machining. A reference value for each investigated dimension has been measured by means of a CMM. The measured CT values have always been compared to these CMM reference values, resulting in a measurement error (see equation 1.2). Table 5.1 denotes the measurands with the reference values. The reference values are achieved on the Mitutoyo FN905 CMM with a probing stylus with diameter $0.66mm$.

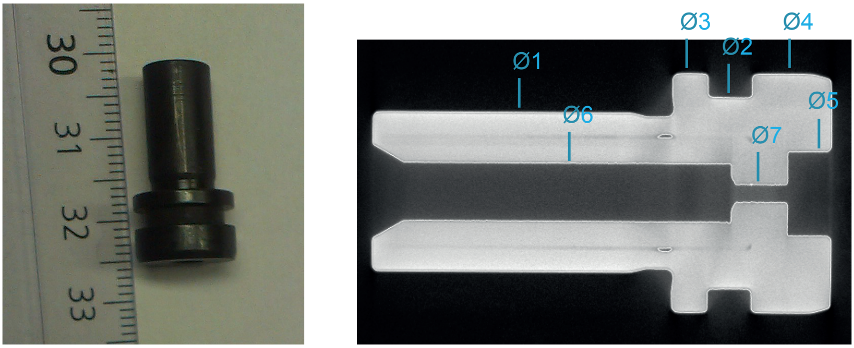

(a) (b)

Figure 5.2: Industrial object (a) and designation of the cylinders of this object (b). This object was delivered by the company Maex Precision-Production nv [78] and used as a case study object in frame of the Tetra project 'Multi-sensor cöordinaten meettechniek voor snel en accuraat opmeten van complexe producten (MuSeS - 120167)' funded by 'Innovatie door Wetenschap en Technologie (IWT)'.

	Reference value $[mm]$
Cylinder 1	7.993
Cylinder 2	9.583
Cylinder 3	11.991
Cylinder 4	11.986
Cylinder 5	4.227
Cylinder 6	2.920
Cylinder 7	0.910
Coaxiality 7 to 6	0.034

Table 5.1: Measurands of the industrial object: the measured reference value (by means of the Mitutoyo FN-905 tactile CMM with specification: $U1 = 4.2 + 5 * L/1000\mu m$).

5.2.2 CT measurements

Table 5.2 lists the CT acquisition parameters of the different measurements. Measurement 24 is performed on the Nikon Metrology XT H 450 CT scanner, the others were carried out on the Nikon Metrology XT H 225 ST CT scanner. The table presents the applied filter plate, source voltage and current, voxel size, measurement date and extra information.

Repeated measurements

As a first experiment 10 CT measurements have been repeated while keeping the conditions as similar as possible to fulfill the repeatability condition (section 1.5, definition 1.9). The settings can be found in table 5.2, measurements 1 to 10. These measurements have been carried out one after the other, without any change (the door of the CT device has not been opened and the machine has not been switched off or changed). The results are therefore a measure for the measurement repeatability of the investigated features. Figure 5.3 shows the results. The repeatability will be further discussed in a later section. The standard deviation obtained out of the measurements is between 1 and $3\mu m$.

There is a clear difference in errors for the inside (1-4) and outside (5-7) cylinder diameters. Beam hardening effects at the outside cylinders and a difference in air gray value for the outside/inside air (see figure 5.12) combined with the edge detection are possible reasons explaining this difference.

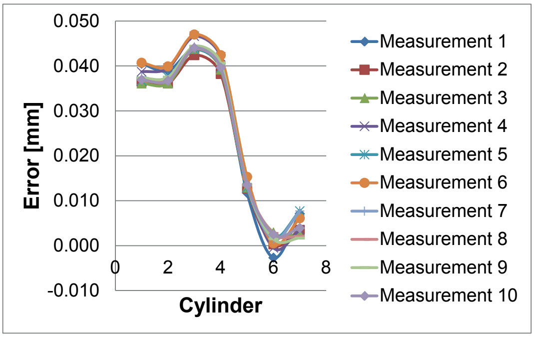

Figure 5.3: Deviations to the CMM reference cylinder diameters for repeated measurements.

Meas.	Filter	Voltage [kV]	Current [μA]	Voxel size [mm]	Date	Extra comment
1 to 10	Cu 2mm	210	290	0.019	January 6	
11	Cu 2mm	210	290	0.019	November 23	Repositioned
12	Cu 2mm	210	290	0.019	January 6	Repositioned
13	Cu 2mm	200	319	0.019	September 21	
14	Cu 1.5mm	210	225	0.019	September 21	
15	Cu 2.5mm	210	364	0.019	September 21	
16	Sn 1mm	210	459	0.019	September 21	
17	Cu 2mm	210	290	0.019	September 23	
18	Cu 2mm	210	290	0.026	September 23	
19	Cu 2mm	210	290	0.052	September 23	
20	Cu 2mm	210	290	0.069	September 23	
21	Cu 2mm	210	290	0.091	September 23	
22	Sn 0.25mm	220	400	0.015	November 8	Gain 18dB, other operator
23	Al 1mm	225	185	0.015	September 5	Gain 12dB
24	Cu 2mm	200	280	0.034	/	X TH 450 CT

Table 5.2: CT acquisition parameters for the different measurements of the industrial object.

Different days, object orientation

This section compares measurements 1, 11, 12 and 17 (table 5.2). These measurements use the same settings, but the date of measurement and the object orientation differ (figure 5.4). High differences between the measurements are observed ranging to $60\mu m$ (figure 5.5). It can be seen that the combination between measurement day and object orientation highly influenced the measurement result.

Afterwards alignment errors between source, rotation table and detector were diagnosed for this CT scanner. These alignment errors combined with different orientations of the object can explain the high differences between these measurements which have the same selected settings (except for object orientation). The influence of the object orientation/position with respect to the rotation table coordinate system will be further investigated in section 5.4.3, subsection 'object position'. Other important influencing factors explaining these errors are the rotation overshoot (rotation table turning too far) and start angle of the rotation table which will be discussed in section 5.4.3, subsections 'overshoot' and 'start angle'.

Different magnifications

Measurements 17 to 21 have been carried out one after each other, only varying the magnification position (figure 5.7). The other settings are kept the same, the door of the CT scanner has not been opened between the measurements. Figure 5.6 shows the results, there is clearly a big influence of the magnification position on the measurement results. Errors ranging to $20\mu m$ between the different magnification positions are observed. The largest magnifications (measurements 17 and 18) give the best results in this particular case. Furthermore a difference in errors for the inside (1-4) and outside (5-7) cylinder diameters is again visible.

Different filter plates and settings

Measurements 13 to 16 are also carried out one after each other. The rotation table and object stay in the same position but the filter plate and hence the acquisition settings (voltage and current) have been changed. Measurements 13 to 15 use copper filters of different thicknesses (2, 1.5 and $2.5mm$), whereas measurement 16 applies a tin filter of $1mm$. Different filter plates give clear differences up to values between 40 and $50\mu m$ (see figure 5.8). Measurement 16 (Sn filter) produces clearly worse results in this case. Regarding the

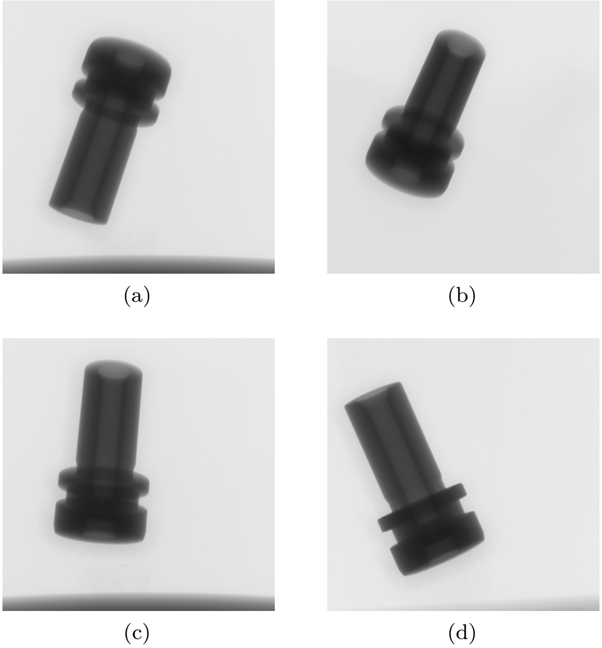

Figure 5.4: First projection image of measurements 1 (a), 11 (b), 12 (c) and 17 (d).

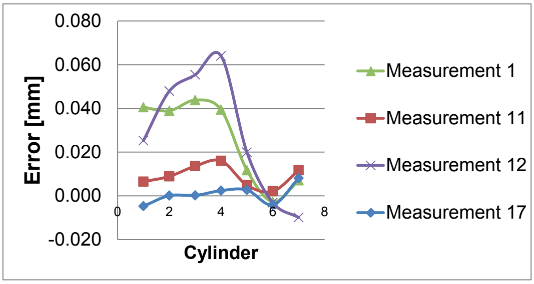

Figure 5.5: Deviations to the CMM reference cylinder diameters for similar measurements on different days and with different object orientation (see table 5.2).

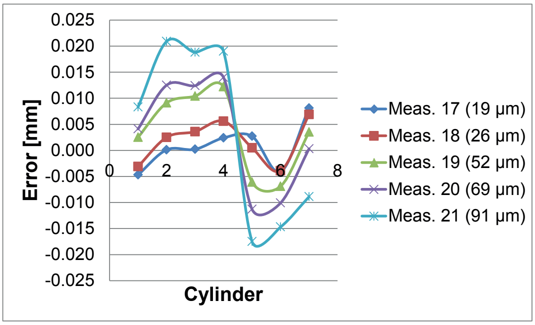

Figure 5.6: Deviations to the CMM reference cylinder diameters for measurements with the same settings but on different magnifications leading to different voxel sizes (noted between the brackets).

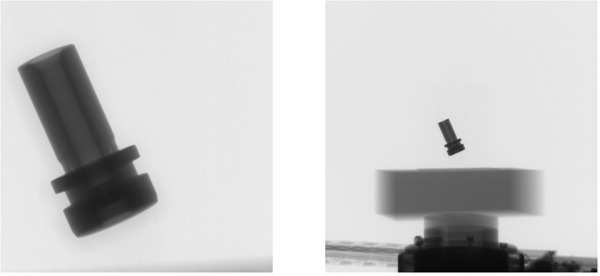

(a) (b)

Figure 5.7: First projection image of measurement 17 (a) and 21 (b).

measurements with the copper filter plate: measurement 13 and 14 are quite similar while measurement 15, which has the highest filter thickness, differs more. Different beam hardening effects, different contrasts between air and material combined with the edge detection are possible aspects explaining these differences.

Repeatability and reproducibility of the diameter measurements

Figure 5.10 gives an overview of all the CT measurements, furthermore a value for the repeatability limits (based on measurements 1 tot 10) and reproducibility limits (based on all measurements) have been calculated based on the standard deviation of these measurements using equations 5.1 and 5.2 to define the upper

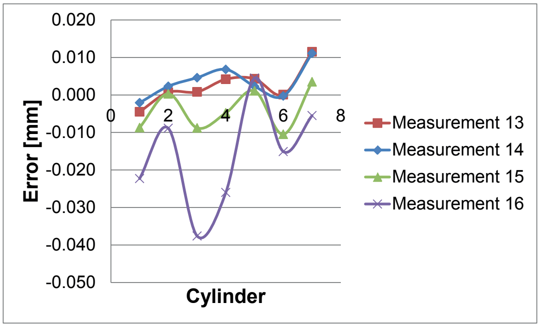

Figure 5.8: Deviations to the CMM reference cylinder diameters for measurements with different filter plates and acquisition settings.

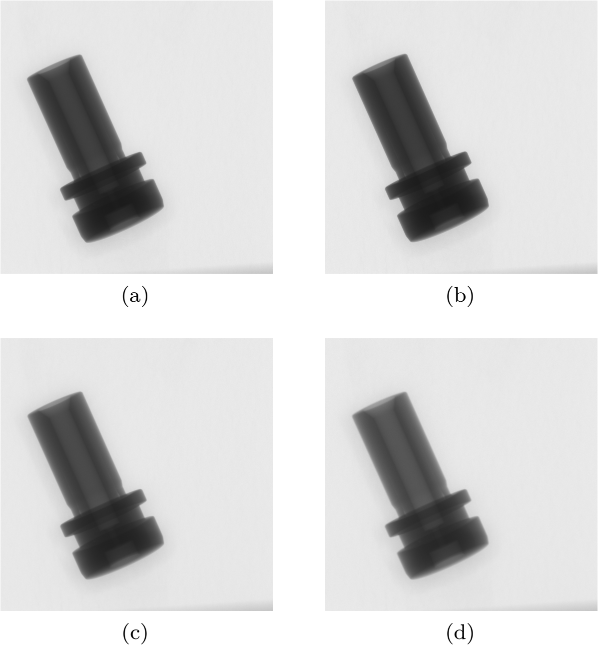

Figure 5.9: First projection image of measurement 13 (a), 14 (b), 15 (c) and 16 (d).

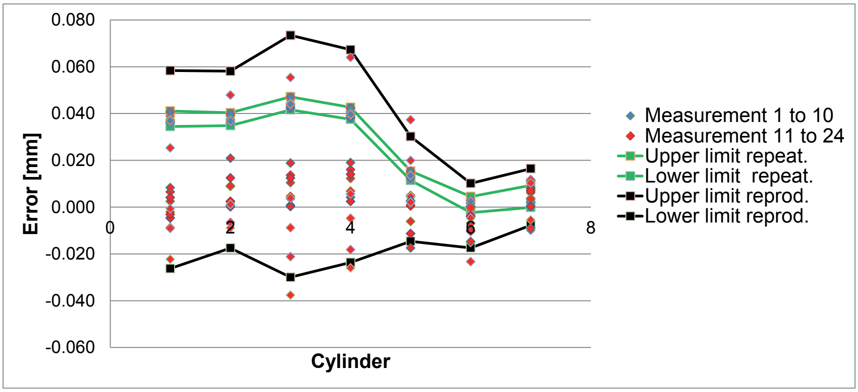

Figure 5.10: Summary of the diameters measurements of the industrial object, including limits for the repeatability and reproducibility.

and lower limits according to 95% confidence interval. The standard deviations obtained out of the measurements used for repeatability are between 1 and $3\mu m$. The standard deviations obtained out of the measurements used for reproducibility is between 6 and $26\mu m$. The upper and lower limits have been calculated as follows.

$$Upperlimit = \overline{x} + t \cdot s \tag{5.1}$$

$$Lowerlimit = \overline{x} - t \cdot s \tag{5.2}$$

where:

$\overline{x}$ = Estimated average value of the investigated measurements.
s = Estimated standard deviation of the investigated measurements.
t = Parameter of the student distribution. t=2.07 (9 degrees of freedom) in case of the repeatability measurements and t=2.26 in case of the reproducibility measurements (23 degrees of freedom).

There is a clear difference between inner (cylinders 1 to 4) and outer diameter (cylinders 5 to 7) evaluation. First of all is there an offset between the inner (errors between 0 and $20\mu m$) and outer diameters (errors around $40\mu m$) looking at the measurements used for the repeatability (measurements 1 to 10). Second, the reproducibility is much better for the inner diameters.

Coaxiality

The coaxiality from cylinder 7 to cylinder 6 is another investigated measurand. Figure 5.11 shows the obtained result concerning this measurand for different scans. The obtained eccentricities range from 31 to 43μm, which is outside the stated tolerance of 5μm (table 5.1), but is within the range of the CMM reference value (0.034μm). The standard deviation of these CT measurements (4μm) is much better compared to the results of the diameter measurements (see standard deviation obtained out of reproducibility measurements, figure 5.10). This measurand encounters less problems than a diameter measurement when using computed tomography.

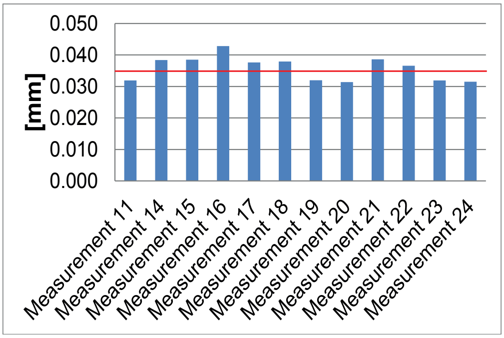

Figure 5.11: Measurements of the coaxiality eccentricity from cylinder 7 to reference cylinder 6. The red line pictures the CMM reference value.

Start contour

Figure 5.12 shows the voxel gray-value histogram for a scan of the object. Three peaks are distinguished: the air peak, the air inside the object, and a material peak. Figure 5.13 shows the errors on the diameters measured by the CMM (reference value) and by the CT scanner using advanced thresholding starting from start contour A, B and C (see section 2.6.2 for the explanation on thresholding). Start contours A, B and C are obtained by applying a global threshold gray values as chosen in figure 5.12.

As long as the search distance (search domain) is large enough one expects the start contour to have no influence, i.e. the resulting contour and dimensions should be similar independent of the start contour. The start contour however clearly influences the results. The start contour for advanced thresholding can lead to differences of 30μm and the influence differs for the different diameters.

Again the magnitude of the influence is different for inside (1-4) and outside (5-7) cylinder diameters. Beam hardening effects at the outside cylinders and a difference in air gray value for the outside/inside air (see figure 5.13) are possible explanations for these different effects.

it should be noted that start contour A, which moves the threshold value in air direction, logically gives lower values for the inner dimensions and higher values for the outer dimensions, see figure 2.27 which illustrates this effect.

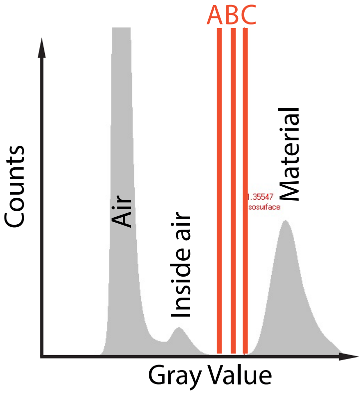

Figure 5.12: Gray-value histogram of the voxel model. Three different possible start contours are pictured. The abscissa denotes the gray value, where the ordinate represents the number of pixels having this gray value.

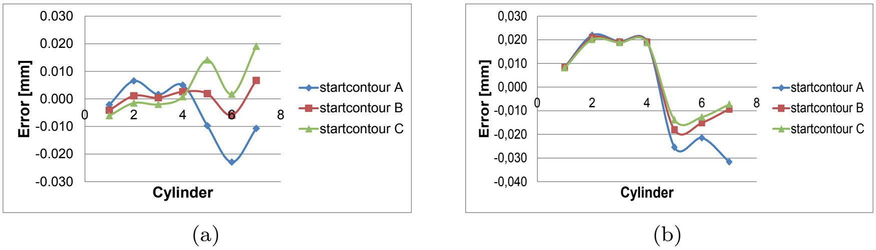

(a) (b)

Figure 5.13: Deviations to the CMM reference cylinder diameters for measurements with different start contour for advanced thresholding. The illustrated results are obtained from measurements 17 (a) ($2mm$ Cu filter, voxel size $19\mu m$) and 21 (b) ($2mm$ Cu filter, voxel size $91\mu m$).

5.2.3 Conclusion

This section illustrates the difficulties in X-ray CT metrology. CT scans of the same object lead to different measurement results of the same measurands. The measurements were carried out on a Nikon Metrology XT H 225 ST CT scanner. Different parameters were varied resulting in different diameter measurements of the same cylinders. Similar scans on different days, and using different object orientation leads to differences ranging to $60 \mu m$. Varying the magnification position gives errors ranging to $20 \mu m$. Changing the filter plate and voltage/current settings results in difference between 40 and $50 \mu m$. These values were combined to estimate the repeatability and reproducibility of the diameter measurements. The obtained standard deviations where between 1 and $3 \mu m$ for the repeatability and between 6 and $26 \mu m$ for the reproducibility. At last the influence of the start contour for advanced thresholding was examined. It leads to differences of up to $30 \mu m$ for the small inner cylinder of diameter $0.9 mm$ and differences of $5 \mu m$ for the outer cylinder of diameter $8 mm$, these differences furthermore change for the different diameters.

5.3 CT audit

This section presents the results of a CT audit, organized by the University of Padova, in which our group was one of the participants. This CT audit enabled to explore the possibilities and to compare the achievable accuracies in dimensional X-ray CT metrology between different experts in the field. A description of the CT audit project organized by the University of Padova (under supervision of Simone Carmignato, Anna Pierobon and Enrico Savio) can be found in [25]: '*The CT Audit project is the first international interlaboratory comparison of CT systems for dimensional metrology. It was organized by University of Padova and carried out in the period from September 2009 to June 2011. The intercomparison involved 15 CT systems, from various laboratories in Europe, America and Asia, which were selected among the most experienced users of CT systems for dimensional metrology, and including national metrology institutes, research institutes, CT systems manufacturers, and industrial users. The project was based on the circulation of four calibrated samples that were sent from one Participant to the next one, in a sequential participation scheme, together with detailed measurement procedures and reporting instructions. The circulation phase started in March 2010 and ended in March 2011. At the end of the circulation, the measurement results collected from the Participants were analyzed and summarized in the final report, which compares anonymously the CT measurement results and their uncertainties. The confidentiality of results* *of single Participants was ensured by the project coordinator through association of an anonymous identification code to the results of each Participant. The four calibrated samples were chosen in order to represent a variety of dimensions, geometries and materials; they were designed and manufactured suitably for testing several measurement characteristics on different CT systems. They were protected in thin plastic sealed boxes for reducing the risk of damages, limiting contamination and avoiding measurements with other sensors. During the entire circulation, no damages were reported to the samples, the big interest and motivation of the Participants being the main reason for this. The dimensional stability of the four items was verified by CMMs calibrations before and after the circulation, showing deviations below the calibration uncertainty for all relevant characteristics, with the only exception of the ballplate inside Item 4. For this reason it was decided to exclude the ball-plate's spheres distances from the results of the CT Audit intercomparison.'*

5.3.1 Object description

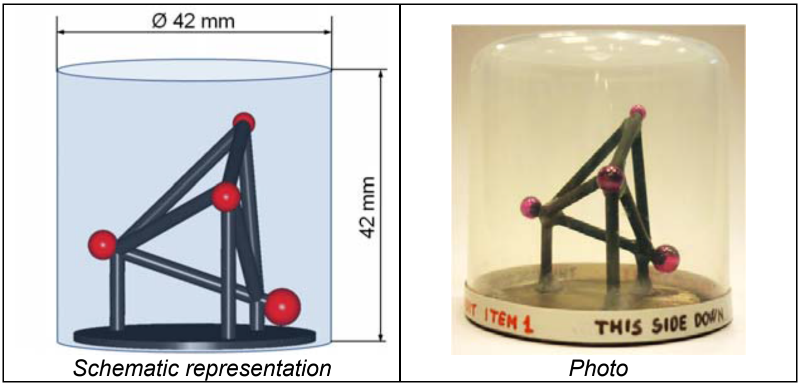

Figure 5.14: Item 1 enclosed in its sealed cylindrical box. [25]

A detailed description of the different objects and the measurement procedure can be found in the CT audit report [25]. Only a small overview of this description is given here. Additional to the values of the measurement results, the participants were required to specify the uncertainties.

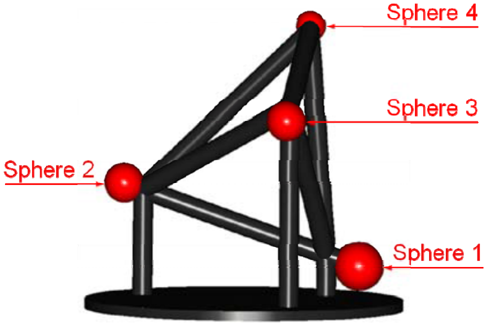

Sphere Nr.	*Nominal diameter*
Sphere 1	*5 mm*
Sphere 2	*4 mm*
Sphere 3	*4 mm*
Sphere 4	*3 mm*

Figure 5.15: Designation of the four spheres of item 1. [25]

Item 1

Figure 5.14 shows the first item, the 'CT tetrahedron' which is property of the University of Padova, Italy. This item consists of four ruby spheres supported by a carbon fibre frame. Figure 5.15 enumerates the different spheres and lists the nominal diameters. The carbon fibre bars have a diameter of $2mm$. The item is put in a sealed cylindrical box made of polyethylene and having a wall thickness of $0.8mm$. Details on the materials characteristics are denoted in table 5.3.

	Material	$\rho[g/cm^3]$	$CTE[K^{-1}]$
Spheres	Synth. ruby monocrystal (Al_2O_3)	3.99	$(5.4 \pm 0.5) \times 10^{-6}$
Frame	Carbon fibre rods (unidirect.)	1.50	$(0.0 \pm 0.5) \times 10^{-6}$
Sealed box	Polyethylene (HDPE)	0.95	Not relevant

Table 5.3: Materials characteristics of item 1.

A reference coordinate system is defined by firstly taking the center of sphere 1, as origin. The vector from sphere center 1 to sphere center 2 defines the x-axis. The plane through the centers of spheres 1, 2 and 3 is chosen as the xy plane, resulting in a y-axis perpendicular to the x-axis and its direction such that the y-coordinate of the center of sphere 3 is positive. The z-axis is now defined taking into account a right-handed cartesian coordinate system. This results in the sphere coordinates of table 5.4. The required measurement results were the diameters, form errors and coordinates of the four sphere centers.

	Coordinates of spheres centers		
	X	Y	Z
Sphere 1	$x_1 = 0$	$y_1 = 0$	$z_1 = 0$
Sphere 2	x_2	$y_2 = 0$	$z_2 = 0$
Sphere 3	x_3	y_3	$z_3 = 0$
Sphere 4	x_4	y_4	z_4

Table 5.4: Coordinates of spheres centers according to the reference coordinate system.

Item 2

The second item of the CT audit is a 'Pan Flute Gauge', also property of the University of Padova, Italy. This item (figures 5.16 and 5.17) is constructed of five glass tubes supported by a carbon fibre frame. The five tubes are numbered in figure 5.18 which also shows their lengths. The nominal inner diameters are $1.5mm$ and the nominal outer diameters are $1.9mm$. This item is again sealed with a cylindrical box of polyethylene with wall thickness $0.8mm$. Table 5.5 depicts the material characteristics. It was requested to measure all tube diameters (inner and outer) and the tube lengths.

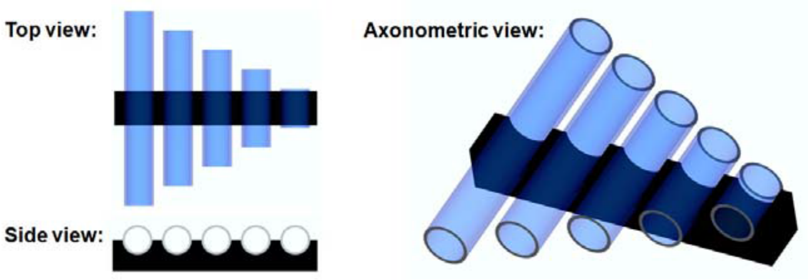

Figure 5.16: Schematic representation of item 2. [25]

	Material	$\rho[g/cm^3]$	$CTE[K^{-1}]$
Tubes	Borosilicate glass	3.99	$(5.5 \pm 0.5) \times 10^{-6}$
Frame	Carbon fibre rods (unidirect.)	1.50	$(0.0 \pm 0.5) \times 10^{-6}$
Sealed box	Polyethylene (HDPE)	0.95	Not relevant

Table 5.5: Materials characteristics of item 2.

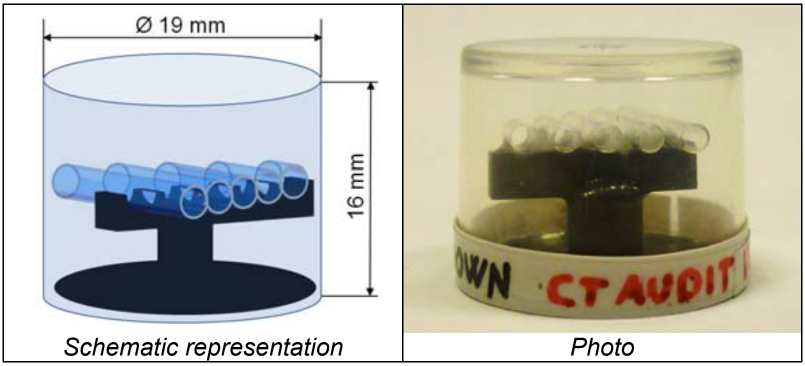

Schematic representation

Photo

Figure 5.17: Item 2 enclosed in its sealed cylindrical box. [25]

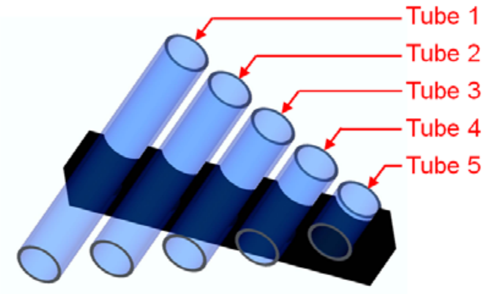

Tube Nr.	*Nominal length*
Tube 1	*12.5 mm*
Tube 2	*10.0 mm*
Tube 3	*7.5 mm*
Tube 4	*5.0 mm*
Tube 5	*2.5 mm*

Figure 5.18: Designation of the five tubes of item 2. [25]

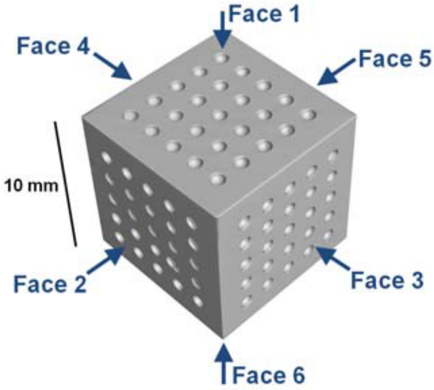

Figure 5.19: Calotte cube with indication of the six faces names. Faces 1, 2 and 3 are visible in this picture. [25]

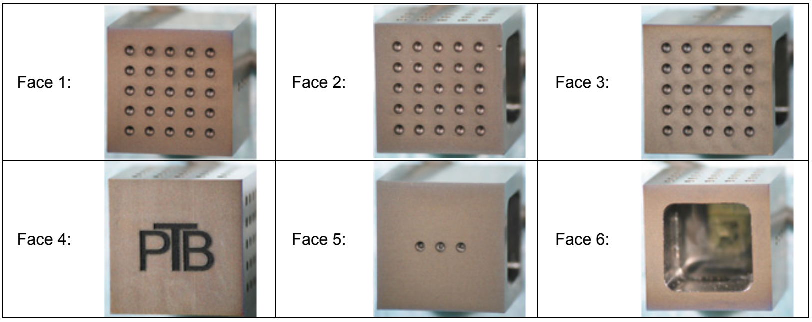

Figure 5.20: Views of the six faces of the calotte cube. [25]

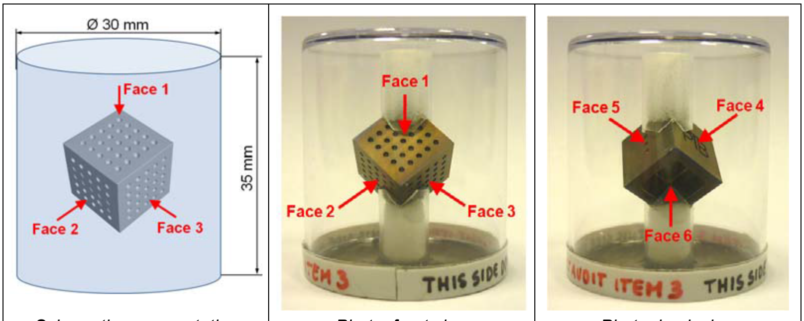

Schematic representation *Photo, front view* *Photo, back view*

Figure 5.21: Item 3 enclosed in its sealed cylindrical box. [25]

Item 3

Item 3, the 'Calotte Cube', is property of Physikalisch-Technische Bundesanstalt (PTB), Germany. It is a hollow titanium cube, with 75 spherical calottes on three sides of the cube and nominal edge length $10mm$ (figures 5.19, 5.20 and 5.21). Face 6 of figure 5.20 shows a deep stepped cavity with nominal depth $8.5mm$ and front length and with equal to $7mm$. The item is again sealed within a cylindrical box with wall thickness $0.8mm$. Inside this box the object is supported by two cylindrical polyethylene tubes. Material characteristics are available in table 5.6.

Figure 5.22 shows the reference coordinate system. The origin is in the center of calotte 111. The x-axis is defined by the vector from the center of calotte 111 to the center of calotte 151. Subsequently the xy-plane is defined by the centers of calottes 111, 151 and 115. This results in the y-axis, perpendicular to the

	Material	$\rho[g/cm^3]$	$CTE[K^{-1}]$
Calotte cube	Titanium alloy (Ti6Al4V)	4.43	$(8.6 \pm 0.5) \times 10^{-6}$
Base	Carbon fibre sheet (bidirect.)	1.50	Not relevant
Sealed box	Polyethylene (HDPE)	0.95	Not relevant

Table 5.6: Materials characteristics of item 3.

x-axis, directed such that the y-coordinate of the center of calotte 115 has a positive value. The required measurements are the diameters, form errors and center coordinates of the 75 calottes and furthermore the distances between ten calotte center couples (115-151, 131-135, 133-233, 135-335, 145-214, 213-253, 231-235, 245-341, 251-355 and 315-351).

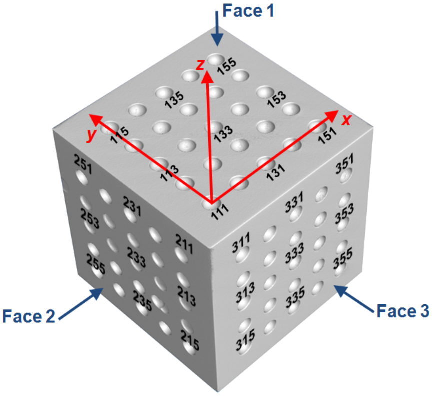

Figure 5.22: Definition of reference coordinate system and designation of calottes numbers. [25]

	Coordinates of calottes centers		
	X	Y	Z
Calotte 111	$x_{111} = 0$	$y_{111} = 0$	$z_{111} = 0$
Calotte 151	x_{151}	$y_{151} = 0$	$z_{151} = 0$
Calotte 115	x_{115}	y_{115}	$z_{115} = 0$
Calotte IJK	x_{IJK}	y_{IJK}	z_{IJK}

Table 5.7: Coordinates of calottes centers.

Item 4

The fourth item is the QFM Cylinder (figures 5.23, 5.24 and 5.25), which is developed by the University of Erlangen-Nuremberg - Chair Quality Management and Manufacturing Metrology (QFM), Germany. It consists of a hollow titanium cylinder with a nominal height of $80mm$, nominal outer diameter of $50mm$ and inner diameter of $40mm$. It contains 28 calotte spheres embodied on top and bottom and 14 calotte spheres located on the cylinder barrel. There are furthermore two symmetrical breakouts containing several micro structures: micro spikes in different sizes and micro cylinders of radii 0.2 to $1.3mm$. A ball plate carrying five sapphire spheres with nominal diameters $4mm$ is clamped inside the cylinder. Their distances range from 17 to $42mm$. This item is sealed with a cylindrical box made of polypropylene with a wall thickness of $5mm$ at the top and bottom and $1mm$ in the middle, i.e. where the artifact is located. Table 5.8 indicates the material characteristics for this item. The needed measurements are the outer and inner diameter of the titanium cylinder. Furthermore the diameters of the calotte spheres on top and bottom faces of the cylinder pictured in figure 5.24. Also the spheres distances of the ball plate were requested (5.24). At last the diameter of the smallest measurable cylindrical micro structure was asked.

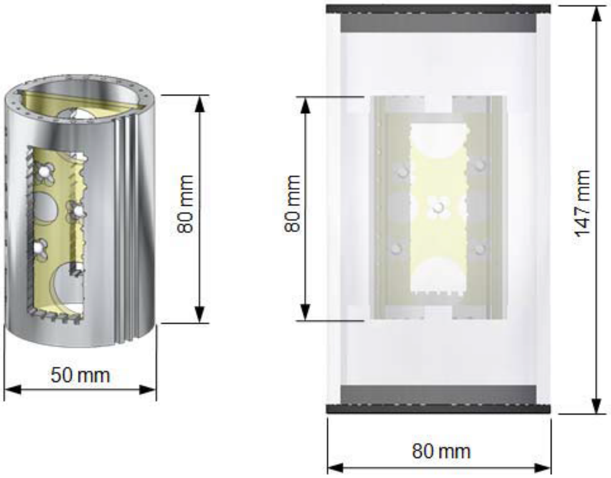

Figure 5.23: Item 4 (without protective sealed box). [25]

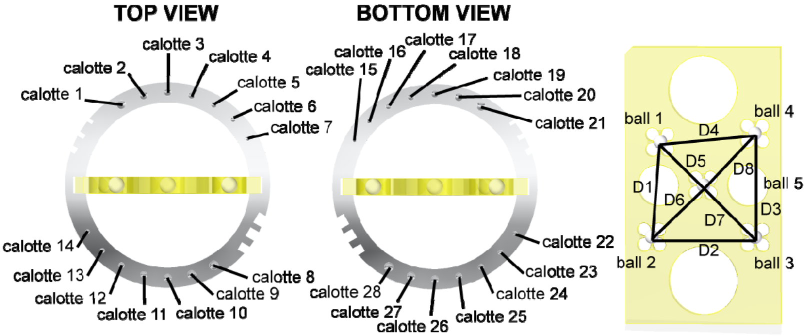

Figure 5.24: Identification of calotte spheres, balls and distances.[25]

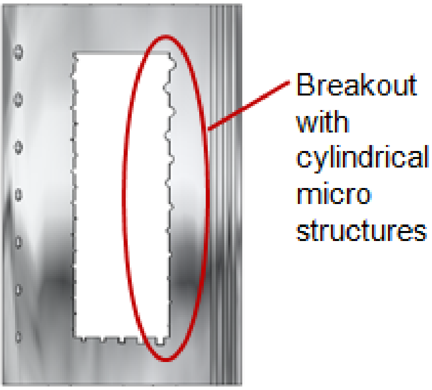

Figure 5.25: Location of breakout with cylindrical micro structures. [25]

	Material	$\rho[g/cm^3]$	$CTE[K^{-1}]$
Cylinder	Titanium grade 4	4.51	$(9.2 \pm 0.5) \times 10^{-6}$
Plate	Epoxy resin	1.1	$(69.5 \pm 1.5) \times 10^{-6}$
Balls	Sapphire	3.98	$(8.4 \pm 0.5) \times 10^{-6}$
Sealed box	Polypropylene	0.855 – 0.946	Not relevant

Table 5.8: Materials characteristics of item 4.

5.3.2 Uncertainty calculation

Additional to the measured values it was asked to specify the uncertainties on the measurements. Suggested methods were:

- U_A) Uncertainty budget through analytical calculation of uncertainty contributors.
- U_B) Evaluation based on the use of similar calibrated items and substitution method.
- U_C) Evaluation based on the experience of the Participant on similar measurement tasks.
- U_D) Evaluation based on measuring performance specification stated by the CT system manufacturer.

This uncertainty had to be expressed with a confidence level of 95% (expanded uncertainty statement).

In our case a combination of these methods is used. An analytical formula has been defined (U_A), using input from similar calibrated objects (U_B) and experience of the user (U_C).

Determination of the measurement uncertainty is not straightforward, as will appear during the discussion of the results (section 5.3.3). The measurement uncertainty is dependent on different parameters. A short overview of the main parameters:

- Measured feature.
- Object material.
- Orientation of the object.
- Type of measurand: edge dependent or edge independent.
- Rescaling.
- Used magnification.

The influence of these parameters is different for each measurement: measurement uncertainties are therefore task-specific. We categorized the measurands in three groups to facilitate the determination of the measurement uncertainties. An analytical expression is obtained for each group to specify the measurement uncertainty. The three groups are:

- Measurands which are independent of the selected edge: e.g. distances between sphere centers.
- Measurands dependent of the selected edge.
- Form error measurements.

Formulas to define the combined measurement uncertainty for each group will now be described. Hereafter the parameters in this formula will be discussed.

Combined uncertainties

Combined standard uncertainty for edge independent values. Following uncertainties contribute to the combined standard uncertainty for edge independent values:

- Uncertainties revealed by a reproducibility test: u_{rep}.
- Uncertainties due to rescaling: u_{res}.
- Other uncertainties, which are not included in the previous categories: u_{oth}.

This results in a combined standard uncertainty:

$$u_{cei} = \sqrt{u_{rep}^2 + u_{res}^2 + u_{oth}^2} \tag{5.3}$$

Combined standard uncertainty for edge dependent values. Following uncertainties contribute to the combined standard uncertainty for edge dependent values:

- Uncertainties revealed by a reproducibility test: u_{rep}.
- Uncertainties due to rescaling: u_{res}.
- Uncertainty due to edge correction : u_{edg}.
- Other uncertainties, which are not included in the previous categories: u_{oth}.

This results in a combined standard uncertainty:

$$u_{ced} = \sqrt{u_{rep}^2 + u_{res}^2 + u_{edg}^2 + u_{oth}^2} \tag{5.4}$$

Combined standard uncertainty for form deviations. These are special cases and are therefore determined by expert knowledge. For instance by taking the measured value as uncertainty value: The ruby spheres of item 1 are known to have submicrometer accuracy concerning the form deviation. The measurement uncertainty on a measured form error of $15\mu m$ is therefore taken as $15\mu m$.

Quantification of uncertainty parameters

Reproducibility value u_{rep}. A description of the meaning of reproducibility can be found in definitions 1.8, 1.10 and 1.11 in chapter 1. This value has been determined in different ways for the different items. Possibilities to define this value are:

- From the actual measurement part. This method is very interesting because it allows for reliable task specific measurement uncertainties. Unfortunately this method is very time consuming and therefore not always feasible in practice. During these reproducibility tests all influencing measurement conditions should be varied within reasonable limits.
- From similar parts. This method is also reliable if one can ensure that the results for similar measurements are representative for the actual measurements. The more similar the measurement task, the more reliable the uncertainty estimates, but the more effort it will cost.
- Based on expert knowledge. If no reproducibility data can be calculated u_{rep} should be taken zero and uncertainties determined by expert knowledge should be included in u_{oth}.

Standard uncertainty due to rescaling with a reference length: u_{res}. Two factors contribute to this uncertainty: the uncertainty of the reference measurement on the rescaling object and the uncertainty on the CT measurement (u_{ct-res}) of the rescaling object.

The reference measurement is carried out on the Mitutoyo FN-905 CMM with a specification as defined in equation 5.5. This value is an MPE value. Such a value results in a rectangular distribution with associated variance as described in equation 5.6.

$$U1 = (4.2 + 5L * 10^{-3})\mu m \tag{5.5}$$

$$u^2 = \frac{a^2}{3} \tag{5.6}$$

where:

$a =$ The range of variability.
$L =$ Measured length $[mm]$.

This leads to formula 5.7 for the standard uncertainty due to rescaling with reference length L_{ref}.

$$u_{res} = \sqrt{(\frac{4.2 + 5L_{ref} * 10^{-3}}{\sqrt{3}})^2 + u_{ct-res}^2} * \frac{S}{L_{ref}} \tag{5.7}$$

where:

L_{ref} = Measured reference length $[mm]$.
S = Measured value $[mm]$.

The term u_{ct-res} can be omitted if the reference artifact for rescaling is remeasured during the reproducibility test.

Standard uncertainty due to edge correction with a reference length: u_{edg}. Here again two uncertainty contributors can be defined: the uncertainty on the reference measurement of the calibration artifact and the uncertainty on the CT measurement of the reference $(ct - edg)$ artifact. The reference measurement is again performed using the Mitutoyo FN-905 CMM with a specification as defined in equation 5.5. This leads to equation 5.8 for u_{edg}:

$$u_{edg} = \sqrt{(\frac{4.2 + 5D_{ref} * 10^{-3}}{\sqrt{3}})^2 + u_{ct-edg}^2} * \frac{S}{D_{ref}} \tag{5.8}$$

where:

D_{ref} = Measured reference value $[mm]$.

Other uncertainties, not included in the previous categories: u_{oth}. Uncertainties which are not included in the standard uncertainties from the reproducibility test, rescaling or edge correction could be included in this term. It can include random and systematic components. This term is determined by expert knowledge.

Expanded uncertainties

The expanded uncertainties are determined by multiplying the standard uncertainty by a coverage factor $k = 2$ for a confidence level of 95%.

$$U = k \times u \tag{5.9}$$

Special issues

- Some calculated uncertainties have been adapted based on available knowledge. Take for instance the coordinates of sphere 1 from item 1. The center of sphere 1 is defined as the origin (see table 5.4), hence the center coordinates have zero uncertainty.
- Care has been taken considering the resulting values for expanded uncertainty. The real value should always be included in the uncertainty interval. If certain cases interval determination based on expert knowledge was selected to cover insufficiently studied influence factors, enlarging the uncertainty interval.

5.3.3 CT measurements

This section summarizes the results of the different participants [25] and focuses on our results (participant 6). Our measurements were carried out on the Nikon Metrology XT H 225 CT scanner which we could access at the Nikon Metrology facilities. The represented graphs are obtained from the CT audit report [25]. The error bars represent the expanded uncertainty as stated by the participants. The two horizontal red dashed lines ('Max. Ref. Unc.') show the expanded calibration uncertainty of the reference values as stated by the organizer [25]. In case different reference values in one figure have different uncertainties, then the red dashed lines are placed in correspondence of the maximum uncertainty of the reference values. Participants 13 and 14 did not give any values for the expanded uncertainty. Table 5.9 lists the applied voxel sizes. Data correction has been applied by us for all 4 items: all items have been rescaled (equation 2.8) and edge correction (equation 2.9) is applied for items 1 to 3.

Item 1

Two correction have been performed during our evaluation to obtain the requested dimensions. A calibration object consisting of 2 ruby spheres is scanned together with item 1. The distance between the sphere centers is used to correct for the voxel size. The diameter of the spheres is applied to calculate the edge offset.

Figure 5.26 illustrates the diameters measurements of item 1. Different participants have large deviations to the reference value. Furthermore it is clear that the specified uncertainty ranges are quite different (participants 12, 13 and 14 did not give an uncertainty value). Participant 9 gives quite large uncertainty

Participant Nr.	Voxel size [μm]			
	Item 1	Item 2	Item 3	Item 4
1	20.1	10.1	9.7	53.1
2	40.0	10.0	10.0	60.0
3	47.0	30.0	30.9	95.0
4	27.5	10.3	14.0	67.4
5	42.0	63.0	33.0	108.0
6	37.8	19.4	29.5	64.2
7	44.2	24.8	24.8	/
8	49.9	25.0	25.0	/
9	49.5	15.7	25.4	57.3
10	45.5	16.5	25.6	/
11	50.9	9.3	/	/
12	50.0	50.0	/	65.0
13	16.6	9.3	15.1	/
14	20.3	10.0	10.0	/
15	54.0	16.0	/	/
Average	39.7	21.3	21.1	71.3

Table 5.9: Voxel sizes of the CT measurements.

intervals, which leads to the fact that the reference value (zero deviation) is included, even though the deviations are quite large (between 50 and $100\mu m$). Other participants have relatively small deviations but do not manage to have the reference value in their uncertainty interval (e.g. participant 1, participant 11 sphere 2). It is clear that a correct uncertainty determination is a big issue: it should not be too large (an overestimation), but it should contain the real value.

Our results show deviations between -1.1 and $1.3\mu m$. The reference value was clearly situated in the uncertainty zone.

Figure 5.27 quantifies the form errors. Many participants have high deviations and the reference value often is not included in their uncertainty interval. It is clear that the uncertainty interval is generally heavily underestimated. Participant 8 seems to have the best determination of the form deviation. They always specify values around $2\mu m$ which is close to the reference value.

Our form error is stated around $14\mu m$ for each sphere. The form deviation for a ruby sphere is known to be quite accurate, it has sub micrometer accuracy which can also be seen from the reference value of the form deviation given by the organizer. We therefore took the measurement uncertainty equal to the measured form error. This is clearly visible in the picture: the edge of our uncertainty interval is at the zero deviation point. We could also have subtracted the difference between the CT measured form deviation of the calibration artifacts sphere and its reference value from the measured form deviations. Participant 8 probably applied such a strategy.

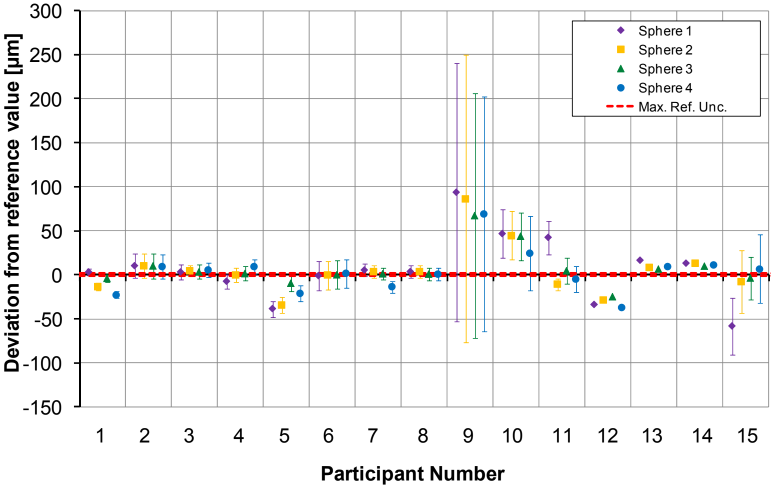

Figure 5.26: Comparison of diameter measurement results of all participants for item 1. [25]

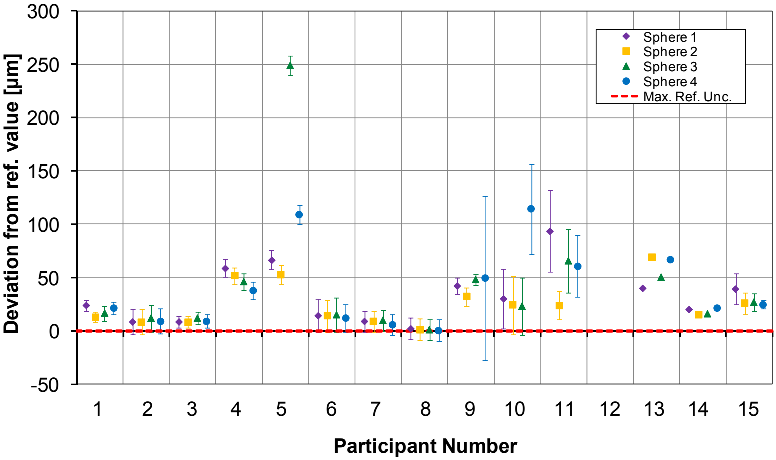

Figure 5.27: Comparison of form error measurement results of all participants for item 1. [25]

Figure 5.28 defines the sphere distance values. Again the reference value is not included in the uncertainty range of many participants, even when the deviations are quite small (e.g. participant 8). This again illustrates the problem of a good uncertainty determination.

In our case, all reference values are situated in the uncertainty interval, but it is clear that all our measured distances are too small (errors between -6 and $-9\mu m$). This indicates that, even though we rescaled our voxel model, still scaling errors remain.

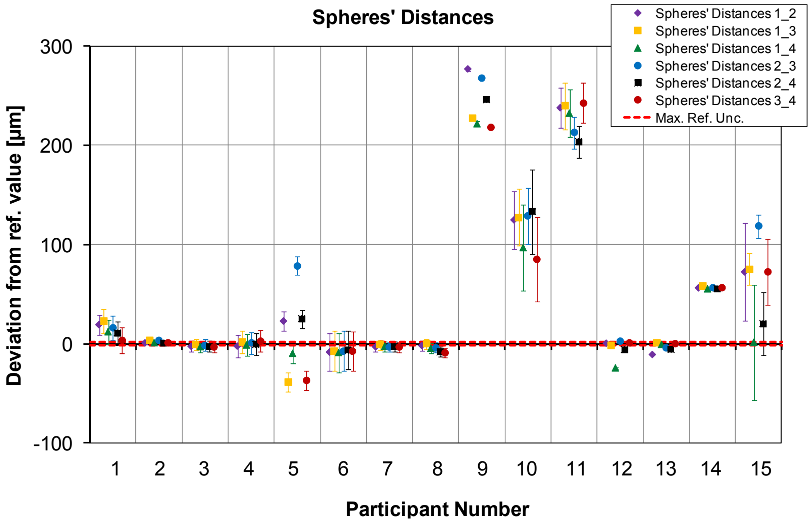

Figure 5.28: Comparison of spheres' distance measurement results of all participants for item 1. [25]

Item 2

The processing of the data from item 2 was done in two rounds. The organizers of the CT audit sent all the reference values of the inner and outer diameters of item 2 to all participants after the first round. The participants could reconsider their measured tube lengths with this new knowledge in the second round.

First we have a look at the corrections performed to our measurements in the first round. A glass tube is this time used for the edge correction. Regarding the rescaling of the voxel sizes 2 objects have been used: the glass tube (using the average of the inner and outer diameter as reference dimension) and the spheres calibration object (using the sphere distance as reference length). Correction by these two objects lead to different results. Therefore a combination of these results has been used.

After the first round, the reference values of the inner and outer diameters of item 2 were sent to us by the organizers and analyzed. In our case the conclusion was mainly that rescaling using the sphere distance gave better results. Therefore this time only this item was used for rescaling; the edge offset correction was again performed with the glass tube. Probably the difference in edge offset for inner and outer diameters deteriorated the results when using the average diameter of the glass tube to calculate the rescaling factor.

Figures 5.29 and 5.30 give the results for the outer and inner diameters. An interesting fact is that the outer diameters are almost always measured too large and the inner diameters are always measured too small.

Our errors were around $-5\mu m$ for the inner diameters and between -1 and $6.2\mu m$ for the outer diameters.

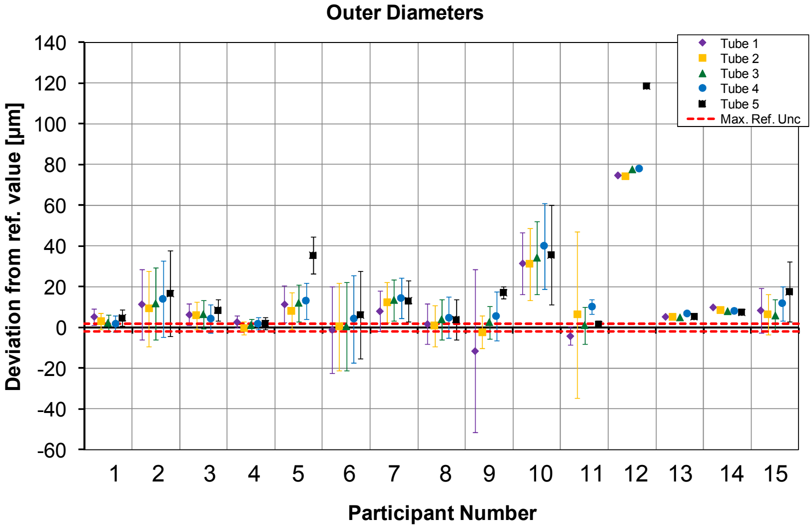

Figure 5.29: Comparison of outer diameters measurement results of all participants for item 2. [25]

Figure 5.31 shows the measured tube lengths. Figure 5.32 repeats this figure for the participants which changed their measured values after receiving the inner and outer reference diameters. Figure 5.33 gives the updated values for these participants. Most of the participants obtained improvements of their values.

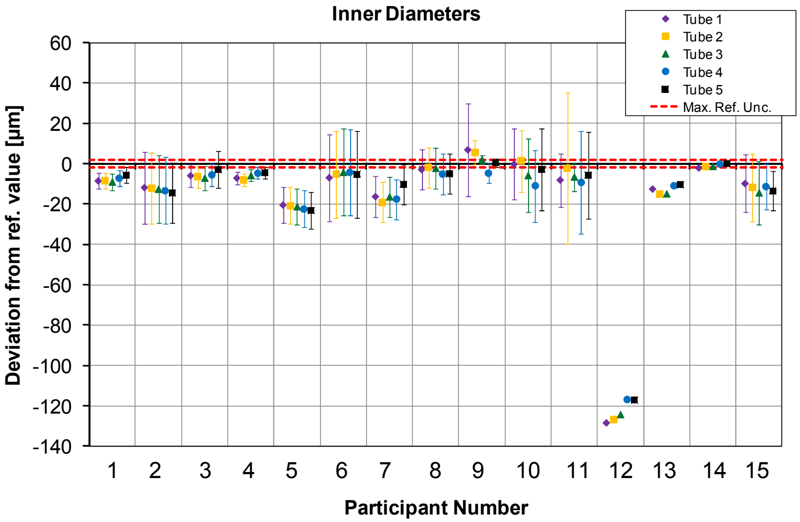

Figure 5.30: Comparison of inner diameters measurement results of all participants for item 2. [25]

In our case the error values were first situated between 4.1 and 7.7μm, whereas the values are now between -1.1 and $-1.5\mu m$ for tubes 1 to 4. Only tube 5 has a bit a different error i.e. 3.8μm.

Many choices have to be made during the reconstruction, e.g. beam hardening correction (BHC) preset number 2 (table 2.1) was used to reconstruct this object. Furthermore the reconstruction algorithm, all user defined decisions like the applied BHC preset, threshold determination and feature recognition will affect the result. The simulation program was used to check the influence of these aspects on the measurement results. The object was simulated with the nominal values and reconstructed using the settings as were used for the real measurement. Table 5.10 shows the results. The reconstruction, applied user settings, threshold determination and feature recognition on its own lead to errors of 6μm. It is furthermore clear an offset error with different sign is obtained for the inner and outer diameters. The inner diameters are thus appearing too small, the outer too large.

Item 3

Item 3 is again rescaled using the reference object consisting of 2 ruby spheres. A calibration object made in the same material (Ti6Al4V) as item 3 with 2

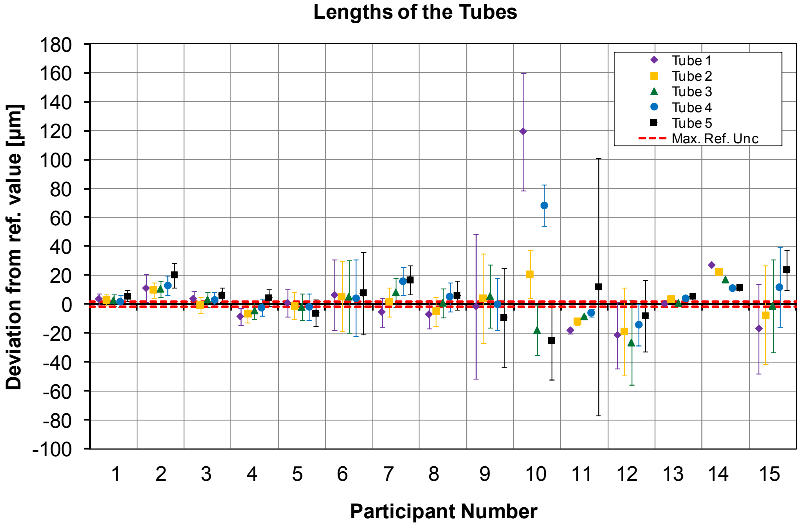

Figure 5.31: Comparison of tube length measurement results of all participants for item 2. [25]

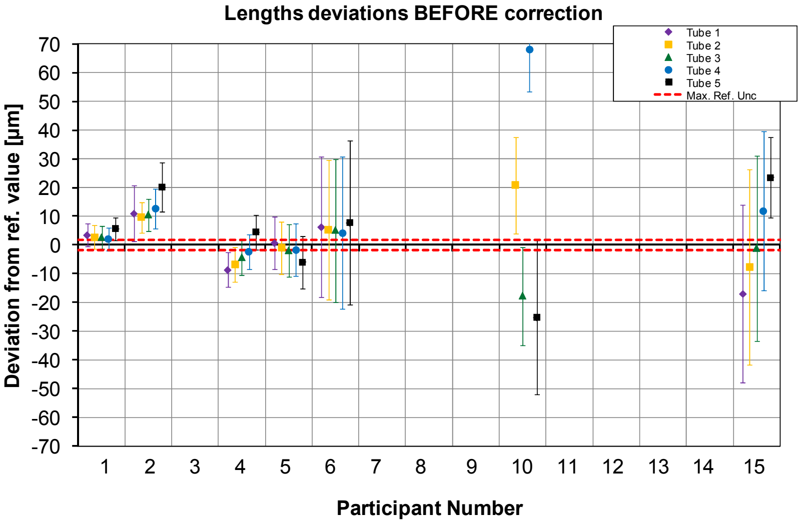

Figure 5.32: Lengths deviations of participants nr. 1, 2, 4, 5, 6, 10 and 15, before correction. [25]

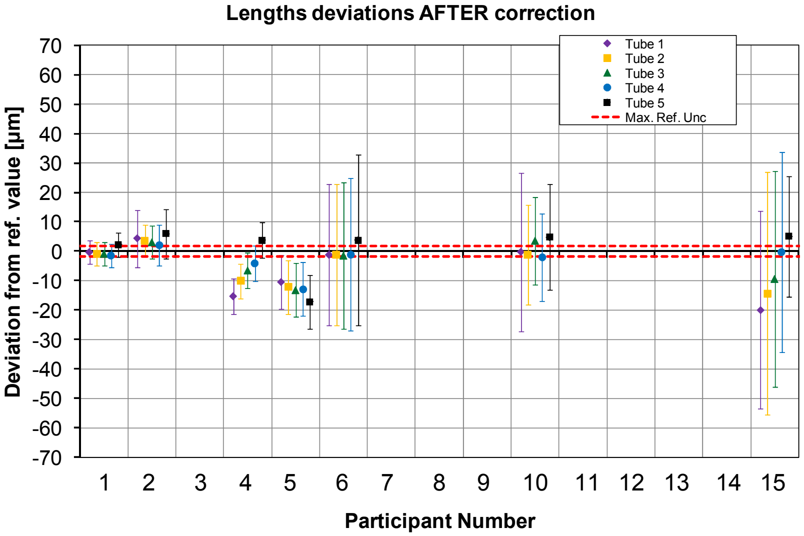

Figure 5.33: Lengths deviations of participants nr. 1, 2, 4, 5, 6, 10 and 15, after correction. [25]

	Tube				
	1	2	3	4	5
Inner	-0.006	-0.006	-0.004	-0.003	-0.001
Outer	0.006	0.006	0.006	0.003	0.002
Length	0.002	0.004	0.000	-0.001	0.000

Table 5.10: Deviations in $[mm]$ to the nominal values when using the same user selected settings as for the real measurement (e.g. BHC preset 2). These values have been obtained by simulation.

cylindrical holes is used for the edge offset calculation (figure 5.34). The edge offset is determined by comparing the CT measured diameters of the holes with the reference (CMM measured) values.

Figure 5.35 gives an overview of the form measurements of all participants. This again emphasizes the fact that all participants overestimate the form errors.

Figure 5.36 reveals the calculated diameter and their uncertainty ranges for 5 of the calottes. Most participants (participant 1 to 8 and 14) have errors in the range of -15 to $15\mu m$. Participants 9, 10 and 13 show higher deviations. Again difficulties in defining a good uncertainty interval can be observed.

In our case, the error of the 75 measured spherical calottes' diameters varied

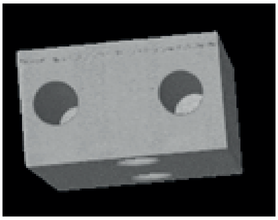

Figure 5.34: Calibration object for item 3.

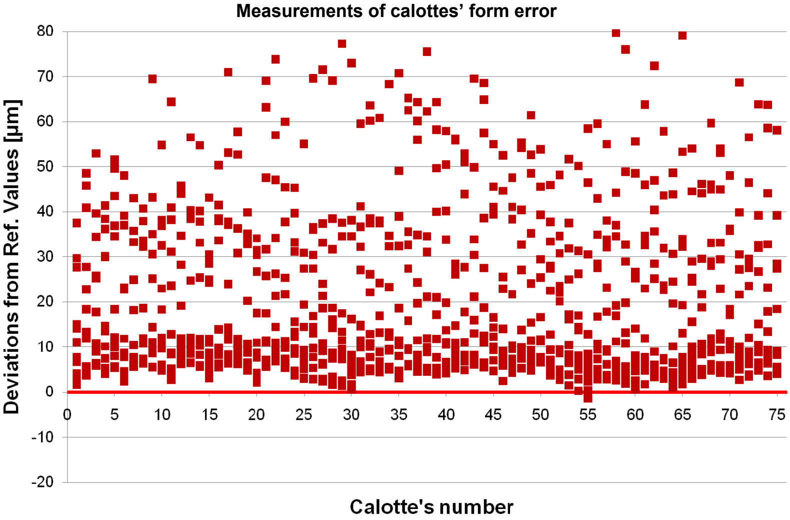

Figure 5.35: Result of form measurements on calottes of item 3. [25]

between -2 to $-12\mu m$ (the reference diameters of the calottes are around $0.79mm$).

Figures 5.37 and 5.38 give the deviations on calottes' center distances for our results. Both figures present the same results but other distances are highlighted. Figure 5.37 highlights the distances in vertical direction, whereas figure 5.38 highlights the distances in horizontal direction. Distances in vertical direction can be found between calottes of face 1 with those of face 2 ('Vertical 1-2'), and calottes of face 1 with those of face 3 ('Vertical 1-3'). Distances in horizontal direction are found in face 1 ('Horizontal 1-1') and by combining calottes of face 2 with those of face 3 ('Horizontal 2-3'). The other distance deviations (all distances besides vertical distances in figure 5.37 and all distances besides horizontal distances in figure 5.38) are pictured by a '+' sign. The fitted line

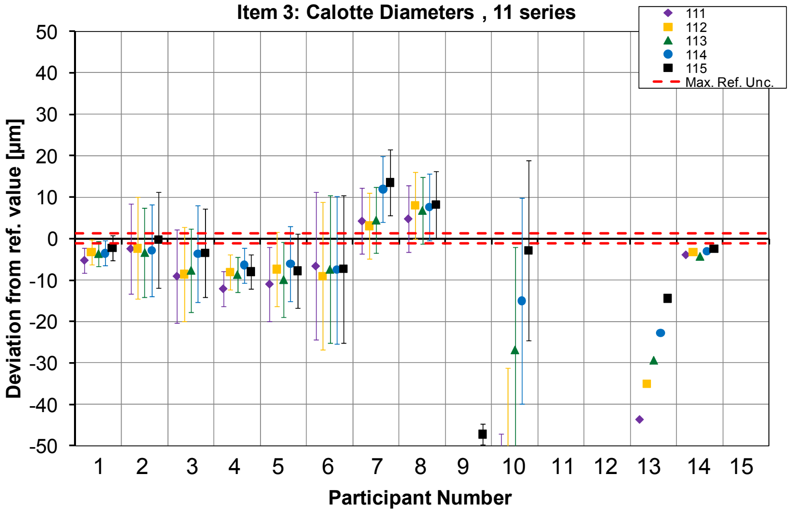

Figure 5.36: Diameter deviations of calottes 111 to 115 for item 3. [25]

is stated to be a measure for the rescaling error. The fact that all errors for certain lengths are situated beneath the line (even always negative) and all errors for other lengths are situated above this line (even all positive) illustrates that there are other significant influences (e.g. alignment errors, overrotation of the rotation table) besides only a scaling error.

Item 4

We only corrected for rescaling errors, as no appropriate calibration object for edge offsetting was available. Again a reference object consisting of 2 ruby spheres has been used for rescaling. The reference object has this time been scanned separately as the item was too large to perform one scan with both objects together.

Only 8 participants were able to scan this item, due to the size and the multimaterial configuration.

Figure 5.39 shows that the diameter results are a lot worse, compared to those of item 1 which had diameters in a similar range (3 to $5mm$ for item 1 and 0.9 and $2.3mm$ for item 4). Our results for these 7 diameters reveals deviations of -1.1 to $21.5\mu m$, but the uncertainty intervals always contain the reference values. Our uncertainty intervals are in fact always a bit overestimated. As stated

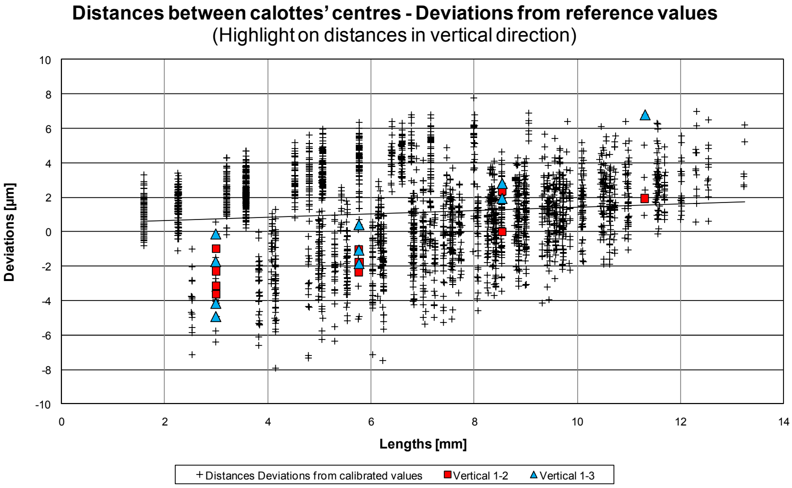

Figure 5.37: Deviations of the distances between calottes' centers in case of our measurement results. Highlight on distances in vertical direction. [25]

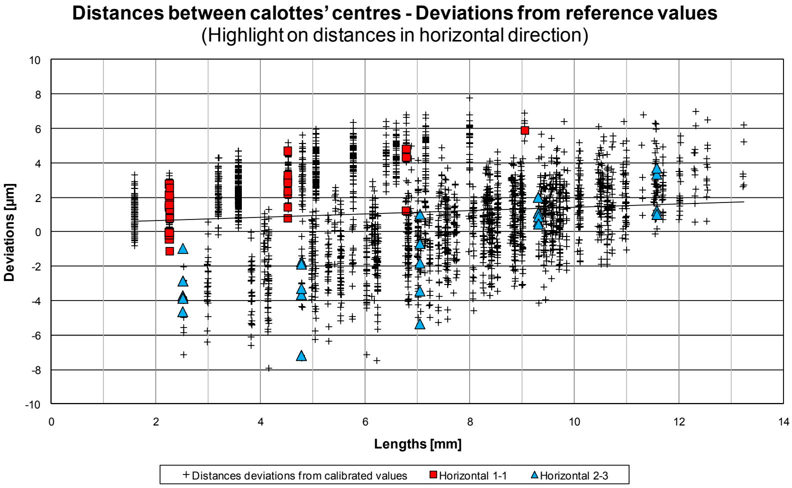

Figure 5.38: Deviations of the distances between calottes' centers in case of our measurement results. Same results are presented as in figure 5.37 but now the distances in horizontal direction are highlighted. [25]

earlier however: it is better to overestimate this interval than to underestimate it resulting in the actual value being outside the interval.

Figure 5.40 shows the results for the diameter of the smallest cylindrical micro structure. There is a lot of variation between the participants. It should be noted that the deviations are this time plotted with respect to the median value of all diameters measured by the various participants. No hard conclusions can be made, except that it seems that we and participant 5 have measured the same cylindrical micro structure while other participants have measured another smaller micro cylinder, which is therefore the correct one (as measurement of the smallest one was requested). Another possibility is that the participants indeed measured the same cylindrical micro structure, but that difficulties determining the correct edge position resulted in these varying results.

Figure 5.41 pictures the inner and outer diameters measurements of the titanium cylinder. The errors obtained by our measurements are -19.9 and $-45.7\mu m$ on the reference diameters with nominal values 40 and $50mm$.

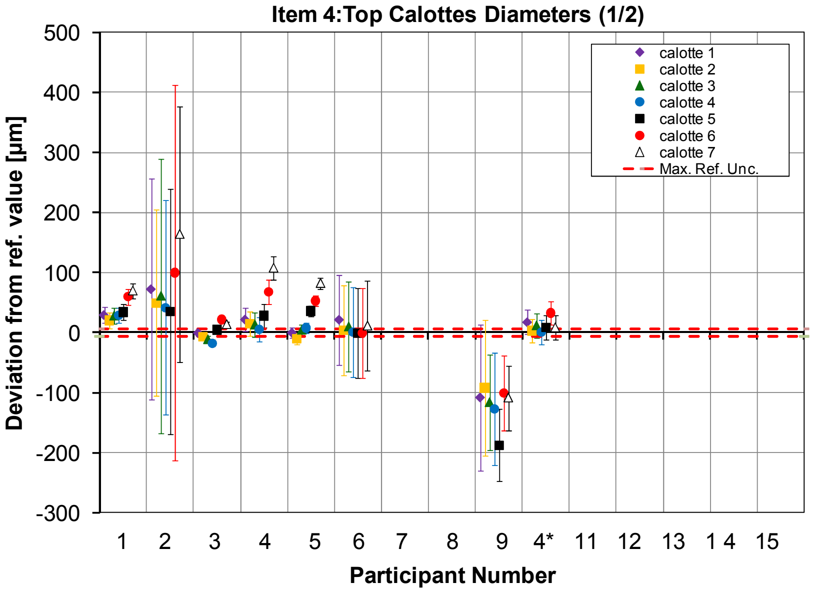

Figure 5.39: Diameter measurements of calottes 1 to 7. The reference values are situated between 0.9 and $2.3mm$. [25]

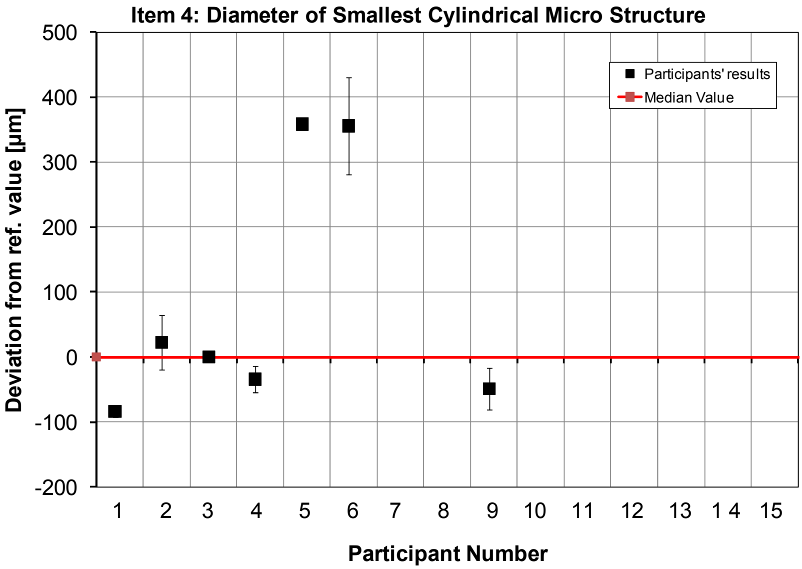

Figure 5.40: Diameter of smallest cylindrical micro structure. Deviation to the Participants' median value (the reference value is in this case the Participants' median value) [25]

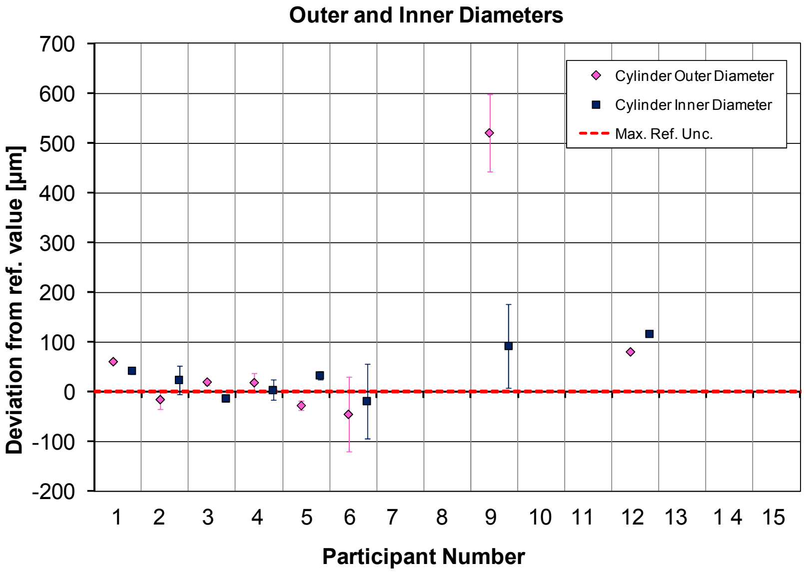

Figure 5.41: Outer and inner diameter of the titanium cylinder. [25]

5.3.4 Conclusions

This section discussed the results of the CT audit and focused on our strategy and results. Table 5.11 summarizes the main results. It denotes the largest measured deviation by a participant and our results for the different measurands. The largest deviations are determined by all available results [25] and not only the ones described in the text. It should be notified that our group always tried to correct the data in two manners: using an artifact for rescaling and an artifact to correct for edge offsets. This of course improves the results heavily and is not always possible. Our results of item 4 are clearly worse than our other results. Item 4 was the most difficult item, and no correction of the edge offset could be executed. In general did all participants have more troubles concerning the form measurements than measurements of size. It was moreover clear that all participants encountered problems defining a good measurement uncertainty: it is either defined too large (overestimation) or it is defined too small and does not contain the real value. It is furthermore interesting to compare the voxel sizes of table 5.9 with the measurement results (for instance for our results: participant 6, see also table 5.11). The obtained accuracy can be much better than the voxel sizes, but is of course dependent of the measurand.

Item	Feature	Nom./ref. values	Largest deviation	Our result	Our voxel size
Item 1	ruby sphere diameters	3 to $5mm$	$100\mu m$	-1.1 to $1.3\mu m$	$37.8\mu m$
Item 1	sphere form errors	0 to $1\mu m$	$250\mu m$	$14\mu m$	$37.8\mu m$
Item 1	sphere distances	$25mm$	$280\mu m$	-6 to $-9\mu m$	$37.8\mu m$
Item 2	outer diameters	$1.9mm$	$120\mu m$	around $-5\mu m$	$19.4\mu m$
Item 2	inner diameters	$1.5mm$	$25\mu m$	-1 to $6.2\mu m$	$19.4\mu m$
Item 2	tube lengths	2.5 to $12.5mm$	$120\mu m$	4.1 to $7.7\mu m$	$19.4\mu m$
Item 2	tube lengths reconsidered	2.5 to $12.5mm$	$20\mu m$	-1.5 to $3.8\mu m$	$19.4\mu m$
Item 3	form errors	up to $10\mu m$	$200\mu m$	$-1.5\mu m$ to $10\mu m$	$29.5\mu m$
Item 3	diameters	$0.8mm$	$200\mu m$	-2 to $-12\mu m$	$29.5\mu m$
Item 4	7 calotte diameters	$0.9mm$ to $2.3mm$	$180\mu m$	-1.1 to $21.5\mu m$	$64.2\mu m$
Item 4	inner cylinder diameter	$40mm$	$120\mu m$	$-45.7\mu m$	$64.2\mu m$
Item 4	outer cylinder diameter	$50mm$	$520\mu m$	$-19.9\mu m$	$64.2\mu m$

Table 5.11: Summary of the main results: item, feature and nominal or reference values. Furthermore the largest measured deviation by a participant and our results are denoted.

5.4 Ruby styli object

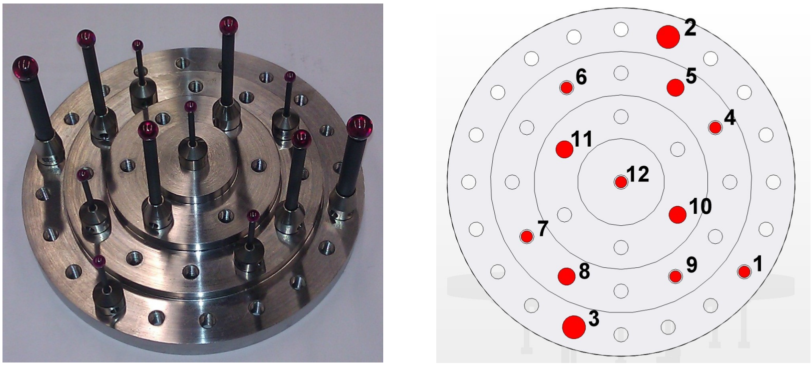

(a) (b)

Figure 5.42: Styli object (a) and its schematic representation (b).

The ruby styli object is developed and produced by fixing CMM probing styli on a socket (figure 5.42). Use of such styli has already been described in literature [76]. [76] makes use of 27 identical styli (same material, diameter, shaft height). In a first step (this section 5.4) we used a styli object containing styli of different lengths and diameters.

A second step (section 5.5) introduces a combination of spheres with different materials (Si_3N_4 and ZrO_2) in the object.

The experimental investigations on these objects have been mainly performed in the master theses of Denis Indesteege [55] and Tom Hendrickx [49]. [161] and [160] presented the first results for these objects.

5.4.1 Object description

Figure 5.43 contains the technical drawing of the socket. The socket has screw holes on distances 22.5, 37.5 and 52.5mm to the center and has different steps. It is designed in such a way that, in combination with the different styli lengths, only few spheres are positioned at the same height.

The styli are made of ruby (Al_2O_3) spheres on carbon fiber rods, with different diameters: table 5.12. Carbon fibre rods are chosen instead of the standard

Sphere	Diameter [mm]	Material
Sphere 1	4	Al_2O_3
Sphere 2	8	Al_2O_3
Sphere 3	8	Al_2O_3
Sphere 4	4	Al_2O_3
Sphere 5	6	Al_2O_3
Sphere 6	4	Al_2O_3
Sphere 7	4	Al_2O_3
Sphere 8	6	Al_2O_3
Sphere 9	4	Al_2O_3
Sphere 10	6	Al_2O_3
Sphere 11	6	Al_2O_3
Sphere 12	4	Al_2O_3

Table 5.12: Nominal diameter and material of the different sphere styli.

Distance	Sphere diameters
2-3	$8mm$
4-7	$4mm$
4-12	$4mm$
5-8	$6mm$
6-9	$4mm$
6-12	$4mm$
7-12	$4mm$
9-12	$4mm$
10-11	$6mm$

Table 5.13: Measured sphere distance and corresponding sphere diameters.

metallic rods for their lower impact on the penetrating X-rays, as this would hinder the reconstruction and subsequent sphere measurements.

The application of the reference object is multiple. Firstly, it is possible to measure distances between sphere centers. Using sphere centers cancels out existing beam hardening and threshold errors. The sphere centers are independent of the sphere diameter. Secondly, sphere diameters can be measured to quantify beam hardening and/or threshold errors. At last, multiple distances and diameters are available, allowing to check multiple measurands at a time and answering following questions: Is it enough to rescale the voxel sizes with 1 reference distance (distance between two spheres) like often applied? Is it sufficient to correct for edge determination errors by adding/subtracting one fixed value for a certain material?

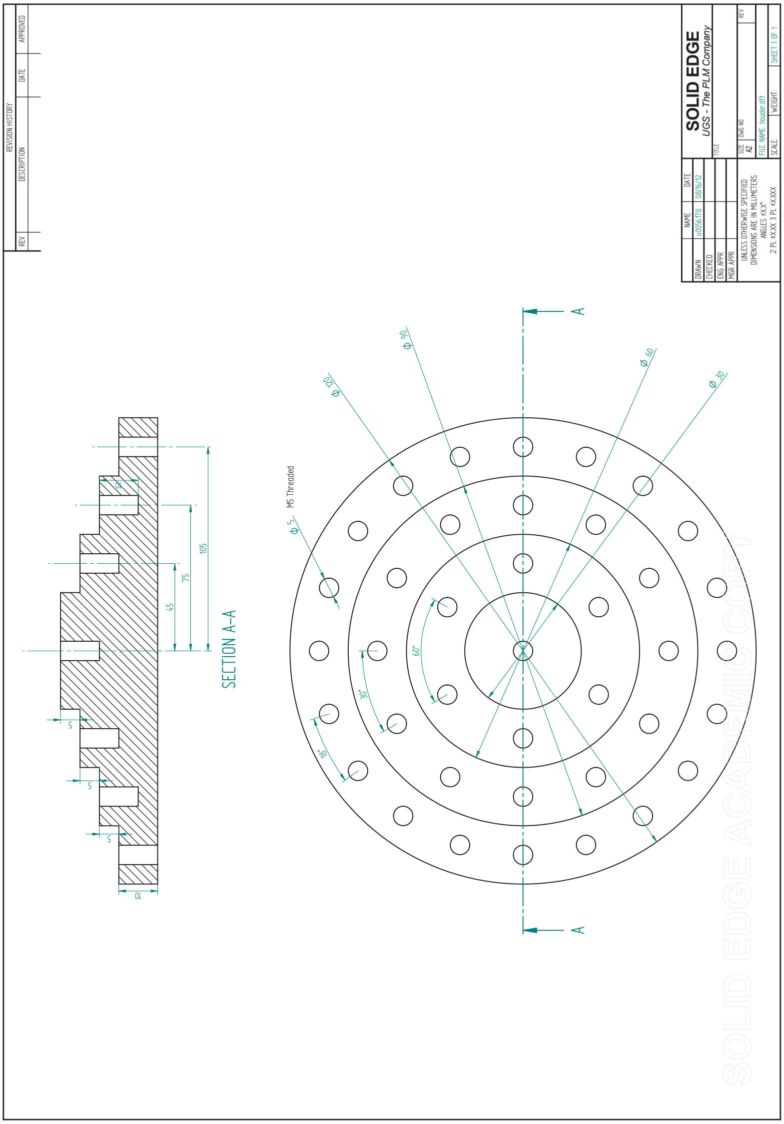

Figure 5.43: Technical drawing of the socket.

5.4.2 Calibration

As a reference, the sphere distances (listed in table 5.13) between several spheres are measured with a conventional tactile CMM Mitutoyo FN 905 with specified accuracy: $U1 = 4.2 + 5.L/1000\mu m$ (with L in mm, for each axis). Each investigated distance has been measured 13 times, spread over 3 days and each time differently positioned in the measuring volume of the CMM. Afterwards the standard deviation on each distance has been calculated, resulting in a maximum standard deviation value of $1\mu m$ (see table 5.15). Figure 5.44 shows the CMM measurement results for the distance between spheres 2 and 3.

The sphere diameters are calibrated by an external calibration lab. Table 5.14 summarizes the results.

Sphere	Nominal d	Calibration val $[mm]$
1	4	3.9998
2	8	7.9993
3	8	7.9996
4	4	3.9999
5	6	5.9982
6	4	3.9998
7	4	3.9999
8	6	5.9983
9	4	3.9998
10	6	5.9982
11	6	5.9983
12	4	4.0000

Table 5.14: Calibration values for the sphere diameters. The expanded uncertainty of measurement for all values is $1\mu m$.

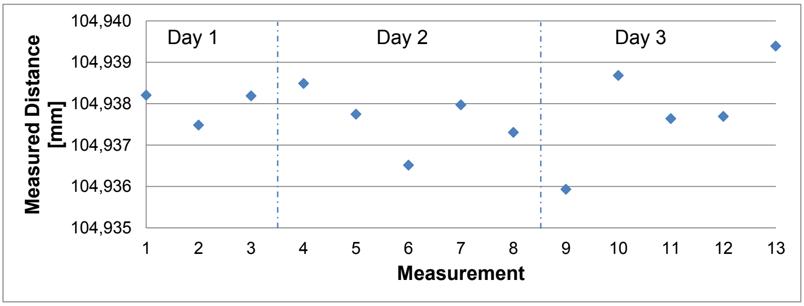

Figure 5.44: Measured CMM distance (distance 2-3) in function of measurement number.

Distance	Average $[mm]$	Stand. Dev. $[mm]$	Range $[mm]$
2-3	104,938	0,001	0,003
4-7	75,863	0,001	0,004
4-12	39,574	0,001	0,002
5-8	75,455	0,001	0,003
6-9	75,644	0,001	0,002
6-12	38,830	0,001	0,003
7-12	38,865	0,001	0,003
9-12	39,413	0,001	0,002
10-11	45,060	0,000	0,002

Table 5.15: Average value, standard deviation and range for the measured sphere distances. Each measurement has been repeated 13 times at a different position in the measurement volume of the CMM.

5.4.3 CT measurements

Acquisition settings

Different CT measurements have been carried out on the Nikon Metrology XT H 450 CT scanner. First of all different filter plates have been investigated. Dependent of the filter plate other settings for the source voltage $[kV]$ and source current $[\mu A]$ have been used to obtain an optimal scan. Table 5.16 shows the applied settings. Furthermore the standard shading correction procedure (2 reference images) has been applied. The detector exposure time is set to $1000ms$ and the number of views was set to 1000. This results in a scan time (only capturing of the X-ray projection images taken into account) of more or less 20 minutes.

Besides the use of different filter plates, also the position of the magnification axis has been varied. Table 5.17 shows the magnification for each measurement position with corresponding voxel size (see section 2.3.5 for the relation between the voxel size and magnification). Measurement position 1 and 2 are the same. This enables to check whether there is a difference if the same measurement is repeated. Next the object is always less magnified till measurement position 6. Then the same measurement positions have been repeated in the reverse order (low magnification to high magnification) to end at measurement position 10, which corresponds to measurement position 1 and 2. So in total 30 scans have been taken (3 filter plates, and 10 measurement positions per filter plate).

Filtering	Voltage $[kV]$	Current $[\mu A]$
No Filter	125	133
$3mmAl$	135	145
$2mmCu$	200	270

Table 5.16: Applied settings to measure the styli model.

	Magnification [/]	Voxel size $[mm]$
Measurement position 1	2.66	0.075
Measurement position 2	2.66	0.075
Measurement position 3	2.21	0.091
Measurement position 4	1.88	0.106
Measurement position 5	1.64	0.122
Measurement position 6	1.46	0.137
Measurement position 7	1.64	0.122
Measurement position 8	1.88	0.106
Measurement position 9	2.21	0.091
Measurement position 10	2.66	0.075

Table 5.17: Magnification and corresponding voxel sizes of the different measurements.

Rescaling the voxel sizes

After performing a CT scan and reconstructing the voxel model, this voxel model is loaded in VGStudio Max. Because of the inaccuracy of the magnification axis, it is necessary to rescale the voxel model by adjusting the voxel size in VGStudio. Equation 2.8 explained the corrected voxel size calculation. Determining the correct voxel size is done by compensating one of the CT measured distances to the calibration value (CMM measurement of the same distance).

The distance used to calculate the rescaling factor is often a distance between two spheres, as this distance is less influenced by beam hardening and threshold errors. Table 5.18 and figure 5.45 show the effect of rescaling on all investigated distances (results of the scans with $2mm$ Cu filter). Table 5.18 gives the errors to the reference (CMM) value for the original values, values after rescaling on distance 10-11 and the values after rescaling on distance 2-3. The average error of the measurements on 10 measurement positions as well as the maximum error of these 10 measurement positions is noted. Figure 5.45 pictures the results for distances 2-3, 10-11 and 6-9.

It is evident from the numerical values and the graphs that rescaling on the largest distance (2-3) provides the best results (distance between spheres 10-11 is obviously best when rescaling with distance 10-11). Although the results are better, errors of magnitude $10\mu m$ still exist, with maximum deviations up to $15\mu m$. This immediately gives an idea of the correctness of a generally applied rescaling procedure: i.e. rescaling on base of the distance between two spheres.

It is furthermore clear that in this case the obtained values are repeatable for the same measurement position (measurement position 1-2-10, 3-9, 4-8, 5-7).

The influence of rescaling will be a lot smaller for the sphere diameters as rescaling is relative to the measurand size. The presented results for the diameters are always rescaled on distance 2-3.

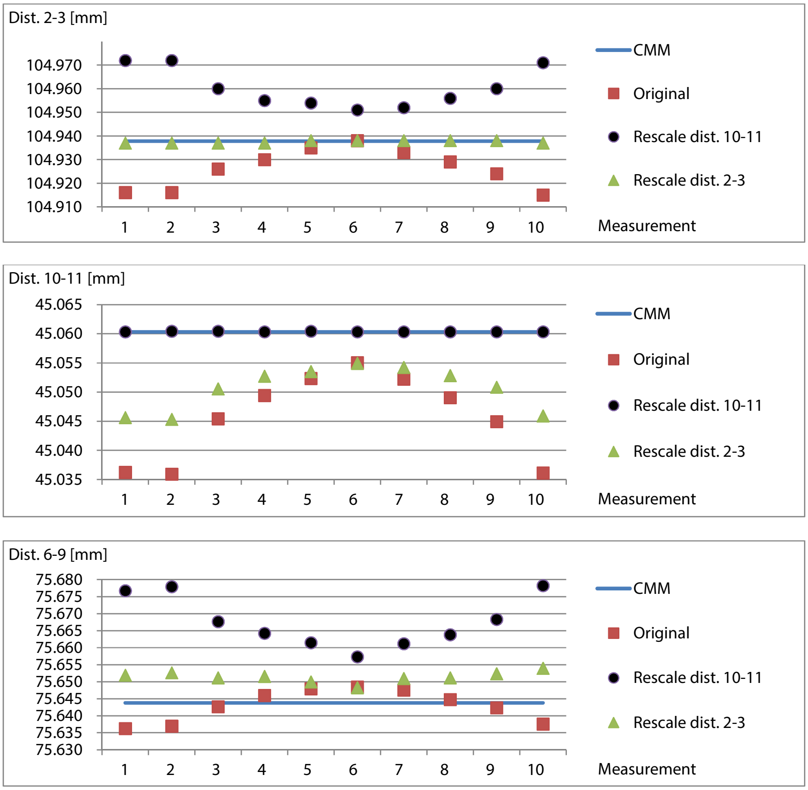

Figure 5.45: Effect of different rescalings on distance 2-3 (top), 10-11 (middle) and 6-9 (bottom): reference value (CMM), original value and value obtained after rescaling on distances 2-3 and 10-11 for each measurement position.

	Reference value	Original		Rescale dist. 10-11		Rescale dist. 2-3	
		Average difference	Maximum difference	Average difference	Maximum difference	Average difference	Maximum difference
Dist. 2-3	104.938	-0.012	-0.023	0.023	0.034	0.000	-0.001
Dist. 4-7	75.863	-0.001	-0.007	0.024	0.034	0.008	0.009
Dist. 4-12	39.574	-0.002	-0.005	0.011	0.017	0.002	0.004
Dist. 5-8	75.455	-0.019	-0.031	0.006	0.010	-0.010	-0.015
Dist. 6-9	75.644	-0.001	-0.008	0.024	0.034	0.008	0.010
Dist. 6-12	38.830	-0.001	-0.005	0.012	0.017	0.003	0.004
Dist. 7-12	38.865	0.000	-0.005	0.013	0.017	0.004	0.005
Dist. 9-12	39.413	-0.002	-0.006	0.011	0.017	0.003	0.004
Dist. 10-11	45.060	-0.015	-0.024	0.000	0.000	-0.010	-0.015

Table 5.18: Deviations (average and maximum from 10 measurement positions) to the reference distances: to the original values, after rescale on distance 10-11 and after rescaling on distance 2-3. All values are expressed in $[mm]$.

Rescaling before reconstruction

Adapting the source-object and source-detector distance before reconstruction is another method for rescaling. This has been tested and compared to the results after rescaling the voxel sizes. The results stay identical. This means that in case of small errors of the source-detector and source-object distance, adapting these distances or rescaling the voxel model afterwards has the same effect. In case of larger errors, this will differ.

Multi-material aspect

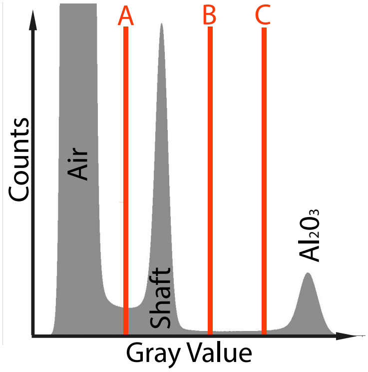

Figure 5.46: Histogram of a ruby stylus. Three different possible start contours are pictured.

This object forms a multi-material object, although that only ruby spheres are used. This can be clearly seen on figure 5.46, which pictures the histogram of a stylus. Three peaks are present: air, shaft material (carbon fibre) and the sphere material (ruby). As explained in section 2.6 edge detection should be executed before feature detection can be carried out. Figure 5.47 shows the influence of the starting contour in relation to the multi-material aspect. Figure 5.47a shows the situation (start contour and resulting contour, resp. thin and thick line, after advanced edge thresholding) when the gray value for the start contour is chosen between the ruby and carbon fibre peak (line B in figure 5.46). Figure 5.47b illustrates the situation when the start contour is defined between the air peak and carbon fibre peak. A detailed situation at the transition between the ruby sphere and the carbon fiber rod is pictured in figure 5.47c. The white line is the achieved contour (resulting contour from figure 5.47a) after using advanced thresholding starting from a start contour defined between the ruby peak and carbon fibre peak (line B in figure 5.46). The

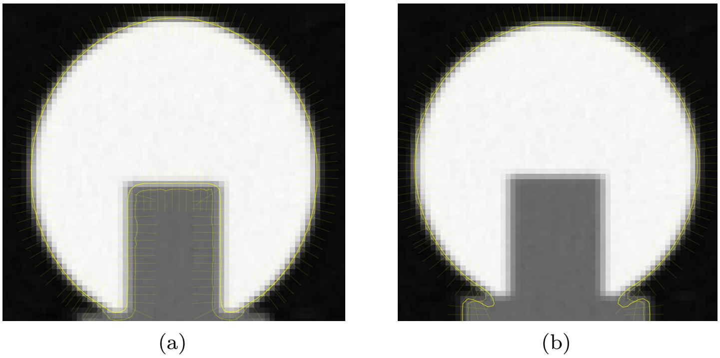

(a) (b)

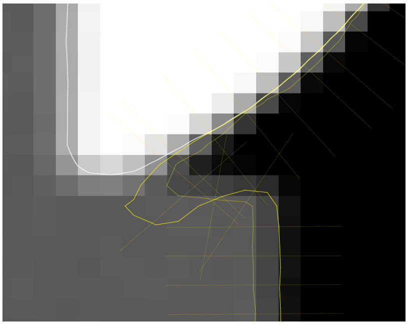

(c)

Figure 5.47: Influence of the start contour in case of line B (a) and line A (b) as start gray value (see figure 5.46). (c) gives a detailed situation picturing the resulting contour of situation (a) and the start and resulting contour of situation (b).

thin yellow line is the new starting contour (defined between the air peak and carbon fibre peak, line A in figure 5.46) and the thick yellow line is the resulting contour after using advanced thresholding starting from the thin yellow line (the thick and thin yellow line resemble the same lines as pictured in figure 5.47b). Comparing the white line and thick yellow line (both contours obtained after advanced thresholding) shows a difference at the location where the sphere surface is interrupted to provide room for the carbon rod. This difference will induce errors in the algorithm that defines the spheres, causing different results dependent of the chosen start contour for edge thresholding, even when using advanced thresholding.

Edge detection

Despite the use of VGStudio's advanced mode edge detection, the final contour is highly dependent of the starting contour like shown in previous section. Even varying a start contour between the carbon fibre and ruby peak gives inconsistent results. Two start contours have been taken (at line B and C in figure 5.46). Figure 5.48 shows the results of applying advanced thresholding on these start contours. The white line (current contour) has been kept the same for both graphs, and can therefore be used for comparison. It is clear that the obtained contour (thick yellow line) is different at the bottom part. Table 5.19 shows the resulting diameters and the difference when using start contour B or C for advanced thresholding. Diameter differences up to $44\mu m$ are achieved by shifting the start contour for advanced thresholding.

Sphere	Start contour B	Start contour C	Difference
Sphere 1	3.991	3.960	0.031
Sphere 2	8.010	7.966	0.044
Sphere 3	8.004	7.969	0.035
Sphere 4	3.991	3.973	0.018
Sphere 5	5.994	5.973	0.021
Sphere 6	3.991	3.975	0.017
Sphere 7	3.991	3.974	0.017
Sphere 8	5.993	5.975	0.018
Sphere 9	3.990	3.974	0.016
Sphere 10	5.990	5.981	0.010
Sphere 11	5.990	5.980	0.011
Sphere 12	3.991	3.986	0.005

Table 5.19: Comparison of measured sphere diameters after using start contour B or C for advanced thresholding. All values are expressed in $[mm]$.

Use of Region Of Interest (ROI)

Both aforementioned problems can be largely solved by using a region of interest (ROI). Selecting the region only containing the sphere as ROI eliminates the transition part between ruby and carbon (figure 5.49). Figure 5.50 gives the histograms in case of the entire stylus (a) and in case of the region of interest (b). The center peak (peak of the carbon fibre material) disappears in the latter situation.

Table 5.20 gives the average and maximum deviation out of the measurements on 10 positions after rescaling on distance 2-3, and after an additional selection of a ROI to work with (rescaling redone after selection of ROI). Figure 5.51

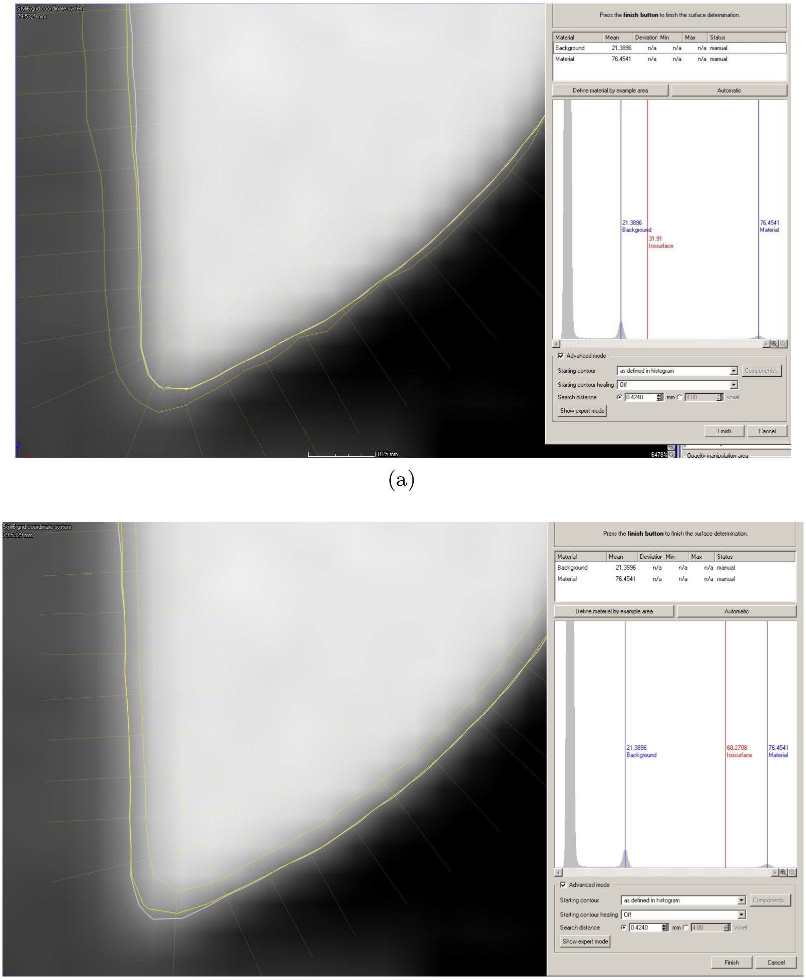

Press the **finish button** to finish the surface determination.

Material	Mean	Deviation	Min	Max	Status
Background	21.3896	n/a	n/a	n/a	manual
Material	76.4541	n/a	n/a	n/a	manual

☑ Advanced mode
Starting contour: as defined in histogram
Starting contour healing: Off
Search distance: ● 0.4240 mm ○ 4.00 voxel

(a)

Press the **finish button** to finish the surface determination.

Material	Mean	Deviation	Min	Max	Status
Background	21.3896	n/a	n/a	n/a	manual
Material	76.4541	n/a	n/a	n/a	manual

☑ Advanced mode
Starting contour: as defined in histogram
Starting contour healing: Off
Search distance: ● 0.4240 mm ○ 4.00 voxel

(b)

Figure 5.48: Result of advanced thresholding when using start contour value B (a) and C (b) (figure 5.46).

gives the diameter results for the $4mm$ spheres in both cases. The errors have almost been halved. The range of -25 to $-50\mu m$ for the average distances and the range from -31 to $-65\mu m$ for the maximum differences ameliorates to a range of -16 to $-27\mu m$ for the average distances and a range of -18 to $-29\mu m$ for the maximum differences. The influence of the starting contour for advanced thresholding also decreased but has not disappeared. The distance measurements between spheres is almost not influenced by the use of a ROI, as the influence on the center position is small. It is clear that the use of a ROI is necessary, and this will be done for further measurements.

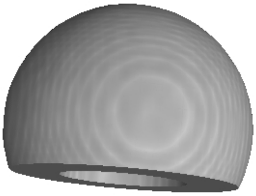

Figure 5.49: Styli sphere: Region Of Interest (ROI).

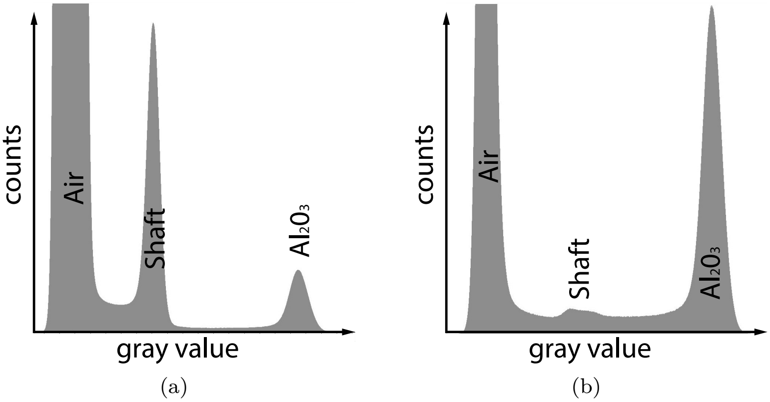

(a) (b)

Figure 5.50: Histogram of entire stylus (a) and ROI (b). The abscissa denotes the gray value, where the ordinate represents the number of occurrences for this gray value.

	Reference value	Rescale dist. 2-3		Selection ROI	
		Average difference	Maximum difference	Average difference	Maximum difference
Sphere 1	4.000	-0.050	-0.065	-0.027	-0.029
Sphere 2	7.999	-0.035	-0.046	-0.017	-0.020
Sphere 3	8.000	-0.035	-0.046	-0.018	-0.021
Sphere 4	4.000	-0.036	-0.047	-0.021	-0.022
Sphere 5	5.998	-0.035	-0.043	-0.020	-0.023
Sphere 6	4.000	-0.036	-0.046	-0.021	-0.022
Sphere 7	4.000	-0.035	-0.045	-0.021	-0.022
Sphere 8	5.998	-0.035	-0.043	-0.020	-0.022
Sphere 9	4.000	-0.036	-0.046	-0.021	-0.023
Sphere 10	5.998	-0.029	-0.034	-0.019	-0.021
Sphere 11	5.998	-0.029	-0.035	-0.018	-0.021
Sphere 12	4.000	-0.025	-0.031	-0.016	-0.018

Table 5.20: Average and maximum deviation out of the measurements on 10 positions after rescaling on distance 2-3, and after an additional selection of a ROI. All values are expressed in $[mm]$.

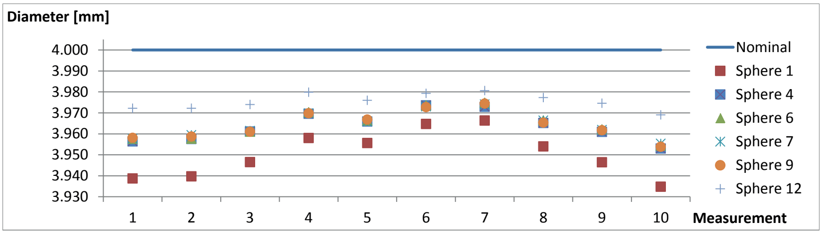

(a)

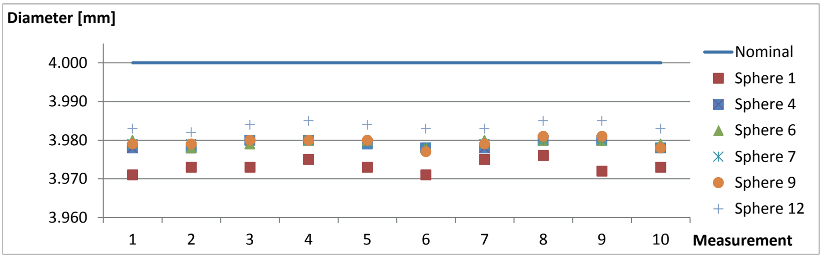

(b)

Figure 5.51: Measured sphere diameters: when rescaling on distance 2-3 (a) and after selection of ROI (b). (The markers of spheres 4, 6, 7 and 9 are laying on top of each other and are therefore not separately visible)

Object position

When observing the $4mm$ spheres in figures 5.51 and 5.42 there is a trend visible for all measurements: the diameter of the center sphere (i.e. sphere 12) is always the largest, the sphere the furthest away from the center (sphere 1) always has the smallest diameter and the other spheres seem to have comparable diameters. While performing the CT scans the entire object was placed in the center of the rotation table, i.e. sphere 12 was located close to the rotation axis of the CT scanner while measuring. As a test, a new CT scan has been executed with sphere 6 closest to the rotation axis. The results are shown in figure 5.53 and table 5.21. A similar trend is present: again the sphere diameters are dependent on the distance to the axis of rotation.

Figure 5.52 shows the deviations of a large number of points on a CT measured sphere with respect to its least square fitted sphere. This least square fit is assumed to represent the real physical sphere since this sphere is highly accurate with very small unroundness. Those deviation plots allow to evaluate the sphere form errors introduced by the CT measurement: the real sphere being assumed to have no or minimal form errors. Figure 5.52 compares the sphere near the axis of rotation (left) and another sphere (right). It is clear that the latter sphere (right) suffers from a form deviation introduced by the CT measurement.

The simulation program, described in chapter 4, is applied to verify these observations. Figure 5.54 again shows deviations of a large number of points on a CT measured sphere with respect to its least square fitted sphere but this time in case of simulation with the calculated mechanical errors (section 3.4.4, alignment 1) and without these errors. There is a clear analogy in form errors to the real situation in case of the simulation with mechanical errors . The simulation without errors shows similar fit points deviations for both spheres. Figure 5.55 pictures the acquired diameter values for the $4mm$ spheres in case of the simulation with errors (sphere 12 on the rotation axis and magnification 2.66). This again shows a similar trend as for the real CT measurements (see figure 5.51b).

Reconstruction resolution quality

The resolution quality can be changed during reconstruction as explained in section 2.6.1. The common value is 100 percent. The effect of changing the value to 150 percent has been investigated. Tables 5.22 and 5.23 give the resulting errors on distances and diameters using resolution quality 100 and 150 percent. Rescaling has been done on distance 2-3. No clear improvements can be observed, despite the large increase in calculation time.

	Reference value	Stylus 6 central	
		Average difference	Maximum difference
Sphere 1	4.000	-0.035	-0.038
Sphere 2	7.999	-0.012	-0.017
Sphere 3	8.000	-0.019	-0.024
Sphere 4	4.000	-0.020	-0.024
Sphere 5	5.998	-0.016	-0.021
Sphere 6	4.000	-0.011	-0.016
Sphere 7	4.000	-0.018	-0.023
Sphere 8	5.998	-0.020	-0.025
Sphere 9	4.000	-0.027	-0.031
Sphere 10	5.998	-0.019	-0.024
Sphere 11	5.998	-0.013	-0.018
Sphere 12	4.000	-0.014	-0.019

Table 5.21: Average and maximum deviation when stylus 6 is positioned near the rotation axis. All values are expressed in $[mm]$.

	Reference value	Resolution Quality 100%		Resolution Quality 150%	
		Average difference	Maximum difference	Average difference	Maximum difference
Dist. 2-3	104.938	0.000	-0.001	0.000	0.000
Dist. 4-7	75.863	0.008	0.009	0.008	0.009
Dist. 4-12	39.574	0.002	0.004	0.002	0.002
Dist. 5-8	75.455	-0.010	-0.015	-0.011	-0.017
Dist. 6-9	75.644	0.008	0.010	0.008	0.009
Dist. 6-12	38.830	0.003	0.004	0.002	0.003
Dist. 7-12	38.865	0.004	0.005	0.003	0.004
Dist. 9-12	39.413	0.003	0.004	0.002	0.003
Dist. 10-11	45.060	-0.010	-0.015	-0.011	-0.017

Table 5.22: Average and maximum deviation of the distances using resolution quality 100% and 150%. All values are expressed in $[mm]$.

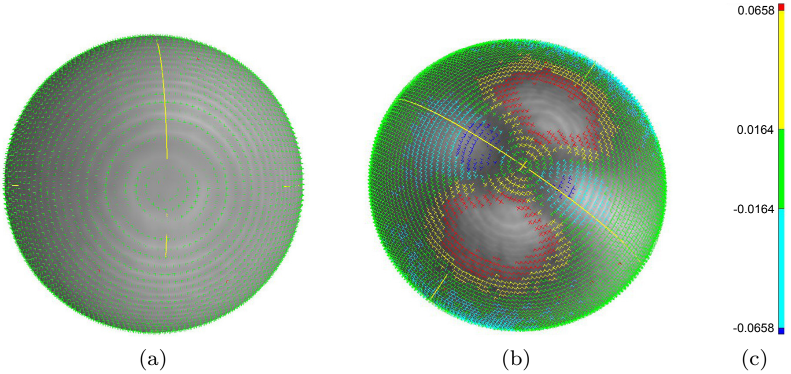

(a) (b) (c)

Figure 5.52: Fitpoint deviations: sphere near the rotation axis (a), other sphere (b) and deviation scale in $[mm]$ (c).

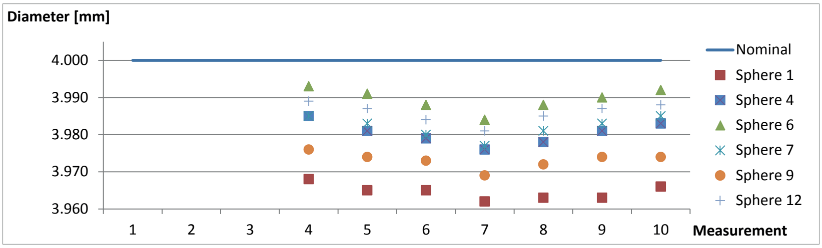

Figure 5.53: Measured sphere diameters in case of sphere 6 near the axis of rotation (only measurements 4 to 10 have been executed).

Minimize ring artifacts

The option 'Minimize ring artifacts' has been tested (see section 2.3.15 for more information). Only one measurement has been performed as the scanning time increases largely. A measurement has been executed on measurement position 1 (same as position 2 and 10, see table 5.17) with a $2mm$ Cu filter. The obtained spheres (see figure 5.56) were visually worse than those obtained by continuous scanning. Tables 5.24 and 5.25 give the resp. distances and diameters. The distance measurement are much worse than in case of using normal continuous scanning (see e.g. table 5.18).

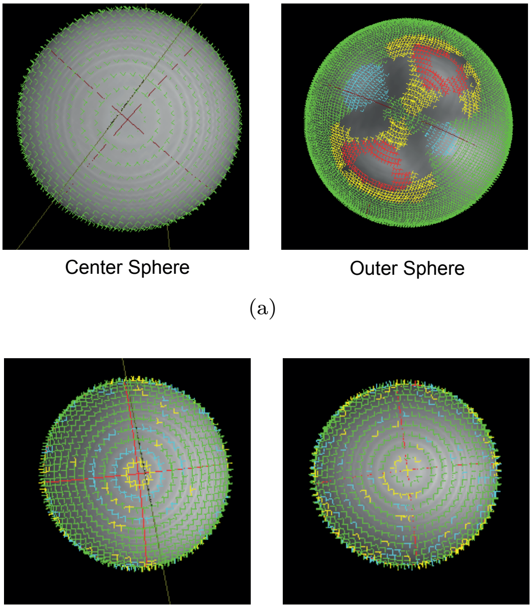

(a)

(b)

Figure 5.54: Fitpoint deviations: sphere near the rotation axis (left) and other sphere (right) in case of simulation with errors (a) and the ideal case (b).

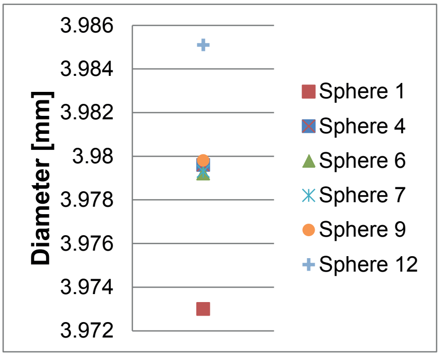

Figure 5.55: Measured sphere diameters of the simulation containing several alignment errors. (The markers of spheres 4, 6, 7 and 9 are laying on top of each other and therefore not separately visible.).

	Reference value	Resolution Quality 100%		Resolution Quality 150%	
		Average difference	Maximum difference	Average difference	Maximum difference
Sphere 1	4.000	-0.027	-0.029	-0.028	-0.031
Sphere 2	7.999	-0.017	-0.020	-0.014	-0.018
Sphere 3	8.000	-0.018	-0.021	-0.015	-0.019
Sphere 4	4.000	-0.021	-0.022	-0.022	-0.024
Sphere 5	5.998	-0.020	-0.023	-0.018	-0.021
Sphere 6	4.000	-0.021	-0.022	-0.021	-0.025
Sphere 7	4.000	-0.021	-0.022	-0.022	-0.025
Sphere 8	5.998	-0.020	-0.022	-0.019	-0.021
Sphere 9	4.000	-0.021	-0.023	-0.022	-0.025
Sphere 10	5.998	-0.019	-0.021	-0.018	-0.020
Sphere 11	5.998	-0.018	-0.021	-0.018	-0.020
Sphere 12	4.000	-0.016	-0.018	-0.016	-0.019

Table 5.23: Average and maximum deviation of the sphere diameters using resolution quality 100% and 150%. All values are expressed in $[mm]$.

	Reference value	Minimize ring artifacts	
		Measured value	Difference
Dist. 2-3	104.938	104.938	0.000
Dist. 4-7	75.863	75.792	-0.071
Dist. 4-12	39.574	39.539	-0.035
Dist. 5-8	75.455	75.412	-0.043
Dist. 6-9	75.644	75.644	0.000
Dist. 6-12	38.830	38.823	-0.007
Dist. 7-12	38.865	38.824	-0.041
Dist. 9-12	39.413	39.414	0.001
Dist. 10-11	45.060	45.007	-0.053

Table 5.24: Measured distances when using the 'Minimize ring artifacts' option. All values are expressed in $[mm]$.

Figure 5.56: Use of 'Minimize ring artifacts' option: reconstructed sphere.

	Reference value	Minimize ring artifacts	
		Measured value	Difference
Sphere 1	4.000	3.968	-0.032
Sphere 2	7.999	7.988	-0.012
Sphere 3	8.000	7.987	-0.013
Sphere 4	4.000	3.972	-0.028
Sphere 5	5.998	5.981	-0.019
Sphere 6	4.000	3.974	-0.026
Sphere 7	4.000	3.977	-0.023
Sphere 8	5.998	5.979	-0.021
Sphere 9	4.000	3.975	-0.025
Sphere 10	5.998	5.979	-0.021
Sphere 11	5.998	5.977	-0.023
Sphere 12	4.000	3.979	-0.021

Table 5.25: Measured diameters when using the 'Minimize ring artifacts' option. All values are expressed in $[mm]$.

Stepwise rotation

A stepwise rotating scan has been performed by setting the displacement to zero when using the 'minimize ring artifacts' option. The results where still worse than while using continuous scanning.

Filter plate material

Using a filter plate gives the advantage that it absorbs the soft X-rays. Absorbing these low energy X-rays in the filter, diminishes beam hardening from occurring when penetrating the object. A more attenuating filter plate will however decrease the signal-to-noise ratio. A more attenuating filter plate will furthermore require a higher power setting as shown by the settings in table 5.16, which enlarges the X-ray spot size.

Use of different filter plates did not give any significant changes in the results for the distances between spheres which is logical as these distances are edge independent.

The use of different filters however seems to have an influence on the determined sphere diameters when we look at figure 5.57. Aluminum filtering and no filtering gives similar results (figures (a) and (b)). The measured diameters decrease with a lower magnification for these filters (measurement 6 has the lowest magnification). The measurements with the copper filter plate gives less differences when changing the magnification.

The diameter differences between different filters and different magnifications can be brought back to an offset difference. This (offset) error to the nominal diameter is larger when using a $2mm$ copper filter. The offset error, which is for instance caused by the different filter plate combined with the edge detection, can easily be compensated by adding a compensation value. During the CT audit this technique was often applied: in case of item 1 from the CT audit, a sphere with similar diameter and material was used to calculate the offset value (see section 5.3.3). Compensating this offset difference by adding or subtracting an offset value to the sphere diameters measured with a certain filter/magnification combination will therefore lead to the same results.

Number of views

The measurement on measurement position 2 (magnification 2.66), using the $3mm$ Al filter, has been repeated with 3142 views. Tables 5.26 and 5.27 represent the results. There is no clear difference related to the distances. There is a small improvement in case of the diameters .

	Reference value	1000 views	3142 views
		Difference	Difference
Dist. 2-3	104.938	0.000	0.000
Dist. 4-7	75.863	0.008	0.008
Dist. 4-12	39.574	0.000	-0.002
Dist. 5-8	75.455	-0.014	-0.014
Dist. 6-9	75.644	0.009	0.008
Dist. 6-12	38.830	-0.001	-0.002
Dist. 7-12	38.865	0.000	0.000
Dist. 9-12	39.413	0.000	-0.001
Dist. 10-11	45.060	-0.019	-0.019
Average absolute error		0.006	0.006

Table 5.26: Comparison of the distance measurement error using 1000 views or 3142 views. All values are expressed in $[mm]$.

Fit point deviations: statistical analysis

A statistical study on the sphere fit point deviations of sphere 1 and sphere 12 (after selection of a region of interest applied as in figure 5.49) has been worked out in the framework of the PhD course *Measurement uncertainty estimation*

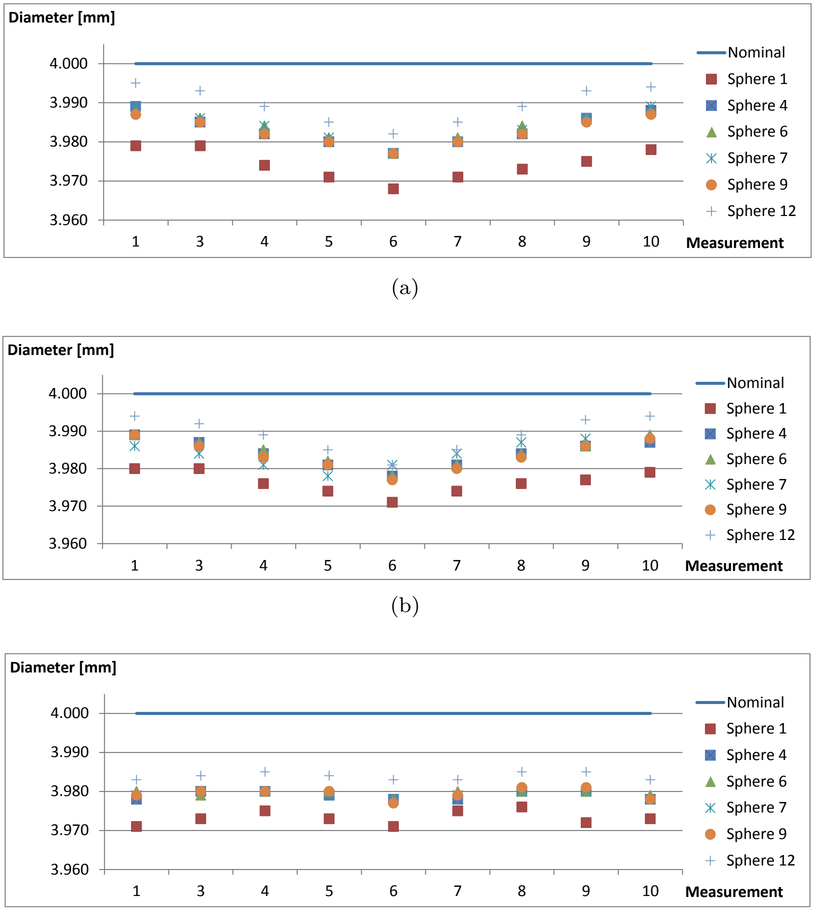

(a)

(b)

(c)

Figure 5.57: Measured sphere diameters when using no filter plate (a), Al filter plate (b) and Cu filter plate (c)

	Reference value	1000 views	3142 views
		Difference	Difference
Sphere 1	4.000	-0.020	-0.013
Sphere 2	7.999	-0.007	0.000
Sphere 3	8.000	-0.011	-0.004
Sphere 4	4.000	-0.011	-0.009
Sphere 5	5.998	-0.012	-0.009
Sphere 6	4.000	-0.011	-0.008
Sphere 7	4.000	-0.011	-0.009
Sphere 8	5.998	-0.012	-0.009
Sphere 9	4.000	-0.011	-0.009
Sphere 10	5.998	-0.011	-0.010
Sphere 11	5.998	-0.011	-0.010
Sphere 12	4.000	-0.006	-0.006
Average absolute error		0.011	0.008

Table 5.27: Comparison of the diameter measurement error using 1000 views or 3142 views. All values are expressed in $[mm]$.

using statistical methods taught at the Technical University of Denmark (DTU) under responsibility of Professor Leonardo De Chiffre, Professor Giulio Barbato and Dr Gianfranco Genta [158]. Different statistical analyses have been applied to the data:

Chauvenet's criterion. Chauvenet's criterion is applied for the elimination of statistical outliers.

Box plots. Box plots of the data have been drawn. These box plots contain the minimum, maximum, first and third quartile.

Frequency distribution and Pearson's chi-squared test. A frequency distribution plot and Pearson's chi-squared test is executed to test the null hypothesis of normal distribution.

Normal probability plot. A normal probability plot is pictured. Normal distributed data results in a straight line.

Test hypothesis 1. This is a test on the column effects. The column averages are checked as compared with the average distribution.

Test hypothesis 2. This is a test on variability of the column effects. The column variances are checked as compared with variance distribution.

ANOVA. Execution of an analysis of variance (ANOVA).

The data consists of the fit point deviations with respect to the least square fitted sphere. This least square fitted sphere is assumed to represent the real physical sphere since the styli spheres are highly accurate with very small unroundness. Fit point data of 9 different scans has been used corresponding to measurement positions 2 to 10 of table 5.17. The data has been organized such that the columns correspond to the different measurement positions (magnifications). The rows correspond to the fit points. The amount of fit points differed dependent of the measured spheres and magnifications. The number of fit points has been equalized as this is easier to handle during the analyses. This has been done by randomly taking 900 fit points out of the initial fit points of each sphere. This will have negligible influence on the results as still 900 fit points remain and as they were taken randomly. This results in 900 rows for the data analysis.

Figure 5.58a plots the fit point deviations of sphere 1 in function of the z coordinate of the fit point (the figure shows the results in case of measurement position 10). There is a clear dependency of the fit point deviation with respect to the z coordinate. The z-axis points upwards and these high deviations therefore correspond to the fit points at the top of the sphere (in correspondence to the deviations plotted in figure 5.52b). The data analysis is therefore repeated after eliminating the fit points with high z values. This results in 4 analyses:

- Analysis of sphere 1. Data consists of fit point deviations divided in 9 columns and 900 rows. The 9 columns correspond to the 9 different measurement positions. The 900 rows correspond to the 900 fit points which are randomly ordered.
- Analysis of sphere 1, with exclusion of the top part. Data consists of fit point deviations divided in 9 columns and 746 rows. The 9 columns correspond to the 9 different measurement positions. The 746 rows correspond to the 746 fit points which are this time ordered in function of the z coordinate.
- Analysis of sphere 12. Data consists of fit point deviations divided in 9 columns and 900 rows. The 9 columns correspond to the 9 different measurement positions. The 900 rows correspond to the 900 fit points which are randomly ordered.
- Analysis of sphere 12, with exclusion of the top part. Data consists of fit point deviations divided in 9 columns and 746 rows. The 9 columns correspond to the 9 different measurement positions. The 746 rows correspond to the 746 fit points which are this time ordered in function of the z coordinate.

Figure 5.58 shows the fit point deviations in function of the z coordinate. The discrete steps between the z values clearly illustrates the use of a grid for the fit points positions. Exclusion of the top part of sphere 1 (figure 5.58b) improves the deviations from a range of $196\mu m$ to a range of $51\mu m$. Figure 5.58c gives the results in case of sphere 12 and measurement position 10. This time no dependency on the z coordinate is distinguished. The deviations have a range of $20\mu m$. Figure 5.58d shows the results in case of sphere 12 and measurement position 8. This time there is again a dependency on the z coordinate visible but only resulting in deviations up to $30\mu m$.

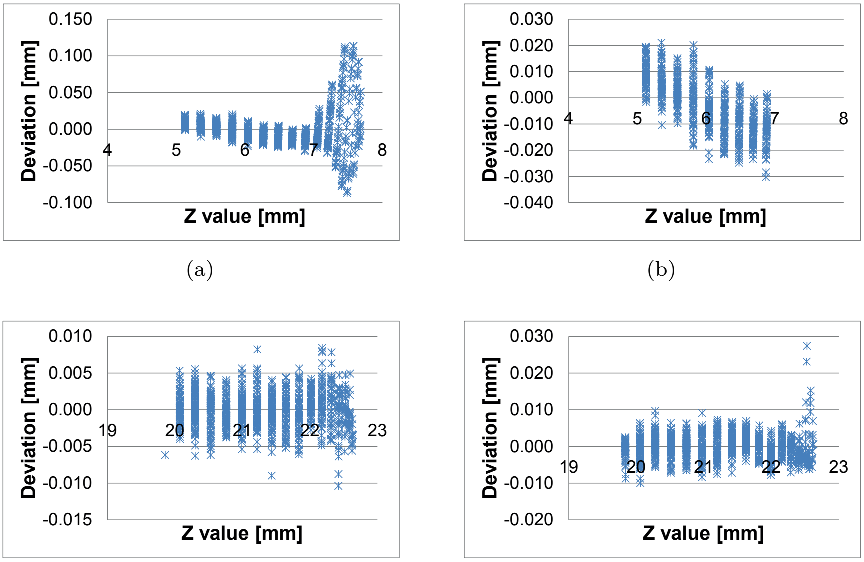

(a) (b)

(c) (d)

Figure 5.58: Fit point deviations in function of their z coordinate for sphere 1 (a), sphere 1 with the top points eliminated (b) and sphere 12 (c) for measurement position 10. (d) shows the fit point deviations of sphere 12 in case of measurement position 8.

Figure 5.59 pictures the **boxplots** of the different analyzed spheres and measurement positions. Figures 5.59a and 5.59b show a symmetric trend which is logical as measurement positions 2-10, 3-9, 4-8, 5-7 are the same (table 5.17). Figure 5.59c however does not show this trend. See also figures 5.58c and 5.58d which show the dependency of z for one measurement position and not for the other. Figure 5.59d has quite similar boxplots independent of the measurement position. There is clearly a difference between sphere 1 and 12, and between the entire sphere and the sphere where the top points are excluded. The box plots of sphere 1 improve when applying a smaller magnification (measurement position 6 has the smallest magnification). The ranges, which are a measure for the measured form deviation, are therefore highly dependent on magnification, sphere number and used fit points. It should be repeated that these spheres have sub micrometer accuracy on their form error.

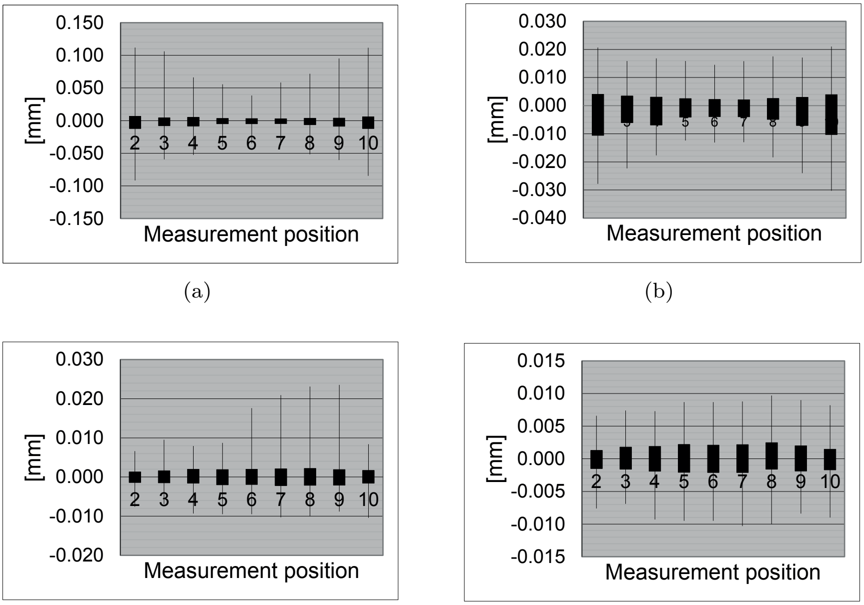

(a) (b)

(c) (d)

Figure 5.59: Boxplots of the fit point deviation data of sphere 1 (a), sphere 1 with the top points eliminated (b), sphere 12 (c) and sphere 12 with the top points eliminated (d).

The **frequency distributions** are pictured in figure 5.60. The fitpoint deviations of sphere 1 (figure 5.60a) are clearly not normally distributed. The other plots already tend more to a normal distribution. The chi-squared test however always evidenced systematic errors, even with a low risk of error.

Figure 5.61 illustrates the **normal probability plots**. A straight line indicates a normal distribution, which is not the case. The normal probability plots of the spheres with exclusion of the top points (figures 5.61b and 5.61d) show a linear trend in the middle, but tails at both sides. Sphere 12 (figure 5.61c) has a large tail at one side: this corresponds to the high positive deviations of figure 5.58d.

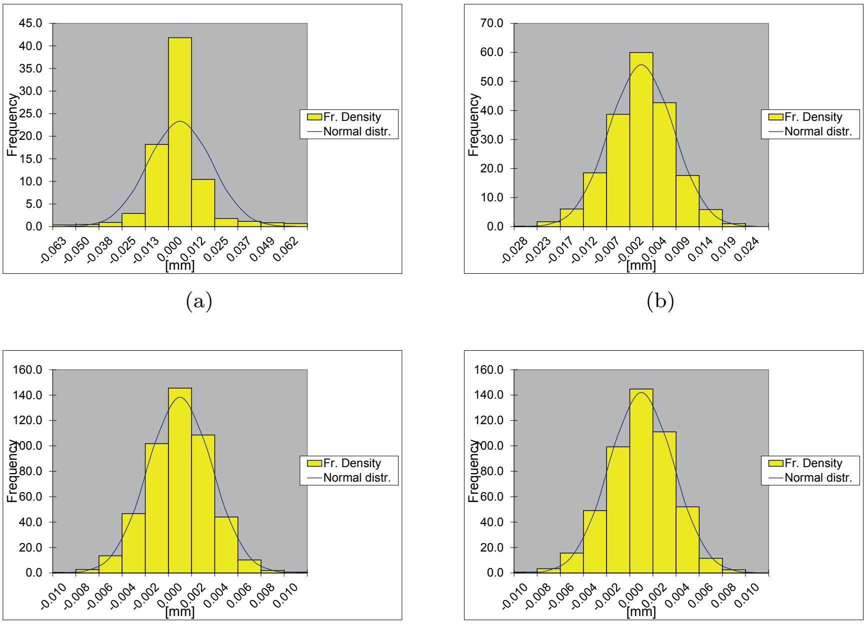

(a) (b)

(c) (d)

Figure 5.60: Frequency distributions of the fit point deviation data of sphere 1 (a), sphere 1 with the top points eliminated (b), sphere 12 (c) and sphere 12 with the top points eliminated (d).

Test hypothesis 1 and ANOVA did not show any evidenced systematic differences between the mean deviation values for the different magnifications in case of **sphere 1 and 12, without exclusion of the top points**. This makes sense as these are the fit point deviations with respect to the least-square sphere through these fit points. Applying ANOVA on the rows did not make sense as the sphere points were ordered randomly.

Test hypothesis 1 and ANOVA evidenced that the differences between the measurement positions and the differences between the fit points (only application of ANOVA) are systematic in case of **sphere 1 with the top part excluded**. This clearly illustrates that cutting (the top) part of the sphere will have its influence on the average deviation values. This will result in another least-square sphere when cutting the top part points. Hence another diameter and center coordinate will be found.

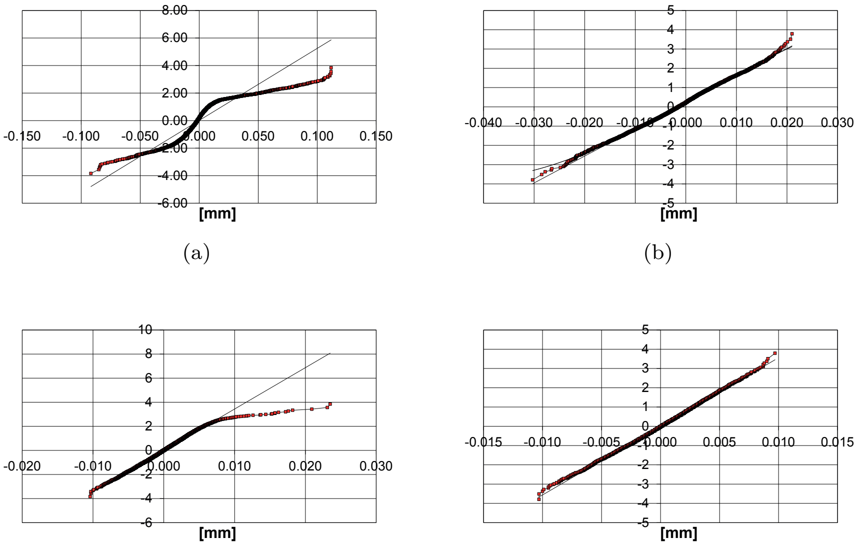

(a) (b)

(c) (d)

Figure 5.61: Normal probability plots of the fit point deviation data of sphere 1 (a), sphere 1 with the top points eliminated (b), sphere 12 (c) and sphere 12 with the top points eliminated (d).

The statistical analysis of **sphere 12 with the top part excluded** is more complicated. Test hypothesis 1 shows systematic differences between the mean deviation values for some of the different magnifications. With a risk of error of 20 percent the measurement positions 4 and 8 resulted to be different from the others, instead with a risk of error of 5 percent only measurement position 8 resulted to be different from the others. In case of ANOVA, differences can or cannot be evidenced for the different magnifications. It is dependent on the applied confidence limit (and therefore the risk). With a risk of error of 20 percent both magnifications and order of fitpoints resulted to be significant, instead with a risk of error of 5 percent only order of fitpoints resulted to be significant.

Test hypothesis 2 concerned the variability of the column effects (i.e. different magnifications). The column variances were checked as compared with variance distribution. This test evidenced systematic differences concerning the variances for the magnifications in case of all 4 investigated spheres. Figure 5.62 plots the variances in function of the magnification (measurement position 6 has the lowest magnification). In case of sphere 1 lowering the magnification leads to smaller variances of the fit point deviation data, whereas for sphere 12 this trend is not present.

It can furthermore be noted that these figures confirm the results of figure 5.52, which showed the fit point deviations of a sphere near the axis of rotation and another sphere: sphere 12 (near the axis of rotation) results in smaller variances, compared to spheres further away from the axis of rotation (in this case sphere 1), this can also be concluded from figure 5.52.

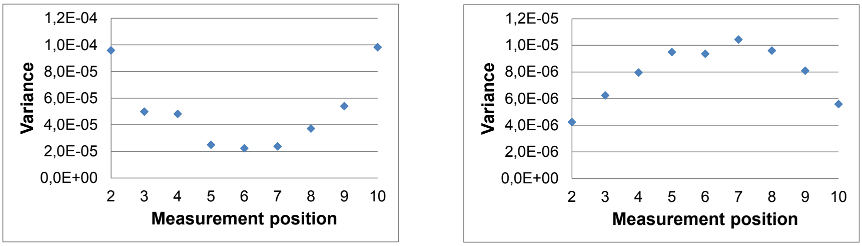

(a) (b)

Figure 5.62: Variance of the fit point deviations for sphere 1 (a) and sphere 12 (b) in function of the magnification.

Fit points: uncertainty on sphere coordinates and diameter

This section researches the uncertainty on the measured sphere coordinates and diameter, and the influence of the fitpoints on these parameters. The investigation has been done for sphere 1 and 12 of measurement position 10 (table 5.17). This section is also worked out in the frame of the PhD course *Measurement uncertainty estimation using statistical methods* taught at the Technical University of Denmark (DTU) [158].

The estimated uncertainty (standard deviation) of the radius and position of the center point (x,y,z) has been calculated. This is done by randomly selecting 300 fit points, calculating the least-square sphere trough these fit points, and hence obtaining the radius and center point coordinates. So 1 radius and 1 center position is obtained. This procedure has been repeated and such it is possible to estimate the uncertainty (standard deviation of the radius and center position coordinates).

Spheres 1 and 12 have been investigated. The number of fit points (coordinates) available was 1008 for both spheres. Sphere 1 has been processed twice. One time with all available fit points and one time with the the top part excluded.

Table 5.28 shows the results. Sphere 12 has the smallest standard deviations. The standard deviations of sphere 1 improves when the top part is excluded. Sphere 1 has mainly a high standard deviation value for the z coordinate of the center point.

Elimination of the top part of sphere 1 causes a shift of the average z position around $4\mu m$. The calculated radius (which has a small standard deviation) is different for sphere 1, sphere 1 with elimination of the top part and sphere 12. This while the calibrated reference values are similar (table 5.14).

	Sphere 1	Truncated Sphere 1	Sphere 12
x	77.6685	77.6674	na
y	114.4690	114.4709	na
z	5.6998	5.6735	na
s_x	0.0020	0.0006	0.0002
s_y	0.0014	0.0005	0.0002
s_z	0.0055	0.0013	0.0004
d	3.9776	3.9810	3.9940
s_d	0.0016	0.0008	0.0004

Table 5.28: Average and standard devations on calculated center point (x,y,z) and diameter of different analysed spheres. All values are expressed in $[mm]$.

Distance errors: statistical analysis

This section is again carried out in the frame of the PhD course *Measurement uncertainty estimation using statistical methods* taught at the Technical University of Denmark (DTU). A statistical analysis similar to the one on the fit points discussed earlier is performed. Five distance errors are investigated: sphere distance 2-3, 10-11, 5-8, 4-7 and 6-9. The reference value (table 5.15) was substracted from the CT measured values. This resulted in data having 5 columns (the 5 CT distances subtracted with the reference distances) and 9 rows which correspond to the 9 measurement positions (position 2 to 10 of table 5.17).

Figure 5.63 shows the boxplots for the analyzed distances. Sphere distance 2-3 is really good. This is logical as this distance was used for rescaling. Distances 10-11 and 5-8 have a negative deviation between -5 and $-20\mu m$, and distances 4-7 and 6-9 have a positive deviation of 5 to $8\mu m$.

Test hypothesis 1 showed systematic differences between the mean deviation values of the different analyzed distances, which is confirmed by ANOVA. The ANAVO did not show evidenced differences for the different measurement positions.

Test hypothesis 2 evidenced systematic differences concerning the variances for the different analyzed distances.

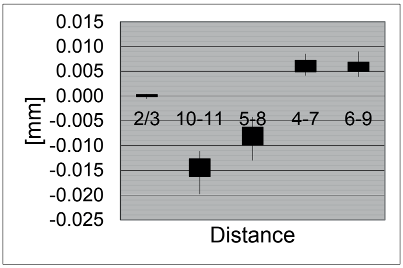

Figure 5.63: Boxplots for errors on sphere distances 2-3, 10-11, 5-8, 4-7 and 6-9.

Gray value profile

Figure 5.64 shows the gray value profiles when using different filter materials. The gray values along a line (from A to B) is given. There are no beam hardening artifacts visible. A different filter plate will result in a different contrast between air and Al_2O_3: the contrast (difference in gray value) is much smaller using the Cu filter.

5.4.4 Conclusion

This section investigated the accuracy with the help of a ruby styli object. The object has been calibrated with the Mitutoyo FN-905 CMM for sphere distance measurements. The sphere diameters were calibrated by an external calibration lab. Measurements are carried out on different magnifications and using different filter plates.

Rescaling of the voxel sizes improved the results. The largest effects were visible on the sphere distances (table 5.18). The original average distance (out of 10 measurements) had a range from -19 to $0\mu m$ with a maximum individual deviation $-31\mu m$. This improved after rescaling (using distance 2-3) to a range of -10 to $8\mu m$, with a maximum deviation of $-15\mu m$. The **rescaling method**

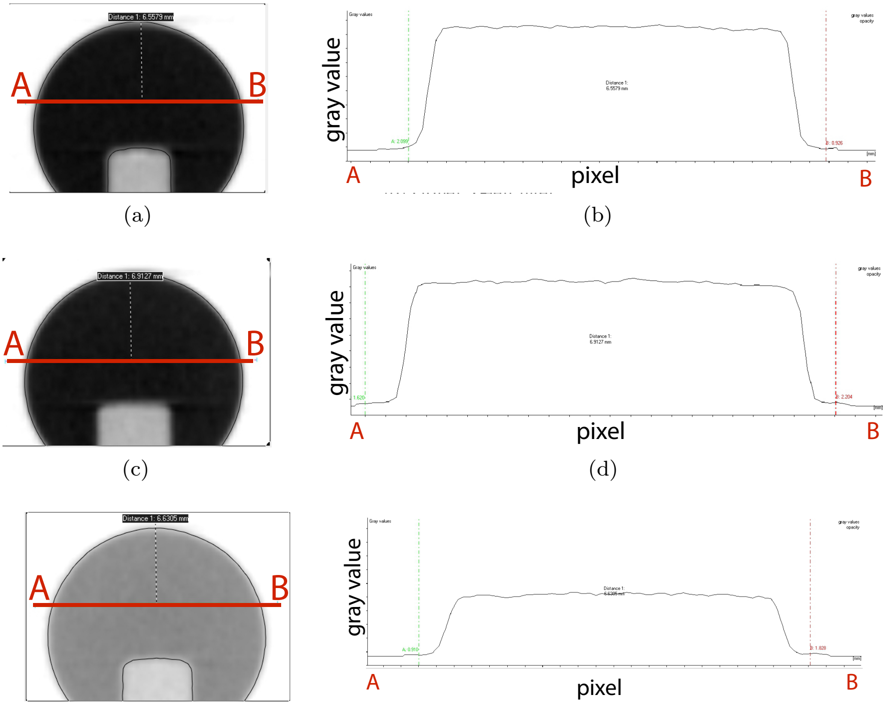

(a) (b)

(c) (d)

(e) (f)

Figure 5.64: Gray value profiles of the Al_2O_3 sphere using no filter (b), a $3mm$ Al filter (d) and a $2mm$ Cu filter (f). The left side of the images show the corresponding reconstructed sphere and the line AB on which the gray value profile is shown.

(rescaling of the voxel size from the reconstructed voxel model versus rescaling by adapting the source-object and source-detector distance) gave no differences.

Although only ruby styli were used, one can still consider it is a multi-material object due to the transition between ruby sphere and carbon fibre stem. This suggested the **use of a region of interest** (ROI). The original diameters (after rescaling on distance sphere distance 2-3) had an average deviation between -50 and $-25\mu m$, with a maximum deviation of $-65\mu m$. Use of a ROI improved the diameter results to a range of -27 to $-16\mu m$, with a maximum deviation of $-29\mu m$.

Changing the **filter plate material** did not give any significant difference regarding the distances. There were however differences regarding the diameter, but this seems to be an offset distance. Adapting the **number of views** from 1000 to 3142 views gave no significant difference for the distance measurements and a small improvement of the diameters. Another investigated influence is the **reconstruction resolution quality** which has no significant influence. Working with the **'minimize ring artifacts'** option only deteriorated the results.

A crucial influence factor appears to be the **object position**. The sphere near the axis of rotation always appears to have the largest value, which is confirmed by positioning another sphere near the axis of rotation. Simulation confirmed this trend and the observed form deviations of the spheres.

It should be added that no diameter measurement compensation has been carried out using the calculated deviation of one 'reference' diameter. This would of course improve the results largely.

In-depth statistical analyses have been performed in the frame of the PhD course *Measurement uncertainty estimation using statistical methods* taught at the Technical University of Denmark (DTU) [158]. First a statistical analysis on the **fit point deviations** of sphere 1 and 12 was considered. Deviation plots of the fit points in function of the z-coordinate (coordinate in height) clearly shows dependency of the z-coordinates. Cutting the top part of the sphere (fit points with high z-coordinate) will reduce the average deviation values and result in other diameter and center coordinate values. The next statistical analysis was on an **uncertainty calculation of the sphere coordinate and diameter**. This was performed by randomly picking a number of fit points and determining the least-squares sphere with according diameter and center point. Elimination of the top part of sphere 1 caused a shift of the average z-position around $4\mu m$. The calculated radius (which has a small calculated standard deviation) was different for sphere 1, sphere 1 with elimination of the top part and sphere 12. This while the calibrated reference values for the radii of sphere 1 and 12 are similar. Sphere 1 mainly had a high standard deviation value for the z-coordinate of the center point: $5.5\mu m$ when top points are not eliminated, $1.3\mu m$ otherwise. The last considered statistical analysis concerns the **distance errors**. Systematic differences between the mean deviation values of the different analyzed distances were confirmed.

These results clearly show the influence of the often applied rescaling procedure using a distance between 2 spheres. The obtained errors between the other sphere distances give an immediate idea of the correctness of this rescaling procedure.

5.5 Multi-material styli object

5.5.1 Object description

The multi-material styli object is pictured in figure 5.65. It is similar to the styli object of previous section, but this time extended with styli of other materials. Table 5.29 gives an overview of the different styli spheres. Styli 13 to 16 are additional to the previous styli object. Styli 13 and 14 have Si_3N_4 spheres of diameter $3mm$. Styli 15 and 16 contain ZrO_2 spheres of $4mm$. The experimental investigations on this object have been mainly performed in the master theses of Denis Indesteege [55] and Tom Hendrickx [49]. [161] and [160] reported the first results for this objects.

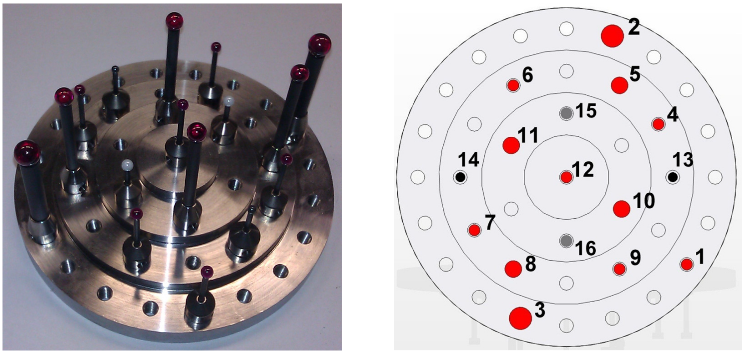

(a) (b)

Figure 5.65: Extended styli object (a) and its schematic representation (b).

5.5.2 Calibration

The extended styli object has been calibrated using the conventional tactile CMM Mitutoyo FN 905 with specified accuracy: $U1 = 4.2 + 5.L/1000\mu m$ (with L in mm, for each axis). The object has been calibrated two times (year A and year B). The object has each time been cleaned and the styli have been tightened again. Tables 5.31 and 5.32 lists the measured distances and results. The measurements have been carried out spread over 2 days. Figure 5.66 shows the CMM measurement results for the distance between spheres 2-3 and 13-14 of year A. Afterwards the standard deviation on each distance has been calculated,

Sphere	Diameter $[mm]$	Material
Sphere 1	4	Al_2O_3
Sphere 2	8	Al_2O_3
Sphere 3	8	Al_2O_3
Sphere 4	4	Al_2O_3
Sphere 5	6	Al_2O_3
Sphere 6	4	Al_2O_3
Sphere 7	4	Al_2O_3
Sphere 8	6	Al_2O_3
Sphere 9	4	Al_2O_3
Sphere 10	6	Al_2O_3
Sphere 11	6	Al_2O_3
Sphere 12	4	Al_2O_3
Sphere 13	3	Si_3N_4
Sphere 14	3	Si_3N_4
Sphere 15	4	ZrO_2
Sphere 16	4	ZrO_2

Table 5.29: Nominal diameter and material of the different sphere styli of the extended styli object.

	Distance	Sphere diameters
1	2-3	$8mm$
2	4-7	$4mm$
3	4-12	$4mm$
4	5-8	$6mm$
5	6-9	$4mm$
6	6-12	$4mm$
7	7-12	$4mm$
8	9-12	$4mm$
9	10-11	$6mm$
10	12-13	4 and $3mm$
11	12-14	4 and $3mm$
12	12-15	$4mm$
13	12-16	$4mm$
14	13-14	$4mm$
15	15-16	$4mm$

Table 5.30: Measured sphere distance and corresponding sphere diameters of the extended styli object.

resulting in a maximum standard deviation value of $1\mu m$ (see tables 5.31 and 5.32)

The calibration values for the sphere diameters are denoted in table 5.33. The calibration measurements are carried out by an external calibration lab.

Distance	Average $[mm]$	Stand. Dev. $[mm]$	Range $[mm]$
2-3	104.946	0.001	0.001
4-7	74.846	0.000	0.001
4-12	38.728	0.001	0.002
5-8	75.334	0.000	0.001
6-9	75.555	0.001	0.002
6-12	38.750	0.001	0.002
7-12	38.761	0.001	0.001
9-12	39.409	0.001	0.002
10-11	44.997	0.000	0.001
12-13	40.924	0.000	0.001
12-14	40.800	0.000	0.001
12-15	26.800	0.001	0.002
12-16	27.124	0.001	0.003
13-14	74.664	0.001	0.001
15-16	44.935	0.000	0.001

Table 5.31: Calibration results for year A. Average value, standard deviation and range for the measured sphere distances. Each measurement has been repeated 5 times at a different position in the measurement volume of the CMM.

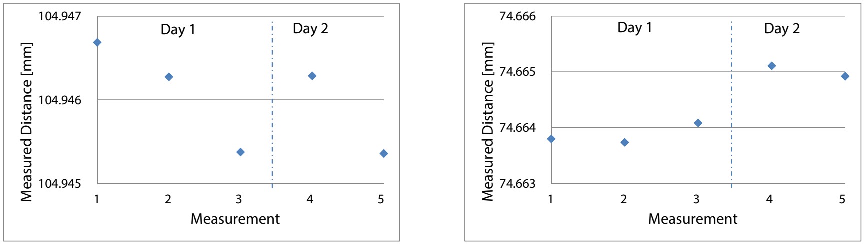

(a) (b)

Figure 5.66: Measured CMM distance in function of measurement number: distance 2-3 (a) and 13-14 (b).

Distance	Average $[mm]$	Stand. Dev. $[mm]$	Range $[mm]$
2-3	104.948	0.001	0.001
4-7	74.846	0.001	0.002
4-12	38.728	0.001	0.002
5-8	75.329	0.001	0.002
6-9	75.522	0.001	0.002
6-12	38.722	0.001	0.002
7-12	38.761	0.000	0.001
9-12	39.408	0.001	0.002
10-11	45.001	0.001	0.002
12-13	40.924	0.001	0.003
12-14	40.799	0.001	0.002
12-15	26.799	0.001	0.001
12-16	27.124	0.001	0.002
13-14	74.664	0.001	0.003
15-16	44.935	0.000	0.001

Table 5.32: Calibration results for year B. Average value, standard deviation and range for the measured sphere distances. Each measurement has been repeated 6 times at a different position in the measurement volume of the CMM.

Sphere	Nominal d	Calibration val $[mm]$
1	4	3.9998
2	8	7.9993
3	8	7.9996
4	4	3.9999
5	6	5.9982
6	4	3.9998
7	4	3.9999
8	6	5.9983
9	4	3.9998
10	6	5.9982
11	6	5.9983
12	4	4.0000
13	3	2.9998
14	3	2.9998
15	4	4.0004
16	4	4.0003

Table 5.33: Calibration values for the sphere diameters. The expanded uncertainty of measurement for all values is $1\mu m$.

5.5.3 CT measurements

Table 5.34 lists the applied settings for the executed CT measurements. It has to be noticed that the measurements using the Al filter have been performed in another time period than the other measurements (therefore year A versus year B).

Filtering	Voltage $[kV]$	Current $[\mu A]$	Year
$3mm$ Al	150	125	year A
$2mm$ Sn	235	490	year B
$4mm$ Sn	320	410	year B
$4mm$ Cu	210	455	year B

Table 5.34: Applied settings to measure the extended styli model.

Table 5.35 shows the sequence of measurements for the Al filter (with magnification value, corresponding voxel size and number of views). Table 5.36 denotes the magnification settings for the scans using the other filter plates, these scans have all been carried out with 1000 views.

	Magnification [/]	Voxel size $[mm]$	Views
Measurement position 1	2.66	0.075	1000
Measurement position 2	2.21	0.091	1000
Measurement position 3	1.88	0.106	1000
Measurement position 4	1.64	0.122	1000
Measurement position 5	1.46	0.137	1000
Measurement position 6	2.66	0.075	3142
Measurement position 7	1.64	0.122	3142
Measurement position 8	1.46	0.137	3142

Table 5.35: Number of views, magnification and corresponding voxel sizes of the different measurements for year A.

Processing of the results

The voxel sizes have always been rescaled using the distance between spheres 2 and 3. Regions of interest are again used instead of the entire spheres, similar as for the ruby styli object (figure 5.49).

Filter plate	Magnification [/]	Voxel size [mm]
$2mm$ Sn	3.25	0.062
	2.8	0.071
	2.66	0.075
	2.21	0.090
	1.88	0.106
	1.8	0.111
	1.46	0.137
$4mm$ Sn	3.25	0.062
	2.35	0.085
	2.21	0.090
	1.88	0.106
	1.8	0.111
$4mm$ Cu	3.25	0.062
	3	0.067
	2.75	0.073
	2.5	0.080
	2.25	0.089
	2	0.100
	1.75	0.114
	1.5	0.133

Table 5.36: Magnification and corresponding voxel sizes for the different measurements per filter of year B.

Gray values

Figure 5.67 compares the projection images of the styli model used in section 5.4 and the extended styli model introduced in this section. The ZrO_2 spheres can easily be recognized: they attenuate the X-rays heavily, and are therefore quite dark in the image. The 2 additional Si_3N_4 spheres can also be seen as two low styli spheres located at both sides of the central stylus, but seem to have similar attenuation properties to the ruby spheres.

Figure 5.68 shows the histogram (after selection of region of interests in a similar way as in figure 5.49) for the styli model containing only ruby spheres and the extended styli model. There is a peak at the right with a much higher gray value. This peaks represents the $Zr0_2$ material. The Si_3N_4 material is difficult to distinguish from the Al_2O_3 material, but there is a small extra peak.

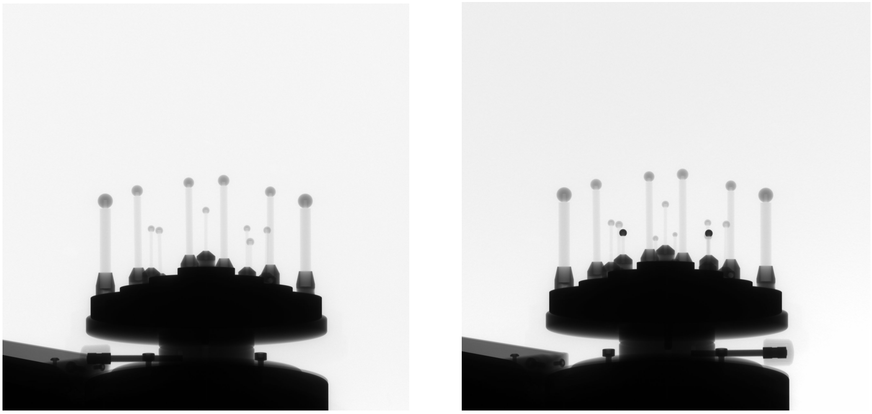

(a) (b)

Figure 5.67: Projection image of the ruby styli object (a) and of the extended styli object (b).

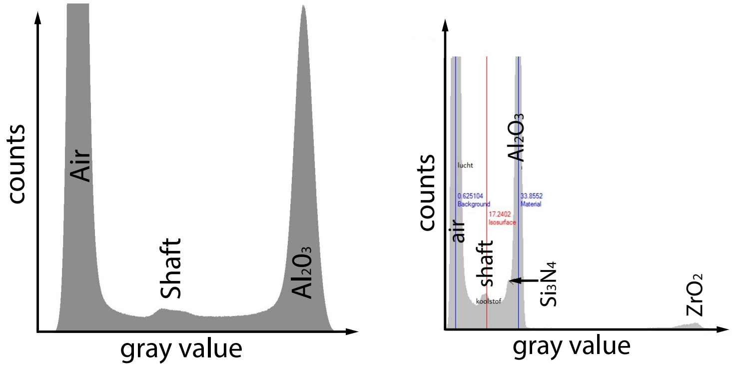

(a) (b)

Figure 5.68: Histogram of the sphere styli of the ruby styli object (a) and of the extended styli object (b).

Number of views

The influence of the number of views has been investigated for the measurements with the $3mm$ Al filter plate (see table 5.35). First we have a look at the effect on the distance measurements. Table 5.37 gives the errors to the reference value after rescaling on distance 2-3 in case of 1000 and 3142 views. The average error of the measurement set as well as the maximum error of these measurement positions is noted (measurement positions listed in table 5.35). Furthermore the average absolute error is calculated. Figure 5.69 pictures the results for distances 13-14 and 5-8 (it must be noted that measurement 1 and 6, 4 and 7, 5 and 8 have the same magnification). No clear difference can be distinguished between the measurements with 1000 and 3142 views.

	Reference value	1000 views		3142 views	
		Average difference	Maximum difference	Average difference	Maximum difference
Dist. 2-3	104.946	0.000	-0.001	0.000	0.000
Dist. 4-7	74.846	0.009	0.011	0.010	0.013
Dist. 4-12	38.728	0.001	0.002	0.001	0.001
Dist. 5-8	75.334	-0.009	-0.014	-0.009	-0.013
Dist. 6-9	75.555	0.008	0.010	0.008	0.011
Dist. 6-12	38.750	-0.001	-0.003	0.000	-0.002
Dist. 7-12	38.761	0.002	0.004	0.003	0.004
Dist. 9-12	39.409	0.001	0.003	0.001	0.002
Dist. 10-11	44.997	-0.009	-0.015	-0.008	-0.013
Dist. 12-13	40.924	0.000	-0.002	0.000	-0.003
Dist. 12-14	40.800	0.000	-0.002	0.001	0.002
Dist. 12-15	26.800	-0.003	-0.007	-0.004	-0.008
Dist. 12-16	27.124	0.001	0.003	0.000	-0.003
Dist. 13-14	74.664	0.012	0.017	0.012	0.018
Dist. 15-16	44.935	0.008	0.010	0.008	0.010
Average absolute error		0.004		0.004	

Table 5.37: Deviations (average and maximum) to the reference distances for 1000 views and 3142 views. All values are expressed in $[mm]$.

Table 5.38 shows the results of the sphere diameters. Figure 5.70 includes the deviations of the $4mm$ spheres. The results of table 5.38 seem to show a small improvement when using 3142 views instead of 1000 views. But if we look at figure 5.70 and compare the scans on the same magnification values (measurement 1 and 6, 4 and 7, 5 and 8) then its difficult to make hard conclusions.

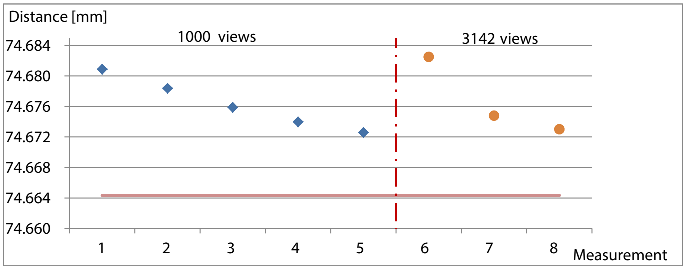

(a)

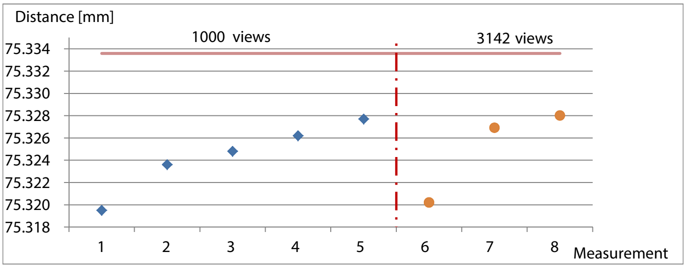

(b)

Figure 5.69: Distances measurements 13-14 (a) and 5-8 (b) in function of the measurements according to table 5.35.

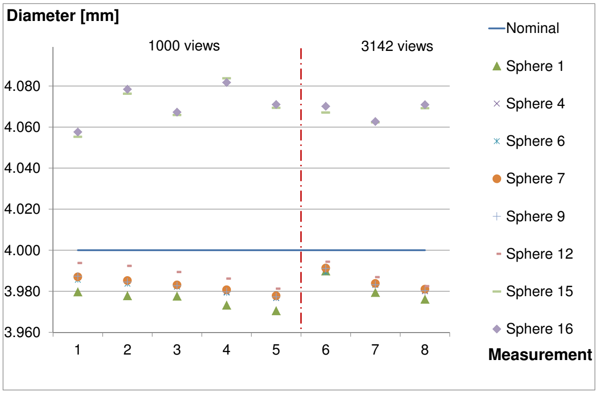

Figure 5.70: Diameter measurement results in function of the measurements according to table 5.35.

	Reference value	1000 views		3142 views	
		Average difference	Maximum difference	Average difference	Maximum difference
Sphere 1	4.000	-0.024	-0.030	-0.018	-0.024
Sphere 2	8.000	-0.015	-0.022	-0.010	-0.016
Sphere 3	8.000	-0.016	-0.022	-0.011	-0.016
Sphere 4	4.000	-0.018	-0.023	-0.015	-0.020
Sphere 5	6.000	-0.018	-0.024	-0.015	-0.020
Sphere 6	4.000	-0.018	-0.023	-0.016	-0.019
Sphere 7	4.000	-0.017	-0.022	-0.015	-0.019
Sphere 8	6.000	-0.017	-0.024	-0.015	-0.020
Sphere 9	4.000	-0.018	-0.023	-0.015	-0.020
Sphere 10	6.000	-0.016	-0.022	-0.016	-0.020
Sphere 11	6.000	-0.016	-0.021	-0.015	-0.019
Sphere 12	4.000	-0.011	-0.019	-0.012	-0.018
Sphere 13	3.000	-0.018	-0.026	-0.016	-0.022
Sphere 14	3.000	-0.019	-0.027	-0.017	-0.023
Sphere 15	4.000	0.070	0.084	0.066	0.069
Sphere 16	4.000	0.071	0.082	0.068	0.071
Average absolute error		0.024		0.021	

Table 5.38: Deviations (average and maximum) to the reference diameter for 1000 views and 3142 views. All values are expressed in $[mm]$.

Gray value profiles

Figure 5.71 compares the gray values profiles for the different investigated spheres using a $3mm$ Al filter. The profile line of the ZrO_2 sphere clearly shows artifacts from beam hardening (cupping effect).

Figure 5.72 pictures the gray value profiles of the ZrO_2 spheres using different filters. As already said there is quite some cupping effect visible while using the $3mm$ Al filter. This cupping effect is also visible for the $2mm$ Sn and $4mm$ Cu filter. This cupping effect is not detectable anymore in case of the $4mm$ Sn filter.

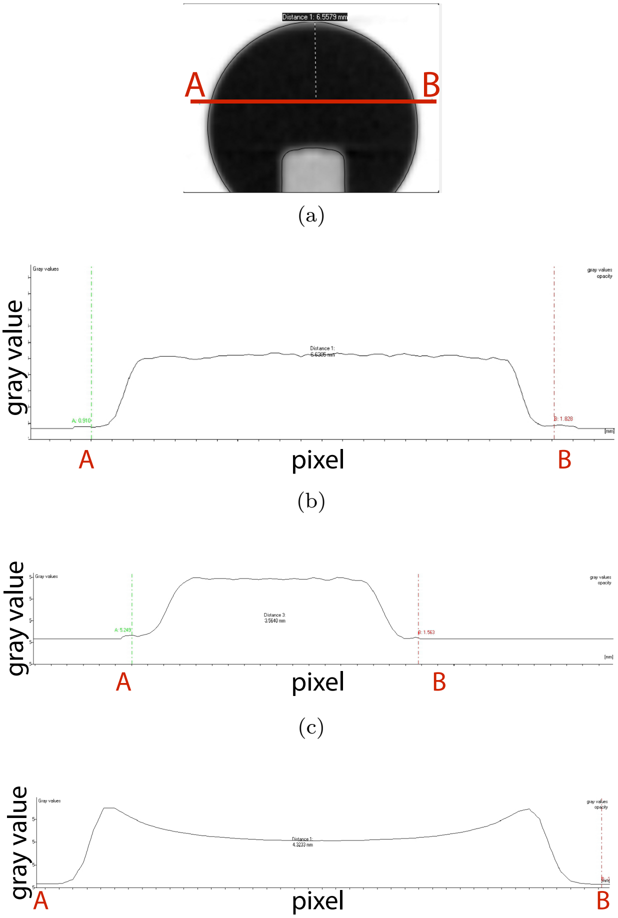

(a)

(b)

(c)

(d)

Figure 5.71: Gray value profile for different sphere materials. The gray values over line A-B (figure (a)) are plotted in case of the ruby sphere (b), the Si_3N_4 (c) and the ZrO_2 sphere (d).

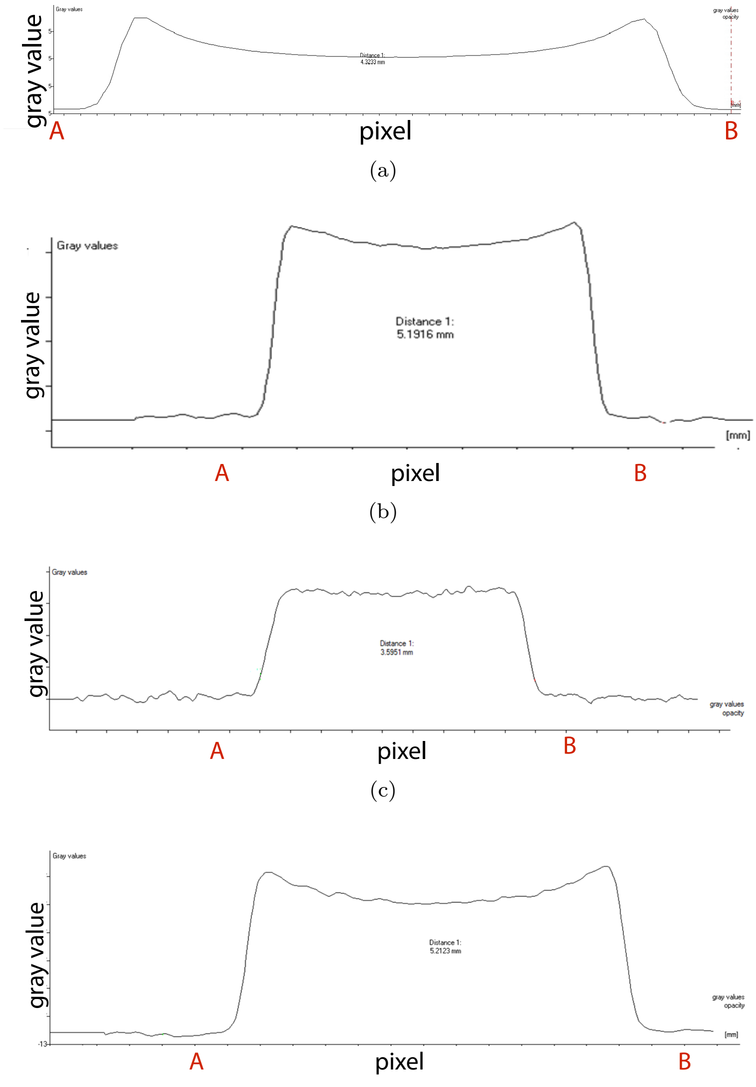

(a)

(b)

(c)

(d)

Figure 5.72: Gray value profile for the ZrO_2 sphere in case of $3mm$ Al filter (a), $2mm$ Sn filter (b), $4mm$ Sn filter (c) and $4mm$ Cu filter.

Recalibration of SDD and SOD distances

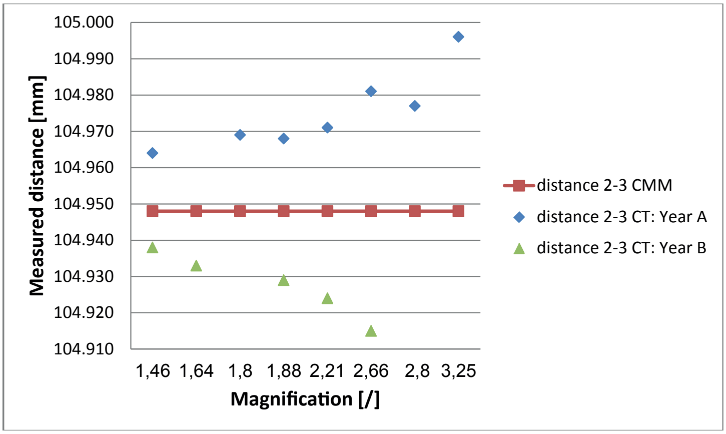

Figure 5.73: Comparison of the distance 2-3 measurement of year A and year B. No rescaling has been applied to these measurements.

This section looks at the results of distance 2-3 when no rescaling is applied. Figure 5.73 compares the measurement values on different magnifications to the reference distance for year A and for year B. The period between the capturing of both measurement sets is more or less a year. There is obviously a difference between these measurement sets. The values of set year A are always too large and these of year B are always too small. Moreover there is for both sets a trend visible with respect to the magnification. The measured value increases with a higher magnification for the set year A, where it decreases for the set year B. The machine values for the source-object distance (SOD) and source-detector distance (SDD) have not been changed between the capturing of both measurement sets (section 2.2.3). The question raises whether a shift of the spot position (due to e.g. a replacement of the filament) explains these differences.

The SOD and SDD values are therefore recalculated using the measured distance results. The SOD and SDD values are normally calculated by the manufacturer using a known distance between 2 spheres, measured at different magnifications (as explained in section 2.2.3). This calculation has been redone for both measurement sets, but this time also the error of the magnification axis (error on the magnification position to the nominal value, calculated in chapter 3) is taken into account. Equations 5.10 to 5.14 show the equation for calculating the actual SOD and SDD values. Table 5.40 lists the calculation values for year B.

All the measured values are firstly recalculated to the values at the detector with equation 5.10.

$$Distance_{detector} = Distance_{Measured} \times \frac{SDD_{CT}}{SOD_{CT}} \tag{5.10}$$

where:

$Distance_{Measured}$ = Measured values as pictured in figure 5.73 $[mm]$.
SDD_{CT} = Available machine value for the source-detector distance $[mm]$.
SOD_{CT} = Available machine value for the source-object distance $[mm]$.

Equation 5.11 now gives the actual (new) source-object distance. The actual source-object distance (SOD) is the current source-object distance used for calculations added with the error on the magnification axis and an unknown constant (offset on the SOD).

$$SOD_{new} = SOD_{CT} + error_{mag} + offset_{SOD} \tag{5.11}$$

where:

$offset_{SOD}$ = Offset (a constant) on the source-object distance $[mm]$.
$error_{mag}$ = Calculated position error on the magnification axis $[mm]$.
SOD_{CT} = Available machine value for the source-object distance $[mm]$.

In theory the value V of equation 5.12 should be a constant independent of the magnification. It is therefore needed to optimize the parameter $offset_{SOD}$ to make V as equal as possible for the different magnification. This results in the offset on the current source-object distance $offset_{SOD}$, and therefore also in the actual Source-Object distance.

$$V = SOD_{new} \times Distance_{detector} \tag{5.12}$$

The next step is to update the source-detector distance. This is done by minimizing the error of the measured value. Equation 5.13 gives the formula for the resulting measured distance. The source-detector distance will be changed to minimize the overall errors (equation 5.14) on the different magnifications.

$$Distance_{MeasuredNew} = Distance_{detector} \times \frac{SOD_{new}}{SDD_{new}} = \frac{V}{SDD_{new}} \quad (5.13)$$

$$Error = ReferenceValue - Distance_{MeasuredNew} \quad (5.14)$$

where:

$ReferenceValue =$ Reference (CMM) value of distance 2-3 $[mm]$.

The resulting source-detector distances and source-object offset distances can be found in table 5.39. The results can be interpreted as a shift of the source spot position of $0.3mm$ along the magnification axis. This clearly shows that the source spot position shifts over time. A regular recalculation of the source-object and source-detector distances is therefore needed or rescaling needs to be performed. Perfect calculation of the source-object and source-detector distances at one single time is not sufficient. Comparison of the new SDD values (1026.802 and $1026.508mm$) and old SDD value $1027.974mm$ furthermore points out the difference whether taking into account the positional error of the magnification axis.

	Year A	Year B	Difference
SDD	1026.802	1026.508	0.294
$offset_{SOD}$	-0.589	-0.892	0.303

Table 5.39: Calculated source-detector distances and source-object offset distances for year A and year B. All values are expressed in $[mm]$.

	Meas 1	Meas 2	Meas 3	Meas 4	Meas 5
Measured distance	104.964	104.969	104.968	104.971	104.981
Current SOD (SOD_{CT})	704.856	570.726	545.394	465.825	385.789
Current SDD (SDD_{CT})	1027.974	1027.974	1027.974	1027.974	1027.974
Distance on detector	153.081	189.067	197.847	231.648	279.733
Error magnification axis	-0.227	-0.028	0.015	0.122	0.229
SOD with error magnification axis	704.629	570.699	545.409	465.947	386.017
New SOD (SOD_{new})	703.737	569.807	544.517	465.055	385.125
V	107728.965	107731.518	107730.804	107729.043	107732.164
New measured distance	104.947	104.950	104.949	104.947	104.950
Error on real value	-0.001	0.002	0.001	-0.001	0.002

Table 5.40: Calculation method to define the actual source-object and source-detector distances. Example calculation performed for measurements of year B. All values (except for V) are expressed in $[mm]$.

Alignment error

Table 5.41 gives the deviations to the reference lenghts for the different investigated distances with respect to the measurement magnification. The presented results are the scans taken with a $2mm$ Sn filter plate. A remarkable observation is that the distance 5-8 and distance 10-11 is always measured to small, and distance 4-7 is always measured too large. Looking back at tables 5.37, 5.22 and 5.18 (after rescaling on distance 2-3) leads to the same conclusions. A possible explanation is the tilt of the rotation axis around x in relationship with the sphere position (see figure 5.74), as explained in table 3.1, alignment 1.

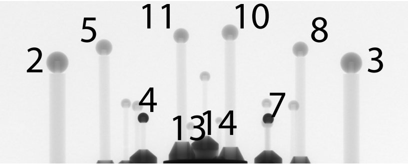

Figure 5.74: Positions of spheres 4, 5, 7, 8, 10 and 11 in the multi-material styli object. This figure is a detail of figure 5.67b.

Furthermore there was the trend seen during the scans of the styli object with ruby spheres only: i.e. the diameter of the center sphere (i.e. sphere 12) is always the largest, the sphere the furthest away from the center (sphere 1) always has the smallest diameter and the other ruby spheres seem to have comparable diameters. (figures 5.51 and 5.42). This trend also still appears as can be concluded out of e.g. table 5.38.

Magnification

Analyzing table 5.41 shows trends for some sphere distances with respect to the magnification: e.g. distance error 13-14 increases while distance errors 5-8 and 10-11 decrease in function of the magnification. A possible cause explaining this observation is the resulting tilt angle of the rotation axis around x (in combination with the sphere position) which is dependent of the magnification position (see angular error component eaz in figure 3.5).

Rescaling method

Figure 5.75 gives the deviations to the nominal values when rescaling after reconstruction using distance 2-3 and the deviations when the reconstruction has been performed using the adapted SOD and SDD values of table 5.39.

	Magnification						
	1.46	1.8	1.88	2.21	2.66	2.8	3.25
Dist. 2-3	0.000	0.000	0.000	0.000	0.000	0.000	0.000
Dist. 4-7	0.016	0.017	0.016	0.020	0.019	0.018	0.022
Dist. 4-12	0.004	0.004	0.005	0.007	0.006	0.005	0.007
Dist. 5-8	-0.002	-0.005	-0.006	-0.008	-0.014	-0.016	-0.019
Dist. 6-9	0.007	0.005	0.004	0.009	0.008	0.010	0.013
Dist. 6-12	0.002	-0.002	-0.001	0.001	-0.001	0.000	0.004
Dist. 7-12	0.009	0.007	0.007	0.008	0.007	0.005	0.005
Dist. 9-12	0.002	0.001	0.000	0.003	-0.001	0.001	0.003
Dist. 10-11	-0.003	-0.006	-0.007	-0.007	-0.014	-0.015	-0.020
Dist. 12-13	0.005	0.007	0.010	0.007	0.010	0.011	0.014
Dist. 12-14	0.008	0.006	0.008	0.011	0.009	0.011	0.017
Dist. 12-15	0.002	0.001	0.006	0.003	0.002	-0.002	0.000
Dist. 12-16	0.003	0.005	0.005	0.004	0.003	0.000	0.001
Dist. 13-14	0.018	0.022	0.022	0.025	0.027	0.026	0.032
Dist. 15-16	0.007	0.006	0.008	0.009	0.010	0.010	0.012

Table 5.41: Distance deviations to the reference lenghts for the different investigated distances.

There is a small difference in distance errors, this is because the SOD and SDD values have been calculated taking into account 5 magnification positions. The errors on the sphere diameters are the same except for sphere 1 which has a small difference. There is no significant difference visible between adapting the SOD/SDD values or rescaling after reconstruction.

Place of filtering

This section researches the effect of the position of the filter plate. The filter plate can be positioned between source and object, or between object and detector. The latter requires a larger plate, but it can be beneficial for extra absorption of scattered X-rays coming from the object. As a test four measurements has been carried out in a row without moving the object to exclude other influences as much as possible. Table 5.42 shows the place of filtering (between source and object, or between object and detector). Measurements 1 and 3 and measurements 2 and 4 are the same. This excludes incorrect conclusions due to e.g. source drift, warming up. Figure 5.76 shows the results: no clear difference can be observed.

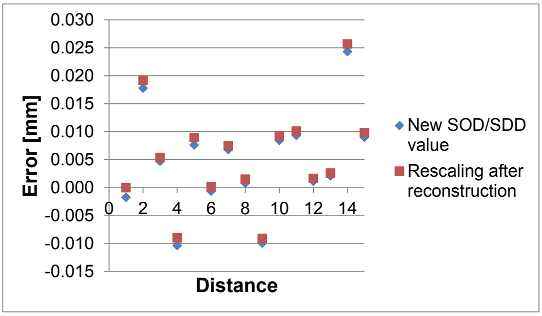

(a)

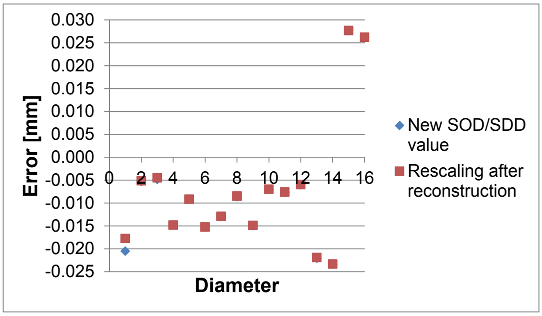

(b)

Figure 5.75: Deviations to the reference value when using an adapted SOD/SDD value compared to rescaling after reconstruction. Errors on the distances (a) and diameters (b). Distance numbering as in table 5.30.

Measurement	Place
Measurement 1	Source
Measurement 2	Detector
Measurement 3	Source
Measurement 4	Detector

Table 5.42: Measurements to investigate the influence of the filter plate position.

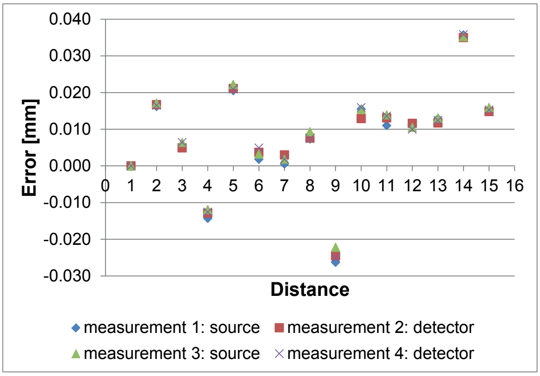

(a)

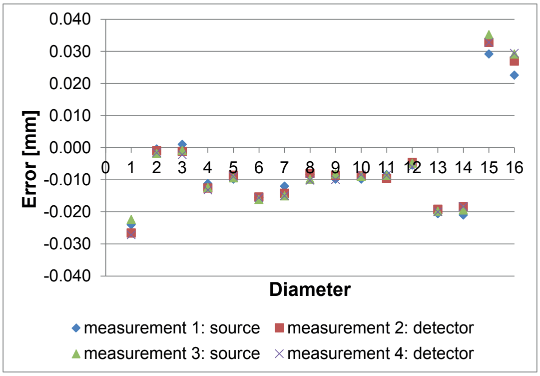

(b)

Figure 5.76: Comparison of the position of the filter plate: errors on the distances (a) and diameters (b). Distance numbering as in table 5.30.

Realignment

It has already been proven that the measurements were subject to alignment errors. The manufacturer was therefore asked to redo the alignment (see section 3.4.4). Two scans (the scans with magnification 1.46 and 3.25 and a $2mm$ Sn filter) are repeated after the realignment by the manufacturer. Figure 5.77 compares the resulting distances of these scans and the same scans with the old alignment. There is clearly a big difference between the 2 alignments. The new alignment has worse results than the previous alignment. The maximum absolute error has changed from around $20\mu m$ to a value around $50\mu m$. Following conclusions can be made regarding distances 4 and 9, which were always measured too small with the previous alignment. Distance 4 (distance between spheres 5 and 8) is still measured too small, but distance 9 (distance between spheres 10 and 11) is now measured too large. These results will be reevaluated in the 'overshoot' section.

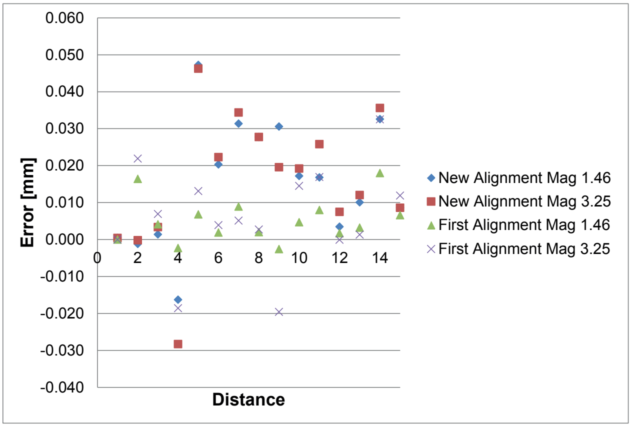

Figure 5.77: Comparison of distance measurements with alignment 1 and alignment 2 (new). Distance numbering as in table 5.30.

Results of the Nikon Metrology XT H 225 ST CT scanner

As the results of the new alignment are worse than the previous results the question was raised if there was maybe an error in the reference values. The distances where once more measured by means of a CMM and the reference values appeared to be correct. A CT scan with the Nikon Metrology XT H 225 CT scanner has also been performed to compare and verify the results. Figure 5.78 pictures the results. It is clear that the large errors found after the new alignment of the XT H 450 CT scanner are not present here. It can thus be concluded that the large errors are indeed due to the XT H 450 CT scanner measurement. The errors obtained by the Nikon Metrology XT H 225 CT scanner are in general better. There are however still errors on some distances of $-15\mu m$ and $+7\mu m$ (these results are obtained after rescaling on distance 2-3). These results will be reevaluated in the next 'overshoot' section.

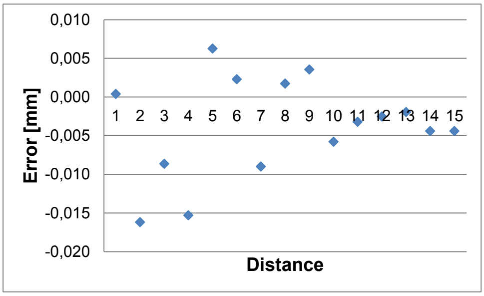

Figure 5.78: Results of the Nikon Metrology XT H 225 CT scanner: Errors on the distance measurements. Distance numbering as in table 5.30.

Overshoot

Figure 5.79 plots the angular errors, in the position of the rotation table, for each view with respect to the nominal angle. It pictures the errors for the measurement performed after alignment 2 of the XT H 450 CT scanner (see figure 5.77). This figure clearly shows the rotation table turning too far. It ends at 360.35 instead of 360 degrees (figure 5.79a).

Figure 5.80 investigates the influence of the rotation angle on distance measurements. Figure 5.80a plots the acquired distance deviations as plotted in figure 5.77, the simulated deviations with all observed mechanical errors and the same simulation with adapted angle. This adapted angle concerns the angle used for the reconstruction. The angle applied in the reconstruction algorithm is normally automatically set to the normal rotation angle. Adapting this value to the estimated rotation angle per view (0.36035 instead of 0.360 degrees) gives the result obtained by 'simulation adapted angle'. This clearly shows one can improve the results by changing the rotation angle value during reconstruction. Figure 5.80b plots the original distance deviations of real CT measurement (same as in figure 5.80a, no simulation), and the deviations after reconstruction of the real projection images (not simulated images) using the adapted rotation angle value. This clearly improves the results. The absolute errors ranging from $-30\mu m$ to $50\mu m$ ameliorate to $-20\mu m$ to $10\mu m$.

The distance results obtained by the 225 kV CT scanner are also repeated with an adapted rotation angle for this scan (see figure 5.81). This again changes the obtained results largely.

This section clearly illustrates the importance of simulation to support experimental research: a researcher would normally relate the difference in deviations of figure 5.77 to the fact the machine has been realigned instead of the hidden overshoot parameter.

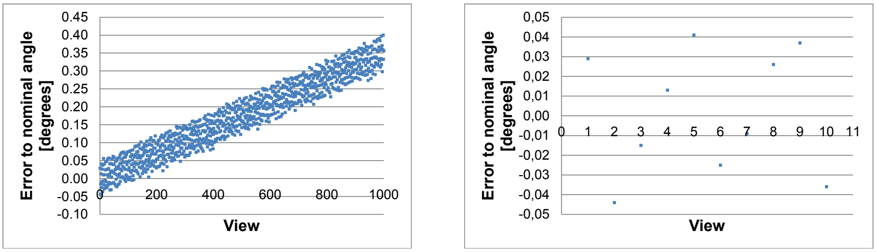

(a) (b)

Figure 5.79: Angular deviation of each view with respect to the nominal angle for all 1001 views (a) and for the 10 first views (b).

Start angle

The overshoot of the rotation table has another crucial consequence: a different start angle (or a rotation of the object around the rotation axis) results in different measurement results. Figure 5.82 shows the influence of the start angle. It pictures two situations for a simulation of the multi-material styli object. Figure 5.82a compares two different start angles in case there is an overshoot (rotation table turning too far) and 5.82b gives the same situation without an overshoot of the rotation table. The start angle clearly affects the results when the rotation table has an overshoot error.

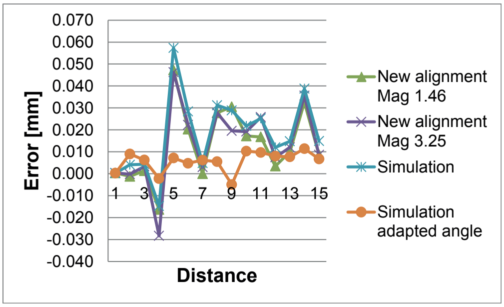

(a)

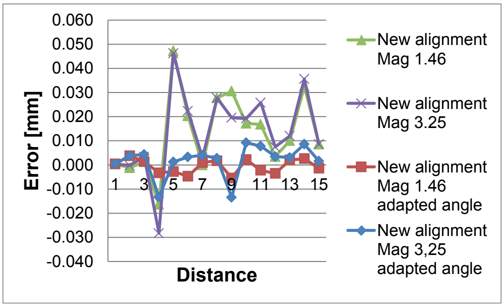

(b)

Figure 5.80: Distance measurements with alignment 2 of the XT H 450 CT scanner: original values ('new alignment mag 1.46' and 'new alignment mag 3.25' in figures (a) and (b)), values after adapting the rotation angle in the reconstruction ('adapted angle' in figure (b)) and simulation (see figure (a)) of the original value ('simulation') and after adapting the rotation angle in the reconstruction ('simulation adapted angle'). Distance numbering as in table 5.30.

Alignment investigation using simulation

Simulation was used to verify the actual influence of the alignment as investigation based on the real CT measurement is hindered due to overshoot errors, different object position, etc. The simulation is based on the CT measurement parameters of year A. The detailed parameter set can be found in table 5.43. The parameters for alignment 1 and 2 can be found in section 3.4.4. The alignment clearly influences the results (figure 5.83). The diameter results are better with alignment 2, whereas the distance results are more accurate with alignment 1.

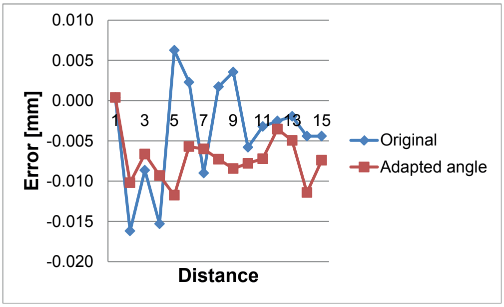

Figure 5.81: Results of the Nikon Metrology XT H 225 CT scanner: original errors on the distance measurements and obtained errors after adapting the rotation angle in the reconstruction. Distance numbering as in table 5.30.

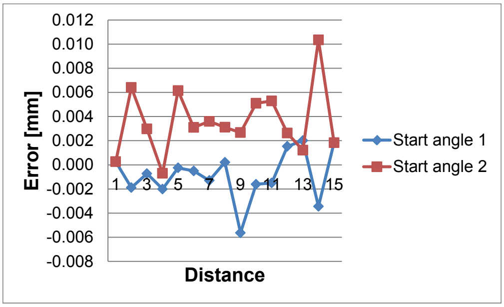

(a)

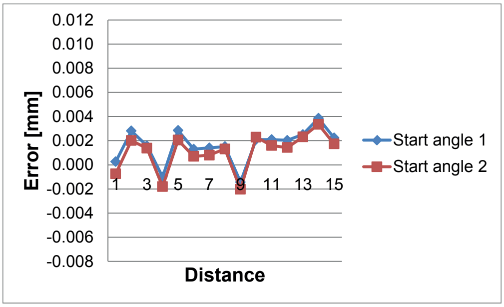

(b)

Figure 5.82: Diameter distance results in relationship to the start angle: with (a) and without (b) an angular overshoot of the rotation table.

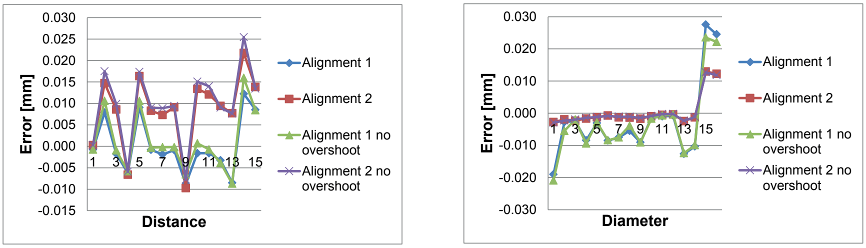

(a) (b)

Figure 5.83: Investigation of the alignment influence (section 3.4.4) using simulation: distances (a) and diameters (b).

Filter plate

Figure 5.84 denotes the resulting distance and diameter deviations when using different filter plates. A $2mm$ Sn filter, $4mm$ Sn filter and a $4mm$ Cu filter are compared with scans taken at magnification 3.25. Figure 5.84a shows similar results on the distance errors for the Sn filters but different results for the Cu filter. Reconstructing all data using an adapted rotation angle in the reconstruction (figure 5.84b) makes the results more similar but there are still some differences. Figure 5.84c mainly shows diameter differences for the $Zr0_2$ spheres; adapting the reconstruction angle value mainly changes the $Zr0_2$ sphere diameters (figure 5.84d).

Multi-material

The diameter measurements are clearly influenced by the sphere material, as can be seen in figures 5.84c, 5.84d and 5.70. Especially the $Zr0_2$ sphere measurements (sphere 15 and 16) differ.

Start contour

Often a single start contour is applied and used for advanced thresholding of the entire object. This section compares the results of using one start contour (i.e. the average value of the air peak value and Al_2O_3 peak gray value) and material-specific start contours. In the latter case three different start contours are applied. The ruby spheres are determined applying advanced thresholding using as start contour the average value of the air peak value and Al_2O_3 peak

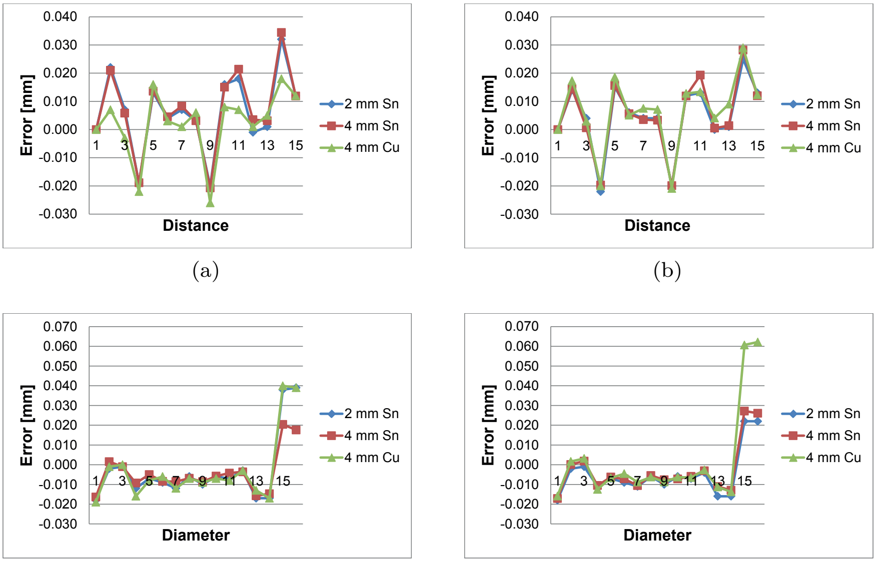

(a) (b)

(c) (d)

Figure 5.84: Comparison of different filter plates: original errors on the distances (a), errors on the distances with adapted rotation angle for reconstruction (b), original diameter errors (c) and diameters errors using an adapted rotation angle for reconstruction. Distance numbering as in table 5.30.

value (figure 5.85a). The average value of the air peak value and Si_3N_4 peak value (figure 5.85b) is taken in case of the Si_3N_4 spheres . The average value of the air peak value and ZrO_2 peak value (figure 5.85c) has been used in case of the ZrO_2 sphere.

Figure 5.86 pictures the same results as in figure 5.84 but obtained after using advanced thresholding applying a material dependent start contour. Figures 5.86a and 5.86b show the distance deviations. Distances 10, 11, 12 and 13 differ, the other distance deviations are similar to figure 5.84. Distances 10 (dist. 12-13, Al_2O_3-Si_3N_4), 11 (dist. 12-14, Al_2O_3-Si_3N_4), 12 (dist. 12-15, Al_2O_3-ZrO_2), 13 (dist. 12-16, Al_2O_3-ZrO_2) are distances between different sphere materials, whereas the other distances are obtained between identical sphere materials. The diameter errors are also different to the original values of figure 5.84. The diameters of the ZrO_2 spheres (spheres 15 and 16) clearly change and improve. Deviations from up to $60\mu m$ decrease to $12\mu m$, but there is still a difference with the other sphere materials.

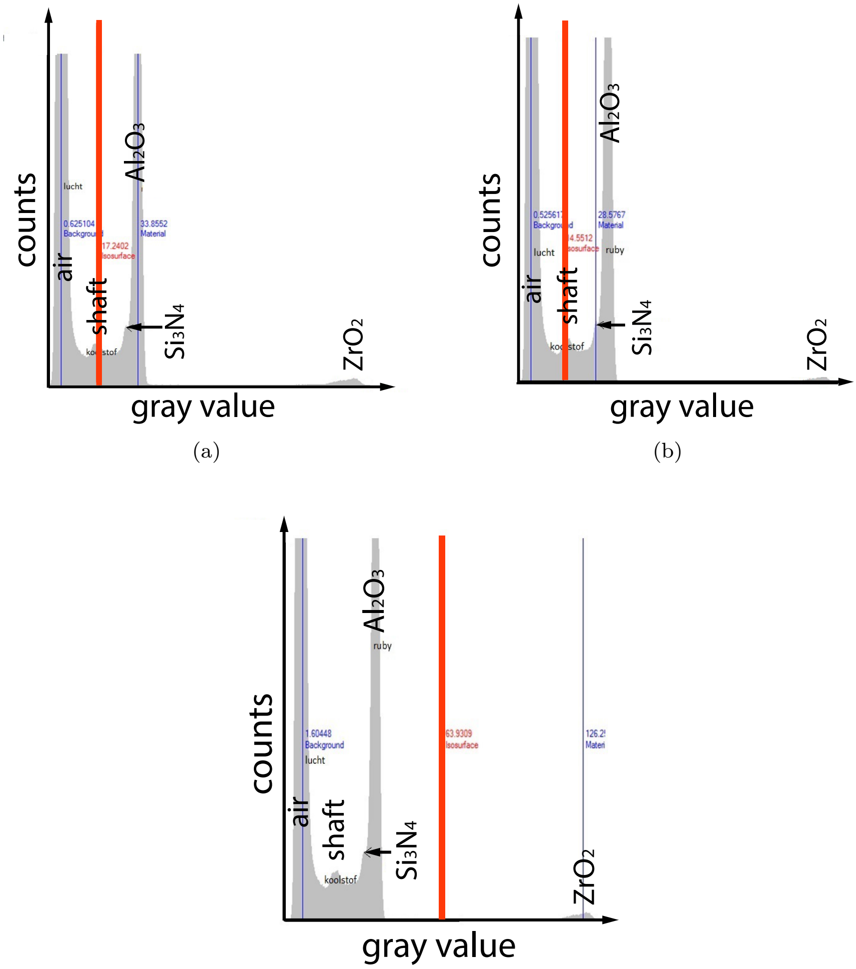

(a) (b)

(c)

Figure 5.85: Histograms with the applied value for the start contour (red line) for material dependent advanced thresholding. Start contour in case of Al_2O_3 (a), Si_3N_4 (b) and ZrO_2 (c) spheres.

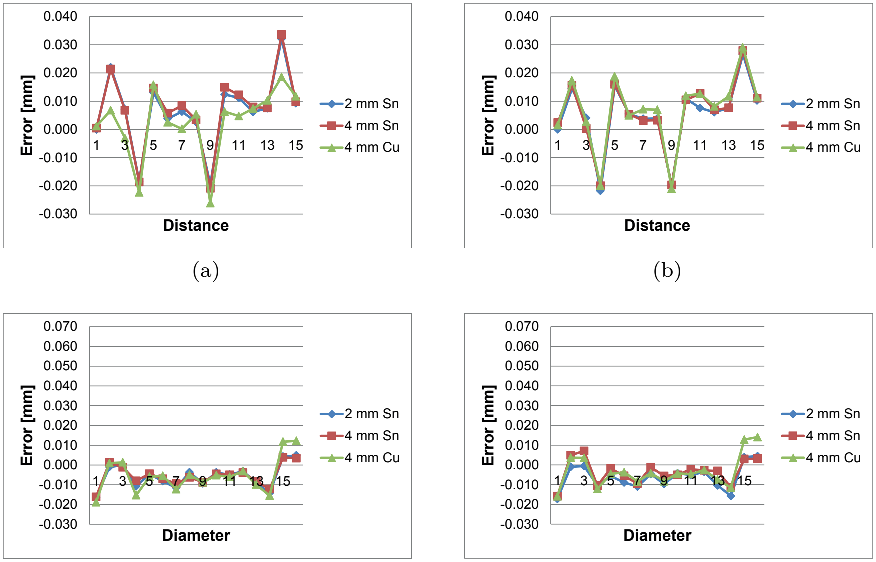

(a) (b)

(c) (d)

Figure 5.86: Comparison of different filters using special thresholding: original errors on the distances (a), errors on the distances with adapted rotation angle for reconstruction (b), original diameter errors (c) and diameters errors using an adapted rotation angle for reconstruction. Distance numbering as in table 5.30.

Stepwise versus continuous scanning (simulation)

Figure 5.87 compares the influence of stepwise versus continuous scanning using simulations. A different scanning method mainly establishes a difference regarding the sphere diameters: up to $10\mu m$ for some diameters. The simulation of the multi-material styli object is performed similar to the CT measurement of year A, measurement position 1 (see tables 5.34 and 5.35). The diameter offset between a measurements with a $2mm$ Cu filter plate and a $3mm$ Al filter plate of figure 5.57 can also be seen in this simulation.

This figure does however not allow to conclude whether using stepwise/continuous or Al/Cu filtering is better. Aluminum filtering with stepwise rotations gives in this particular case the best results for most diameters but not for all. The fact that these errors are furthermore dependent on the position/diameter of the spheres, alignment errors of the mechanical structure and the edge detection algorithm make it impossible to draw hard conclusions regarding the best method to be applied.

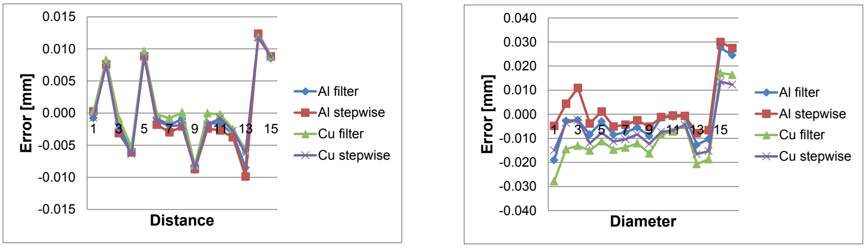

(a) (b)

Figure 5.87: Continuous versus stepwise scanning in case of different filter plates: distances (a) and diameters (b). These results are obtained by simulation.

Parameter variation

A simulation of the multi-material styli object has been performed similar to the CT measurement of year A, measurement position 1 (see tables 5.34 and 5.35). Table 5.43 shows an entire list of the applied simulation settings with their defined uncertainty values. The nominal value and uncertainty values are based on the obtained values in previous chapters and the real CT measurements of the object. A simulation using the nominal value of each parameter has been carried out and multiple simulations with values randomly chosen between the uncertainty limits have been executed.

Figure 5.88 pictures the results and compares it to the real CT measurement. The blue values are the values obtained by multiple simulation runs while choosing a random value from the uncertainty interval. Figure 5.88a shows the distance results: the nominal simulation (simulation using the nominal values) and real measurement slightly differ but it is already a good estimation. Except for distance 4, all distances are included in the range of blue values. This can be due to several facts:

- The correct combination of parameter values has not been accessed yet.
- An important parameter has not been considered yet.
- The real value of a parameter is not in the uncertainty range.

It should be noted that distances 4 (between spheres 5 and 8) and 9 (between spheres 10 and 11) are always too small as was observed in the real CT measurements.

Factor	Nominal value	LUL	UUL
Voltage $[kV]$	150	/	/
Current $[\mu A]$	124	/	/
Filter	$3mm$ Al	/	/
White level	60000	/	/
Applied spectrum	'simulated'	/	/
Spot size $[\mu m]$	Eq. 2.1	-10	+10
Source position x $[mm]$	0	-0.2	0.2
Source position y $[mm]$	0	-0.2	0.2
Source position z $[mm]$	0	-0.2	0.2
Error per source point x $[mm]$	0	-0.01	0.01
Error per source point y $[mm]$	0	-0.01	0.01
Error per source point z $[mm]$	0	-0.01	0.01
Source drift type	'arctan'	/	/
Source drift increment x $[\mu m]$	20	-20	30
Source drift increment y $[\mu m]$	0	-10	10
Source drift increment z $[\mu m]$	40	-40	30
Object translation x $[mm]$	/	-3	3
Object translation y $[mm]$	/	-3	3
Object translation z $[mm]$	/	-3	3
Object rotation x $[rad]$	/	-0.04	0.04
Object rotation y $[rad]$	/	-0.04	0.04
Object rotation z $[rad]$	/	-0.012	0.012
Number of views [/]	1001	/	/
Continuous scan	5	/	/
Distance source-object $[mm]$	384.928	-1	1
Rotation vector	[0,0,-1]	/	/
Include mech. structure errors	1	/	/
Table position	[0 520.295 -70]	/	/
Table zero position	596.5	/	/
Rotation origin x $[mm]$	0	0	0
Rotation origin y $[mm]$	0	-0.05	0.05
Rotation origin z $[mm]$	Formula	-5	5
Additional y error	0.0127	/	/
Tilt rotation axis x $[mm/m]$	-0.6	-1	1
Tilt rotation axis y $[mm/m]$	-5.8	-2	2
Calculation angle errors	'automatically'	/	/
Overshoot $[degrees]$	0.023	-0.08	0.08
Wobble type	'automatically'	/	/
Maximum wobble in x $[\mu rad]$	10	-10	0
Maximum wobble in y $[\mu rad]$	10	-10	0
Eccentricity type	'automatically'	/	/
Maximum eccentricity $[\mu m]$	1	-1	1
Pixel size $[\mu m]$	200	/	/
Detector pixels [/]	2000 by 2000	/	/
Distance source-detector $[mm]$	1026.802	/	/
Magnification error factor [/]	/	0.9995	1.0005
Tilt detector x $[mm/m]$	0.7	-1	1
Tilt detector y $[mm/m]$	0	-2	2
Tilt detector z $[mm/m]$	6	-2	2
Shift detector y $[mm]$	0.5	-0.3	0.3
Shift detector z $[mm]$	0	-0.3	0.3

Table 5.43: Simulation of the multi-material styli object: nominal values and uncertainty ranges defined by the lower uncertainty limit (LUL) and upper uncertainty limit (UUL).

In case of the diameter simulations there seems to be an offset value for the Al_2O_3 spheres (spheres 1 to 12). The main focus has been on the mechanical errors and not yet on the physics related parameters like the voltage, spectrum, exact filter plate material, exact object composition. Figure 5.89 pictures the results of year B and a simulation. In this case the offset is in the other direction. Notify the presence of the observed trend for the $4mm$ spheres in the real measurements: sphere 1 is the smallest; spheres 4, 6, 7 and 9 have similar diameters; and sphere 12 is the largest.

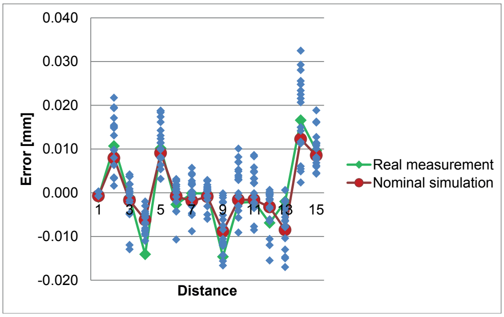

(a)

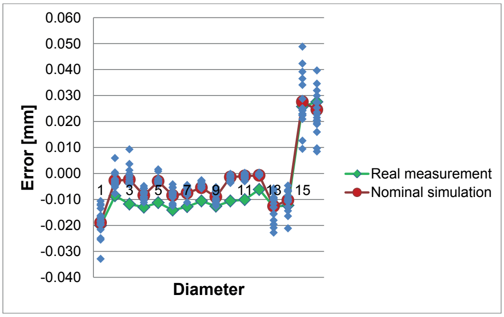

(b)

Figure 5.88: Parameter variation simulations using the settings of table 5.43: distances (a) and diameter (b) errors. The real measurement (green), simulation with the nominal values (red) and simulation results obtained by multiple simulation runs while choosing a random value from the uncertainty interval (blue) are pictured.

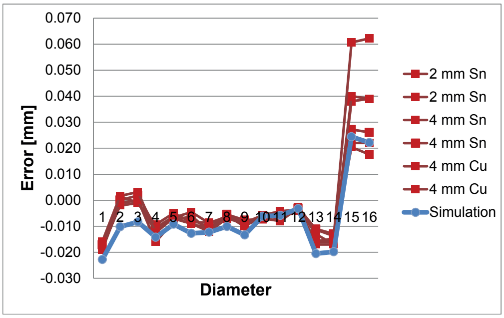

Figure 5.89: Simulation of the multi-material styli object using the settings in accordance with figure 5.84.

CT measurements with line detector

The Nikon Metrology XT H 450 CT scanner is equipped with an additional detector, i.e. the curved linear diode array detector (CLDA) (section 1.7). This section investigates the results acquired by the CLDA detector. This scan requires an extra movement. After each scan of a 2D slice of the object the object moves upwards to scan the next slice (section 2.2.2). The entire styli model has been scanned slice by slice. The reconstructed volume has afterwards been rescaled using distance 2-3 as before. Figure 5.90 compares the results of the CLDA detector and a set of results obtained by the flat panel detector. It is clear that the results obtained by the flat panel detector are much better. Different reasons can cause these deviations.

Incorrect source position with respect to CLDA. The CLDA detector is theoretically a curved detector with a radius of $1200mm$. The source should be positioned in the center point of this curvature, but possibly is not.

Incorrect source-detector distance. The source-detector distance used for reconstruction is set to exactly $1200mm$ (as this should be the distance as explained in previous point), but maybe is not $1200mm$.

Incorrect source-object distance. The source-object distance used for reconstruction was different from the source-object distance used in the reconstruction for the scans with the flat panel detector. This should theoretically be the same distance.

Incorrect software-based geometrical correction. The CLDA detector should theoretically have all its pixels on a perfect curvature. This is in reality not possible, so this should be corrected.

Incorrect rotation vector relative to source-detector plane. The rotation vector should be perpendicular to the plane constructed by the source and detector.

Incorrect movement of the rotation table. The vertical table movement should be perpendicular to the plane constructed by the source and detector. See figure 3.6, error components eyz which contributes to this error.

After discussion with the manufacturer, a maintenance has been carried out. The source-object distance has been repeated and set equal to the distance calculated with the flat panel detector. Furthermore the calibration for the software-based geometrical correction has been repeated. Figure 5.91 pictures the results before and after maintenance. The results are still not good. The first results give negative deviations of $150\mu m$ on the distances which is now shifted to positive errors of $170\mu m$. The largest deviations on the sphere diameters changed from $55\mu m$ to $200\mu m$. A possible improvement is by rescaling each slice by its own scaling factor. This can be done by using a calibration artifact which is scanned each slice, e.g. distance between two cylinders. Nowadays the CLDA is often used for scanning slices of turbine blades. Often only a few slices are scanned and these slices are separately rescaled instead of using one global rescaling factor as done in our experiment.

5.5.4 Conclusion

This section interrogated the accuracy of the Nikon Metrology XT H 450 CT scanner with the help of a multi-material styli object. This object is an extension of the previous ruby styli object. The voxel sizes have always been rescaled using the distance between spheres 2 and 3. Regions of interest are again used instead of the entire spheres, similar as for the ruby styli object.

The section started with an analysis of the **gray values**. Three different sphere material peaks could be distinguished, the ZrO_2 peak was clearly separate, whereas the peak of Si_3N_4 was laying close to the Al_2O_3 peak.

Measurements on this object were carried out on 2 different years. Comparison of these measurements and recalculating the source-object and source-detector distance, taking into account the magnification errors, led to a calculated **source position shift** of $0.3mm$ between the two years.

The observed **trends** during the ruby styli sphere object were again visible: distance 5-8 and distance 10-11 is always measured to small; the diameter of the center sphere (i.e. sphere 12) is always the largest; the sphere the furthest

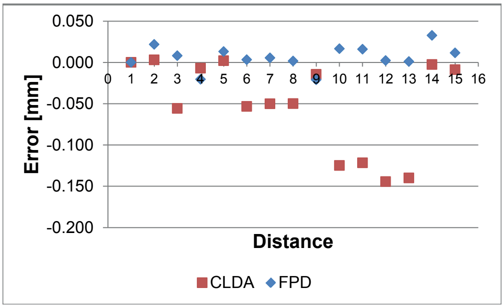

(a)

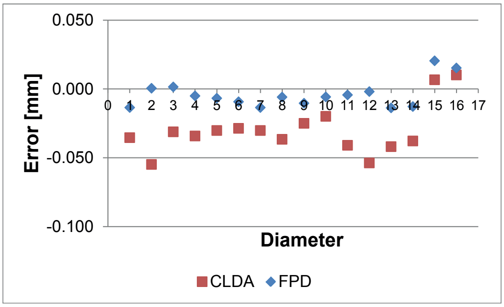

(b)

Figure 5.90: Comparison of the results (deviations of the sphere diameter and distances) obtained by the flat panel detector and CLDA. Distance numbering as in table 5.30.

away from the center (sphere 1) always has the smallest diameter and the other ruby spheres seem to have comparable diameters. These trends were confirmed by simulation.

The **rescaling method**, **place of filtering** and **number of views** did not show clear differences.

Changing the **magnification** gave trends dependent on the measured sphere distance couple.

Scans before and after **realignment** of the source, rotation table and detector positions first resulted in a change of maximum absolute errors for the distances from $20\mu m$ to a value around $50\mu m$. Simulation however pointed out the underlying influence factor: the **overshoot** of the rotation table. Reconsidering the **reconstruction angle** improved the distance results of the new alignment from a range of -30 to $50\mu m$ to a range of -20 up to $10\mu m$. Simulation is

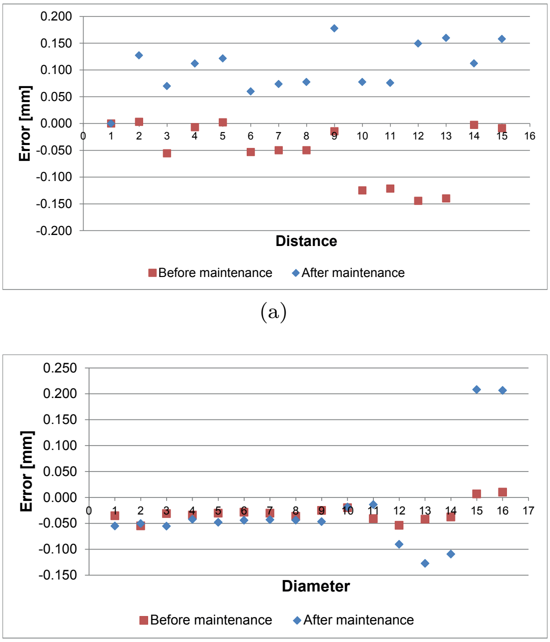

(a)

(b)

Figure 5.91: Comparison of the results (deviations of the sphere diameter and distances) obtained by the CLDA before and after maintenance. Distance numbering as in table 5.30.

used to verify the actual influence of the alignment: alignment 1 gave better results for the distances whereas the diameters where measured more accurate with alignment 2. The unwanted overshoot parameter revealed another crucial consequence: a different **start angle** results in different measurement results. This was interrogated with simulation. Simulation clearly illustrated this difference in case of a rotation overshoot.

The influence of different sphere materials was undoubtedly visible in the results. There is clearly an offset on the diameter measurements. Use of a **filter plate** mainly results in differences for the sphere diameter measurements of the ZrO_2 spheres. Applying a **material dependent start contour** clearly changed and improved the ZrO_2 sphere diameters. Deviations from up to $60\mu m$ decrease to $12\mu m$, but there is still a difference with the other sphere materials. A material dependent start contour also changed the sphere distance couple measurements between spheres of different material.

Simulation has been applied multiple times to support the experimental investigation. The simulation results show many parallels to the real CT measurements: the trends were similar and the obtained values were quite similar. Only an offset on the diameter measurements was visible and should be further investigated. Simulation was furthermore used to compare **stepwise versus continuous scanning**. Differences for the sphere diameters up to $10\mu m$ were obtained.

The multi-material styli object was at last also measured with the **curved linear diode array detector (CLDA)**. The results were much worse than those obtained by the flat panel detector. Two scans were considered: before and after maintenance. The first results gave negative deviations of $150\mu m$ on the distances which is shifted to positive errors of $170\mu m$ after maintenance. The largest deviations on the sphere diameters changed from $55\mu m$ to $200\mu m$.

It should be reminded that no additional correction for material dependent edge errors has been carried out. Compensation by measuring a reference object of the same material would improve the diameter measurements heavily.

5.6 Stepped cylinder

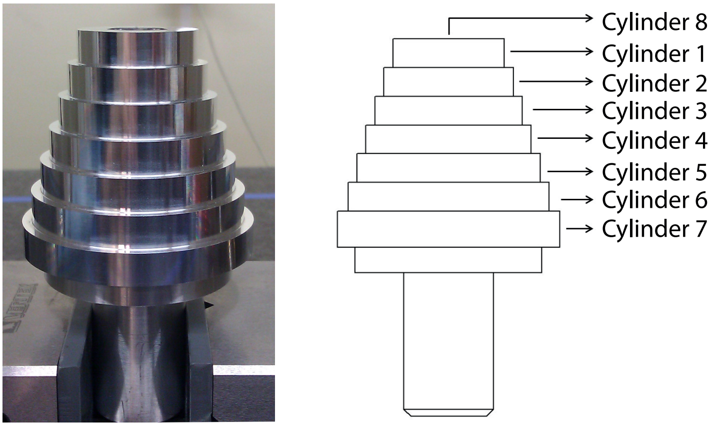

(a) (b)

Figure 5.92: Stepped cylinder (a) and its schematic representation (b).

Figure 5.92 shows the next investigated object: a stepped cylinder. As discussed earlier there is today a lack of well defined reference objects and procedures suited to assess the accuracy of CT-based CMMs, and to compare the

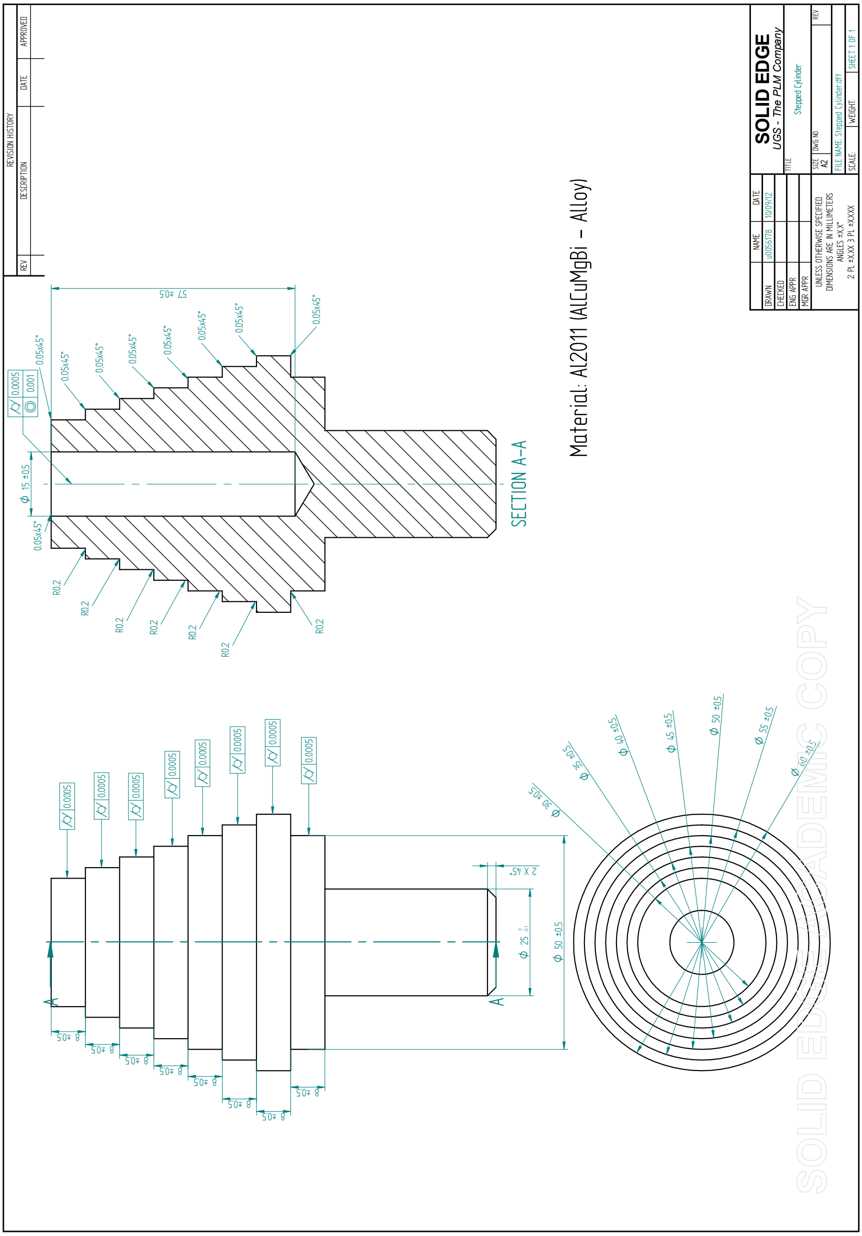

Figure 5.93: Technical drawing of the stepped cylinder.

performance of various CT measuring devices. However there is the VDI/VDE 2630 standard [147] with guidelines. These guideline discusses the use of a stepped cylinder with an extra internal hollow cylinder. This guideline has been applied to design the object.

The experimental investigations of this object have been mainly performed in the master theses of Denis Indesteege [55] and Tom Hendrickx [49].

5.6.1 Object description

The technical drawing can be found in figure 5.93. The object is made of Aluminum, more in particular Al2011. The 2000 series are alloyed with copper and can be precipitation hardened to strengths comparable to steel. Applications of the 2000 series are for instance found in aerospace domain. The material is therefore representative for measurements to be carried out by the Nikon Metrology XT H 450 CT scanner.

The stepped cylinder has been produced in two steps. The first step is performed on a conventional manual lathe. It includes a rough turning step with a material excess of $1mm$, and the drilling of the inner hole. Next the object has been finished on the SB-CNC Spinner lathe (figure 5.94). The inner as well as the outer diameter has been finished with a diamond cutting tool.

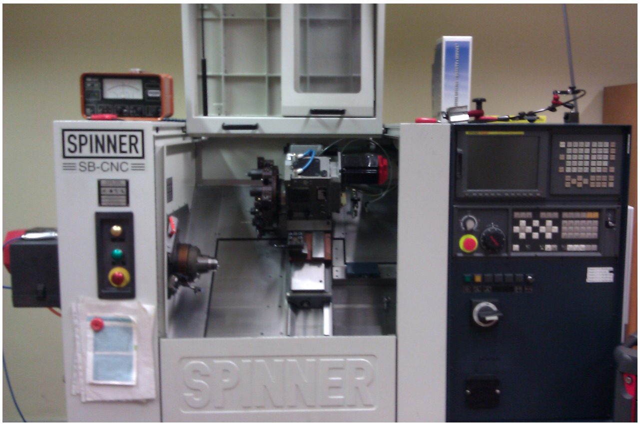

Figure 5.94: Spinner SB-CNC.

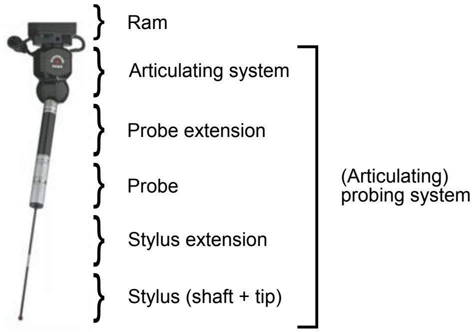

Figure 5.95: Components of a CMM probing system.

5.6.2 Calibration

Similar to the measurements on the extended stylus object, measurements of the stepped cylinder have been carried out in two different years (year A and year B). Table 5.44 shows the used probe configuration (designation as in figure 5.95) for the CMM measurements in year A. The inner diameter and outer diameters have been measured with a different setup (i.e stylus diameter, with/without probe extension). This enables to measure the entire inner cylinder, but also a larger part of the outer cylinders.

Probe type	Medium force
Stylus length for inner cylinder	$60mm$
Stylus diameter for inner cylinder	$5mm$
Stylus setup for inner cylinders	Without probe extension
Stylus diameter for outer cylinders	$2mm$
Stylus setup for outer cylinders	With probe extension

Table 5.44: CMM probe configuration for the measurements of year A.

Table 5.45 summarizes the results of the calibration of year A. Seven measurements have been carried out spread over 2 days, where the object is repositioned between the measurements.

The object has been recalibrated for year B. Whereas the calibration value of the styli model can slightly change due to cleaning and tightening again of the styli, it is expected that the stepped cylinder has not changed. Table 5.46 shows the measurement setup and table 5.47 the results. It is clear that the values differ from the previously obtained results of year A. Furthermore the standard deviation and ranges are higher. This is probably due to the use of the high

	Average $[mm]$	Stand. Dev. $[mm]$	Range $[mm]$
Cylinder 1	30.001	0.000	0.001
Cylinder 2	35.003	0.000	0.001
Cylinder 3	40.003	0.000	0.001
Cylinder 4	45.004	0.001	0.002
Cylinder 5	50.003	0.001	0.002
Cylinder 6	55.004	0.000	0.001
Cylinder 7	60.008	0.001	0.002
Cylinder 8	14.999	0.001	0.003

Table 5.45: Reference results of year A. Average value, standard deviation and range for the measured cylinder diameters. Each measurement has been repeated 7 times at a different position in the measurement volume of the CMM.

force probe instead of the medium force probe. Comparison of the diameters of year A and B (table 5.48) shows an offset between the two measurements, with opposite sign for inner and outer diameters.

Probe type	High force
Stylus length	$60mm$
Stylus diameter	$5mm$

Table 5.46: CMM probe configuration for the measurements of year B 1.

	Average $[mm]$	Stand. Dev. $[mm]$	Range $[mm]$
Cylinder 1	29.995	0.002	0.004
Cylinder 2	34.997	0.002	0.006
Cylinder 3	39.997	0.001	0.002
Cylinder 4	44.996	0.001	0.002
Cylinder 5	49.995	0.001	0.003
Cylinder 6	54.998	0.001	0.003
Cylinder 7	60.002	0.002	0.004
Cylinder 8	15.006	0.001	0.003

Table 5.47: Reference results of year B1. Average value, standard deviation and range for the measured cylinder diameters. Each measurement has been repeated 7 times at a different position in the measurement volume of the CMM.

The measurements have been repeated on two different days (results addressed as year B2 and year B3) with the measurement setups in table 5.49, but this time ring gauges have been measured together with the stepped cylinder. The average deviation of the measured ring gauge diameters to the nominal diameter is calculated, and the diameters of the cylinders are compensated by

	Year A $[mm]$	Year B1 $[mm]$	Difference
Cylinder 1	30.001	29.995	-0.006
Cylinder 2	35.003	34.997	-0.006
Cylinder 3	40.003	39.997	-0.006
Cylinder 4	45.004	44.997	-0.007
Cylinder 5	50.003	49.996	-0.007
Cylinder 6	55.004	54.998	-0.006
Cylinder 7	60.008	60.002	-0.006
Cylinder 8	14.999	15.007	0.007

Table 5.48: Comparison of the results of year A and year B1.

adding/subtracting this value. Figure 5.96a gives the results without correction using the ring gauges. Figure 5.96b shows the results for measurements with setup 2 and 3 of year B, where the deviation to the ring gauge diameters is used to compensate for offset errors. The compensated results are similar in contrary to the non compensated results.

Probe type	Medium force
Stylus length	$25mm$
Stylus diameter	$2.5mm$

Table 5.49: CMM probe configuration for the measurements of year B 2 and year B 3.

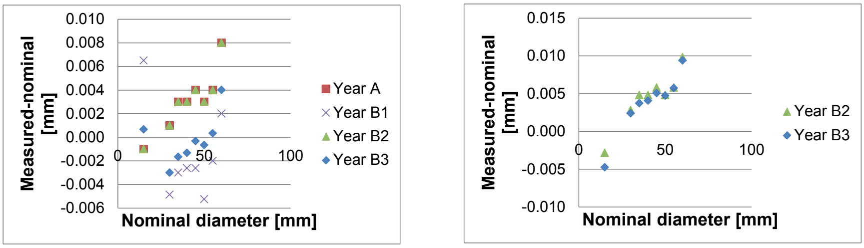

(a) (b)

Figure 5.96: CMM results of the stepped cylinder diameters: without compensation (a) and with compensation using ring gauges (b).

5.6.3 CT measurements

The stepped cylinder has also been scanned by means of computed tomography in two different time periods: year A and year B. The influence of different magnifications has been investigated in year A, with the acquisition settings of table 5.50 and the magnification settings in table 5.51.

Gain $[dB]$	Exposure time $[ms]$	Voltage $[kV]$	Current $[\mu A]$	Filter
24	1000	360	110	$2mm$ Cu

Table 5.50: CT acquisition settings year A.

	Magnification [/]	Voxel size $[mm]$	Views
Measurement position 1	4.55	0.044	1000
Measurement position 2	3.16	0.063	1000
Measurement position 3	2.26	0.089	1000
Measurement position 4	1.85	0.108	1000
Measurement position 5	1.57	0.127	1000
Measurement position 6	1.57	0.127	1650
Measurement position 7	2.26	0.089	1984
Measurement position 8	4.55	0.044	3142

Table 5.51: Number of views, magnification and corresponding voxel sizes of the different measurements of year A.

Table 5.52 shows the acquisition settings of year B used to investigate the influence of gain and exposure time. Furthermore the difference between using a filter plate between the source and object and between the object and detector has been explored using the measurements represented in table 5.53.

	Gain $[dB]$	Exposure time $[ms]$	Voltage $[kV]$	Current $[\mu A]$	Filter
Meas. 1	24	1000	215	215	$2mm$ Cu
Meas. 2	18	2000	215	215	$2mm$ Cu
Meas. 3	12	4000	215	215	$2mm$ Cu
Meas. 4	6	4000	215	410	$2mm$ Cu
Meas. 5	0	4000	215	365	$2mm$ Cu

Table 5.52: CT acquisition settings year B, set 1.

Gain	$0dB$
Exposure time	$4000ms$
Voltage	$220kV$
Current	$365\mu A$
Magnification	3
Filtering meas. 1	$2mm$ Cu source
Filtering meas. 1	$2mm$ Cu detector
Filtering meas. 1	$2mm$ Cu source
Filtering meas. 1	$2mm$ Cu detector

Table 5.53: CT acquisition settings year B, set 2.

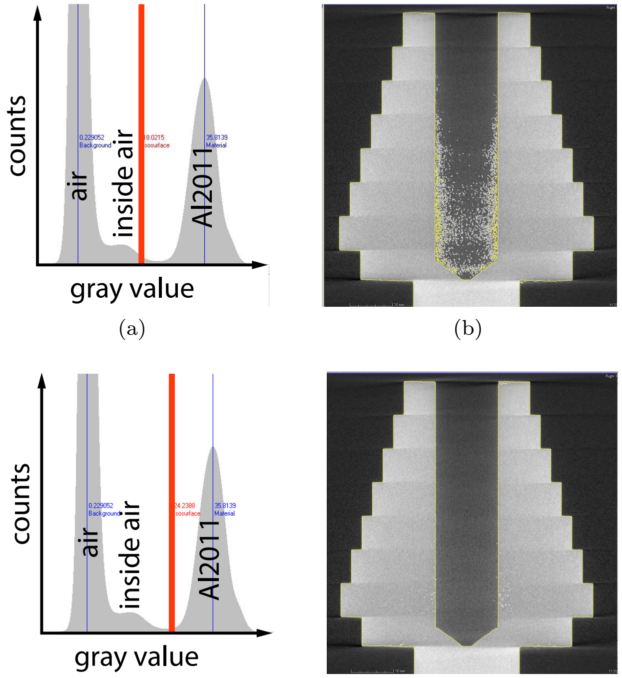

(a) (b)

(c) (d)

Figure 5.97: Influence of start contour on reconstructed image for the measurement of year A: start contour (red line) closer to the $Al2011$ peak (c) gives less artifacts (d).

Start contour

First we have a look at the influence of the start contour. Figure 5.97 shows the reconstructed images after use of two different start contours for the measurements of year A. The start contour in the center between the air and $Al2011$ peak (5.97a) leads to image artifacts (5.97b). Taking the start contour closer to the $Al2011$ peak solves this problem (figures 5.97c and 5.97d), but shifting the start contour influences the dimensional measurements. Furthermore it is to be noticed on figures 5.97 (a) and (c) that there is also a small third peak: i.e. the air inside the stepped cylinder. Figure 5.99 shows the gray value profile over a line AB. Also here the gray value of air is clearly higher in the center (inside the stepped cylinder) than outside the object. Figure 5.98 pictures results obtained with the simulation program. Simulation with a polychromatic source concludes the same: gray value of the air inside the stepped cylinder is higher than outside. A monochromatic simulation gives the same gray value for in and outside the object.

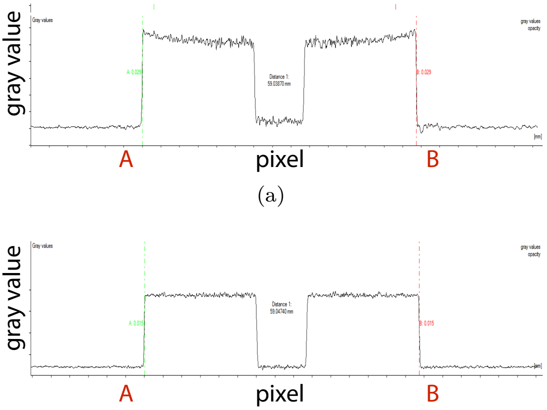

(a)

(b)

Figure 5.98: Simulated gray profile in case of polychromatic (a) and monochromatic (b) X-ray spectrum.

Gain/exposure time combination

The influence of detector gain and exposure time is investigated (see section 2.3 for an explanation on these values). Table 5.52 gives the used settings. The gain has been lowered and the exposure time has been raised. Only lowering the gain would result in dark images, so we have to compensate for this in a way, e.g. by raising the exposure time. $4000ms$ is the maximum available exposure,

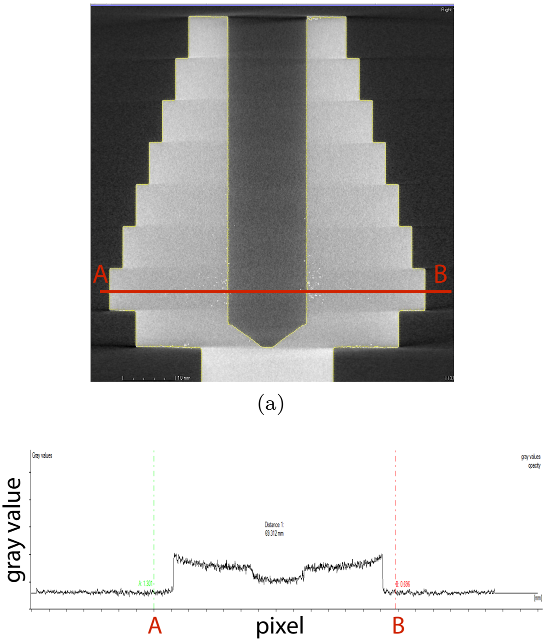

(a)

(b)

Figure 5.99: Gray value profile (b) on line AB of the reconstructed object (a) in case of CT scan of year A.

therefore the current is raised in measurement 4 to keep a good setting. The target was turned before measurement 5, explaining the lower current here compared to measurement 4.

Figure 5.100 pictures the gray value profile lines for the scans with different gains (table 5.52). There is clearly an effect of the different combinations of gains and exposure times on the gray value profile. The noise has lowered. This positive effect can also clearly be seen on the reconstructed images. Figure 5.101 compares the reconstructed image when using gains $24dB$ and $0dB$. It was not possible to obtain a nice image for the settings of gain $24dB$.

Figure 5.102 gives the histogram for the $0dB$ CT scan. Here we can distinguish some extra peaks. The $Al2011$ material is divided in the stepped cylinder material and the socket material of the stepped cylinder (full cylinder). Furthermore this socket is clamped in a wooden block which we can also see in the gray value histogram.

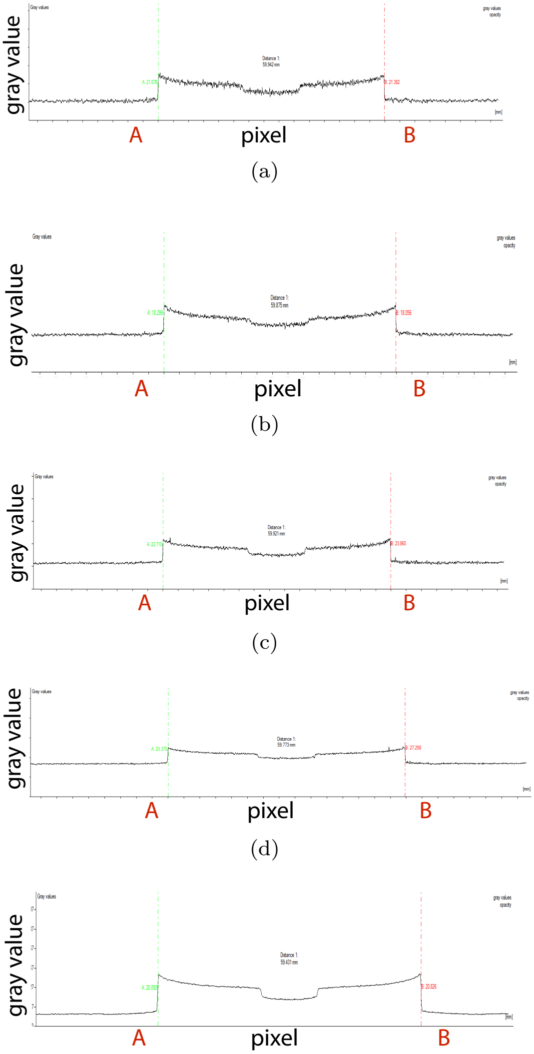

(a)

(b)

(c)

(d)

(e)

Figure 5.100: Gray value profiles on line AB (figure 5.99a) for different gains according to the settings of table 5.52: $24dB$ (a), $18dB$ (b), $12dB$ (c), $6dB$ (d), $0dB$ (e).

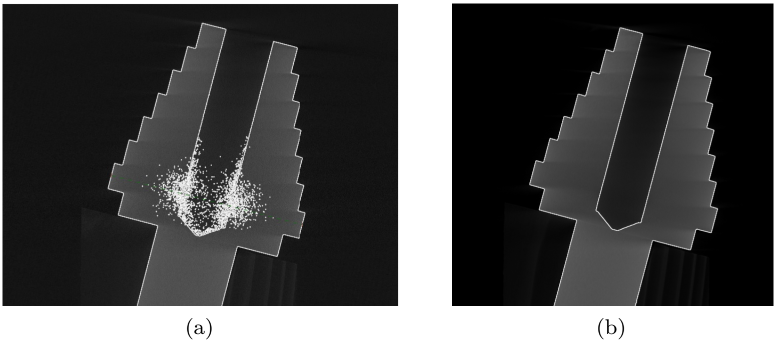
(a) (b)

Figure 5.101: Reconstructed stepped cylinder in case of using $24dB$ (a) and $0dB$ (b). (settings of measurement 1 and 5 in table 5.52)

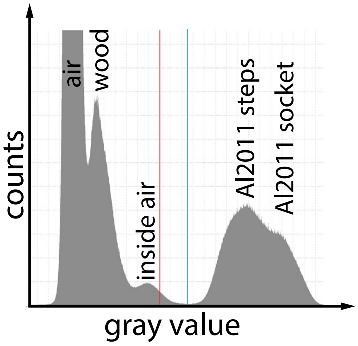

Figure 5.102: Histogram of the stepped cylinder in case of $0dB$. (table 5.52, measurement 5)

Place of filtering

Figure 5.103 compares the place of filtering (settings of table 5.53). The deviation to the reference is pictured (without voxel size rescaling). No clear difference is visible regarding the position of the filter plate.

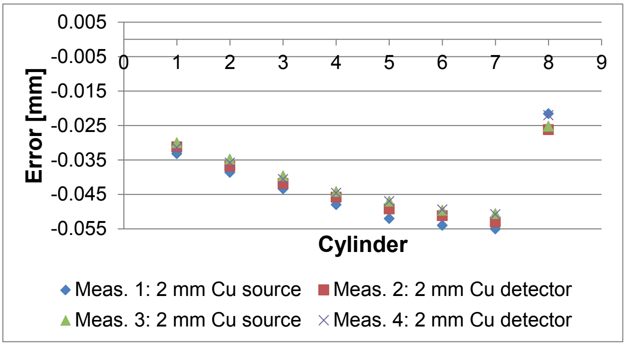

Figure 5.103: Influence of filtering between source and object on the one hand, and filtering between object and detector on the other hand: settings as in table 5.53. Deviation to the nominal value is pictured for each cylinder (figure 5.92).

Rescaling

To correct for the incorrect magnification value, a voxel size rescaling is carried out via equation 2.8.

Three different methods can be applied:

- Rescaling on a combination of an external and internal diameter.
- Rescaling on 2 external diameters.
- Rescaling using another calibration object.

Before discussing these methods it is important to point out the difference of influence of an incorrect edge on outer and inner diameters. This has been explained earlier in figure 2.27. Shifting the edge to the air side enlarges the outer diameter value, while it diminishes the value of the inner diameter. Our reference measurement used for rescaling should be independent of this effect.

Rescaling on a combination of an external and internal diameter. The first method uses a combination of an external and internal diameter. Adding the two values as in equations 5.15 and 5.16 (example using external cylinder 7 and internal cylinder 8), takes into account the difference in edge error for inside and outside diameters. This however assumes the edge difference being equal for inner and outer diameters. Instead of using the entire inside cylinder only, the part at the level of the outer cylinder (in this case the part of cylinder 7) has been used.

$$Distance_{Ref} = Cyl_{7CMM} + Cyl_{8CMM} \tag{5.15}$$

$$Distance_0 = Cyl_{7CT} + Cyl_{8CT} \tag{5.16}$$

where:

Cyl_{7CMM} = Reference diameter value of cylinder 7 $[mm]$.
Cyl_{8CMM} = Reference diameter value of cylinder 8 $[mm]$.
Cyl_{7CT} = Initial CT measured diameter of cylinder 7 $[mm]$.
Cyl_{8CT} = Initial CT measured diameter of cylinder 8 $[mm]$.

Rescaling on 2 external diameters. This method used two external diameters, excluding the different edge offset value for internal and external dimensions. This time the diameters have to be subtracted from each other as in equations 5.17 and 5.18 in case of external diameters 2 and 3. In this case it is supposed that the edge error offset is similar for different outside diameters.

$$Distance_{Ref} = Cyl_{3CMM} - Cyl_{2CMM} \tag{5.17}$$

$$Distance_0 = Cyl_{3CT} - Cyl_{2CT} \tag{5.18}$$

where:

Cyl_{2CMM} = Reference diameter value of cylinder 2 $[mm]$.
Cyl_{3CMM} = Reference diameter value of cylinder 3 $[mm]$.
Cyl_{2CT} = Initial CT measured diameter of cylinder 2 $[mm]$.
Cyl_{3CT} = Initial CT measured diameter of cylinder 3 $[mm]$.

Rescaling using another calibration object. The multi-material styli object is used to calculate the rescaling factor for this option.

The influence of different rescaling methods using a combination of 2 outer diameters, a combination of an inner and outer diameter and using another calibration object has been pictured in figure 5.104. The three different rescaling factor calculation methods gave similar results: rescaling using a combination of cylinders 2 and 3; rescaling applying a combination of the outer cylinder 7 and the corresponding inner cylinder at this level; and rescaling using the styli object. The error points are therefore not always separately visible on the graph.

The errors clearly improved after rescaling. No rescaling gives deviations between -33 and $-55\mu m$ for the outer diameters and between -20 and $-25\mu m$ for the inner diameters. Using a combination of the outer diameter and corresponding inner diameter of cylinder 3 results in deviations ranging from 3 to $20\mu m$ for the outer diameters and -2 to $-6\mu m$ for the inner diameters. Rescaling using a combination of cylinders 2 and 3; combination of the outer cylinder 7 and the corresponding inner cylinder; and using the styli object gave even better results for the outer diameter but worse results for the inner diameter. It produces errors between -5 and $6\mu m$ for the outer diameters and errors between -6 and $-11\mu m$ for the inner diameters. This clearly shows an improvement when rescaling. Other factors like the alignment errors between rotation table, source and detector will obviously also have their influence. Beam hardening corrections and edge threshold correction are furthermore not applied which would also improve the results.

Magnification

The influence of magnification is investigated in year A, in which alignment 1 was still active. Figures 5.105 and 5.106 show the diameter results after rescaling on the inner-outer diameter combination of respectively cylinder 4 and cylinder 7 for the different measurement positions (table 5.51). Table 5.54 gives for both rescaling methods the average absolute errors of the diameters per measurement and the maximum diameter error. The best results are obtained for measurement positions 5 and 6: two measurements with a small magnification but a different number of views. These magnifications result in an average absolute error of $14\mu m$ and a maximum error of respectively -22 and $-24\mu m$ when rescaling on outer and corresponding inner diameter of cylinder 7. Rescaling on the outer and corresponding inner diameter of cylinder 4 gave other results for measurement 6, i.e. an average absolute error of $10\mu m$ and a maximum error of respectively $33\mu m$. The magnification position and the rescaling cylinder clearly influence the results.

5.6.4 Conclusion

The last investigated object is a stepped cylinder. This cylinder has been calibrated with the Mitutoyo FN-905 CMM. The calibration results of year A and B were different at first, this can be solved by measuring a ring gauge

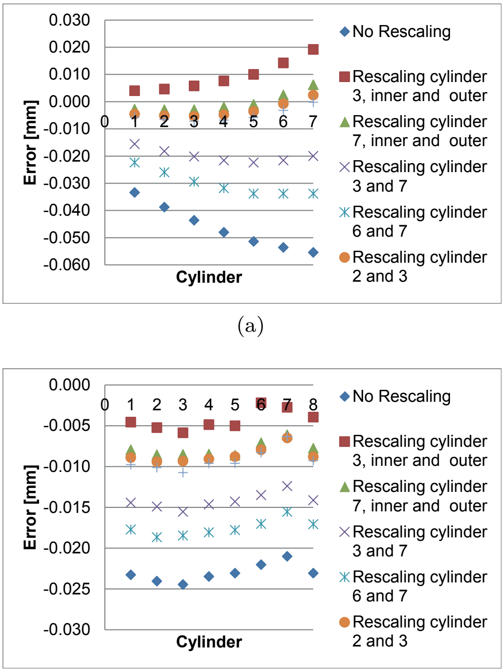

Figure 5.104: Influence of rescaling. Deviation to the reference diameter for the outer (a) and inner (b) cylinders of measurement 1 of table 5.53. In case of the inner cylinder, a cylinder is measured at the level of the corresponding outer cylinders (cylinder 1 is the inner cylinder measured at the position of outer cylinder 1). Cylinder 8 represents the entire inner cylinder.

	Rescaling cylinder 7		Rescaling cylinder 4	
	Average abs. diff.	Maximum difference	Average abs. diff.	Maximum difference
Meas. 1	0.029	-0.055	0.019	0.081
Meas. 2	0.021	-0.038	0.013	0.053
Meas. 3	0.016	-0.030	0.011	0.037
Meas. 4	0.015	-0.024	0.011	0.036
Meas. 5	0.014	-0.022	0.014	-0.022
Meas. 6	0.014	-0.024	0.010	0.033
Meas. 7	0.016	-0.030	0.011	0.039
Meas. 8	0.029	-0.060	0.018	0.066

Table 5.54: Average and maximum deviation of the 14 measured cylinders (7 outer and 7 corresponding inner cylinders) for each measurement position (table 5.51). All values are expressed in $[mm]$.

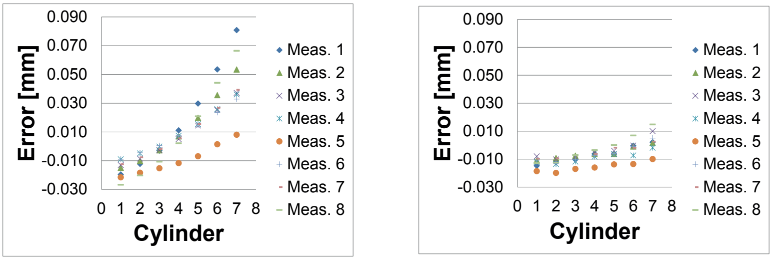

(a) (b)

Figure 5.105: Influence of magnification: deviations to the reference diameter (outer diameters: (a), inner diameters: (b)) for the measurements with settings of table 5.50 and measurement positions of table 5.51 after rescaling on the inner and outer diameter of cylinder 4.

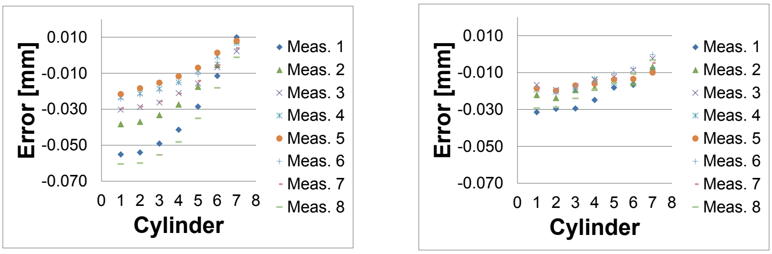

(a) (b)

Figure 5.106: Influence of magnification: deviations to the reference diameter (outer diameters: (a), inner diameters: (b)) for the measurements with settings of table 5.50 and measurement positions of table 5.51 after rescaling on the inner and outer diameter of cylinder 7.

for offset compensation. This emphasizes the importance of a well-performed calibration measurement.

The object is quite difficult to scan. Playing with the **start contour** for advanced thresholding and the **gain/exposure time combination** improves the scan possibilities. The noise can be lowered, but this will also influence the dimensional measurements.

The **place of the filter plate**, between source and object or between object and detector, was again compared. This again led to no clear differences.

Three different reference calculation values for **rescaling** were compared. Rescaling indeed improves the results. No rescaling gives deviations between -33 and $-55\mu m$ for the outer diameters and between -20 and $-25\mu m$ for the inner diameters. Using a combination of the outer diameter and corresponding inner diameter of cylinder 3 results in deviations ranging from 3 to $20\mu m$ for the outer diameters and -2 to $-6\mu m$ for the inner diameters. Rescaling using a combination of cylinders 2 and 3; combination of the outer cylinder 7 and the corresponding inner cylinder; and using the multi-material styli object of figure 5.65 produces errors between -5 and $6\mu m$ for the outer diameters and errors between -6 and $-11\mu m$ for the inner diameters.

At last the influence of **magnification** was investigated. The best results are obtained for measurement positions 5 and 6: two measurements with a small magnification but a different number of views. These magnifications result in an average absolute error of $14\mu m$ and a maximum error of respectively -22 and $-24\mu m$ when rescaling on outer and corresponding inner diameter of cylinder 7. Rescaling on the outer and corresponding inner diameter of cylinder 4 gave other results for measurement 6, i.e. an average absolute error of $10\mu m$ and a maximum error of respectively $33\mu m$.

5.7 Conclusion

This chapter has investigated the dimensional accuracy of a CT scanner using calibrated objects. The investigation has been based on real CT measurements supported by simulation. The simulation program offered the possibility to research separate parameters, to confirm observed results and furthermore did the obtained simulation knowledge help to improve the measurement results. Simulation and experimental research are clearly both needed to perform in-depth research on the dimensional measurement accuracy and to ameliorate this accuracy.

Problem description results

The chapter has started with a problem description: CT measurements of the same object led to different dimensional results. This illustrates the issues in dimensional X-ray CT metrology.

CT audit results

The chapter has continued by reporting the results of the CT audit organized by the University of Padova. It presented a large variation in obtained measurement results for the same objects by the different participants. Our group presented deviations up to $14\mu m$ for three of the objects. The results of these objects had been corrected in two manners: using an artifact for rescaling and an artifact to correct for edge offsets. Only for the last object, no artifact to correct for edge offsets was available. For this object deviations up to $46\mu m$ were visible.

Three interesting remarks should be made within the results of this CT audit:

- The participants encounter more problems concerning the form measurements than measurements of size.
- No participant was able to define a good measurement uncertainty: it was either defined too large (overestimation) or it was defined too small and did not contain the real value.
- The obtained accuracy can be much better than the voxel sizes.

Styli objects results

The chapter has continued with an investigation of the available 450 kV CT scanner with two styli objects (ruby and multi-material). Different improvements appeared to be necessary to obtain more accurate data. The original average distance errors (out of 10 measurements) showed a range from -19 to $0\mu m$ with a maximum deviation of $-31\mu m$. **Rescaling** improved this range to -10 up to $8\mu m$, with a maximum deviation of $-15\mu m$. A second improvement is the use of a **region of interest** (ROI). A first diameter error set between -50 and $-25\mu m$, with a maximum deviation of $-65\mu m$ ameliorates to a range of -27 to $-16\mu m$, with a maximum deviation of $-29\mu m$.

Despite all improvements, still an offset is observed in the diameter measurements of different sphere materials. Applying a **material dependent start contour** decreases the absolute diameter errors from up to $60\mu m$ to up to $12\mu m$.

Different parameters did not give significant amelioration of the measurements: **rescaling method, reconstruction resolution quality, number of views** (only a small improvement for diameter measurement in case of ruby styli object), **'minimize ring artifacts' option, place of filter plate**.

A next considered parameter concerns the applied **magnification**. Changing the magnification can give increasing and decreasing error trends dependent on the measured sphere distance couple.

The **alignment**, relative position of source, rotation table and detector, is another investigated parameter. The manufacturer of the CT device was asked to redo this alignment. Realignment at first deteriorated the measurement results. Simulation pointed the **rotation overshoot** as being the underlying reason. An adapted reconstruction angle improved the distance measurements results of the new alignment: the error range from -30 to $50\mu m$ shifted to a range of -20 up to $10\mu m$. The simulation program was applied to demonstrate the real effect of the two different alignments: alignment 1 gave better results for the distances whereas the diameters where measured more accurate with alignment 2. The **start angle** appeared to be another, often not considered, influence factor. Simulation clearly illustrated the influence in case of a rotation overshoot.

Measurements of the objects were carried out over 2 different years. Comparison of these results led to following two observations. The **source spot position** has shifted towards the detector over $0.3mm$. This emphasizes the importance of rescaling. Calibration of the source-object and source-detector distances once is not sufficient: it should be redone regularly. A second observation was the repetition of some trends regarding some distances and the $4mm$ diameter spheres in both years which was confirmed by simulation. Distance 5-8 and distance 10-11 is always measured to small; the diameter of the center sphere (i.e. sphere 12) is always the largest; the sphere the furthest away from the center (sphere 1) always has the smallest measured diameter and the other ruby spheres seem to have comparable diameters.

Changing the **object position** changes the measured diameters, but aforementioned trend will remain: the further away of the rotation axis the smaller the measured diameter.

Simulation and experimental research revealed form errors dependent of the sphere position with respect to the axis of rotation. These form errors are clearly visible at the top part of the sphere when plotting the fit point deviations to the least-squares sphere. Statistical analysis illustrated the influence of cutting the **top part of the sphere** (highest fit point deviations): this can result in $4\mu m$ shifts of the height position and diameter of the sphere.

A last parameter **stepwise versus continuous scanning**, which was investigated by simulation, resulted in diameter differences up to $10\mu m$.

The multi-material styli object was also measured with the **curved linear detector array**. Measurements with the curved linear detector array (CLDA) gave bad results: sphere diameter deviations up to $200\mu m$ were obtained. Further research is hereby required.

It should be reminded that no additional correction for material dependent edge errors was carried out for the investigations. Compensation by measuring a reference object of the same material would improve the diameter measurements heavily. The measured sphere distance errors furthermore give a good estimation of the accuracy of a common used rescaling method, i.e. rescaling with a distance between two spheres.

Stepped cylinder object results

The last section has researched the accuracy in measuring a stepped cylinder object. Difficulties in **CMM calibration** emphasized the importance of a well-performed calibration measurement. Improvements were obtained by shifting the **start contour**, varying **gain/exposure time combination**, **rescaling** and **magnification**. Shifting the start contour and varying gain/exposure time combination lowers the noise. **Rescaling** can improve the results from a range -33 to $-55\mu m$ for outer diameters and -20 to $-25\mu m$ for inner diameters to a range of -5 to $-6\mu m$ for outer diameters and -6 to $-11\mu m$ for inner diameters.

General result

This chapter has investigated the accuracy of dimensional X-ray CT metrology with the help of calibrated artifacts and simulation. Different influence factors have been considered and manners to improve the accuracy have been discussed. Edge-dependent measurands still show measurement offsets. These measurement errors can be decreased by compensation with an artifact of the same material. Simulation clearly proved to be an indispensable supplement to experimental investigation.

Chapter 6

General conclusions

This thesis explores the wonderful world of dimensional X-ray CT metrology. This chapter summarizes the main results. It starts with the research context, continues with the conclusions on the main contributions of the conducted research and finishes with suggestions for future research.

6.1 Context of the research

Dimensional X-ray CT metrology combines the worlds of X-ray computed tomography and dimensional metrology. It is a new evolution which enables to measure inside dimensions of an object in a non-destructive manner. It is therefore the ideal way to investigate assemblies, complex structures and additive manufacturing parts with inner geometries. The newness of dimensional CT metrology at the start of this PhD research was visible by the inability of experts to define decent measurement accuracies and uncertainties. It was moreover emphasized by the lack of a good understanding of the process and its influence factors. These observations illustrated the importance of in-depth research on this new, attractive and unique domain of dimensional CT metrology. This research helps to understand the process, highlights critical factors, demonstrates the possibilities of dimensional CT metrology and indicates possible accuracies and related accuracy problems.

The main goal of this thesis can be summarized as:

Analyze the accuracy of dimensional X-ray CT metrology.

6.2 Main contributions

6.2.1 Discussion on the influence factors

Earlier research discusses the influence factors related to X-ray computed tomography on the one hand and dimensional metrology on the other hand. This text focused on the parameters for the combined field i.e. dimensional X-ray CT metrology. Some parameters are similar to the parameters of the 'ancestors'. But there are furthermore many different parameters and influences when discussing X-ray CT metrology. Dimensional X-ray CT metrology reveals new parameters and additionally the parameters 'inherited' from the 'ancestors' often have a different influence and importance.

The many factors affecting the dimensional X-ray CT measurements and therefore the measurement accuracy have been identified, analyzed, discussed and their effects on projection images have been illustrated using examples. The discussions did not restrict itself to the commonly considered influence factors but tried to cover all possible influence factors. This approach was taken to overcome a general problem: a researcher investigates a single or multiple parameters by varying this single or these multiple parameters. Unfortunately this researcher often makes conclusions based on the assumption that the observed differences are due to the applied parameter variation, but the researcher forgets additional parameters which might have changed and the researcher consequently draws incorrect conclusions.

6.2.2 Detailed analysis of the mechanical structure

It has been demonstrated that the mechanical structure of an X-ray CT scanner is an important error source. **A kinematic model for the X-ray CT scanner under investigation has been described and quantified.** This kinematic model is one part of the mechanical structure, the other part contains the relative errors between source, rotation vector and detector, referred to as alignment errors. **A method and object to calculate the alignment errors has been worked out.** The results lead to a good understanding of the errors related to the mechanical structure of our X-ray CT scanner. **These results have been implemented in the simulation program together with the earlier investigated and quantified influence factors.** This allowed to correlate experimental and simulated results. The approach has been worked out for the X-ray CT scanner under investigation but can easily be adapted to other CT scanners.

6.2.3 Simulation program

Repeating the same experiment a month later often leads to different conclusions which is of course unacceptable. The use of simulation helps to overcome this issue. **Simulation software has been written in matlab® environment. The different influence factors discussed earlier have been implemented in the program.** Parts of the code can easily be adapted or added by the user. The most important aspects of this code are the flexibility, the many implemented options (option to perform continuous scanning, etc.), and the availability of the source code to the user, giving him insight in each detail of the code. This simulation software has been essential to verify or confirm observations made during the accuracy analysis summarized in section 6.2.4.

6.2.4 Accuracy analysis based on calibrated objects

A thorough analysis of the accuracy has been performed using calibrated objects. Accurate objects were hereby manufactured or acquired to be able to perform an in-depth accuracy analysis. A lot of attention was hereby paid to receive good calibration values.

This work has succeeded to give an indication of measurement accuracies obtained by dimensional X-ray CT metrology. Furthermore the accuracy problems have been analyzed, which enabled to detect the error sources. One important factor which can influence the X-ray CT scans is the rotational accuracy of the rotation table. An over rotation of this table will deteriorate the measurements heavily. This factor is often not considered, but appeared to be a crucial one. **Simulation as well as experimental research has been carried out to evaluate the measurement accuracy. Analyzing the influence factors and detecting the main error sources has enabled to improve the measurement accuracy.** Some improvements have already been carried out, but the obtained information can be further utilized to improve the overall accuracy. One of the key aspects will be to improve the mechanical structure and software (e.g. edge detection algorithm).

6.3 Suggestions for future research

The combination of computed tomography and dimensional metrology (resulting in dimensional X-ray CT metrology) was only just in its earliest stages at the start of this PhD thesis. The knowledge and simulation program acquired in this research can now be used for further in-depth investigation on dimensional X-ray

CT metrology. The author wants to stress the importance of well-considered conclusions. Often incorrect conclusions are drawn by researchers due to the many (often unknown) influence factors. Critical aspects which will enable a correct conclusion making are a good understanding of the CT process, a critical approach and multiple verifications of the conclusions. Simulation is for instance a good method to verify the experimental conclusions.

This thesis had a more general look at the new domain of dimensional X-ray CT metrology. The concepts learned in this thesis as well as from other works during this period of cultivation can now be used for in-depth research dealing with specific areas as micro-manufacturing, additive manufacturing, multi-material, porosity distribution, injection molding, uncertainty determination, etc. Here some considerations are listed on different aspects to improve dimensional X-ray CT metrology in the future.

- *Mechanical structure and stability*

  This thesis emphasized the importance of the mechanical structure. This mechanical structure will define the alignment between source, rotation axis and detector. A well-made and stable device is needed to be able to obtain a good and constant alignment between these three parts for all positions of the rotation table. Stability with respect to the source point position, temperature, time and machine design is therefore needed. These topics should be further investigated and improved. Simulation should hereby be addressed to find the critical issues. Stability will furthermore give the necessary repeatable conditions (repeating the same measurement should give the same result). Improving the stability starts by designing a stable set-up with stable materials, e.g. using granite as in CMMs. Further considerations are among others the rotation axis angles, and spot position.

  It is definitely important to keep everything as constant and close to the ideal conditions as possible. It is furthermore necessary to keep track of all events which change the conditions to the best extent, e.g. temperature variation, changes of the rotation speed, collisions, etc.

- *Research on the curved linear diode array detector*

  Much more research is needed for the curved linear diode array detector. This detector generates nice images but poor results in terms of dimensional accuracy. The calibration procedures are quite complex and should be reconsidered. The extra required movement, the one of the rotation table along the vertical direction, gives an extra inaccuracy which needs to be improved. A good first object to investigate this type of detector further is a large cylinder. Analyzing the cylinder form and plotting the diameter in function of height can hereby help. Rescaling on individual slices instead of using one general rescaling factors should also be considered.

- *Reconstruction software*

  The reconstruction algorithms (throughout this thesis CT Pro has been used) still needs to be updated. It should cover the typical CT related problems such as multi-material object properties, beam hardening, etc. It is hereby important to receive correct reconstructions, not only with respect to the image quality but also regarding correctness in terms of dimensions. Speeding up the calculation time is of course interesting but the correctness should not decrease as a trade-off. A further development related to the reconstruction software also contains the compensation of known errors like alignment errors, drift errors etc.

- *Evaluation software*

  The evaluation software (throughout this thesis VGStudio Max has been used) is still an area of concern. Edge detection and feature recognition are extremely important, but is not yet implemented as it should be. Research into better algorithms should be carried out. These algorithms should be suited for outside dimensions as well as for inside dimensions and also for different material transitions.

- *Simulation software*

  The simulation software developed in this thesis should be further elaborated. Different modules have already been implemented but still much more modules, needed for research, can be implemented. Possible improvements are the ability to work with freeform surfaces, and a user-friendly graphical user interface. It is furthermore always possible to ameliorate the code and the calculation speed, e.g. by implementing the code into another programming language (C, C++, etc.).

6.4 General conclusion

Research has been carried out to explore and investigate the new concept 'dimensional X-ray CT metrology'. The possibilities, accuracies, difficulties, problems and several improvements have been examined. Data obtained by several CT scanners and users as well as from own-developed simulation software has therefore been analyzed. The topic of dimensional X-ray CT metrology can be concluded in following statement:

Dimensional X-ray CT metrology is an interesting and attractive, but tricky business.

Bibliography

[1] Aaron, G.F. The history, development, and impact of computed imaging in neurological diagnosis and neurosurgery: CT, MRI, DTI. In *Nature Proceedings doi:10.1038/npre.2009.3267.5* (2009).

[2] Alvarez, R.E. and Macovski, A. Energy-selective reconstructions in X-ray computerised tomography. *Phys. Med. Biol* (1976), Vol. 21, pp. 733–744.

[3] Ambrose, J., and Hounsfield, G. Computerized transverse axial tomography. *British journal of radiology 46* (1973), 1023–1047.

[4] Amirkhanov, A., Heinzl, C., Reiter, M., Kastner, J. and Groller, M.E. Projection-Based Metal-Artifact Reduction for Industrial 3D X-ray Computed Tomography. *IEEE transactions on visualization and computer graphics 17 (12)* (2011).

[5] Andreu, V., Lettenbauer, H., and Yagüe, J. Analysis of the error sources of a Computer Tomography Machine. In *Proceedings of the Lamdamap conference* (2009).

[6] Angel, J. *Quality assurance of CT scanning for industrial applications.* PhD thesis, Department of Mechanical Engineering, Technical University of Denmark, 2014.

[7] Angel, J., and De Chiffre, L. Final report: Inter-laboratory comparison on Industrial Computed Tomography, 2013.

[8] Arenhart, F.A., Nardelli, V.C., Donatelli, G.D., Porath, M.C., Isenberg, C. and Schmitt, R. Design of a multi-wave standard to evaluate the frequency response of CT measuring systems. In *Proceedings of the 11th International Symposium on Measurement and Quality Control (ISMQC-2013)* (2013).

[9] ASTM E1165 - 12. *Standard test method for measurement of focal spots of industrial X-ray tubes by pinhole imaging.* ASTM.

[10] Ay, M., Ghafrain, P., and Zaidi, H. A hybrid approach for fast simulation of X-ray computed tomography. *IEEE Nuclear Science Symposium Conference Record* (2007).

[11] Ball, J., and Moore, A. *Essential Physics for Radiographers.* Blackwell Science, 1997.

[12] Balsamo, A. Effects of Arbitrary Coefficients of CMM Error Maps on Probe Qualification. *CIRP Ann. 44* (1995), 475–478.

[13] Balsamo, A., Colonnetti, G., Franke, M., Trapet, E., Wäldele, F., De Jonge, L., and Vanherck, P. Results of the CIRP-Euromet Intercomparison of Ball Plate-Based Techniques for Determining CMM Parametric Errors. *CIRP Ann. 64*, 1 (1997), 463–466.

[14] Bartscher, M., Hilpert, U., Goebbels, J., and Weidemann, G. Enhancement and proof of accuracy of industrial computed tomography (CT) Measurements. *CIRP Ann. 56* (2007), 495–498.

[15] Bartscher, M., Hilpert, U., Härtig, F., Neuschaefer-Rube, U., Goebbels, J., and Staude, A. Industrial Computed Tomography, an emerging coordinate measurement technology with high potential. In *Proceedings of NCSL international Workshop and Symposium* (2008).

[16] Bartscher, M., Neukamm, M., Hilpert, U., Neuschaefer-Rube, U., Härtig, F., Kniel, K., Ehrig, K., Staube, A., and Goebbels, J. Achieving traceability of industrial computed tomography. *Key Engineering Materials 437* (2010), 79–83.

[17] Bartscher, M., Neuschaefer-Rube, U., and Wäldele, F. Computed Tomography - a highly potential tool for Industrial quality control and production near measurement. In *Proceedings of the 8th Intern. Symp. on Measurement and Quality Control in Production* (2004).

[18] Bellon, C., and Jaenisch, G. ARTist – Analytical RT Inspection Simulation Tool. In *Proceedings of the International Symposium on Digital industrial Radiology and Computed Tomography* (2007).

[19] Birch, R., and Marschall, M. Computation of bremsstrahlung X-ray spectra and comparison with spectra measured with a Ge(Li) detector. *Phys. Med. Biol* (1978), Vol. 24, No. 3, pp. 505–517.

[20] Boeckmans, B., Tan, Y., Welkenhuyzen, F., Guo, Y.S., Dewulf, W. and Kruth, J.-P. Roughness offset differences between contact and non-contact measurements. In *Proceedings of Euspen 15th International Conference* (2015).

[21] Boone, J., and Seibert, J. An accurate method for computer-generating tungsten anode x-ray spectra from 30 to 140 kv. *Med. Physics* (1997), Vol. 24, 1661.

[22] Brunke, O., and Suppes, A. Precise 3D dimensional metrology using high resolution X-ray computed tomography CT). In *Proceedings of the 10th European Conference on Non-Destructive Testing (ECNDT)* (2010).

[23] Carmignato, S. Accuracy of industrial computed tomography measurements: Experimental results from an international comparison. *CIRP Annals - Manufacturing Technology 61* (2012), 491–494.

[24] Carmignato, S., Dreossi, D., Mancini, L., Marinello, F., Tromba, G., and Savio, E. Testing of x-ray microtomography systems using a traceable geometrical standard. *Meas.Sci.Technol. 20 084021* (2009).

[25] Carmignato, S., Pierobon, A., and Savio, E. CT audit: Interlaboratory comparison of Computed Tomography Systems for Dimensional Metrology. Tech. rep., University of Padova, 2011.

[26] Carmignato, S. et al. CT techniques for reconstructing 3D geometrical models of complex parts: an approach for traceability establishment and uncertainty evaluation. In *Proceedings of IMEKO Int. Symp. and Mediterranean Conference on Measurement* (2004), pp. 387–390.

[27] Cho, Y., Moseley, D. J., Siewerdsen, J. H., and Jaffray, D. A. Accurate technique for complete geometric calibration of cone-beam computed tomography systems. *Med. Physics* (2005), Vol. 32, 968.

[28] Cnudde, V., and Boone, M. High-resolution X-ray computed tomography in geosciences: A review of the current technology and applications. *Earth-science reviews 123* (2013), 1–17.

[29] Cnudde, V., Masschaele, B., Dierick, M., Vlassenbroeck, J., Van Hoorebeke, L., and Jacobs, P. Recent progress in X-ray CT as a geosciences tool. *Applied Geochemistry 21(5)* (2006), 826–832.

[30] Connie, L.D. *Fundamentals of Dimensional Metrology, 5th edition.*

[31] Davis, G., Jain, N., and Elliott, J. A modelling approach to beam hardening correction. In *Proceedings of SPIE, Developments in X-Ray Tomography VI* (2008).

[32] De Chiffre, L., Carmignato, S., Kruth, J.-P., Schmitt, R. and and Weckenmann, A. Industrial applications of computed tomography. *CIRP Ann. 63*, 2 (2014), 655–677.

[33] De Man, B., Nuyts, J., Dupont, P., Marchal, G., and Suetens, P. Metal streak artifacts in X-ray computed tomography: a simulation study. *Nuclear Science, IEEE Transactions on 46* (1999), pp 691 – 696.

[34] Dewulf, W., Tan, Y., and Kiekens, K. Sense and non-sense of beam hardening correction in CT metrology. *Annals of the CIRP, Manufacturing Technology 61(1)* (2012), 495–498.

[35] Dewulf, W., Kiekens, K., Tan, Y., Welkenhuyzen, F. and Kruth, J.-P. Uncertainty Determination and Quantification for Dimensional Measurements with Industrial Computed Tomography. *CIRP Ann. 62*, 1 (2013), 535–538.

[36] DIN EN 12543-5. *Characteristics of focal spots in industrial X-ray systems for use in non-destructive testing.* DIN, 1999.

[37] Ding, M., Odgaard, A., and Hvid., I. Accuracy of cancellous bone volume fraction measured by micro-CT scanning. *Journal of Biomechanics 32 (3)* (1999), 323–326.

[38] Duvauchelle, P., Freud, N., Kaftandjian, V., and Babot, D. A computer code to simulate X-ray imaging techniques. *Nucl. Instr. Meth. B* (2000), vol. 170, pp. 245–258.

[39] Eberly, D. Line-Cone Intersection. `http://www.geometrictools.com/Documentation/IntersectionLineCone.pdf`.

[40] Estler, W.T., Edmundson, K.L., Peggs, G.N., and Parker, D.H. Large-Scale Metrology – An Update. *CIRP Ann. 51*, 2 (2002), 587–609.

[41] Feldkamp, L.A., Davis, L.C. and Kress, J.W. Practical cone-beam algorithm. *J. Opt. Soc. AM.* (1984), A 1, pp. 612–619.

[42] Flannery, B.P., DECKMAN, H.W., ROBERGE W.G. and D'Amico K.L. 3-Dimensional X-Ray Microtomography. *Science 237(4821)* (1987), 1439–1444.

[43] Franco, L., Yagüe-Fabra, J., Jimeneze, R., Maestro, M., and Ontiveros, S. Error sources analysis of computed tomography for dimensional metrology: an experimental approach. In *Proceedings of 11th the European Conference on Non-Destructive Testing (ECNDT)* (2014).

[44] Franz, M., and Kasperl, S. Quality and Speed Improvements in Industrial CT by the Use of an 317 additional Optical. In *Proceedings of the European Conference on Non-Destructive Testing (ECNDT)* (2006).

[45] GE/phoenix. Prüfbericht, 3D Präzisionsprüfung CT, Prüfbericht zur Bestimmung der Messgenauigkeit von CT-Systemen. Tech. rep., 2009.

[46] Hammersberg, P. et al. Measurements of absolute energy spectra for an industrial micro focal X-ray source under working conditions measured with a Compton scattering spectrometer. *Journal of X-ray Science* (1998;8), pp 5–18.

[47] Hanke, R., Fuchs, T., and Uhlmann, N. X-ray based methods for non-destructive testing and material characterization. *Nuclear Instruments and Methods in Physics Research A 591* (2008), pp. 14–18.

[48] Heinzl, C., Kastner, J., Georgi, B., and Lettenbauer, H. Comparison of surface detection methods to evaluate cone beam computed tomography data for three dimensional metrology. In *Proceedings of the International Symposium on Digital industrial Radiology and Computed Tomography* (2007).

[49] Hendrickx, T. Dimensionele metrologie met een hoogvermogen CT-scanner: nauwkeurigheid en verbeteringen. Master's thesis, Katholieke Universiteit Leuven, Department of Mechanical Engineering, 2014.

[50] Hiller, J. *Abschätzung van Unsicherheiten beim dimensionellen Messen mit industrieller Röntgen-Computertomographie durch Simulation.* PhD thesis, Albert-Ludwigs-Universität Freiburg, Technischen Fakultät, 2011.

[51] Hiller, J., and Kasperl, S. Analyse von einflussgrössen beim dimensionellen messen mittels röntgencomputertomographie. In *DGZfP*.

[52] Hiller, J., and Reindl, L. M. A computer simulation platform for the estimation of measurement uncertainties in dimensional X-ray computed tomography. *Measurement* (2012), Vol. 45, pp. 2166–2182.

[53] Hilpert, U., Bartscher, M., Neugebauer, M., Goebbels, J., Weidemann, G., and Bellon, C. Simulation-aided computed tomography (CT) for dimensional measurements. In *Proceedings of the International Symposium on Digital industrial Radiology and Computed Tomography* (2007).

[54] Hsieh, J. *computed tomography: Principles, design, artifacts, and recent advances.* SPIE, Bellingham, WA, 2003.

[55] Indesteege, D. Dimensionele nauwkeurigheidsstudie van een 450kV CT-scanner aan de hand van referentieobjecten. Master's thesis, Katholieke Universiteit Leuven, Department of Mechanical Engineering, 2013.

[56] ISO 230-1:1996. *Test code for machine tools – Part 1: Geometric accuracy of machines operating under no-load or finishing conditions.* ISO, 1996.

[57] ISO/IEC Guide 98-3:2008. *Uncertainty of measurement – Part 3: Guide to the expression of uncertainty in measurement (GUM:1995).* ISO/IEC, 2008.

[58] JCGM 200:2012. *International vocabulary of metrology — basic and general concepts and associated terms (3 ed.).* Joint Committee on Guides for Metrology (JCGM), 2012.

[59] Jerrold, T.B., Seibert, J.A., Leidholdt, E.M. and Boone, J.M. *The Essential Physics of Medical Imaging, 3rd edition.* 2011.

[60] Kak, A. C., and Slaney, M. *Principles of Computerized Tomographic Imaging.* Society of Industrial and Applied Mathematics, 2001.

[61] Kasperl, S., Hiller, J., and Krumm, M. Computed Tomography Metrology in Industrial Research and Development. In *Proceedings of the International Symposium on NDT in Aerospace* (2008).

[62] Kempen, K., Welkenhuyzen, F., Qian, J. and Kruth, J.-P. Dimensional accuracy of internal channels in SLM produced parts. In *Proceedings of ASPE spring topical meeting* (2014).

[63] Kerckhofs, G. *Morphological and mechanical quantification of porous structures by means of micro-CT.* PhD thesis, Katholieke Universiteit Leuven, Department of Metallurgy and Materials Engineering, 2009.

[64] Kerckhofs, G., Pyka, G., Loeckx, D., Van Bael, S., Schrooten, J., and Wevers, M. The combined use of micro-CT imaging, in-situ loading and non-rigid image registration for 3D experimental local strain mapping on porous bone tissue engineering scaffolds under compressive loading. In *Proceedings of ECNDT, 10th European Conference on Non-Destructive Testing* (2010).

[65] Kerckhofs, G., Schrooten, J., Van Cleynenbreugel, T., Lomov, S.V. and Wevers, M. Validation of x-ray microfocus computed

tomography as an imaging tool for porous structures. *Review of scientific instruments 79* (2008), 013711–1–013711–9.

[66] Ketcham, R.A. and Carlson, W.D. Acquisition, optimization and interpretation of X-ray computed tomographic imagery: applications to the geosciences. *Computers &Geosciences 27(4)* (2001), 381–400.

[67] Kiekens, K., Tan, Y., Kruth, J.-P., Voet, A. and Dewulf, W. Parameter dependent thresholding for dimensional X-ray computed tomography. In *Proceedings of the International Symposium on Digital Industrial Radiology and Computed Tomography* (2011).

[68] Kiekens, K., Tan, Y., Welkenhuyzen, F., Kruth, J.-P. and Dewulf, W. Uncertainty Determination for Dimensional Measurements with Computed Tomography. In *Proceedings of the International Conference on Industrial Computed Tomography* (2012).

[69] Kiekens, K., Welkenhuyzen, F., Tan, Y., Bleys, P., Voet, A., Dewulf, W. and Kruth, J.-P. A test object for calibration and accuracy assessment in X-ray CT metrology. In *Proceedings of the 10th International Symposium on Measurement and Quality Control (ISMQC-2010)* (2010).

[70] Kiekens, K., Welkenhuyzen, F., Tan, Y., Bleys, P., Voet, A., Kruth, J.-P. and Dewulf, W. A test object with parallel grooves for calibration and accuracy assessment of industrial CT metrology. *Measurement Science and Technology 22* (2011), 1–7.

[71] Krämer, P., and Weckenmann, A. Multi-energy image stack fusion in computed tomography. *Meas. Sci. Technol.* (2010), Vol. 21.

[72] Krumm, M., Kasperl, S., and Franz, M. Reducing non-linear artifacts of multi-material objects in industrial 3D computed tomography. *NDT&E International* (2008), Vol. 41, Iss. 4, pp. 242–251.

[73] Kruth, J.-P., Bartscher, M., Carmignato, S., Schmitt, R., De Chiffre, L. and Weckenmann, A. Computed Tomography for Dimensional Metrology. *CIRP Ann. 60*, 2 (2011).

[74] Kruth, J.-P., Vanherck, P. and De Jonge, L. Self-calibration method and software error correction for three-dimensional coordinate measuring machines using artefact measurements. *Measurement 14*, 2 (1994), 157–167.

[75] Kyriakou, Y., and Kalender, W. X-ray scatter data for flat-panel detector CT. *Physica Medica* (2007), 23(1):3–15.

[76] Lettenbauer, H., Georgi, B., and Weiss, D. Means to verify the accuracy of CT systems for metrology applications (in the absence of established international standards. In *Proceedings of the International Symposium on Digital industrial Radiology and Computed Tomography* (2007).

[77] Lim, K.S. and Barigou, M. X-ray micro-computed tomography of cellular food products. *Food Research International 37(10)* (2004), 1001–1012.

[78] Maex Precision-Production nv. `http://www.maex.be/nl`.

[79] Malusek, A. *Calculation of scatter in cone beam CT.* PhD thesis, Linköping University, Faculty of Health Sciences, Department of Medical and Health Sciences, Radiation Physics, 2008.

[80] McCullough, E. Photon attenuation in computed tomography. *Med. Physics* (1975).

[81] Miceli, A., Thierry, R., Bettuzzi, M., Flisch, A., Hofmann, J., Sennhauser, U., and Casali, F. Comparison of simulated and measured spectra of an industrial 450 kV X-ray tube. *Nuclear Instruments and Methods in Physics Research* (2007), A 580 pp 123–126.

[82] Miceli, A., Thierry, R., Flisch, A., Sennhauser, U., and Casali, F. MC simulation of scatter intensities in a cone-beam CT system employing a 450 kV X-ray tube. *European NDT Days in Prague* (2007).

[83] Miceli, A., Thierry, R., Flisch, A., Sennhauser, U., Casali, F., and Simoncet, M. Monte Carlo simulations of a high-resolution X-ray CT system for industrial applications. *Nuclear Instruments and Methods in Physics Research* (2007), A 583/2–3:313–323.

[84] Mitchel, K. W. A Generalized Approach to Wall Thickness Measurements in CT Images, ISBN 0-931403-89-8. In *Proceedings of the Industrial Computerized Tomography, ASNT* (1989), pp. 120–124.

[85] Müller, P., Hiller, J., Cantatore, A., and De Chiffre, L. Investigation of measuring strategies in computed tomography. In *Proceedings of the International Conference Newtech 2011* (2011).

[86] Müller, P., Hiller, J., Dai, Y., Andreasen, J., Hansen, H., and De Chiffre, L. Estimation of measurement uncertainties in X-ray computed tomography metrology using the substitution method. *CIRP Journal of Manufacturing Science and Technology 7* (2014), pp. 222–232.

[87] Nardelli, V.C., Arenhart, F.A., Donatelli, G.D. and Porath, M.C. Using Calibrated Parts and Integral Surface Analysis to Investigate Dimensional CT Measurements. In *Proceedings of the International Symposium on Digital industrial Radiology and Computed Tomography* (2011).

[88] Nardelli, V.C., Arenhart, F.A., Porath, M.C. and Donatelli, G.D. Investigation of the CT-induced random surface deviations using a multi-wave standard. In *Proceedings of the International Conference on Industrial Computed Tomography* (2012).

[89] Nardelli, V.C., Donatelli, G.D., Arenhart, F.A. and Porath, M.C. Uncertainty evaluation of computed tomography measurements using multiple calibrated workpieces. In *2nd Congresso Internacional de Metrologia Mecânica* (2011).

[90] Nardelli, V.C., Porath, M.C., Arenhart, F.A. and Donatelli, G.D. Modular test parts to assess the quality of computed tomography dimensional measurements. In *Proceedings of the International Conference on Industrial Computed Tomography* (2012).

[91] Neumayer, D., Modrich, K., Maisl, M., and Kasperl, S. Computed Tomography as a tool for industrial measurement. In *Proceedings of the European Conference on Non-Destructive Testing (ECNDT)* (2006).

[92] Nikl, M. Scintillation detectors for x-rays. *Meas. Sci. Technol.* (2006), Vol. 17, R37–R54.

[93] Nikon Metrology, X-tek. *Inspect-X User Manual*, 2004.

[94] Nikon Metrology, X-tek. *CT Pro User Manual*, 2011.

[95] Ning, L., Kim, S.-H., Suh, J.-H., Choc, S.-H., Choic, J.-G., and Kim, M.-H. Virtual X-ray imaging techniques in an immersive casting simulation environment. *Nuclear Instruments and Methods in Physics Research* (2007), pp 143–152.

[96] Nist Xcom database. `http://physics.nist.gov/PhysRefData/Xcom/html/xcom1.html`.

[97] Nobel Prize. The Nobel Prize in Physiology or Medicine 1979. `http://www.nobelprize.org/nobel_prizes/medicine/laureates/1979/press.html`.

[98] Noo, F., Clackdoyle, R., Mennessier, C., White, T. A., and Roney, T. J. Analytic method based on identification of ellipse

parameters for scanner calibration in cone-beam tomography. *Physics in Medicine and Biology 45*, 11 (2000), 3489.

[99] OWEN, S. Ray-Box Intersection. `https://www.siggraph.org/education/materials/HyperGraph/raytrace/rtinter3.htm`.

[100] PARTRIDGE, M., HESSE, B.-M., AND MÜLLER, L. A performance comparison of direct- and indirect-detection flat-panel imagers. *Nuclear Instruments and Methods in Physics Research A 484* (2002), pp. 351–363.

[101] PAULUS, P., KIEKENS, K., WELKENHUYZEN, F., AND BLEYS, P. Time-to-market van producten drastisch ingekort met CT-scannen. *Metallerie, 124* (2009), 25–26.

[102] PERKIN ELMER. `http://www.perkinelmer.com`.

[103] PETERS, J., BRYAN, J.B., ESTLER, W.T., EVANS, C., KUNZMANN, H., LUCCA, D.A., SARTORI, S., SATO, H., THWAITE, E.G., VANHERCK, P., HOCKEN, R.J., PEKLENIK, J., PFEIFER, T., TRUMPOLD, H. AND VORBURGER, T.V. Contribution of CIRP to the Development of Metrology and Surface Quality Evaluation during the last fifty years. *CIRP Ann. 50*, 2 (2001), 471–488.

[104] PEYRIN, F., SALOME, M., CLOETENS, P., LAVAL-JEANTET, A.M., RITMAN, E. AND RÜEGSEGGER, P. Micro-CT examinations of trabecular bone samples at different resolutions: 14, 7 and 2 micron level. *Technology and Health Care 6* (1998), 391–401.

[105] PHOTON ATTENUATION. PhotonAttenuation package, Jaroslaw Tuszynski, Matlab code, 2007. `http://uk.mathworks.com/matlabcentral/fileexchange/12092-photonattenuation-2`.

[106] POLUDNIOWSKI, G. Calculation of x-ray spectra emerging from an x-ray tube. Part II. X-ray production and filtration in x-ray targets. *Med. Physics* (2007), Vol. 34, pp. 2175–6.

[107] POLUDNIOWSKI, G., LANDRY, G., DEBLOIS, F., EVANS, P., AND VERHAEGEN, F. SpekCalc: a program to calculate photon spectra from tungsten anode x-ray tubes. *Phys. Med. Biol* (2009), Vol. 54, pp. N433–N438.

[108] POLUDNIOWSKI, G., AND P., E. Calculation of x-ray spectra emerging from an x-ray tube. Part I. Electron penetration characteristics in x-ray targets. *Med. Physics* (2007), Vol. 34, pp. 2164–74.

[109] Pyka, G., Burakowski, A., Kerckhofs, G., Moesen, M., Van Bael, S., Schrooten, J., and Wevers, M. Surface modification of Ti6Al4V open porous structures produced by additive manufacturing. *Advanced Engineering Materials 14* (2012), 363–370.

[110] Ramsey, A. How to get the most out of your X-Tek CT system. Tech. rep., X-Tek Systems Ltd., Tring, UK., 2008.

[111] Reimers, P., and Goebbels, J. New possibilities of non-destructive evaluation by X-ray computed tomography. *Mater. Eval. 41* (1983), 732–737.

[112] Reisinger, S., Kasperl, S., Franz, M., Hiller, J., and Schmid, U. Simulation-Based Planning of Optimal Conditions for Industrial Computed Tomography. In *Proceedings of the International Symposium on Digital industrial Radiology and Computed Tomography* (2011).

[113] Reiter, M., Malik, M., Heinzl, C., Salaberger, D., Gröller, E., Hubert Lettenbauer, H., and Kastner, J. Improvement of X-Ray image acquisition using a GPU based 3DCT simulation tool. In *Proceedings of the International Conference on Quality Control by Artificial Vision* (2009).

[114] Rocha, J.G., Correia, J.H. and Lanceros-Mendez, S. Modeling of the performance of scintillator based x-ray detectors. In *Proceedings of IEEE* (2004), vol. 3, Proceedings of IEEE, pp. pp 257–1260.

[115] Rouse, J.E. *Characterisation of impact damage in carbon fibre reinforced plastics by 3d X-ray tomography.* PhD thesis, The University of Manchester, 2012.

[116] Rüegsegger, P., Koller, B. and Müller, R. A microtomographic system for the nondestructive evaluation of bone architecture. *Calcified Tissue International 58(1)* (1996), 24–29.

[117] Saewert, H.-C., Fiedler, D., Bartscher, M., and Wäldele, F. Obtaining dimensional information by industrial CT scanning - present and prospective process chain. In *Proceedings of the International Symposium on Digital industrial Radiology and Computed Tomography* (2003).

[118] Salvo, L. et al. X-ray micro-tomography an attractive characterization technique in materials science. *Nuclear instruments & Methods in Physics Research Section B-Beam Interactions with Materials and Atoms* (2003), 200 273–286.

[119] Savio, E., De Chiffre, L., and Schmitt, R. Metrology of freeform shaped parts. *CIRP Ann. 56*, 2 (2007), 810–835.

[120] Schmitt, R., and Niggemann, C. Uncertainty in measurement for x-ray-computed tomography using calibrated work pieces. *Measurement Science and Technology* (2010), Vol. 21, pp. 1–9.

[121] Schmitt, R., and Niggemann, C. Improving the Production using X-Ray Computed Tomography - Potentials and Challenges, 2011. National conference on CT scanning - Application of CT Scanning in Industry, Danish Technological Institute Taastrup.

[122] Schwenke, H., Knapp, W., Haitjema, H., Weckenmann, A., Schmit, R., and Delbressine, F. Geometric error measurement and compensation of machines—An update. *CIRP Ann. 57* (2008), 660–675.

[123] Schwenke, H., Neuschaefer-Rube, U., and Kunzmann, H. Optical Methods for Dimensional Metrology in Production Engineering. *CIRP Ann. 51*, 2 (2002).

[124] Seger, O., and Seger, M. M. The MATLAB/C program take - a program for simulation of X-ray projections from 3D volume data. Demonstration of beam-hardening artefacts in subsequent CT reconstruction. Tech. Rep. LiTH-ISY-R-2682, Dept. EE, Linköping University, SE-581 83 Linköping, Sweden, March 2005.

[125] Siewerdsen, J. H., Waese, A. M., Moseley, D. J., Richard, S. and Jaffray, D. A. Spektr: A computational tool for x-ray spectral analysis and imaging system optimization. *Med. Physics* (2004), Vol. 33, 3057.

[126] Simon, M., Tiseanu, I., Sauerwein, C., Yoo, S.-M., and Cho, I.-S. Advanced multi-sensor and multi-source industrial computed tomography systems. *Insight* (2008), Vol. 50.

[127] Smith, S. W. *The Scientist and Engineer's Guide to Digital Signal Processing, For more information visit the book's website at: www.DSPguide.com.* 1997-1998.

[128] Souvagie, C. X-stralen CT-proces simulatie als hulpmiddel voor dimensionele CT metrologie. Master's thesis, Katholieke Universiteit Leuven, Department of Mechanical Engineering, 2012.

[129] Stopp, F., Winne, C., Jank, E., and Keeve, E. Quality evaluation of image recording strategies for limited angle tomography. *Tsinghua Science and Technology 15* (2010), pp 25–29.

[130] Suetens, P. *Fundamentals of Medical Imaging.* 2009.

[131] Sukowski, F., and Uhlmann, N. *Monte Carlo Simulations in NDT, Applications of Monte Carlo Method in Science and Engineering, Prof. Shaul Mordechai (Ed.), ISBN: 978-953-307-691-1,.* Intech, 2011.

[132] Sun, Y., Hou, Y., Zhao, F., and Hu, J. A Calibration Method for Misaligned Scanner Geometry in Cone-beam Computed Tomography. *NDT&E International* (2006), Vol. 39, pp. 499–513.

[133] Tan, Y. *Scanning and post-processing parameter optimization for CT dimensional metrology.* PhD thesis, Katholieke Universiteit Leuven, Department of Mechanical Engineering, 2015.

[134] Tan, Y., Kiekens, K., Welkenhuyzen, F., Angel, J., De Chiffre, L., Kruth, J.-P. and Dewulf, W. Simulation-aided investigation of beam hardening induced errors in CT dimensional metrology. In *Proceedings of the International Symposium on Measurement Technology and Intelligent Instruments* (2013).

[135] Tan, Y., Kiekens, K., Welkenhuyzen, F., Angel, J., De Chiffre, L., Kruth, J.-P. and Dewulf, W. Simulation-aided investigation of beam hardening induced errors in CT dimensional metrology. *Measurement Science and Technology 25* (2014).

[136] Tan, Y., Kiekens, K., Welkenhuyzen, F., Kruth, J.-P. and Dewulf, W. Beam hardening correction and its influence on the measurement accuracy and repeatability for CT dimensional metrology applications. In *Proceedings of the International Conference on Industrial Computed Tomography* (2012).

[137] Tan, Y., Kiekens, K., Welkenhuyzen, F., Kruth, J.-P. and Dewulf, W. Defining the Optimal Beam Hardening Correction Parameters for CT Dimensional Metrology Applications. In *Proceedings of the International Conference on Competitive Manufacturing* (2013).

[138] Thierry, R., Miceli, A., and Hofmann, J. Hybrid simulation of scattering distribution in cone beam CT. In *Proceedings of the International Symposium on Digital industrial Radiology and Computed Tomography* (2007).

[139] Tucker, D.M., Barnes, G.T. and Chakraborty, D.P. çsemi empirical model for generating tungsten target x-ray spectra. *Med. Physics* (1991), 18(2):211–8.

[140] Tucker, D.M., Barnes, G.T. and Wu, X.Z. Molybdenum target x-ray spectra: a semiempirical model. *Med. Physics* (1991), 18(3):402–7.

[141] Van Bael, S., Kerckhofs, G., Moesen, M., Pyka, G., Schrooten, J. and Kruth, J.-P. Micro-ct-based improvement of geometrical and mechanical controllability of selective laser melted ti6al4v porous structures. *Micro-CT-based improvement of geometrical and mechanical controllability of selective laser melted Ti6Al4V porous structures 528* (2011), 7423–7431.

[142] Van de Casteele, E., Van Dyck, D., Sijbers, J., and Raman, E. An energy-based beam hardening model in tomography. *Phys. Med. Biol* (2002), Vol. 47, pp. 4181–4190.

[143] Van Gestel, N. *Determining Measurement Uncertainties of Feature Measurements on CMMs.* PhD thesis, Katholieke Universiteit Leuven, Department of Mechanical Engineering, 2011.

[144] Van Marcke, P., and Swennen, R. Optimising X-ray Computed Tomography Images with a CT-simulator. *Advances in X-ray Tomography for Geomaterials* (2006), 161–166.

[145] Varian. `http://www.varian.com/us/xray/products/digital_radiography/paxscan_products.html`.

[146] VDI/VDE 2630 Part 1.2. *Computed tomography in dimensional measurement - Influencing variables on measurement results and recommendations for computed tomography dimensional measurements.* VDI/VDE, 2008.

[147] VDI/VDE 2630 Part 1.3. *Accuracy of coordinate measuring machines - Characteristics and their testing; Guideline for the application of DIN EN ISO 10360 for coordinate measuring machines with CT-sensors.* VDI/VDE, 2009.

[148] VDI/VDE 2630 Part 1.4. *Computed tomography in dimensional measurement - Measurements procedure and comparability.* VDI/VDE, 2008.

[149] Vettergren, J. Computed Tomographic Techniques, A survey. Tech. Rep. Reports from MSI: Report 05069, Växjö University, 2005.

[150] Vogeler, F., Verheecke, W., Voet, A., Kruth, J.-P. and Dewulf, W. Positional Stability of 2D X-ray Images for Computer Tomography. In *Proceedings of the International Symposium on Digital industrial Radiology and Computed Tomography* (2011).

[151] Vogeler, F., Welkenhuyzen, F., Bleys, P., Kruth, J.-P., Van Gestel, N., Voet, A. and Mingneau, J. 3D measurement techniques, E-learning.

[152] Volume graphics. *VGStudio Max Reference Manual.*

[153] Wang, X., Han, Y., and Si, J. Non-uniformity emendation technique for amorphous silicon flat-panel detectors used for industrial X-ray digital radiography. *Measurement* (2008), Vol. 41, pp. 817–822.

[154] Weckenmann, A., Estler, T., Peggs, G., and McMurtry, D. Probing Systems in Dimensional Metrology. *CIRP Ann. 53*, 2 (2004), 657–684.

[155] Weckenmann, A., and Krämer, P. Assessment of measurement uncertainty caused in the preparation of measurements using computed tomography. In *Proceedings of the XIX IMEKO world congress, Fundamental and Applied Metrology* (2009).

[156] Weckenmann, A., and Krämer, P. Computed Tomography for Application in Manufacturing Metrology. In *D.S. Rozhdestvensky Optical Society (Publ.): Proc. 9th Int. Symp. On Measurement and Intelligent Instruments - ISMTII* (2009), pp. 1:11–26.

[157] Weckenmann, A., and Krämer, P. Predetermination of measurement uncertainty in the application of computed tomography. In *Proc. of the 11th CIRP Int. Conf. on Computer Aided Tolerancing (CAT 2009)* (2009), pp. 317–330.

[158] Welkenhuyzen, F. Report. PhD course Measurement uncertainty estimation using statistical methods. Responsibles: Professor Leonardo De Chiffre, Professor Giulio Barbato and Dr Gianfranco Genta. Tech. rep., Technical University of Denmark (DTU), 2013.

[159] Welkenhuyzen, F., Boeckmans, B., Kruth, J.-P., Dewulf, W. and Voet, A. Simulation of X-ray projection images for dimensional CT metrology. In *Proceedings of the 5th international conference on optical measurement techniques for structures and systems* (2012).

[160] Welkenhuyzen, F., Boeckmans, B., Tan, Y., Kiekens, K., Dewulf, W. and Kruth, J.-P. Investigation of the kinematic system of a 450 kV CT scanner and its influence on dimensional CT metrology applications. In *Proceedings of the International Conference on Industrial Computed Tomography* (2014).

[161] Welkenhuyzen, F., Indesteege, D., Boeckmans, B., Kiekens, K., Tan, Y., Dewulf, W. and Kruth, J.-P. Accuracy study of a 450 kV CT system with a calibrated test object. In *Proceedings of the 11th International Symposium on Measurement and Quality Control (ISMQC-2013)* (2013).

[162] Welkenhuyzen, F., Kiekens, K., Pierlet, M., Dewulf, W., Bleys, P., Kruth, J.-P. and Voet, A. Industrial computer tomography for dimensional metrology: Overview of influence factors and improvement strategies. In *Proceedings of the 4th international conference on optical measurement techniques for structures and systems* (2009).

[163] Wenig, P., and Kasperl, S. Examination of the measurement uncertainty on dimensional measurements by Xray computed tomography. In *Proceedings of the European Conference on Non-Destructive Testing (ECNDT)* (2006).

[164] Werth Messtechnik, 2011. `http://www.werth.de/de/unser-angebot/`.

[165] Wevers, M., De Meester, P., Lodewijckx, M., Ni, Y., Marchal, G., Jiang, Y., Dequeker, J., Geusens, P., Vandeursen, H., De Ridder, D., Baert, L., Pittomvils, G., and R., B. Application of microfocus X-ray radiography in materials and medical research. *NDT&E International 26*, 3 (1993), 135–140.

[166] Wiacker, H. Dimensionsanalyse mit der Computertomografie am Beispiel Turbinenschaufel vermessung, 2. Seminar Computertomografie, DGZfP BB 22, 1991.

[167] Wilhelm, R.G., Hocken, R. and Schwenke, H. Task specific uncertainty in coordinate measurement. *CIRP Ann. 50*, 2 (2001), 553–563.

[168] Yaffe, M.J. and Rowlands, J.A. . X-ray detectors for digital radiography. *Physics in Medicine and Biology 42*, 1 (1997), 1.

[169] Zou, J., Hu, Z., Gui, J., Junyan Rong, J., Yanming Li, Y., and Zheng, H. Geant4-Based Monte Carlo Simulator for Fan-and Cone-Beam X-ray CT. In *Proceeding of the 4th International Conference on Bioinformatics and Biomedical Engineering (iCBBE)* (2010).

Curriculum vitae

Personal Data

Frank Welkenhuyzen

° October 29th 1983, Maaseik
Address: Vlierhof 83, 3550 Heusden-Zolder
E-mail: frank.welkenhuyzen@gmail.com

Education

- **2010-2016: PhD researcher in Engineering Science: Mechanical Engineering**, KU Leuven.
- **2004-2007: Master of Science in Mechanical-Electrotechnical Engineering**, Katholieke Universiteit Leuven.

  Master thesis: *Verbetering van de nauwkeurigheid van de meetprobe bij mobiele 3D-coördinaten meetmachines*
- **2001-2004: Bachelor in Engineering**, Katholieke Universiteit Leuven.
- **1995-2001: Secondary school**: Mathematics-Sciences, Stedelijke Humaniora, Dilsen.

List of publications

Articles in internationally reviewed scientific journals

- Welkenhuyzen, F., Boeckmans, B., Probst, G., Dewulf, W., Kruth, J.-P. Simulation of projection images for dimensional accuracy analysis of Computed Tomography. In submission.
- Boeckmans, B., Zhang, M., Welkenhuyzen, F., Kruth, J.-P. Determination of Aspect Ratio Limitations, Accuracy and Repeatability of a Laser Line Scanning CMM Probe. *Int. J. of Automation Technology*, vol. 9, no. 5, 2015, pp. 466-471.
- Tan, Y., Kiekens, K., Welkenhuyzen, F., Angel, J., De Chiffre, L., Kruth, J.-P., Dewulf, W. Simulation-aided investigation of beam hardening induced errors in CT dimensional metrology. *Measurement Science & Technology*, vol. 25, no. 6, 2014.
- Dewulf, W., Kiekens, K., Tan, Y., Welkenhuyzen, F., Kruth, J.-P. Uncertainty Determination and Quantification for Dimensional Measurements with Industrial Computed Tomography. *CIRP Annals.* Manufacturing Technology, vol. 62, no. 1, 2013, pp. 535-538.
- Van Gestel, N., Bleys, P., Welkenhuyzen, F., Kruth, J.-P. Influence of feature form deviations on CMM measurement uncertainties. *International Journal of Precision Technology*, vol. 2, no. 2-3, 2011, pp. 192-210.
- Kiekens, K., Welkenhuyzen, F., Tan, Y., Bleys, P., Voet, A., Kruth, J.-P., Dewulf, W. A test object with parallel grooves for calibration and accuracy assessment of industrial CT metrology. *Measurement Science & Technology*, vol. 22, 2011, pp. 1-7.
- Kruth, J.-P., Van Gestel, N., Bleys, P., Welkenhuyzen, F. Uncertainty determination for CMMs by Monte Carlo simulation integrating feature form deviations. *CIRP. Annals*, vol. 58, no. 1, 2009, pp. 463-466.

Papers at international conferences and symposia, published in full in proceedings

- Boeckmans, B., Tan, Y., Welkenhuyzen, F., Guo, Y., Dewulf, W., Kruth, J.-P. Roughness offset differences between contact and non-contact measurements. In *Proceedings of the 15th international conference of the european society for precision engineering and nanotechnology*, 1-5 June 2015, Leuven, 2015, pp. 189-190.
- Qian, J., Kempen, K., Welkenhuyzen, F., Vanderauwera, W., Wang, J., Yang, C., Kruth, J.-P., Reynaerts, D. Manufacturing of μIM Mould Inserts with AMed Cooling Channels. In *Proceedings of the 4M/ICOMM2015 Conference*, 31 March - 2 April 2015, Milano, 2015, pp. 587-590.
- Boeckmans, B., Zhang, M., Welkenhuyzen, F., Dewulf, W., Kruth, J.-P. (2015). CMM Sensor Evaluation Method with Machine Error Exclusion. In: *Laser Metrology and Machine Performance XI. 11th International Conference and Exchibition on Laser Metrolgy, Machine Tool, CMM & Robotic Performance.* pp. 248-257.
- Welkenhuyzen, F., Boeckmans, B., Tan, Y., Kiekens, K., Dewulf, W., Kruth, J.-P. Investigation of the Kinematic System of a 450 kV CT Scanner and its Influence on Dimensional CT Metrology Applications. In *Proceedings of the 5th International Conference on Industrial Computed Tomography*, 25-28 February 2014, Wels, Austria, 2014, pp. 217-225.
- Kempen, K., Welkenhuyzen, F., Qian, J., Kruth, J.-P. Dimensional accuracy of internal channels in SLM produced parts. In *Proceedings of the ASPE spring topical meeting.* 13-16 april 2014, California, US, 2014.
- Boeckmans, B., Zhang, M., Welkenhuyzen, F., Dewulf, W., Kruth, J.-P. Comparison of Aspect Ratio, Accuracy and Repeatability of a Laser Line Scanning Probe and a Tactile Probe. In *Proceedings of the 10th IMEKO Symposium: Laser Metrology for Precision Measurement and Inspection in Industry (LMPMI)*, 2-5 September 2014, Tsukuba, Japan, 2014.
- Tan, Y., Kiekens, K., Welkenhuyzen, F., Angel, J., De Chiffre, L., Kruth, J.-P., Dewulf, W. Simulation-aided investigation of beam hardening induced errors in CT dimensional metrology. In *Proceedings of the International Symposium on Measurement Technology and Intelligent Instruments*, 1-5 July 2013, Aachen, Germany, 2013, pp. 1-7.
- Tan, Y., Kiekens, K., Welkenhuyzen, F., Kruth, J.-P., Dewulf, W. Defining the Optimal Beam Hardening Correction Parameters for CT Dimensional

Metrology Applications. In *Proceedings of the International Conference on Competitive Manufacturing.* 30 January - 1 February 2013, Stellenbosch, South Africa, 2013, pp. 137-143.

- Boeckmans, B., Welkenhuyzen, F., Kruth, J.-P. Accuracy verification of a laser line scanner probe. In *Laser Metrology and Machine Performance.* March 2013, Buckinghamshire, UK, 2013, pp. 279-288.

- Welkenhuyzen, F., Indesteege, D., Boeckmans, B., Kiekens, K., Tan, Y., Dewulf, W., Kruth, J.-P. Accuracy study of a 450 kV CT system with a calibrated test object. In *Proceedings of the 11th IMEKO TC14 International Symposium on Measurement and Quality Control (ISMQC 2013).* 11-13 September 2013, Cracow, Poland, 2013, pp. 297-300.

- Kiekens, K., Tan, Y., Welkenhuyzen, F., Kruth, J.-P., Dewulf, W. Uncertainty Determination for Dimensional Measurements with Computed Tomography. In *Proceedings of the International Conference on Industrial Computed Tomography.* 19-21 September 2012, Wels, Austria, 2012.

- Welkenhuyzen, F., Boeckmans, B., Kruth, J.-P., Dewulf, W., Voet, A. Simulation of X-ray projection images for dimensional CT metrology. In *proceedings of the 5th international conference on optical measurement techniques for structures and systems.* Antwerp, 2012, pp. 477-487.

- Tan, Y., Kiekens, K., Welkenhuyzen, F., Kruth, J.-P., Dewulf, W. Beam hardening correction and its influence on the measurement accuracy and repeatability for CT dimensional metrology applications. In *Proceedings of the International Conference on Industrial Computed Tomography.* 19-21 September 2012, Wels, Austria, 2012.

- Lauwers, B., Kruth, J.-P., Bleys, P., Ten Haaf, P., Saelen, S., Van Gestel, N., Welkenhuyzen, F., Mielnik, K. Evaluation and Implementation of an Integrated Measuring System within a Multi-tasking Machining Centre. In *Proceedings of 4th CIRP International Conference on High Performance Cutting.* 24-26 October 2010, Gifu, Japan, 2010, pp. 233-238.

- Kiekens, K., Welkenhuyzen, F., Tan, Y., Bleys, P., Voet, A., Dewulf, W., Kruth, J.-P. A test object for calibration and accuracy assessment in X-ray CT metrology", In *Proceedings of the 10th International Symposium on Measurement and Quality Control (ISMQC-2010).* 5-9 September 2010, Osaka, Japan, 2010.

- Welkenhuyzen, F., Kiekens, K., Pierlet, M., Dewulf, W., Bleys, P., Kruth, J.-P., Voet, A. Industrial computer tomography for dimensional metrology: Overview of influence factors and improvement strategies. In *Proceedings* *of the 4th International Conference on Optical Measurement Techniques for Structures and Systems: Optimess2009.* 25-26 May 2009, Antwerp, Belgium, 2009, pp. 401-410.

- Van Gestel, N., Welkenhuyzen, F., Bleys, P., Kruth, J.-P. Evaluation of Measurement Uncertainty Contributors for Vision CMMs. In *Proceedings of the 4th International Conference on Optical Measurement Techniques for Structures and Systems.* 25-26 May 2009, Antwerp, Belgium, 2009.

- Welkenhuyzen, F., Van Gestel, N., Bleys, P., Kruth, J.-P. Accuracy enhancement of the measuring probe for a camera based mobile CMM. In *Proceedings of the LAMDAMAP 2009 conference.* 29 June-2 July 2009, Teddington, UK, 2009.

Other journal publications / miscellaneous

- Paulus, P., Kiekens, K., Welkenhuyzen, F., Bleys, P. Time-to-market van producten drastisch ingekort met CT-scannen. In: *Metallerie*, vol. 124, 2009, pp. 25-26.

- Vogeler, F., Welkenhuyzen, F., Bleys, P., Kruth, J.-P., Van Gestel, N., Voet, A. and Mingneau, J. E-learning package: 3D measurement techniques.

FACULTY OF ENGINEERING SCIENCE
DEPARTMENT OF MECHANICAL ENGINEERING
DIVISION OF PRODUCTION ENGINEERING, MACHINE DESIGN AND AUTOMATION
Celestijnenlaan 300B box 2420
B-3001 Heverlee